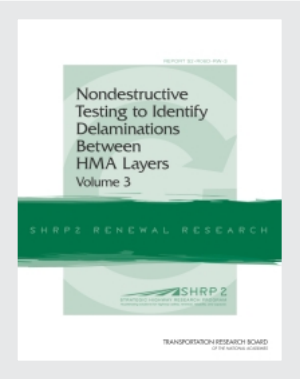

Nondestructive Testing to Identify Delaminations Between HMA Layers, Volume 3 - Controlled Evaluation Reports

DETAILS

0 pages | 8.5 x 11 | PAPERBACK
ISBN 978-0-309-43113-2 | DOI 10.17226/21936

AUTHORS

Heitzman, Michae;l Maser, Kenneth; Tran, Nam H.; Brown, Ray; Bell, Haley; Holland, Steve; Ceylan, Halil; Belli, Kimberly; and Hiltunen, Dennis

The Second
STRATEGIC HIGHWAY RESEARCH PROGRAM

SHRP 2 REPORT S2-R06D-RW-3

Nondestructive Testing to Identify Delaminations Between HMA Layers

Volume 3

MICHAEL HEITZMAN
KENNETH MASER
NAM H. TRAN
RAY BROWN
HALEY BELL
STEVE HOLLAND
HALIL CEYLAN
KIMBERLY BELLI
DENNIS HILTUNEN

National Center for Asphalt Technology at Auburn University
Alabama

TRANSPORTATION RESEARCH BOARD

WASHINGTON, D.C.
2013
www.TRB.org

Subscriber Categories

Construction
Highways
Maintenance and Preservation
Pavements

The Second Strategic Highway Research Program

America's highway system is critical to meeting the mobility and economic needs of local communities, regions, and the nation. Developments in research and technology—such as advanced materials, communications technology, new data collection technologies, and human factors science—offer a new opportunity to improve the safety and reliability of this important national resource. Breakthrough resolution of significant transportation problems, however, requires concentrated resources over a short time frame. Reflecting this need, the second Strategic Highway Research Program (SHRP 2) has an intense, large-scale focus, integrates multiple fields of research and technology, and is fundamentally different from the broad, mission-oriented, discipline-based research programs that have been the mainstay of the highway research industry for half a century.

The need for SHRP 2 was identified in *TRB Special Report 260: Strategic Highway Research: Saving Lives, Reducing Congestion, Improving Quality of Life,* published in 2001 and based on a study sponsored by Congress through the Transportation Equity Act for the 21st Century (TEA-21). SHRP 2, modeled after the first Strategic Highway Research Program, is a focused, time-constrained, management-driven program designed to complement existing highway research programs. SHRP 2 focuses on applied research in four areas: Safety, to prevent or reduce the severity of highway crashes by understanding driver behavior; Renewal, to address the aging infrastructure through rapid design and construction methods that cause minimal disruptions and produce lasting facilities; Reliability, to reduce congestion through incident reduction, management, response, and mitigation; and Capacity, to integrate mobility, economic, environmental, and community needs in the planning and designing of new transportation capacity.

SHRP 2 was authorized in August 2005 as part of the Safe, Accountable, Flexible, Efficient Transportation Equity Act: A Legacy for Users (SAFETEA-LU). The program is managed by the Transportation Research Board (TRB) on behalf of the National Research Council (NRC). SHRP 2 is conducted under a memorandum of understanding among the American Association of State Highway and Transportation Officials (AASHTO), the Federal Highway Administration (FHWA), and the National Academy of Sciences, parent organization of TRB and NRC. The program provides for competitive, merit-based selection of research contractors; independent research project oversight; and dissemination of research results.

SHRP 2 Report S2-R06D-RW-3

ISBN: 978-0-309-27295-7

Copyright Information

Note: SHRP 2 report numbers convey the program, focus area, project number, and publication format. Report numbers ending in "w" are published as web documents only.

Notice

The project that is the subject of this report was a part of the second Strategic Highway Research Program, conducted by the Transportation Research Board with the approval of the Governing Board of the National Research Council.

The members of the technical committee selected to monitor this project and review this report were chosen for their special competencies and with regard for appropriate balance. The report was reviewed by the technical committee and accepted for publication according to procedures established and overseen by the Transportation Research Board and approved by the Governing Board of the National Research Council.

The opinions and conclusions expressed or implied in this report are those of the researchers who performed the research and are not necessarily those of the Transportation Research Board, the National Research Council, or the program sponsors.

The Transportation Research Board of the National Academies, the National Research Council, and the sponsors of the second Strategic Highway Research Program do not endorse products or manufacturers. Trade or manufacturers' names appear herein solely because they are considered essential to the object of the report.

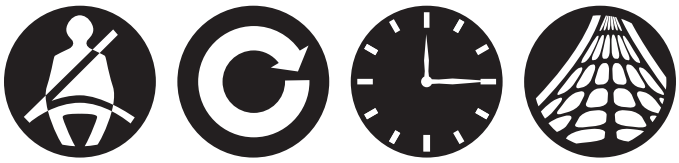

SHRP 2 Reports

Available by subscription and through the TRB online bookstore:
www.TRB.org/bookstore

Contact the TRB Business Office:
202-334-3213

More information about SHRP 2:
www.TRB.org/SHRP2

THE NATIONAL ACADEMIES

Advisers to the Nation on Science, Engineering, and Medicine

The **National Academy of Sciences** is a private, nonprofit, self-perpetuating society of distinguished scholars engaged in scientific and engineering research, dedicated to the furtherance of science and technology and to their use for the general welfare. On the authority of the charter granted to it by Congress in 1863, the Academy has a mandate that requires it to advise the federal government on scientific and technical matters. Dr. Ralph J. Cicerone is president of the National Academy of Sciences.

The **National Academy of Engineering** was established in 1964, under the charter of the National Academy of Sciences, as a parallel organization of outstanding engineers. It is autonomous in its administration and in the selection of its members, sharing with the National Academy of Sciences the responsibility for advising the federal government. The National Academy of Engineering also sponsors engineering programs aimed at meeting national needs, encourages education and research, and recognizes the superior achievements of engineers. Dr. Charles M. Vest is president of the National Academy of Engineering.

The **Institute of Medicine** was established in 1970 by the National Academy of Sciences to secure the services of eminent members of appropriate professions in the examination of policy matters pertaining to the health of the public. The Institute acts under the responsibility given to the National Academy of Sciences by its congressional charter to be an adviser to the federal government and, on its own initiative, to identify issues of medical care, research, and education. Dr. Harvey V. Fineberg is president of the Institute of Medicine.

The **National Research Council** was organized by the National Academy of Sciences in 1916 to associate the broad community of science and technology with the Academy's purposes of furthering knowledge and advising the federal government. Functioning in accordance with general policies determined by the Academy, the Council has become the principal operating agency of both the National Academy of Sciences and the National Academy of Engineering in providing services to the government, the public, and the scientific and engineering communities. The Council is administered jointly by both Academies and the Institute of Medicine. Dr. Ralph J. Cicerone and Dr. Charles M. Vest are chair and vice chair, respectively, of the National Research Council.

The **Transportation Research Board** is one of six major divisions of the National Research Council. The mission of the Transportation Research Board is to provide leadership in transportation innovation and progress through research and information exchange, conducted within a setting that is objective, interdisciplinary, and multimodal. The Board's varied activities annually engage about 7,000 engineers, scientists, and other transportation researchers and practitioners from the public and private sectors and academia, all of whom contribute their expertise in the public interest. The program is supported by state transportation departments, federal agencies including the component administrations of the U.S. Department of Transportation, and other organizations and individuals interested in the development of transportation. **www.TRB.org**

www.national-academies.org

SHRP 2 STAFF

Ann M. Brach, *Director*
Stephen J. Andrle, *Deputy Director*
Neil J. Pedersen, *Deputy Director, Implementation and Communications*
James Bryant, *Senior Program Officer, Renewal*
Kenneth Campbell, *Chief Program Officer, Safety*
JoAnn Coleman, *Senior Program Assistant, Capacity and Reliability*
Eduardo Cusicanqui, *Financial Officer*
Walter Diewald, *Senior Program Officer, Safety*
Jerry DiMaggio, *Implementation Coordinator*
Shantia Douglas, *Senior Financial Assistant*
Charles Fay, *Senior Program Officer, Safety*
Carol Ford, *Senior Program Assistant, Renewal and Safety*
Elizabeth Forney, *Assistant Editor*
Jo Allen Gause, *Senior Program Officer, Capacity*
Rosalind Gomes, *Accounting/Financial Assistant*
Abdelmename Hedhli, *Visiting Professional*
James Hedlund, *Special Consultant, Safety Coordination*
Alyssa Hernandez, *Reports Coordinator*
Ralph Hessian, *Special Consultant, Capacity and Reliability*
Andy Horosko, *Special Consultant, Safety Field Data Collection*
William Hyman, *Senior Program Officer, Reliability*
Michael Marazzi, *Senior Editorial Assistant*
Linda Mason, *Communications Officer*
Reena Mathews, *Senior Program Officer, Capacity and Reliability*
Matthew Miller, *Program Officer, Capacity and Reliability*
Michael Miller, *Senior Program Assistant, Capacity and Reliability*
David Plazak, *Senior Program Officer, Capacity*
Onno Tool, *Visiting Professional*
Dean Trackman, *Managing Editor*
Connie Woldu, *Administrative Coordinator*
Patrick Zelinski, *Communications/Media Associate*

ACKNOWLEDGMENTS

This work was sponsored by the Federal Highway Administration in cooperation with the American Association of State Highway and Transportation Officials. It was conducted in the second Strategic Highway Research Program, which is administered by the Transportation Research Board of the National Academies. The project was managed by Dr. Monica Starnes, Senior Program Officer for SHRP 2 Renewal.

The team recognizes the technical input of the research team's expert panel. In addition to providing the team with valuable comments, the highway agency team members assisted with identification and support of field evaluation sites. The members of the expert panel are Jim Musselman, the Florida Department of Transportation (DOT); Kim Willoughby, the Washington State DOT; Andrew Gisi, the Kansas DOT; Nadarajah Sivaneswaran, FHWA; John Harvey, University of California, Davis; and Harold Von Quintus, Applied Research Associates.

The team recognizes the support of the NDT technology firms that expended their own resources to provide NDT equipment and software to the study. The companies that supported the project were Geophysical Survey Systems, Inc.; MALA AB; 3d-Radar (a Curtiss-Wright Company); Geomedia Research and Development; Olson Instruments, Inc. and Olson Engineering Inc.; and Infrared Cameras, Inc. The study could not have been completed without their generous assistance.

The team especially recognizes the efforts of the hardware and software development staffs of 3d-Radar and Olson Instruments, Inc., for improving the capabilities of their NDT technologies to meet the needs of highway agencies.

FOREWORD

Monica A. Starnes, Ph.D., *Senior Program Officer, Renewal*

Asphalt pavements with delamination problems experience considerable early damage because delaminations provide paths for moisture damage and the development of damage such as stripping, slippage cracks, and pavement deformation. Early detection of the existence, extent, and depth of delaminations in asphalt pavements is key for determining the appropriate rehabilitation strategy and thus extending the life of the given pavement.

This report presents the findings of the first two phases of SHRP 2 Renewal Project R06D, Nondestructive Testing to Identify Delaminations Between HMA Layers. The main objective of the project was to develop nondestructive testing (NDT) techniques capable of detecting and quantifying delaminations in HMA pavements. The NDT techniques should be applicable to construction, project design, and network-level assessments.

During Phase 1 of the project, the research team evaluated NDT methods that could potentially detect the most typical delaminations in asphalt pavements. Both laboratory and field testing were conducted during this task. Based on the findings from this testing, the manufacturers of two promising technologies conducted further development of their products to meet the goals of this project in Phase 2. The two technologies advanced in this research were ground-penetrating radar (GPR) and impact echo/spectral analysis of surface waves (IE/SASW).

Additionally, the project developed guidelines and piloted both NDT technologies in collaboration with highway agencies. Once completed, the results from this additional scope of work will be published as an addendum to this report.

CONTENTS

CHAPTER 1

Controlled Laboratory and Field Evaluations: Construction Report

This chapter was prepared by Dr. Nam Tran and Dr. Michael Heitzman from the National Center for Asphalt Technology (NCAT). It summarizes the planning and construction of the test slabs for controlled laboratory evaluations and the construction of the sections at the NCAT Pavement Test Track. The chapter concludes with a list of lessons learned as the construction progressed.

Task 6 was coordinated by Dr. Tran, and the data analysis was performed by the specialized research groups. To accomplish this task, three subtasks were conducted. Each subtask defined a specific set of activities, but the chronological sequence of the subtasks was divided by the desired temperature and moisture condition of the test pavement. This sequence of testing required each equipment vendor to bring their nondestructive testing (NDT) systems to the NCAT twice. For efficiency of the research and the NDT equipment vendors' time, the measurements for Subtasks 6A and 6B under a prescribed climate condition were obtained at the same time.

- Subtask 6A—Conduct Controlled Laboratory Evaluation.
- Subtask 6B—Conduct Controlled Field Evaluation.
- Subtask 6C—Refine the NDT Equipment or Software.

To conduct the controlled laboratory and field evaluations under Subtasks 6A and 6B, two asphalt slabs and ten 25-ft asphalt pavement sections were constructed at the NCAT Pavement Test Track. The following sections describe how the test slabs and pavement sections were built.

Construction of Test Slabs

Figure 1.1 illustrates the design of the delamination conditions of the two test slabs. Two types of delamination—lack of bond and stripping—were simulated at two depths. Three interface treatments were used to achieve bonded and debonded conditions at the interfaces: (a) optimum amount of tack coat to the receiving surface for achieving full bond, (b) baghouse fines from the hot-mix asphalt (HMA) plant to the receiving surface to achieve no bond, and (c) placement of a separate 1-in.-thick, uncompacted coarse fractionated RAP (reclaimed asphalt pavement) to the receiving surface to represent a stripping condition.

To facilitate construction and transportation, each of the two slabs was supported by four 4-ft by 8-ft laminated sheets of plywood. The plywood base was put on the ground, and hot asphalt tack was sprayed on the plywood surface (Figure 1.2) to ensure a good bond between the asphalt slabs and the plywood base. Then two layers of HMA with a total thickness of 4 to 6 in. were paved over the plywood sheets and carefully compacted.

Before the third asphalt layer was paved, the locations of two slabs were surveyed and marked on the pavement. Baghouse fines and RAP materials were placed on two 4-ft by 4-ft squares as shown in Figure 1.3 to simulate debonding and stripping interfaces at a 4-in. depth for Slab B. For Slab A, asphalt surface was tacked to make a good bond interface at a 4-in. depth. Then the third HMA layer that was approximately 2 in. thick was paved and carefully compacted.

After the third HMA layer was completed, the locations of two slabs were again surveyed and marked on the pavement. To create a debonded interface at a 2-in. depth for Slab A, a 4-ft by 4-ft square covered with baghouse fines was placed as shown in Figure 1.4. Hot asphalt tack was sprayed around the square to make good bond interfaces at a 2-in. depth for Slab B and the other half of Slab A. Then the last (surface) HMA layer was paved to a thickness of approximately 2 in. and carefully compacted.

After the construction was completed, two slabs were cut out of the pavement section (Figure 1.5). The locations of stripped and debonded interfaces were examined. Figure 1.6 shows Slab A, which has one half of the slab with all good bond interfaces, and the other half of the slab with a debonded interface at a depth of 2 in. Slab B, as shown in Figure 1.7, has an approximately 1-in.-thick stripped layer at a depth of approximately

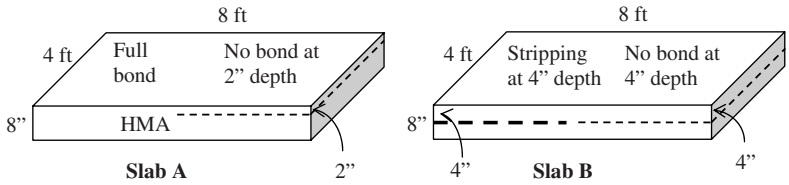

Figure 1.1. Design of two HMA slabs for controlled laboratory evaluation.

Figure 1.2. Two plywood sheets for supporting test slabs.

Figure 1.3. Two squares covered with baghouse fines and RAP materials.

Figure 1.4. One square covered with baghouse fines.

Figure 1.5. Slab A (foreground) and Slab B (background).

(a) (b)

Figure 1.6. Slab A: (a) fully bonded and (b) debonded at depth of 2 in.

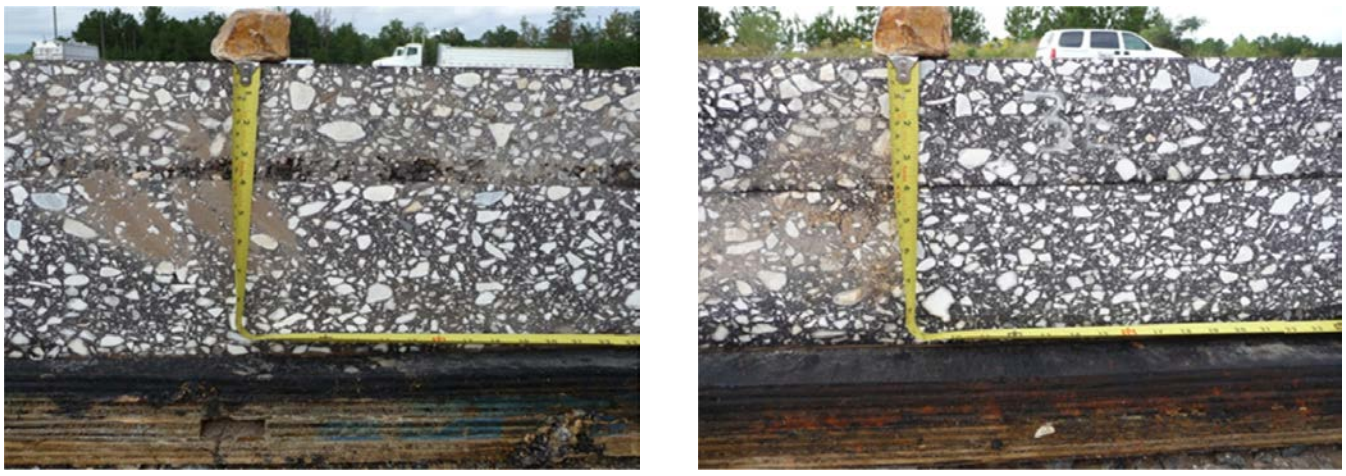

(a) (b)

Figure 1.7. Slab B: (a) stripped and (b) debonded at depth of 4 in.

4 in. in one half and a debonded interface at a depth of 4 in. in the other half. Finally, the two slabs were boarded and transported to the NCAT main laboratory for testing (Figure 1.8). Extreme care was used to lift and transport the slabs without creating tensile stress cracks.

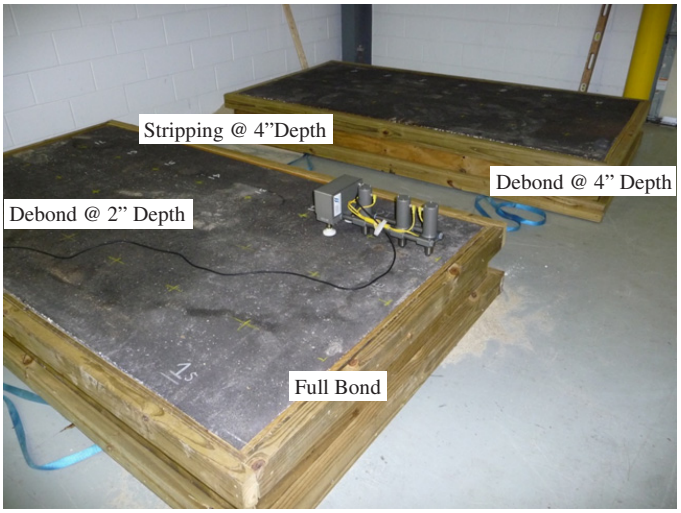

Figure 1.8. Two test slabs in the NCAT laboratory.

Construction of Pavement Test Sections at the NCAT Pavement Test Track

Ten controlled asphalt pavement test sections were built in the inside lane at the NCAT Pavement Test Track for the controlled field evaluations under Subtask 6B. There were no bond and good bond (control) at the interfaces between dense-graded asphalt layers. The research team ensured the good bond by using a tack coat and bad bond by using bond

breakers, including baghouse fines and two layers of heavy kraft paper. A 1-in.-thick, uncompacted coarse-fractionated RAP material was used to simulate a stripping condition.

The design for the controlled field test sections is illustrated in Figure 1.9. The test sections were designed to simulate 10 different bonded and debonded conditions that represent a majority of situations encountered in the top 5 in. of HMA pavements. Both full lane width and partial lane debonding conditions were constructed for evaluating the NDT methods. The partial lane debonding condition included the wheelpath and two 3-ft by 3-ft squared areas. Each test section was 12 ft wide (full paving width) and 25 ft long. To achieve compaction, the full lane width debonded areas were only 10 ft wide. The outer 1 ft was fully bonded to confine the experimental debonded areas for compaction. The detailed designs for these test sections are presented in Figures 1.10 through 1.19.

As previously described, the 10 pavement test sections were built in the inside lane adjacent to Section 5 between Stations 0+15 and 2+65. The old pavement section built between those stations was constructed in 2000 with a 24-in.-thick HMA layer on top of a 6-in.-thick aggregate base. Because there were deep cracks between Stations 50 and 75, repairs were done before construction of the delamination test sections. The asphalt and a portion of the aggregate base layers were milled at the beginning of the old pavement section (Figure 1.20). For the second half of the experimental section, the old asphalt layer was milled approximately 6 in. thick to accommodate the delamination test sections.

After the milling and backfilling work was completed, a 6-in.-thick concrete slab was constructed from Station 0+15 through Station 0+65, as shown in Figure 1.21. Layers of HMA were paved from Station 0+65 through Station 2+65 to

(text continues on page 9)

	Section 1	Section 2	Section 3	Section 4	Section 5	Section 6	Section 7	Section 8	Section 9	Section 10
Top 2-inch lift	Full bond	Full bond	Full bond	Partial no bond	No bond	Partial stripping	Full bond	Full bond	Full bond	Full bond
Bottom 3-inch lift	No bond	Full bond	Full bond	Full bond	Full bond	Full bond	Full bond	Partial stripping	Partial no bond	No bond
Existing surface	PCC	PCC	HMA	HMA	HMA	HMA	HMA	HMA	HMA	HMA

Section 1 – no bond between 5-inch HMA overlay and PCC pavement
Section 2 – full bond between 5-inch HMA overlay and PCC pavement (control section)
Section 3 – full bond between 5-inch HMA overlay and HMA pavement (control section 1 of 2)
Section 4 – partial bond between 2-inch HMA overlay surface lift and 3-inch HMA overlay leveling lift
Section 5 – no bond between 2-inch HMA overlay surface lift and 3-inch HMA overlay leveling lift
Section 6 – simulated stripping in the wheel path between 2-inch HMA surface lift and 3-inch HMA leveling lift
Section 7 – full bond between 5-inch HMA overlay and HMA pavement (control section 2 of 2)
Section 8 – simulated stripping in the wheel path between 3-inch HMA overlay leveling lift and HMA pavement
Section 9 – partial bond between 3-inch HMA overlay leveling lift and HMA pavement
Section 10 – no bond between 3-inch HMA overlay leveling lift and HMA pavement

PCC = Portland cement concrete.

Figure 1.9. Layout of controlled field test sections.

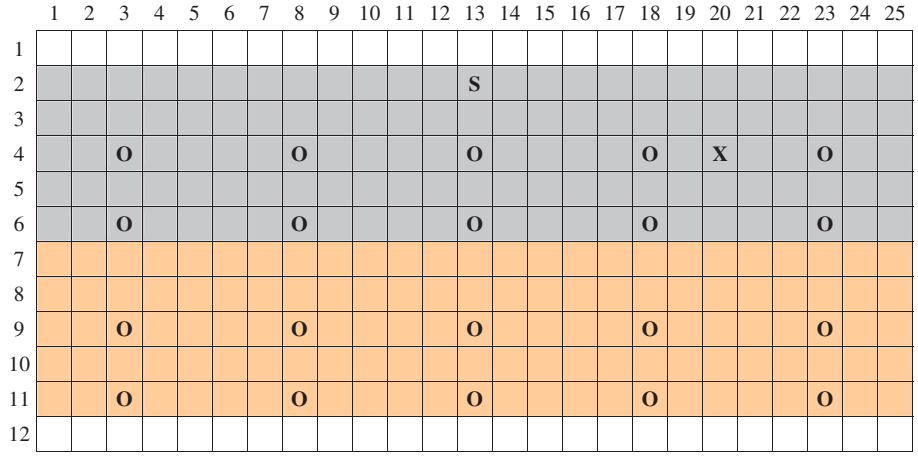

Note: Light gray = baghouse dust; tan = paper; delamination depth = ~ 5 in. (between PCC and HMA); O = locations where point-load methods were conducted; X = verification core; and S = standpipe.

Figure 1.10. Section 1: HMA over PCC (Stations 0+15 to 0+40).

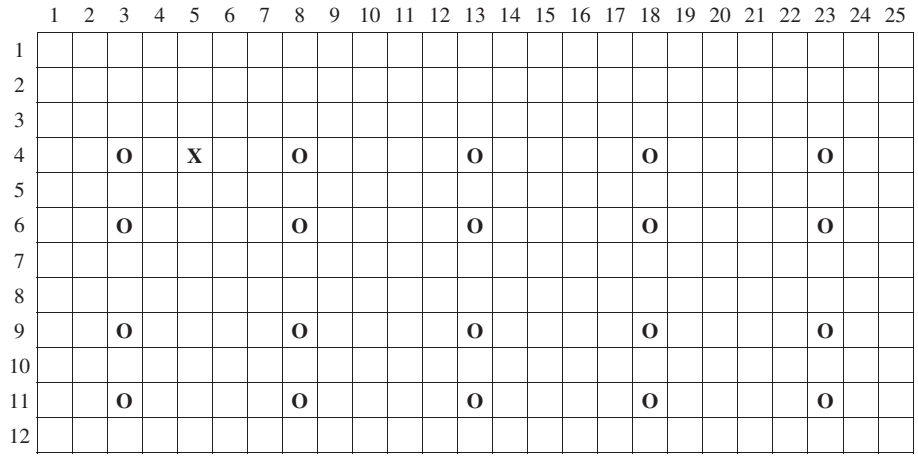

Note: No delamination; O = locations where point-load methods were conducted; and X = verification core.

Figure 1.11. Section 2: HMA over PCC, control section (Stations 0+40 to 0+65).

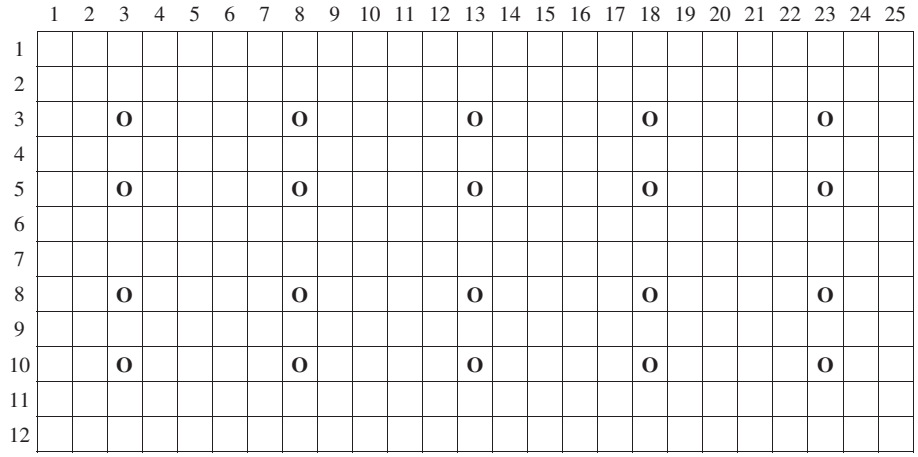

Note: No delamination; O = locations where point-load methods were conducted.

Figure 1.12. Section 3: HMA pavement, control section (Stations 0+65 to 0+90).

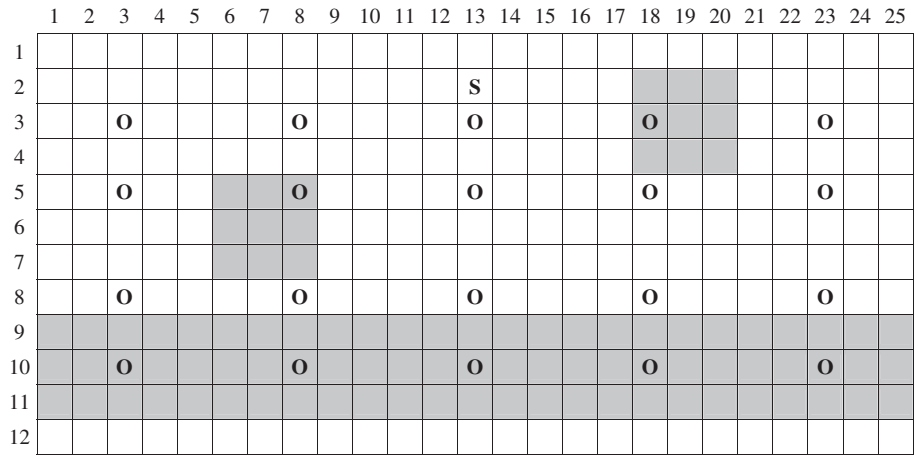

Note: Light gray = baghouse dust; delamination depth = ~ 2 in.; O = locations where point-load methods were conducted; and S = standpipe.

Figure 1.13. Section 4: HMA pavement, wheelpath delamination (Stations 0+90 to 1+15).

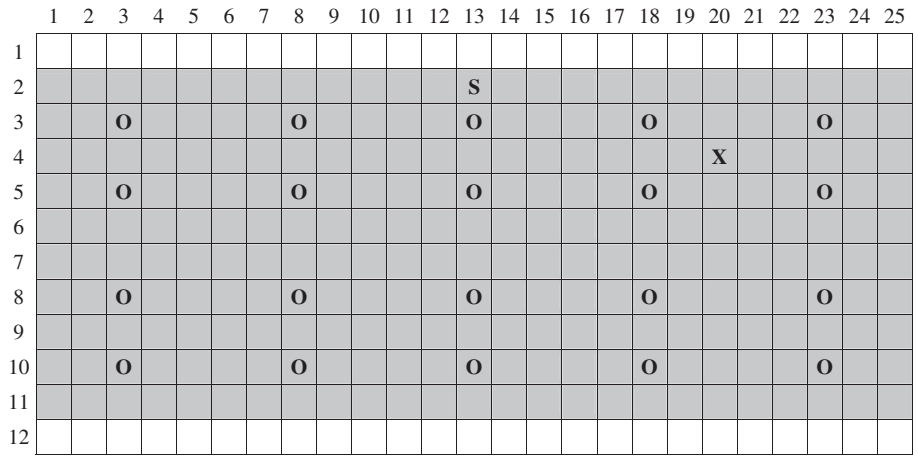

Note: Light gray = baghouse dust; delamination depth = ~ 2 in.; O = locations where point-load methods were conducted; X = verification core; and S = standpipe.

Figure 1.14. Section 5: HMA pavement, full width delamination (Stations 1+15 to 1+40).

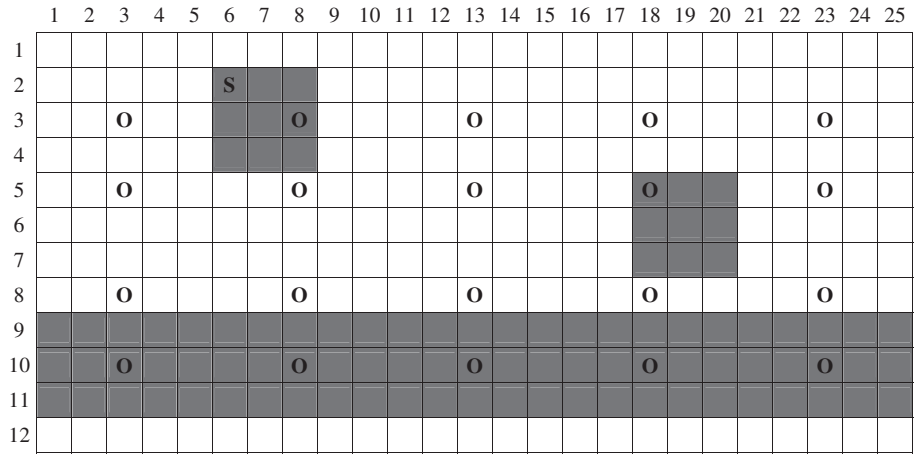

Note: Dark gray = RAP; bottom of delamination = ~ 2 in.; RAP thickness = ~ 0.75 in.; O = locations where point-load methods were conducted; and S = standpipe.

Figure 1.15. Section 6: HMA pavement, partial stripping (Stations 1+40 to 1+65).

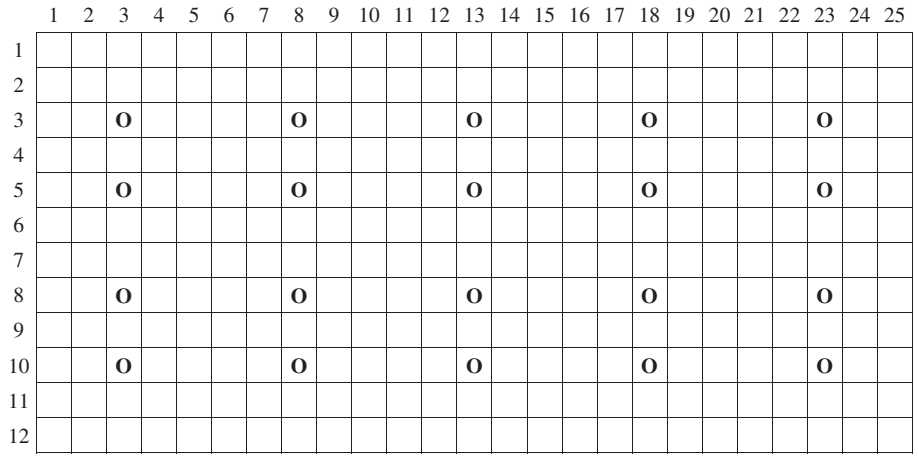

Note: No delamination; O = locations where point-load methods were conducted.

Figure 1.16. Section 7: HMA pavement, control section (Stations 1+65 to 1+90).

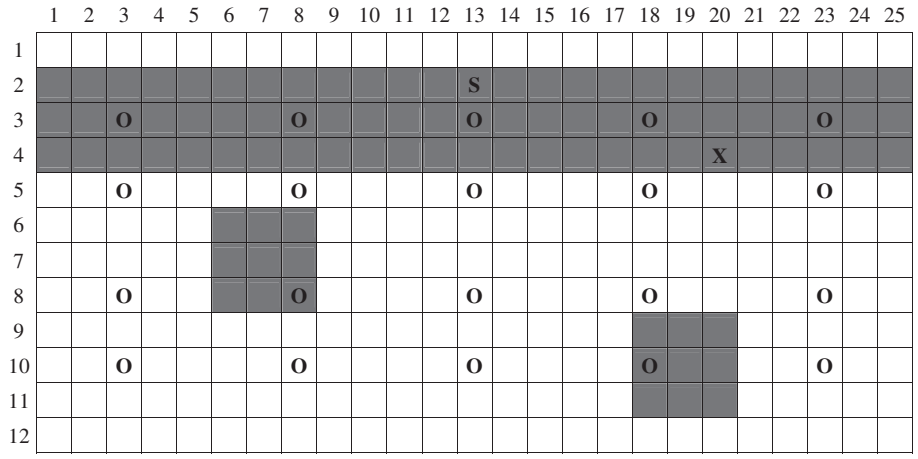

Note: Dark gray = RAP; bottom of delamination = ~ 5 in.; RAP thickness = ~ 0.75 inches; **O** = locations where point-load methods were conducted; **X** = verification core; and **S** = standpipe.

Figure 1.17. Section 8: HMA pavement, partial stripping (Stations 1+90 to 2+15).

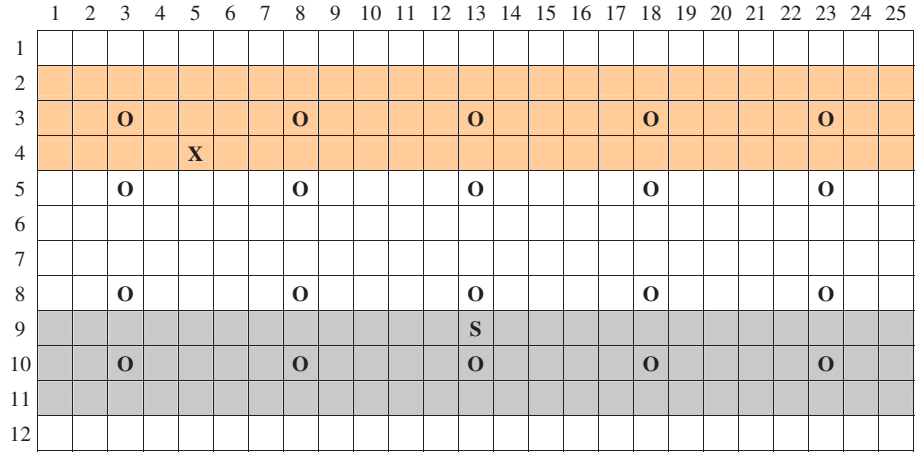

Note: Light gray = baghouse dust; tan = paper; delamination depth = ~ 5 in.; **O** = locations where point-load methods were conducted; **X** = verification core; and **S** = standpipe.

Figure 1.18. Section 9: HMA pavement, wheelpath delamination (Stations 2+15 to 2+40).

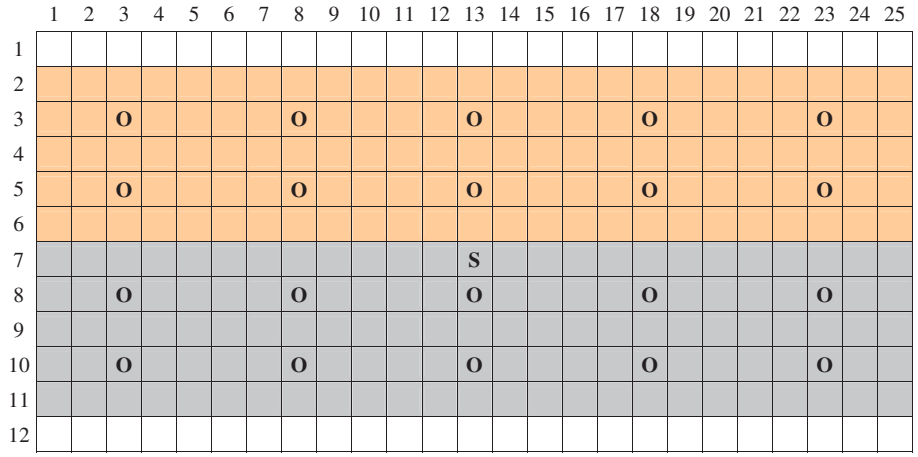

Note: Light gray = baghouse dust; tan = paper; delamination depth = ~ 5 in.; **O** = locations where point-load methods were conducted; and **S** = standpipe.

Figure 1.19. Section 10: HMA pavement, full width delamination (Stations 2+40 to 2+65).

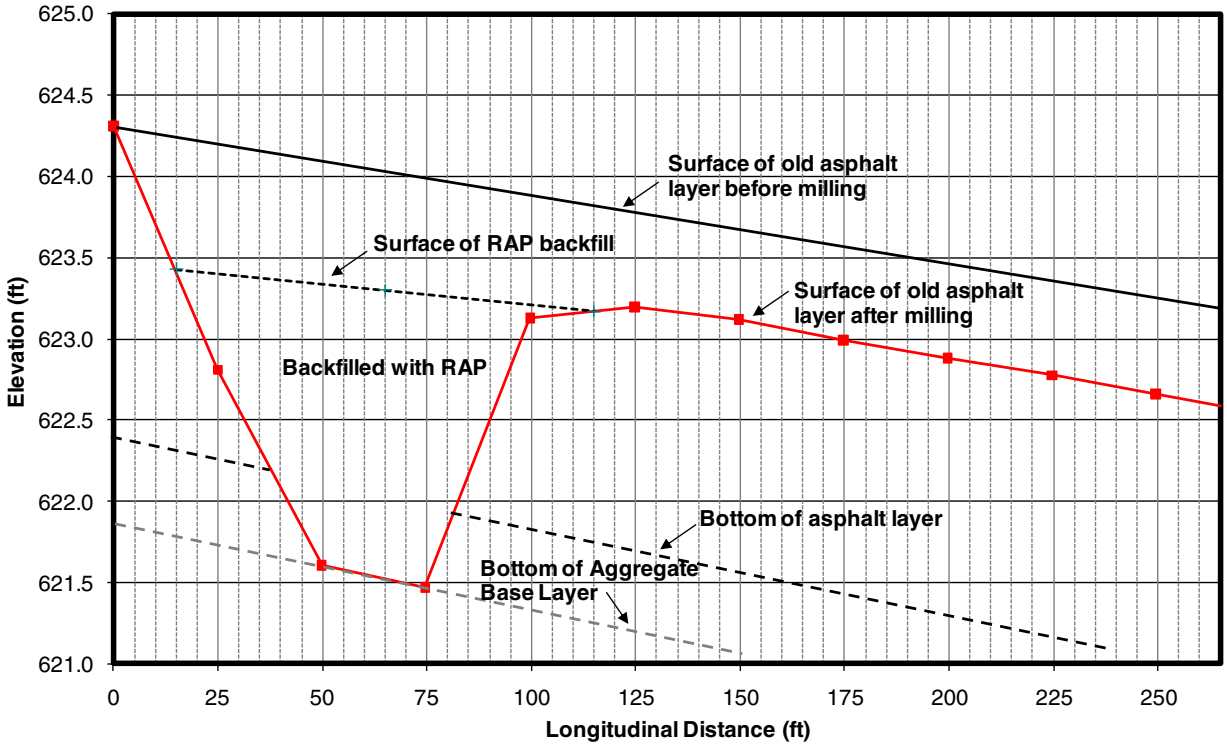

Figure 1.20. Milling and backfilling profile (Stations 0+00 to 2+65).

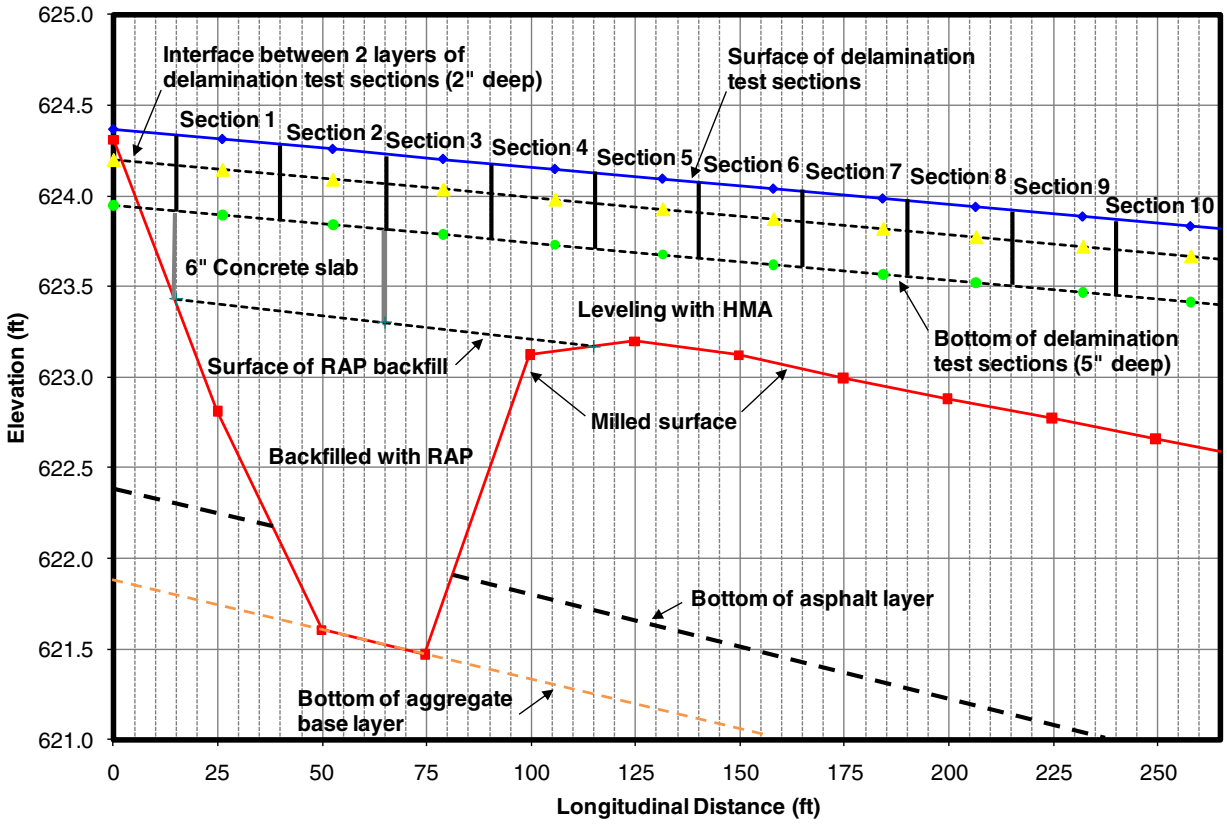

Figure 1.21. Pavement test section profile (Stations 0+00 to 2+65).

Figure 1.22. Concrete slab (Stations 0+15 to 0+65) and leveling HMA (Stations 0+65 to 2+65).

Figure 1.24. Uncompacted RAP material approximately 1 in. thick placed in Section 8 at depth of 5 in.

(continued from page 4)

prepare the bottom surface for the delamination test sections. Figure 1.22 shows the concrete slab and the leveling layers of HMA being constructed between Stations 0+65 and 2+65.

As previously illustrated in Figure 1.9, Sections 1, 8, 9, and 10 were designed to have delamination problems at 5 in. depth. As shown in Figure 1.23, two layers of brown paper were used as a bond breaker on the left, and baghouse fines material was used on the right in Section 1, as shown in Figure 1.10. As previously shown in Figure 1.17, a partial stripping condition was designed at 5 in. depth. An approximately 1-in.-thick, uncompacted RAP layer was used to create the stripping condition in the field (Figure 1.24). Following the proposed designs for Sections 9 (Figure 1.18) and 10 (Figure 1.19), the research team used two layers of brown paper on the right and baghouse fines on the left as bond breakers in the field, as shown in Figure 1.25.

No traffic was permitted on the newly paved experimental sections. A hot spray-applied asphalt tack was placed between lifts, and no tack was placed on delaminated areas. Despite the presence of the delaminated conditions, the placement of the 3-in. bottom lift for the delamination test sections went smoothly, except for two problems: the paver tires picked up the paper, and the screed ripped the top layer of paper at one location in Section 9 (Figure 1.26). The HMA layer was repaired (filled), but the double paper condition was lost.

Figure 1.23. Brown paper (left) and baghouse fines (right) used as bond breakers in Section 1 at depth of 5 in.

Figure 1.25. Brown paper and baghouse fines used at depth of 5 in. in Sections 9 and 10, near Section 8 (Figure 1.24 above).

Figure 1.26. Brown paper torn by paver at one location in Section 9.

After the bottom lift was placed and cooled down, the research team placed the delamination conditions at a depth of 2 in. Because of the problems with the paper as previously discussed, the paper was not used as a bond breaker at the 2-in. depth. Figure 1.27 shows an approximately 1-in.-thick, uncompacted RAP layer that was placed in the three locations in Section 6, as previously detailed in Figure 1.15. Baghouse fines material was used in Sections 4 and 5 as a bond breaker (Figure 1.28), and the dimensions of the delaminated areas in Sections 4 and 5 are shown in Figure 1.13 and Figure 1.14, respectively.

Figure 1.29 shows the paver placing HMA on the delaminated area of baghouse fines at a depth of 2 in. in Section 5. The placement of the 2-in.-thick HMA surface layer in Sections 4 and 5 went smoothly. As shown in Figure 1.30, the paver was moving to the delaminated areas and using uncompacted RAP materials in Section 6. The placement of the surface layer went

Figure 1.27. Approximately 1-in.-thick, uncompacted RAP materials placed in Section 6 at depth of 2 in.

Figure 1.28. Baghouse fines used as bond breaker in Sections 4 and 5 at depth of 2 in.

well at the beginning of Section 6. However, the uncompacted RAP layer may have been too thick for the 2-in.-thick surface layer, because the screed behind the paver was pushing the RAP materials to the surface toward the end of Section 6, as shown in Figure 1.31. The problem was immediately repaired in the field.

After the first round of laboratory and field evaluations under Task 6 in late October and November 2009, the research team extracted five cores to verify the interface conditions of the field test sections. Figure 1.32 shows two portions of Core 1 broke at a depth of approximately 5 in. from the pavement surface during coring. This confirmed that the baghouse fines placed on top of the concrete slab (at a depth of approximately 5 in. from the surface) caused the debonding problem at the interface, as was anticipated. Figure 1.33 shows Core 2 extracted from Section 2 (one

Figure 1.29. Paver placing 2-in. surface lift over baghouse fines in delaminated area in Section 5.

Figure 1.30. Paver moving into delaminated areas and using RAP materials in Section 6.

Figure 1.31. Paver pushing RAP materials to the surface in Section 6.

Figure 1.32. Core 1 from Station 0+35 in Section 1.

Figure 1.33. Core 2 from Station 0+45 in Section 2.

of the control sections), and this core showed no signs of delamination, as expected.

Figure 1.34 shows Core 3 extracted from Section 5. It was anticipated that the interface at approximately 2 in. depth from the pavement surface would break during coring; however, this interface was intact even though a thin layer of baghouse fines could be seen at the interface. More cores will be extracted from this test section to evaluate the delamination condition further.

Core 4 shown in Figure 1.35 was extracted from Section 8. The interface at a depth of approximately 5 in. broke during coring. This interface was delaminated with an approximately 1-in.-thick, uncompacted RAP layer. The last core (Figure 1.36) was cut from Section 9. The core broke at the 5-in. interface where two layers of brown paper were used as a bond breaker. More cores will be extracted after all the field evaluations under Task 6 are completed.

Figure 1.34. Core 3 from Station 1+35 in Section 5.

Figure 1.35. Core 4 from Station 2+10 in Section 8.

Figure 1.36. Core 5 from Station 2+20 in Section 9.

Lessons Learned

The following lessons were drawn from the experience with the construction of the test slabs for controlled laboratory evaluations at the NCAT Pavement Test Track:

- Kraft paper was not strong enough to resist tensile forces generated by HMA paving screed as the screed passed over the paper. The top layer of paper tore and slid with the screed. A heavier or stronger type of paper should be used for the upper layer.
- Delamination sections were built as overlay on a thick HMA pavement that resisted test load deflection.
- After RAP material is placed, the material should be allowed to soften from solar heating and then compacted with one pass of a rubber tire. This process tightens the material in place and reduces the potential for the paver screed to move the material ahead.
- Paper was picked up by paver tires. To avoid that problem, the paper should be covered with loose mix ahead of the paver.

References

Van Dam, T., K. Kirchner, M. Shahin, and E. Blackmon. 1987. *Consequence of Layer Separation on Pavement Performance.* Report DOT/FAA/PM-86/48. U.S. Department of Transportation, Federal Aviation Administration.

Ziari, H., and M. Khabiri. 2007. Interface Condition Interface on Prediction of Flexible Pavement Life. *Journal of Civil Engineering and Management,* Vol. 13, No. 1, pp. 71–76.

CHAPTER 2

Laboratory and Field Evaluations of Ground-Penetrating Radar Systems

This chapter was prepared by Kenneth Maser and the staff of Infrasense, Inc.

The following three ground-penetrating radar (GPR) systems were evaluated in Task 6 of this study:

- A 3-GHz horn antenna and a 2.6-GHz "ground-coupled" antenna provided by Geophysical Survey Systems, Inc. (GSSI);
- A 1.3-GHz ground-coupled antenna array (MIRA) and a 2.3-GHz ground-coupled antenna provided by MALA; and
- A swept frequency (150 MHz to 3 GHz) noncontact antenna array provided by 3d-Radar.

The GSSI system focused on the implementation of new high-frequency antennae, which would have the resolution to detect the small changes associated with pavement delamination. The specific advantage of the horn antenna is that it is noncontact and can be used to survey a pavement at much higher speeds than a ground-coupled antenna, which requires contact with the pavement. The horn antenna tested as part of this work was a prototype. The ground-coupled antenna is a manufactured product.

The MIRA system from MALA is a 16-channel array that has the advantage of obtaining greater coverage with multiple paths from the array of transmitters and receivers. Its disadvantage is that it is a ground-coupled system that is deployed at relatively low (walking) speed, and that the antenna frequency (1.3 GHz) is not optimal for delamination detection. To address these concerns, MALA also tested a 2.3-GHz ground-coupled antenna for which a high-speed deployment arrangement was available.

The 3d-Radar system uses a 29-channel array (14 transmitters and 15 receivers) producing 29 channels of data. The system is operated in a swept frequency mode from 150 MHz to 3.0 GHz, thus producing data over a range of depths. The array has the coverage advantages described above for the MIRA system. In addition, the antenna elements are housed in a single unit that operates about 6 to 12 in. above the pavement surface.

Two rounds of testing were carried out with the equipment described above. The first round took place November 8–9, 2009, and the second round took place March 7–8, 2010.

Laboratory Testing

GSSI System

Because the GSSI system involved individual antennae, a series of survey lines was marked on each test slab, and each slab was scanned by each antenna along these lines. The survey for each slab consisted of 15 parallel lines of data in the long direction, spaced 3 in. apart. The scanning process is shown in Figure 2.1. In Figure 2.1a, a small distance-encoder wheel was used to trigger data collection at regular distance intervals. In Figure 2.1b, the foam block was used to elevate the horn antenna above the slab surface, in lieu of a system for suspending the antenna over the slab.

MALA Systems

Tests were carried out with the 1.3-GHz MIRA array and with individual scans by using the 2.3-GHz antenna. Each test's slab was surveyed with a single pass of the MIRA array. Figure 2.2a shows the MIRA setup. The size of the array was enough to cover a good percentage of the width of each slab. The wooden rails were set up on each side of the tested slab to support the wheels of the MIRA cart. In the first round of testing, three passes with a 2.3-GHz antenna pair were carried out by using the cart arrangement shown in Figure 2.2. In the second round of testing, the cart supported a four-antenna array, and a parallel series of seven profiles provided complete coverage of each slab.

(a) (b)

Figure 2.1. Scanning of slabs with GSSI equipment: (a) 2.6-GHz ground-coupled antenna pair and (b) prototype 3-GHz horn antenna.

(a) (b)

Figure 2.2. Slab tests with MALA equipment: (a) MIRA system and (b) a pair of 2.3-GHz antenna.

Figure 2.3. 3d-Radar equipment setup for laboratory slabs.

3d-Radar System

The 3d-Radar system was used for slab testing, as shown in Figure 2.3. Note that the system is fairly large for the laboratory scale. Therefore, the results were more sensitive to boundary and end conditions. Also, special arrangements for supporting the wheels of the unit were made by using wooden rails outboard off the slab.

Testing of GPR Systems at Test Track

First-round testing of the GSSI and 3d-Radar systems took place November 8–9, 2009, and first-round testing for the MALA system took place November 22, 2009. Second-round testing of all systems took place March 7–8, 2010.

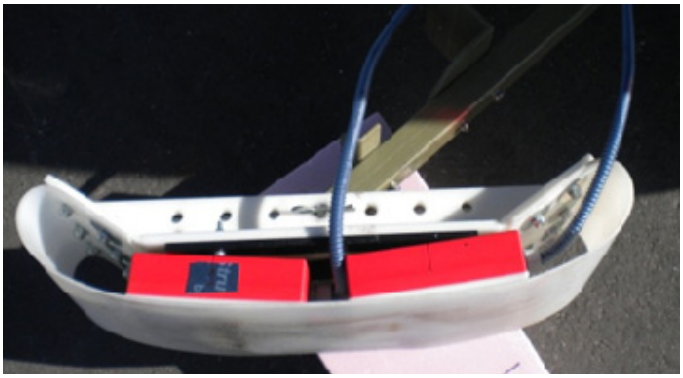

Figure 2.4. Deployment of the GSSI 2.6-GHz ground-coupled antenna pair.

GSSI Systems

GSSI tested the 2.6-GHz ground-coupled antenna pair and the prototype 3-GHz horn antenna at the test track. The initial tests used both systems, and the second round of tests focused on the 3-GHz horn. Initially, the tests were carried out on a series of data lines spaced at approximately 1 to 1.5 ft apart, with data-collection rates ranging from four to 12 scans per foot. Position of the data was registered by using a distance encoder mounted to the wheel of the test vehicle. The 2.6 GHz ground-coupled antenna pair was placed end-to-end on a skid plate, as shown in Figure 2.4. With this arrangement, both antennae were dragged along the ground at a speed of 2 to 3 mph. The horn antenna was suspended about 12 in. above the pavement surface by using a wooden beam for support, as shown in Figure 2.5. The alignment of the data lines was visually maintained by the vehicle driver using spacing markers painted on the pavement surface every 100 ft.

The second round of testing was carried out only with the 3-GHz horn. The scanning consisted of 25 lines of data spaced laterally at 6 in., with a data rate of 12 scans per foot. This closer spacing was used to obtain more detailed resolution in the subsequent imaging of the data.

MALA Systems

At the test track, the conditions were rainy, and the pavement was wet. Testing included a pair of 2.3-GHz ground-coupled antennae and a 16-channel MIRA system using 1.3-GHz antennae. At the test track, the 2.3-GHz antennae were attached end-to-end, and data was collected as a series of parallel survey lines spaced 1 ft apart. The MIRA system, which is about 30 in. wide, covered the full width of the test lane by using 6 overlapping passes. The MIRA data were collected with three transmit-receive antenna configurations: standard (monostatic), endfire array, and common midpoint (CMP) method. The MIRA system was deployed by using a wheeled cart and position of the data was obtained by using a total station (see Figure 2.6a).

The 2.3-GHz antennae were deployed with a wheeled cart, and position was recorded by using a linear distance encoder. Figures 2.6a and 2.6b show these two systems deployed on the

Figure 2.5. Deployment of GSSI 3-GHz horn antenna.

(a)

(b)

Figure 2.6. Testing of MALA systems at the test track: (a) MIRA system and (b) 2.3-GHz antennae in a cart.

test track. The second round of tests was conducted March 7–8, 2010, under more favorable field conditions and using the same antenna systems. However, the 2.3-GHz antenna cart deployed four antennae side-by-side.

3d-Radar System

In the first round of testing, 3d-Radar used a 2.3-m-wide antenna unit housing 29 antenna elements and producing 29 channels of data. The lateral coverage of this array was 2.25 m. The elements produced data by using a swept frequency with a range from 150 MHz to 2.69 GHz. A photograph of this equipment as it was deployed at the test track is shown in Figure 2.7. Signal generation and data acquisition were controlled by a unit called the "GeoScope," which was mounted on top of a tool cabinet in the bed of the test vehicle. Data location was registered by using a linear distance encoder mounted to one of the antenna support wheels. Three acquisition configurations were used to vary the density of the data in the *x* and *y* directions as well as the corresponding speed of data collection.

Full coverage of the test section was obtained by using two overlapping longitudinal runs of the system, one on the left half of the lane and one on the right half. For the second round of testing, 3d-Radar used a smaller, 21-channel unit that had a frequency sweep range of 140 MHz to 3 GHz and a lateral coverage width of 1.5 m. For the second round of tests, the test area was scanned with five parallel, overlapping longitudinal runs.

Analysis of GPR Data

The data analysis has been presented as time-depth slices, showing amplitude variations for the multiple antenna data lines within a particular time range (slice). The time slice was

(a)

(b)

(c)

Figure 2.7. 3d-Radar equipment: (a) GeoScope, (b) Side View, and (c) Rear View.

converted into a depth slice by using an assumed dielectric constant, which for asphalt is typically between 5 and 6. The depth slices presented by each organization were usually accompanied by supporting B-scan samples for individual lines of data.

Laboratory Evaluations

Round 1 laboratory testing was carried out on the slabs as described in the construction report (see this volume, Chapter 1). For Round 2 laboratory testing, water was introduced into the delaminated areas to see whether its presence would affect their detection. The results of the first- and second-round testing on Slab A are shown in Figure 2.8.

Only the GSSI 3-GHz horn antenna depth slice for Round 1 was able to detect a significant anomaly in the delaminated area. However, after the water was introduced in Round 2, each of the three systems detected an anomaly in this area.

Figure 2.9 shows the results obtained for Slab B. Note that in the Round 1 result, an anomaly was detected in the depth slice near the 4-in.-deep debond for both the GSSI and 3d-Radar systems. No anomaly was detected in the stripped area. This was surprising, because (a) the 4-in. debond should be harder to detect than the 2-in. debond would be and (b) the stripped area should be much easier to detect with GPR than the debond would be. This observation suggests that the property discontinuity at the 4-in. debond is more pronounced than one would expect at an interface that is simply debonded. Note also that, as with the 2-in. debond, the detection of the 4-in. debond was enhanced by the introduction of moisture.

Field Evaluations at the Test Track

Figure 2.10 shows the time-depth slices obtained for each GPR system in Sections 4, 5, 6, and 7 of the test track. Note that all systems were sensitive to the stripping condition located in Section 6 and to the presence of moisture in debonded areas, as noted by the standpipe locations. Other than by detecting the presence of moisture, the GPR systems were unable to detect the extensive presence of debonding at a 2-in. depth in Sections 4 and 5.

Figure 2.11 shows similar time-depth slices for Sections 8, 9, and 10. Once again, all systems were able to detect the stripping condition located in Section 8 at a depth of 4 in., as well as the presence of moisture in the 4-in.-deep debonded areas in Sections 9 and 10. None of the systems appeared capable of detecting extensive areas of debonding in Sections 9 and 10 where moisture was not present.

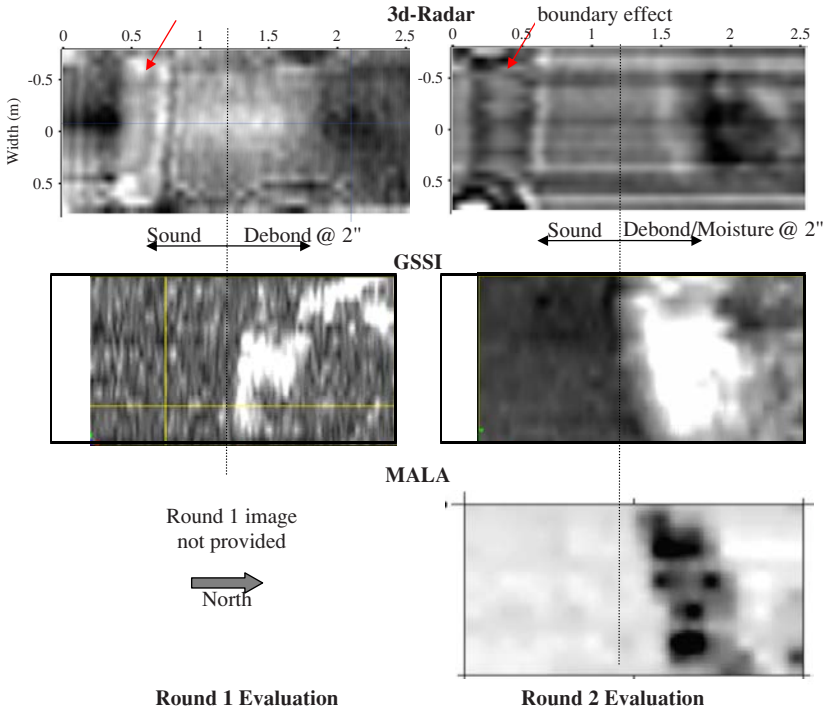

Figure 2.8. Time-depth slices at 2 to 3 in. for first- and second-round testing of Slab A.

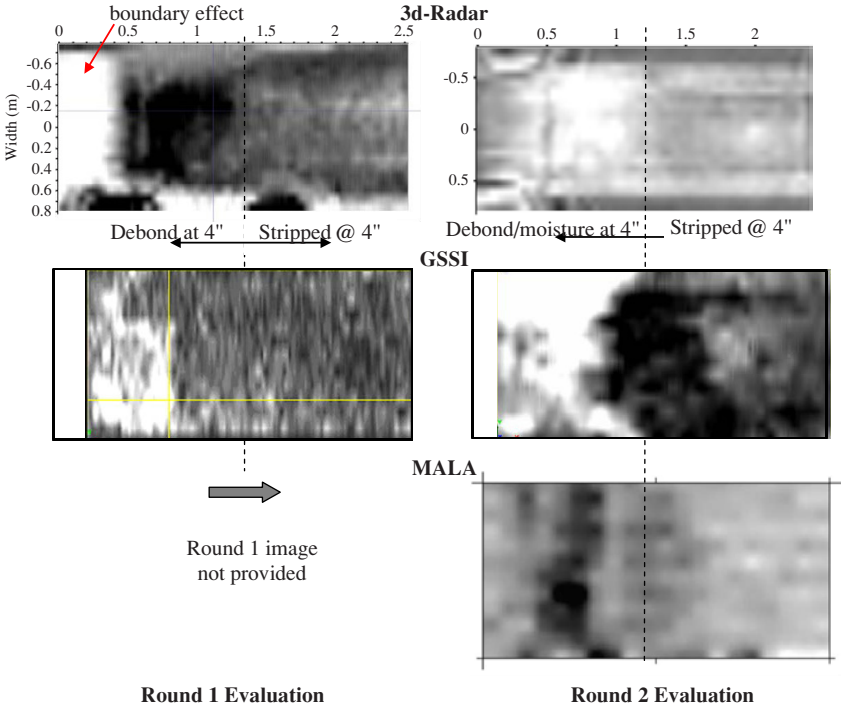

Figure 2.9. Time-depth slices at 4 to 5 in. for first- and second-round testing of Slab B.

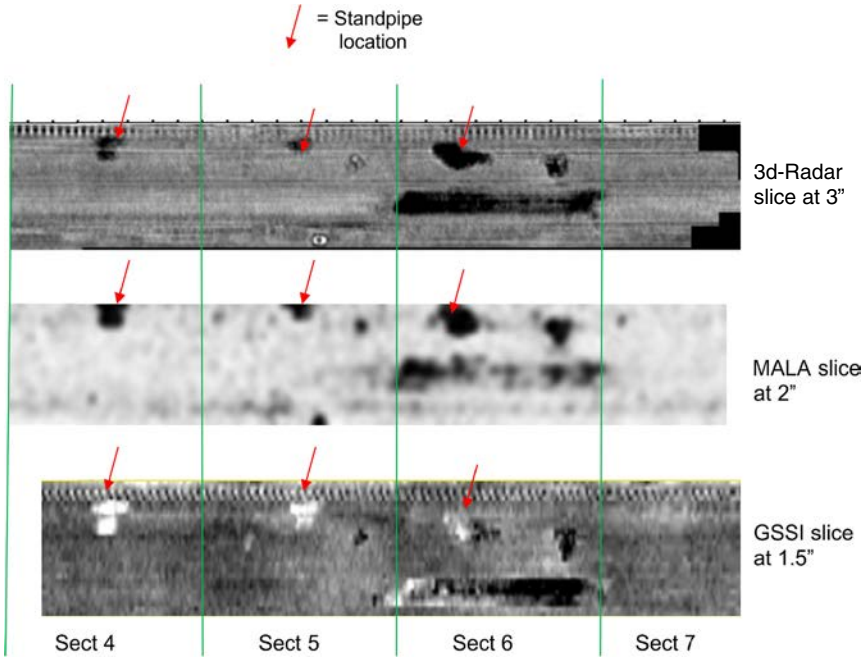

Figure 2.10. GPR time-depth slices for Sections 4, 5, 6, and 7.

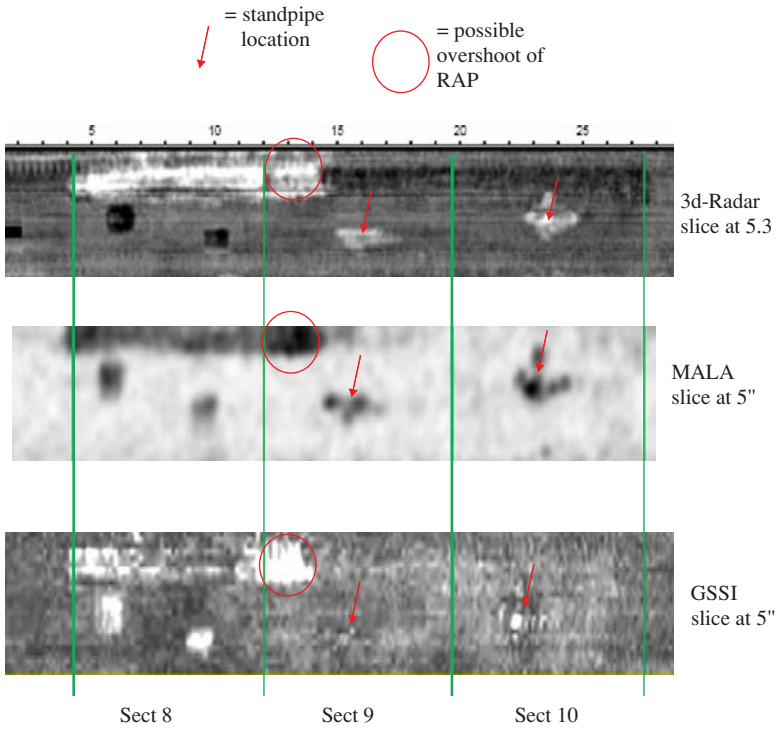

Figure 2.11. GPR time-depth slices for Sections 8, 9, and 10.

CHAPTER 3

Laboratory and Field Evaluations of Infrared Thermography Systems

The chapter was prepared by Kenneth Maser of Infrasense, Inc.

Collection of Infrared Data

Two infrared (IR) cameras were made available for this testing: (a) an Infrared Cameras, Inc. (ICI), 7320 camera and (b) a FLIR A40M camera with a wide-angle lens. The ICI 7320 had a resolution of 320 × 240 pixels and a frame rate of 30 Hz. The FLIR A40M also had the same pixel resolution but a maximum frame rate of 60 Hz. The wide-angle lens was used in conjunction with the FLIR camera so that a full lane width could be imaged from a mounting platform about 13 ft above the pavement surface. ICI offers a similar wide-angle lens, but this lens was not available at the time of testing. The primary difference between the two cameras is size. The FLIR camera weighs about 3 lb and measures 3 in. × 3 in. × 6 in. The ICI camera is about the size of a pocket digital camera.

Laboratory Evaluation

For each test slab, the IR cameras were operated from a ladder to provide sufficient height for a complete IR image view of the entire test slab. A series of still, IR images were recorded at specified times during the heating/cooling cycle of the test slab. The slabs were heated by using an array of eight high-intensity heat lamps, and surface and bottom slab temperature were continuously monitored during the heating process. A photograph of this heating setup is shown in Figure 3.1. During the heating process, the area around the heated slab was enclosed to contain the heat, as shown in Figure 3.2.

After the slabs were heated, IR measurements were made with both the FLIR and ICI cameras from a ladder, with each camera about 11 to 12 ft above the floor. The height was necessary to obtain images that included the full extent of the test slab. The initial testing was carried out with the heating lamps positioned at approximately 2 ft above the slab. The initial results showed a heating pattern that emulated the bulb array, as shown in Figure 3.3. The presence of this pattern prevents the detection of thermal anomalies associated with subsurface defects. As a result, the bulbs were raised to the maximum height possible in the test setup, which was about 3 ft above the surface of the slabs. The resulting heating pattern was more uniform. Figure 3.4 shows thermal anomalies in Slab B.

Field Evaluation at Test Track

For this field testing, Infrasense provided a mounting and recording system that consisted of the following:

- A camera-mounting frame for elevating each IR camera above a survey vehicle approximately 13 ft above the pavement surface, with motorized, remotely controlled pan/tilt head for precise camera positioning;
- A video camera and digital video recorder for collecting standard visual images of the pavement surface in parallel with the IR images;
- A vehicle wheel-mounted distance measuring instrument for encoding distance on the video images and for triggering the collection of data from the IR cameras; and
- Laptop-based data-acquisition software.

The physical setup of the IR data-collection system is shown in Figure 3.5. Testing using the equipment shown in Figure 3.5 was carried out continuously by using a vehicle speed of approximately 3 mph. During each test, IR images were collected at 1-ft intervals and sequentially stored on the laptop hard drive. Simultaneously, a visual video image was recorded to a digital video recorder. The distance traveled was encoded with a counter and superimposed on the video image using a video overlay device. A sample pair of infrared and corresponding video images is shown in Figure 3.6. Note that because the video image was collected at the normal NTSC rate of 30 frames/s, the encoded distance on the video image

Figure 3.1. Heating of test slabs with heat lamps.

Figure 3.2. Test slab enclosure during heating process.

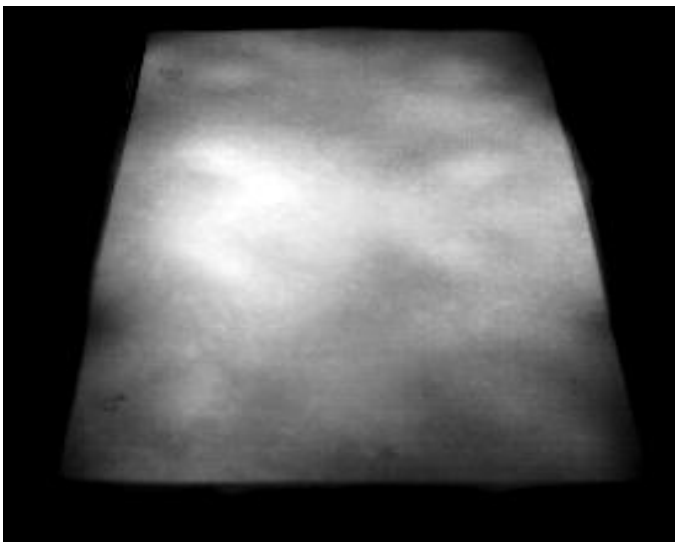

Figure 3.3. IR image of Slab A showing bulb pattern.

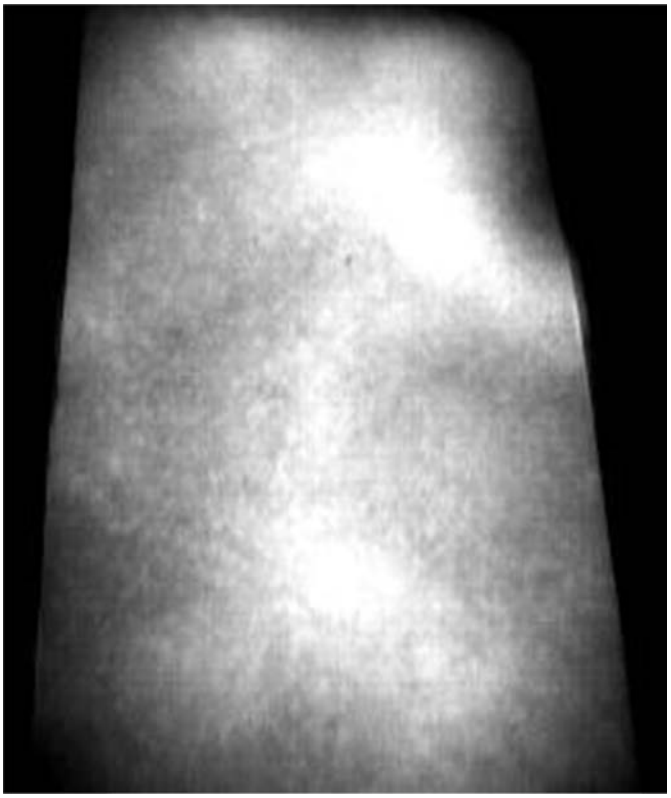

(a)

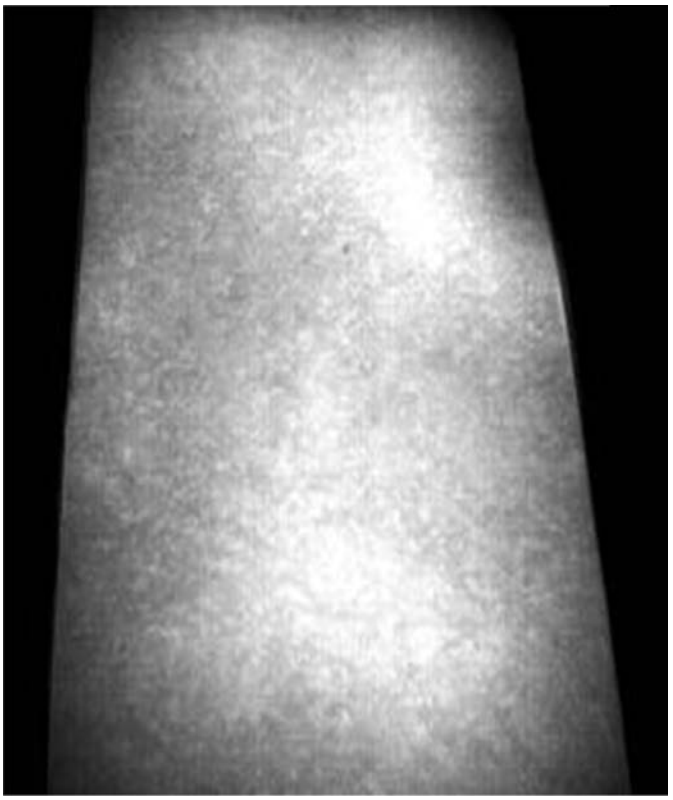

(b)

Figure 3.4. Image of Slab B showing thermal anomalies (a) immediately after heating and (b) 45 minutes after removal of heat.

Figure 3.5. IR thermography setup for track testing.

provided distance registration. The corresponding IR image is Image 143, corresponding to 143 ft of travel.

The initial set of IR system tests was carried out November 8, 2009. Two series of tests were carried out—one from 1 to 2 p.m. and the second from 3 to 4 p.m. The temperature conditions on the track pavement were relatively the same during each series of tests. The weather conditions were sunny with air temperatures of around 60°F.

The second series of tests was carried out March 7 and 8, 2010. One of the objectives of this second series was to explore a larger range of temperatures. During this second series, tests were carried out at the times and ambient temperatures listed in Table 3.1. There was no significant cloud cover during this second series of tests. Note that the range of pavement test temperatures ranged from 35°F to 103°F.

Table 3.1. Thermal Properties of Components in Each Model

Test Time	Ambient Temperature (°F)	Pavement Temperature (°F)
2:00 p.m.	63	NA
4:00 p.m.	60	NA
8:30 p.m.	42	NA
6:00 a.m.	34	35
9:00 a.m.	60	70
10:00 a.m.	60	80
11:30 a.m.	60	95
12:45 p.m.	62	103

Note: NA = not available.

Infrared Data Analysis

Laboratory Evaluation

The laboratory IR data were visually observed and qualitatively correlated with the known defects in the test slab. Figure 3.7 shows thermal images of Slabs A and B taken immediately after heating.

Thermal anomalies are observed on both slab images. For Slab A, the near anomaly is located in the intact section, and thus is apparently caused by factors other than subsurface delamination (e.g., uneven heating). The anomalies in Slab B could be related to the debonding and stripping at 4-in. depth, but the results of Slab A suggest that these anomalies

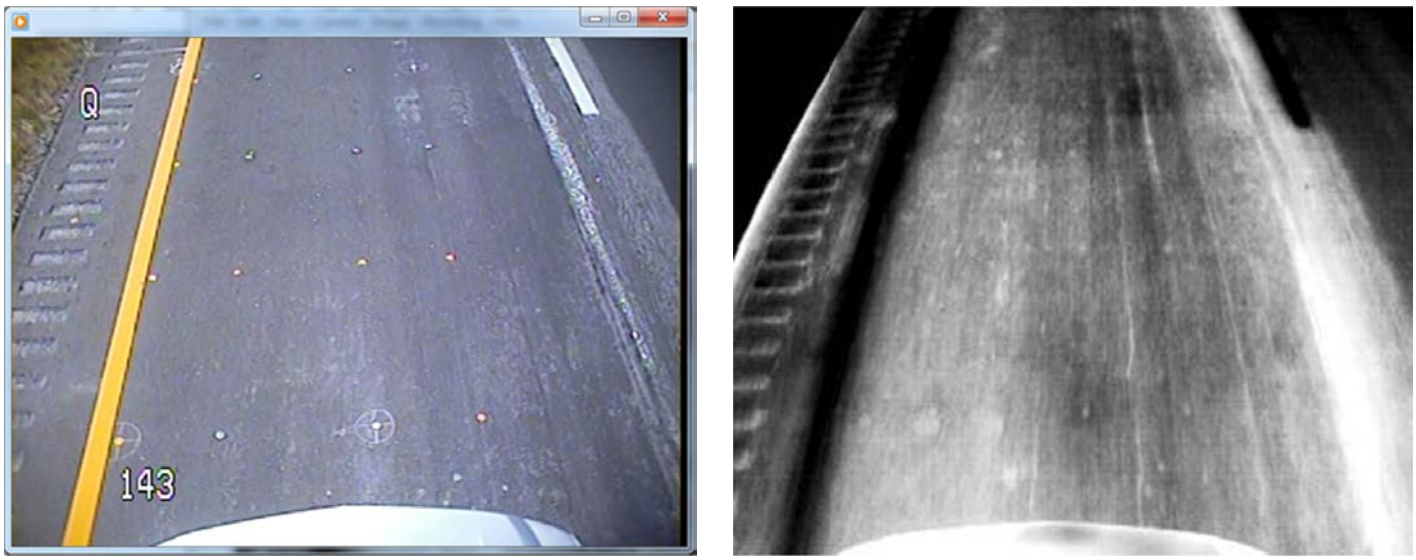

(a) (b)

Figure 3.6. Corresponding IR and video images: (a) video image with encoded distance and (b) IR image.

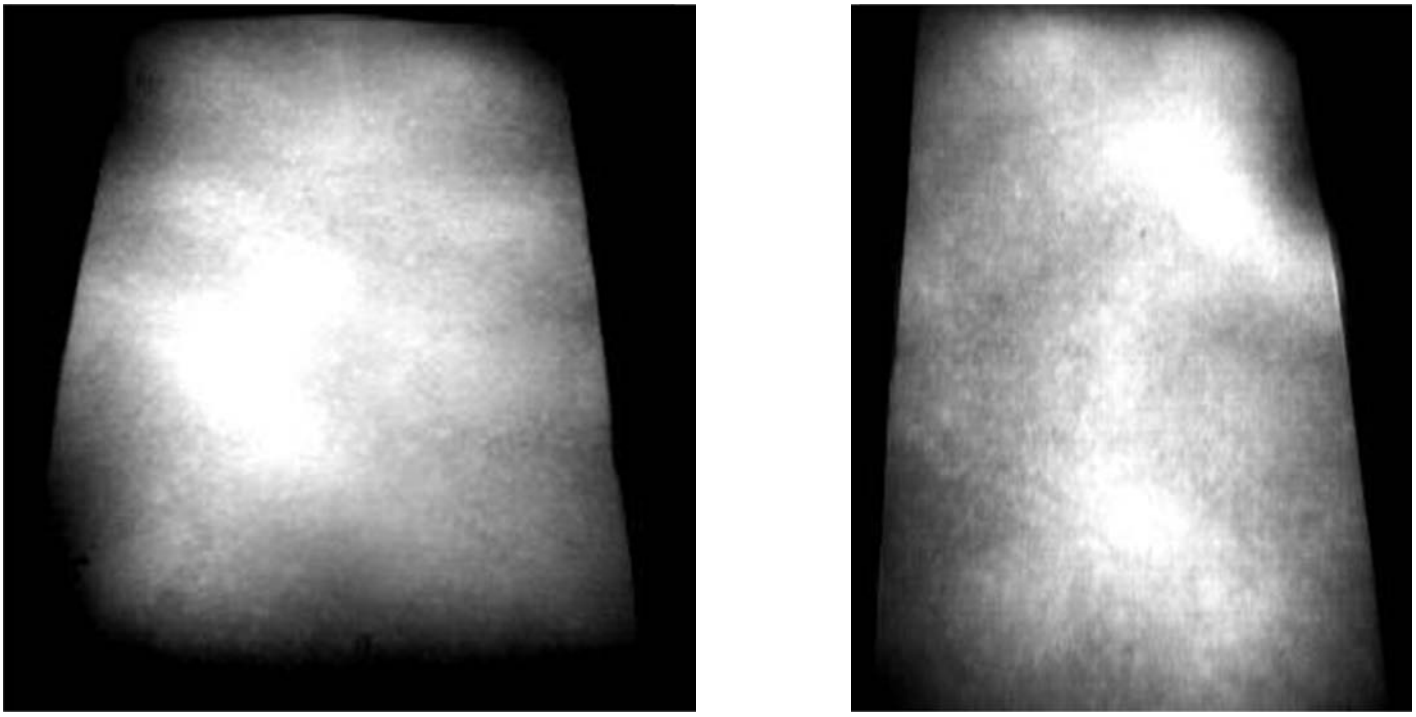

(a) (b)

Figure 3.7. Test slab images immediately after heating for (a) Slab A and (b) Slab B.

could also be due to other factors. Therefore, the laboratory IR tests were inconclusive.

Field Evaluation at Test Track

The IR images from the test track test section were spliced together to produce a single composite strip IR image for the entire test section. One such image was produced for each test. The images were evaluated visually, in conjunction with the visual video data, to identify IR anomalies that could be associated with subsurface debonding, delamination, and stripping.

Figure 3.8 shows an example of the analysis of the IR data. The figure shows a portion of the composite IR image representing Sections 4, 5, 6, and 7 at the test track. The image shows some anomalies in Section 6 in the area where 0.75 in. of reclaimed asphalt pavement was placed 2 in. down from the surface to represent stripping.

However, examination of the surface video shows that these anomalies correspond with surface features and tire marks rather than with subsurface features. In general, the IR image anomalies did not clearly correlate with the known subsurface defects in the test section.

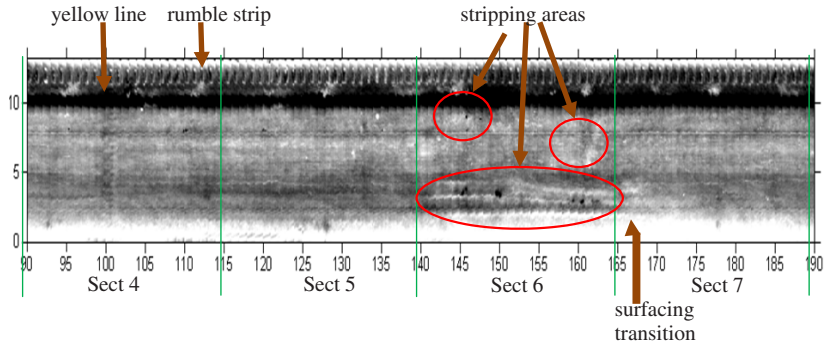

Figure 3.8. IR strip image of Sections 4 through 7.

CHAPTER 4

Controlled Evaluation of Mechanical Wave Technologies: Portable Seismic Pavement Analyzer, Scanning Impact Echo, and Multiple Impact Surface Waves

This chapter was prepared by Ray Brown and Haley Bell of the U.S. Army Corps of Engineers Engineering Research and Development Center (ERDC).

Portable Seismic Pavement Analyzer

Introduction

The portable seismic pavement analyzer (PSPA), developed by Geomedia Research and Development, is a nondestructive testing (NDT) device that measures Young's modulus via ultrasonic surface waves, and completes the test within a few seconds. The PSPA is generally used to measure the in situ seismic modulus of pavements and to determine relative strength parameters for use in pavement evaluations. The device is operated from a laptop computer, which is connected to an electronics box by a cable that transmits power to the two receivers and the source. The source impacts the pavement surface and generates surface waves that are detected by the receivers. The measured signals are returned to the data-acquisition board in the computer. The velocity at which the surface waves propagate is determined, and the modulus is computed. For hot-mix asphalt (HMA) pavements, the PSPA reports the seismic modulus of the pavement temperature at the time of testing. An equation is used to standardize the measured modulus to a temperature of 77°F. Figure 4.1 shows a photograph of the PSPA.

The PSPA was used to test the laboratory samples in the National Center for Asphalt Technology (NCAT) laboratory and to test the sections at the NCAT Pavement Test Track for Round 1 testing in October 2009. For Round 2 testing in February 2010, the PSPA was used only on the test track. Measurements during the Round 1 testing were made with a variety of hardware and software configurations, as shown in Table 4.1. Delamination of the laboratory slabs and the sections on the test track were detected by using modulus estimates. Analyzing modulus measurements alone appeared to be a fair to poor way of detecting HMA delamination. After the testing and data analysis of Round 1, the pavement structure condition of five of the 10 sections (Sections 1, 2, 3, 5, and 8) on the test track and the condition of the laboratory slabs were released to the vendor. Once this information was released, the vendor chose to reanalyze the data from Round 1 and complete Round 2 testing by using Configuration 1 (Table 4.2), which is the standard arrangement for thin HMA pavements, and some changes were made to the original software. All data presented in this report were tested and analyzed by using Configuration 1 and the updated software.

Laboratory Testing

Figure 4.2 shows the extreme waveforms for the four different conditions of the laboratory slabs. These results were determined after the pavement structure of the laboratory slabs was known to the vendor. The four conditions included a shallow delamination, deep delamination, bonded, and delamination with reclaimed asphalt pavement (RAP) (simulating stripping). The red curve in Figure 4.2 is the source, the black curve is the near receiver (A2), and the green curve is the far receiver (A3). The waveforms on the left are the time domains, while the waveforms on the right are the frequency domains. Figure 4.2 shows that the delaminated slabs have large amplitude receiver signals, with late low-frequency energy dissipations. The bonded slab has much lower amplitude receiver signals with a quick energy decay rate. The slab with RAP has waveforms similar to the bonded slab.

Further analysis was completed that identified the probability of each test point to be bonded. Vector distances between the waveform characteristics of the bonded and delaminated slabs were defined. The vector distances were

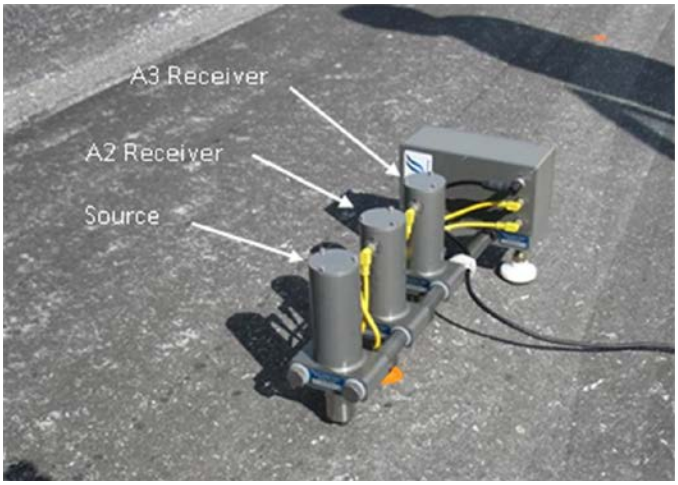

Figure 4.1. PSPA testing device.

scaled as a probability measurement point being taken on a bonded slab. Since the conditions of the laboratory slabs were known, the area with the shallow delamination was used for calibration. This area was deemed to be the worst case and was scaled to give a 5% probability of being bonded. Average vector distances near zero were given a probability of 100% (bonded). Figure 4.3 shows a summary of the probabilities of each test point on the two laboratory slabs to be bonded. The red colors indicate a strong departure from energy being carried in surface waves (delamination), and the green colors indicate bonded areas.

Table 4.1. PSPA Hardware Configurations Originally Used for Round 1 Testing

Configuration	Sensor Spacing (in.)		Frequency Range (kHz)
	Source and A2	A2 and A3	
1	4	4	4 to 40
2	6	8	0.5 to 5
3	4	6	4 to 40
4	3 to 10 walk-away	6	4 to 40

The top part of Figure 4.3 shows Slab 1 while the bottom part shows Slab 2. Columns 1 through 3 of Slab 1 are fully bonded, and Columns 5 through 7 are debonded at a depth of 2 in. Column 4 is most likely a transition area from the fully bonded section to the delaminated section. Columns 8 through 10 of Slab 2 are debonded at a depth of 4 in., while stripping at a depth of 4 in. was simulated with RAP in Columns 13 through 15. Column 11 is most likely a transition area from the delaminated section to the stripped section. There is much variability in the shallow delaminated section of Slab 1 compared to the RAP section in Slab 2. The vendor stated that this variability was due to the plywood on the concrete slab showing more variable scattering characteristics, which were damped out in the RAP section.

Table 4.2. Quantitative Results of PSPA Measurements for Identifying Delamination

Section	Number of Correct Measurements		Total Measurements	Percentage Correct	
	October 2009	February 2010		October 2009	February 2010
1	10	9	10	100	90
2	17	18	20	85	90
3	20	20	20	100	100
4	5	5	12	42	42
5	7	9	20	35	45
6	8	11	12	67	92
7	18	17	20	90	85
8	10	9	12	83	75
9	3	7	10	30	70
10	10	17	20	50	85
Total Sections	108	122	156	69	78
Known Sections	64	65	82	78	79
Unknown Sections	44	57	74	59	77

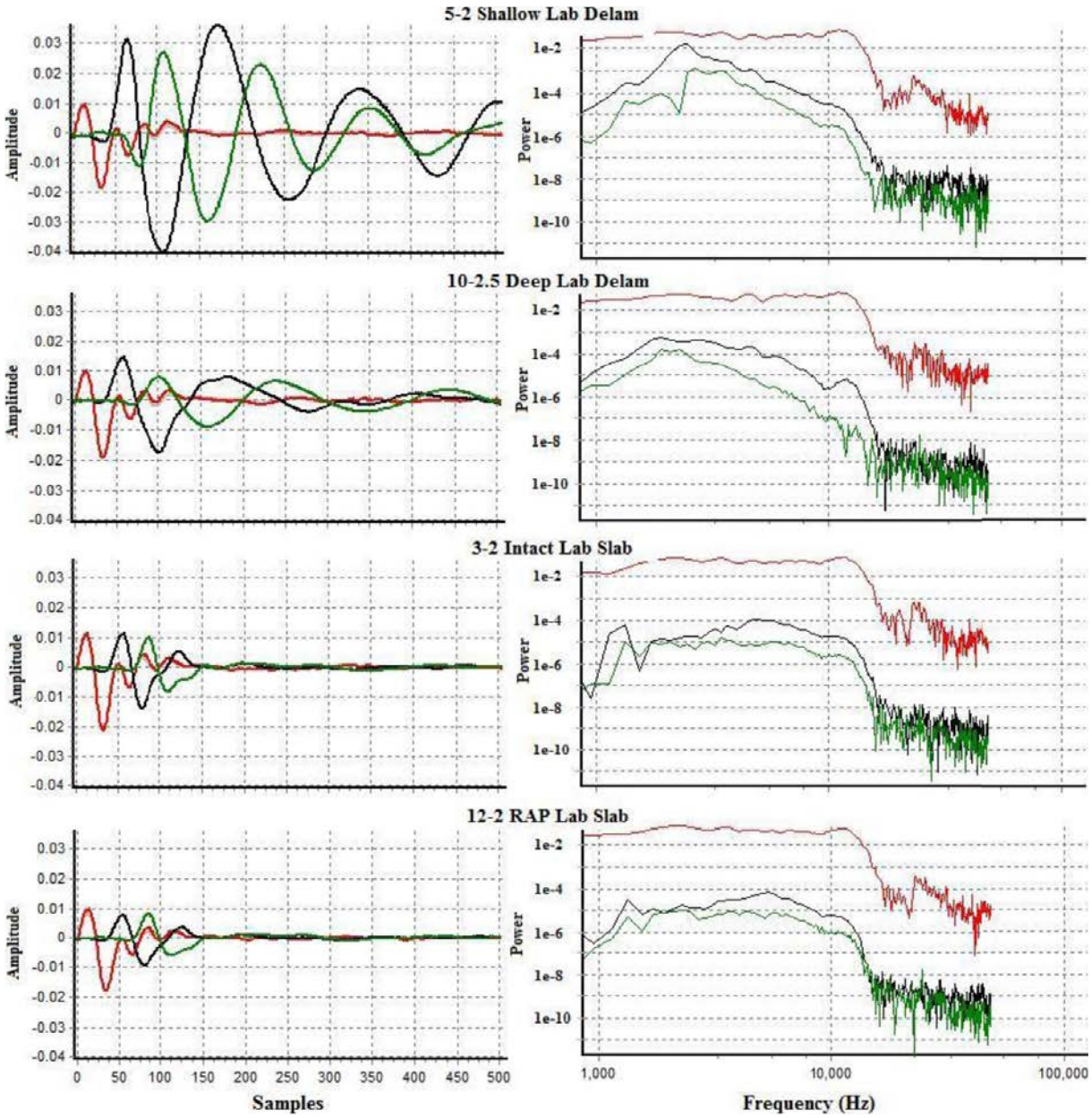

Note: delam = delamination.

Figure 4.2. Time domain and frequency domain power spectra of laboratory slabs.

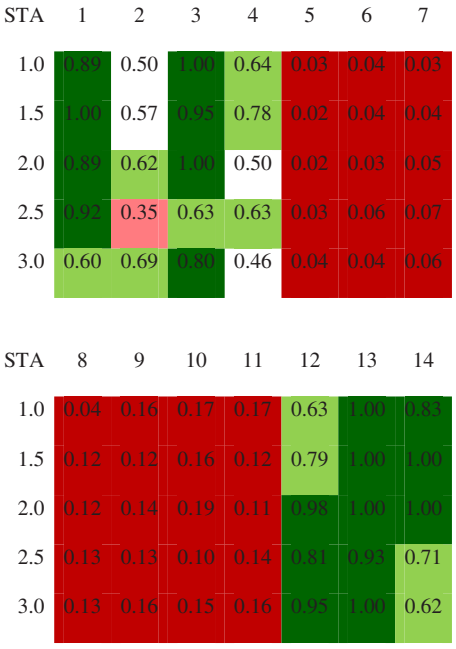

Note: STA = station.

Figure 4.3. Probabilities of laboratory slabs to be bonded.

Field Testing

The conditions of Sections 1, 2, 3, 5, and 8 were known to the vendor during the February testing and for the data analysis presented here. Figures 4.4 and 4.5 show the time and frequency domains of four conditions [i.e., shallow delamination, deep HMA delamination over portland cement concrete (PCC), bonded HMA over PCC, and bonded HMA] in the known areas on the test track for the October and February testing, respectively. The waveforms for each pavement condition at the warmer and cooler temperatures compare well with each other and with the slabs measured in the laboratory. The time domain waveforms of the delaminated areas have larger amplitudes with slower energy decay rates, while the bonded areas have smaller amplitudes with faster energy decay rates.

The same analysis completed in the laboratory showing the probability of a test area to be bonded was completed for the test points on the test track. For the test track data analysis, the shallow delaminated area of the laboratory slab and Section 3 on the test track were used for calibration. The average vector distances of the shallow delaminated portion of the laboratory slab were used as the worst case and assigned a 5% probability of being bonded. The average vector distances of the bonded Section 3 were used as the best case and assigned a 100% chance of being bonded. All other test points were assigned probabilities based on those two representative conditions.

Figure 4.6 shows the probabilities of the test points on the test track to be bonded based on the average vector distances. The probabilities are given for the data collected in October and February along with the pavement temperature at the time of testing. The vendor stated that Section 2 had a more abnormal and sensitive power distribution because the PCC layer may have provided additional reflected energy to confound the simple analysis method. Section 2 consisted of bonded HMA over PCC.

Each test point on the test track was quantified to determine the accuracy of the PSPA for identifying delamination. For this analysis, any probability of 0.6 or more was considered bonded, while any probability of 0.5 or less was considered delaminated. Table 4.2 shows these quantitative results of the PSPA data presented in Figure 4.6. For each section, only the test point locations that were most likely to represent the bonding condition that it was designed to represent were selected to be evaluated. If there were a strong possibility of a location not being representative of the design condition due to being adjacent to another section, then that point was eliminated from the analysis. The analysis was completed for all test sections, including sections known by the vendor as well as those sections not known by the vendor.

Table 4.2 shows that the PSPA was able to accurately detect approximately 69% and 78% of delamination in the warm and cool temperatures, respectively. The high percentages of the section known to the vendor (Sections 1, 2, 3, 5, and 8) were not surprising. For the sections not known to the vendor, the PSPA was able to identify approximately 59% and 77% of the delamination on the test track in October and February, respectively. The PSPA did a better job of identifying the delamination in the cooler pavement temperatures.

Table 4.3 shows the probability of good bond on the basis of PSPA results compared to the actual percentage of bonded points. The probability of bonding determined from the PSPA test compares very well to the percentage of points actually having good bond. For example, all the samples predicted with the PSPA test to have between 0.51 and 0.75 probability of being bonded actually had 67% of these points that were bonded. The actual percentage of bonded points compared well to the predicted probability for other ranges as well. The good comparison between the predicted probability of good bond and the actual percentage of bonded points occurred within sections known to the vendor as well as in sections in which bond conditions were not known by the vendor.

This device measures individual points and does not allow for complete coverage at highway speeds. However, the potential for this test to locate delamination is good, and it is possible that a procedure can be developed later that allows for decreased test time and more complete coverage.

Summary

Overall, the PSPA was able to identify the bonded sections accurately. The nondestructive device had a difficult time

(text continues on page 31)

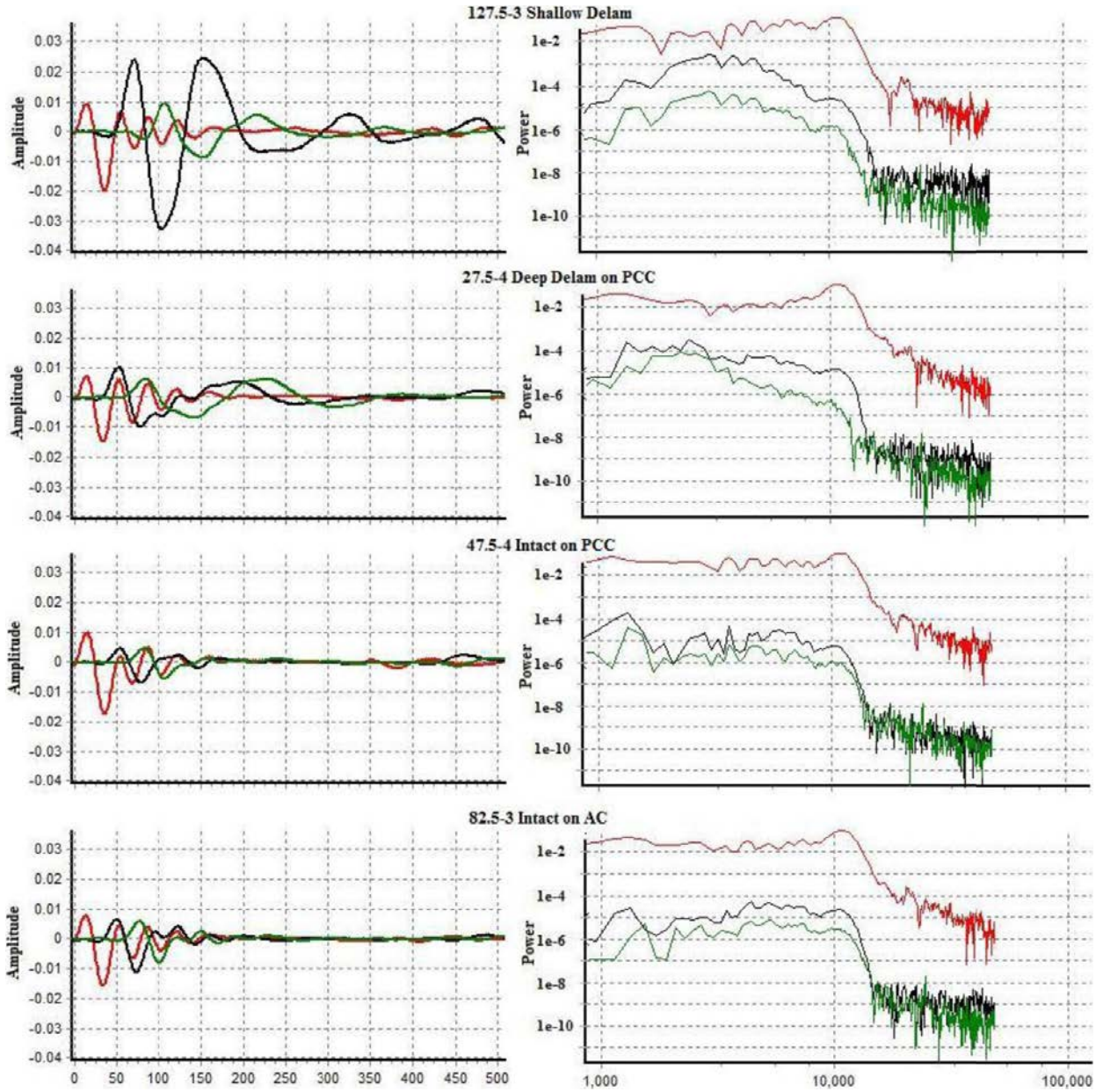

Note: AC = asphalt concrete.

Figure 4.4. Samples of time domain and frequency domain power spectra on test track in October 2009.

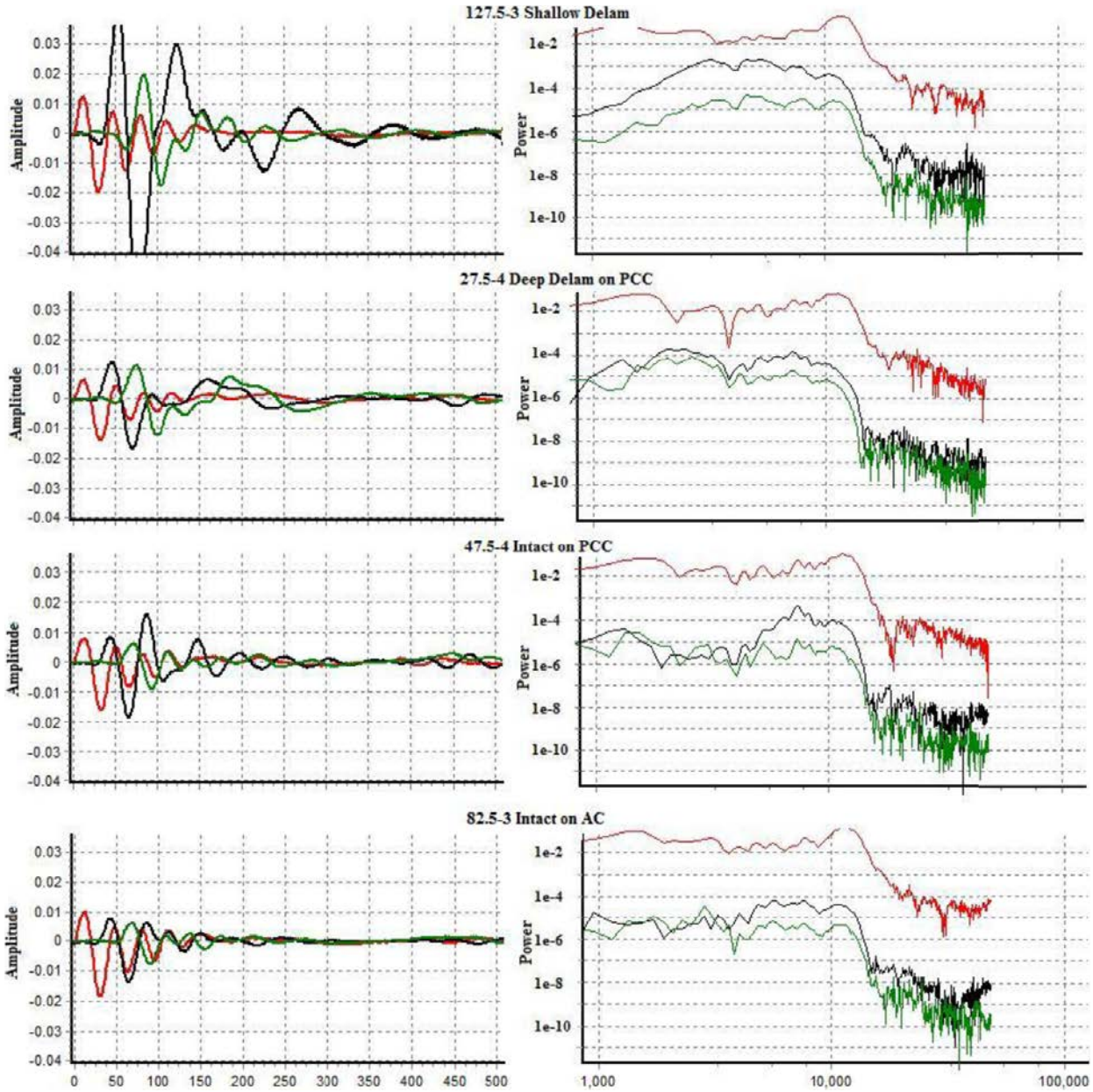

Note: AC = asphalt concrete.

Figure 4.5. Samples of time domain and frequency domain power spectra on test track in February 2010.

	Section 1					Section 2					Section 3					Section 4				
Oct. 2009	17.5	22.5	27.5	32.5	37.5	42.5	47.5	52.5	57.5	62.5	67.5	72.5	77.5	82.5	87.5	92.5	97.5	102.5	107.5	112.5
1	0.1	0.2	0.2	0.2	0.1	0.4	0.9	0.6		0.5	1.0	1.0	0.8	1.0	0.8	0.9		0.6	0.5	0.4
2	0.2	0.3	0.2	0.1	0.1	0.9	0.8	0.9	0.9	1.0	1.0	0.8	1.0	0.7	1.0	0.9	0.9	0.9	1.0	0.8
3	0.2	0.2	0.2	0.3	0.5	1.0	1.0	0.7	1.0	0.8	1.0	1.0	0.9	1.0	1.0	1.0	0.4	0.8	0.2	1.0
4	0.4	0.2	0.1	0.1	0.1	0.8	1.0	0.9	0.9	0.9	1.0	0.9	0.7	1.0	0.7	0.9	1.0	0.9	0.8	0.9
Temp. (°F)	63	64	65	64	66	69	70	70	71	70	70	71	71	70	71	72	74	81	81	84
Feb. 2010																				
1	0.1	0.2	0.2	0.5	0.2	0.7	0.3	0.3	0.7	0.6	0.9	1.0	1.0	0.9	1.0	1.0	1.0	0.5	0.8	0.3
2	0.3	0.2	0.3	0.2	0.3	0.7	0.6	0.6	1.0	1.0	1.0	1.0	1.0	1.0	0.8	0.9	1.0	1.0	1.0	1.0
3	0.2	0.2	0.2	0.3	0.7	0.6	0.6	0.7	0.7	1.0	1.0	0.8	0.8	1.0	1.0	0.8	0.7	1.0	0.2	1.0
4	0.6		0.1	0.1	0.2	0.7	1.0	0.9	0.6	1.0	1.0	0.9	1.0	1.0	0.9	0.9	1.0	1.0	1.0	1.0
Temp. (°F)	41	42	41	41	40	42	44	47	49	51	52	52	53	53	54	55	56	57	59	59

	Section 5					Section 6					Section 7					Section 8				
Oct. 2009	117.5	122.5	127.5	132.5	137.5	142.5	147.5	152.5	157.5	162.5	167.5	172.5	177.5	182.5	187.5	192.5	197.5	202.5	207.5	212.5
1	0.0	0.6	0.3	0.9	0.8	0.8	0.3	0.8	0.7	0.6	0.8	0.7	0.8	0.7	0.8	0.5	0.5	0.6	0.5	0.3
2	0.1	0.3	0.8	0.8	0.7	0.9	0.6	1.0	0.8	0.8	0.7	0.9	0.5	0.7	0.5	0.6	0.6	0.7	0.7	0.2
3	1.0	0.4	0.1	1.0	0.3	0.8	0.6	0.8	0.8	0.8	0.9	1.0	1.0	0.7	0.9	0.8	0.7	0.7	0.8	0.4
4	0.7	1.0	0.7	0.7	0.6	0.2	0.1	0.8	1.0	0.9	0.6	0.7	0.9	0.6	0.7	0.6	0.7	0.7	0.4	0.6
Temp. (°F)	85	85	86	86	86	87	86	86	87	84	84	83	82	82	84	85	84	84	82	52
Feb. 2010																				
1	0.1	0.3	0.2	0.5	1.0	1.0	0.1	0.6	1.0	1.0	1.0	1.0	0.3	0.5	1.0	1.0	0.2	0.4	0.5	0.3
2	0.1	0.2	1.0	1.0	1.0	0.7	0.9	0.8	1.0	1.0	1.0	1.0	1.0	1.0	0.7	0.3	0.4	1.0	1.0	0.3
3	1.0	0.4	0.1	1.0	0.7	1.0	1.0	0.8	0.9	1.0	1.0	1.0	1.0	1.0	1.0	1.0	1.0	0.5	0.6	0.8
4	1.0	1.0	0.8	0.5	0.8	0.2	0.1	0.1	0.2	0.6	1.0	1.0	0.9	1.0	0.5	0.5	1.0	0.6	0.3	1.0
Temp. (°F)	58	53	51	51	52	53	53	51	51	51	51	51	51	51	51	51	51	52	53	53

	Section 9					Section 10				
Oct. 2009	217.5	222.5	227.5	232.5	237.5	242.5	247.5	252.5	257.5	262.5
1	0.3	0.7	0.6	0.5	0.9	0.5	0.3	0.4	0.8	0.2
2	0.8	0.9	1.0	0.6	0.9	0.2	0.3	0.6	0.6	0.3
3	1.0	0.7	0.7	0.5	0.6	0.7	0.6	0.5	1.0	0.6
4	0.6	0.6	0.5	0.6	0.8	0.7	0.8	0.7	0.5	0.4
Temp. (°F)	52	52	52	52	52	53	54	55	58	58
Feb. 2010										
1	0.4	0.4	0.6	0.4	0.5	0.3	0.4	0.3	0.5	0.2
2	0.5	0.5	0.9	0.3	0.3	0.1	0.4	0.1	0.3	0.2
3	0.6	0.2	0.4	0.4	0.3	0.3	0.5	0.4	0.5	0.7
4	0.6	0.4	0.2	0.6	0.3	0.4	0.6	0.8	0.5	0.3
Temp. (°F)	53	54	54	55	57	58	58	58	57	58

Figure 4.6. Probabilities of test track test points to be bonded.

Table 4.3. Probability of Good Bond on the Basis of PSPA Testing Results

All Sections			
Probability	**Number Bonded**	**Number Unbonded**	**% Bonded**
0 to 0.25	0	22	0
0.26 to 0.50	9	28	24
0.51 to 0.75	16	8	67
0.76 to 1.00	56	17	77
Known Sections			
0 to 0.25	0	13	0
0.26 to 0.50	4	9	31
0.51 to 0.75	13	2	87
0.76 to 1.00	30	11	73
Unknown Sections			
0 to 0.25	0	9	0
0.26 to 0.50	5	19	21
0.51 to 0.75	3	6	33
0.76 to 1.00	26	6	81

(*continued from page 27*)
detecting the 2-in.-deep delamination when the baghouse dust was used. The PSPA was able to detect the 5-in.-deep delaminated areas by using the baghouse dust fairly well, particularly with the cooler pavement temperatures. This test does not provide continuous measurement of the bond, but the test does a reasonably accurate job of identifying bond. With some improvements, the PSPA has potential to help state departments of transportation identify pavements with delamination issues.

Scanning Impact Echo and Multiple Impact Surface Waves Methods

Introduction

Olson Engineering, Inc., performed a suite of nondestructive tests during the Round 1 HMA delamination detection testing in October 2009. The tests included scanning impact echo (IE), multiple impact of surface waves (MISW), ground-penetrating radar (GPR), and slab impulse response (SIR). Olson Engineering, Inc., also used a point-by-point IE testing device. The four test methods were conducted on the laboratory slabs and on the test track in October 2009. The conditions of the laboratory slabs and the sections on the test track were unknown to the vendor during the October testing. The purpose of the October testing was to identify HMA delamination at warmer pavement temperatures. Round 2 testing was conducted in March 2010 where the conditions of the laboratory slabs and Sections 1, 2, 3, 5, and 8 on the test track were provided to the vendor after the analysis of Round 1 testing. The purpose of the March testing was to determine whether the vendors could do a better job in identifying delamination in cooler temperatures.

The scanning IE device consists of two synchronized 1-in.-diameter transducer wheels that measure the IE and spectral analysis of surface wave (SASW) vibrations induced by the on-board automated impactor. The scanning IE records a measurement every 6 in. while being towed behind a truck and operating at speeds of 1 to 2 mph. For the laboratory testing, the device was rolled manually. The IE data were analyzed by determining the resonant frequency of the pavement. The MISW method collects data similar to the SASW but involves multichannel data-processing techniques to determine pavement modulus and thickness information. The amount of data collected with the MISW technique is therefore significantly greater than the amount collected with the SASW technology. An accelerometer is placed on the pavement surface, and several impactors are triggered at various distances from the accelerometer, measuring the surface wave responses. The GPR data were collected with 1-ft-wide scans by using a Geophysical Survey Systems, Inc. (GSSI), SIR-3000 computer and a 1,500-MHz antenna. The SIR test method is performed by using a computer, an instrumented 3-lb-impact hammer, and a 4.5-Hz geophone. This test is operated by impacting the HMA pavement and measures the impact force and the resultant vibration to determine the pavement structure's relative stiffness. The SIR data were analyzed by calculating the average mobility, or frequency domain transfer function between the system input and output, between 200 and 800 Hz in the laboratory and 100 to 500 Hz on the test track.

Round 1 Testing Summary

After the testing and analysis of Round 1 data, the pavement structure condition of five of the 10 sections (Sections 1, 2, 3, 5, and 8) on the test track and the condition of the laboratory slabs were released to the vendor. Once this information was released, the vendor chose to reanalyze the laboratory and field data from Round 1. All four methods tested on the laboratory slabs seemed to perform well in identifying the bonded and delaminated areas. However, the scanning IE had a difficult time identifying the RAP section (stripping) in Slab 2. The GPR and MISW data showed that there was a difference between the bonded section and the RAP section. Table 4.4 shows a summary of the four test methods on the laboratory slabs and the in situ condition of the slabs.

Table 4.4. Laboratory Summary Results of Olson Engineering, Inc.

Test Method	Slab 1		Slab 2	
	Test Locations 1-1 to 3-3	Test Locations 5-1 to 7-3	Test Locations 8-1 to 10-3	Test Locations 12-1 to 14-3
Point-by-Point IE	Bonded	Delaminated	Delaminated	Bonded
Scanning IE	Bonded	Delaminated	Delaminated	Bonded
SIR	Bonded	Delaminated	Partially delaminated	Bonded
MISW	Bonded	Delaminated at 2.76 in.	Delaminated at 3.54 in.	Slightly debonded layer at 1.6 in.
GPR	Bonded	Layer boundary at 2 to 3.5 in.	Layer boundary at 3 in.	Layer boundary at 2 to 3 in.
Actual Condition	Bonded	Delamination at 2 in.	Delamination at 4 in.	Stripping at 4 in.

The second analysis of the Round 1 test track data revealed that the SIR performed poorly in identifying delamination. The device showed potential but is not ready to be implemented for identifying delamination. The GPR also performed poorly in identifying delamination in the field; however, the GPR method did show promise for identifying layer thicknesses and material boundaries. The scanning IE method seemed to be good at identifying deeper delaminations (4 to 6 in.), while the MISW method showed potential for identifying delaminations at a variety of depths.

Figure 4.7 shows the results of the scanning IE on the test track sections during the October 2009 testing. The results are displayed in thickness (in.) by using the color scale to the right in the figure. An IE compression wave velocity of 7,000 ft/s was used for all thickness calculations. The resonant frequency displayed in Figure 4.7 is directly related to the pavement structure's thickness. The thicker areas shown in blue, purple, and green (delamination) represent low-frequency flexural resonance of the delamination. Orange and yellow colors are considered to be bonded areas. The red areas have high-frequency resonances, which indicate thin layers or thicker, deeper delaminations. The results show that the IE seemed to do a good job of detecting the 5-in.-deep delaminations simulated with paper and the bonded areas. The scanning IE did a fair-to-poor job of detecting the delaminations simulated with the baghouse

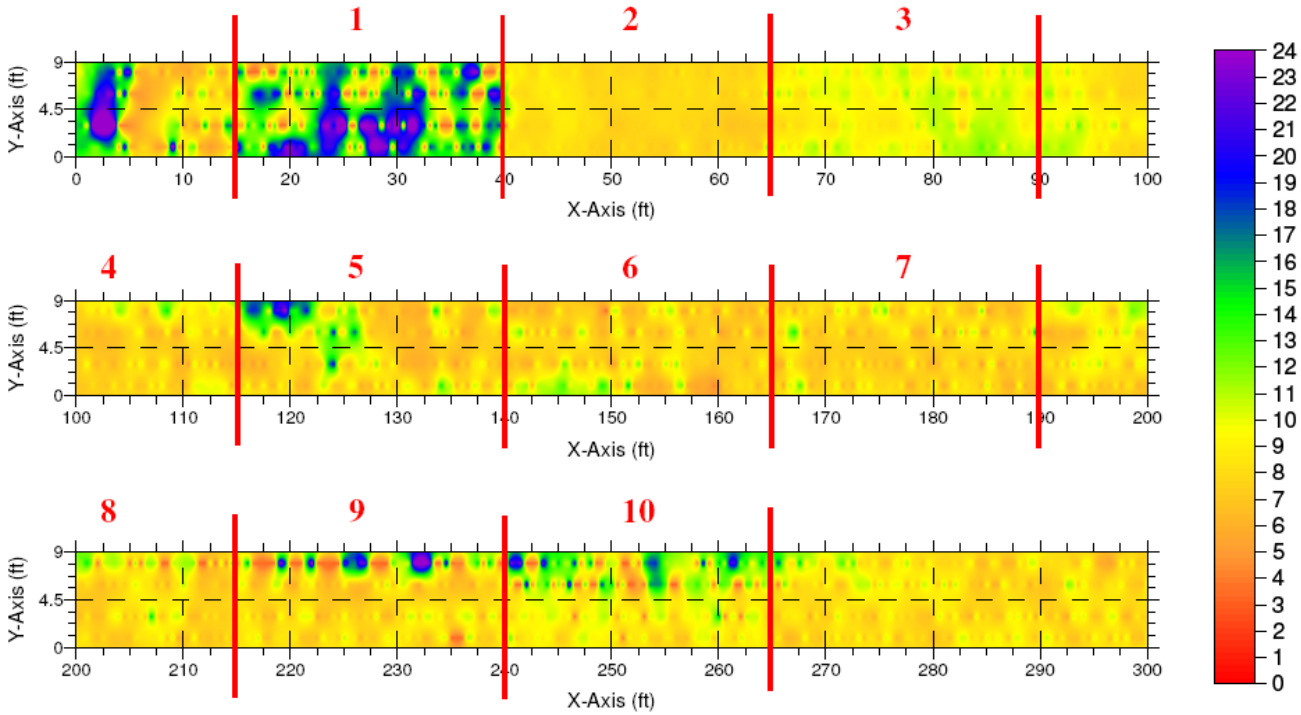

Figure 4.7. Round 1 scanning IE test results on test track.

dust at 5 in. deep. The scanning IE was not able to identify the 2-in.-deep delaminations simulated with the baghouse dust, but the method did a fair job of identifying the sections with RAP at a depth of 2 in.

Table 4.5 shows the results of the MISW on the test track during the October testing compared with the actual conditions on the test track. Tests 1, 2, 13, and 14 shown in that table were outside the test section, which was unknown to the vendor at the time of testing. The MISW accurately predicted bonding or delamination for six of the 10 tests conducted on the test track. The test method had the ability to determine the delamination depth; however, the measurements were not accurate. The findings of the second analysis resulted in the vendor using only the scanning IE and MISW for the Round 2 testing conducted in March 2010.

Round 2 Testing Summary

For Round 2 testing, the scanning IE and MISW were performed only on the test track. Figures 4.8 through 4.12 show detailed results of the scanning IE test in the form of resonant frequencies. The same thickness scale used in Figure 4.7 also applies to these results. The thicker areas shown in blue, purple, and green (delamination) represent low-frequency flexural resonance of the delamination. Orange and yellow colors are considered bonded areas. The red areas have high-

Table 4.5. Round 1 MISW Results on Test Track

Test	Station (ft)	V_s (ft/s)	Delaminated Depth (in.)	Predicted		In Situ	
				Condition	Note	Condition	Note
1	2.5	5,413	4.3	Delaminated	Small, low frequency peak; slow V_s convergence	na	Outside test section
2	2.5	5,741	3.5	Delaminated	Huge, low frequency peak; poor V_s convergence	na	Outside test section
3	52.5	5,906	na	Bonded	Control section	Bonded HMA over PCC	Section 2
4	52.5	5,906	na	Bonded	Control section	Bonded HMA over PCC	Section 2
5	102.5	5,906	Mixed results	Delaminated	Multiple frequency peaks; inconsistent V_s	Bonded	Section 4 = Bonded
6	102.5	5,906	6.5	Delaminated	Sound with debonded layer; extra frequency peak at high frequency	Bonded	Section 4 = Bonded
7	152.5	5,906	na	Bonded	Control Section	Bonded	Section 6
8	152.5	6,234	Mixed results	No conclusion	Frequency spectrum good; poor V_s convergence	Bonded	Section 6
9	202.5	6,070	1.2	Delaminated	Huge, low frequency peak; poor V_s convergence	Delaminated	Section 8 = Delaminated at 5 in. with RAP
10	202.5	5,577	2	Delaminated	Low frequency peak; poor V_s convergence; likely delamination	Bonded	Section 8
11	252.5	5,741	1.5	Delaminated	Low frequency peak; poor V_s convergence; likely multiple layers and delamination	Delaminated	Section 10 = Delaminated at 5 in. with paper
12	252.5	6,070	2	Delaminated	Frequency spectrum good; poor V_s convergence	Delaminated	Section 10 = Delaminated at 5 in. with paper
13	297.5	6,234	1.5	Delaminated	Low frequency peak; poor V_s convergence; likely delamination	na	Outside test section
14	297.5	6,070	5.5	Delaminated	Sound with debonded layer; extra frequency peak at high frequency	na	Outside test section

Note: V_s = shear wave velocity.

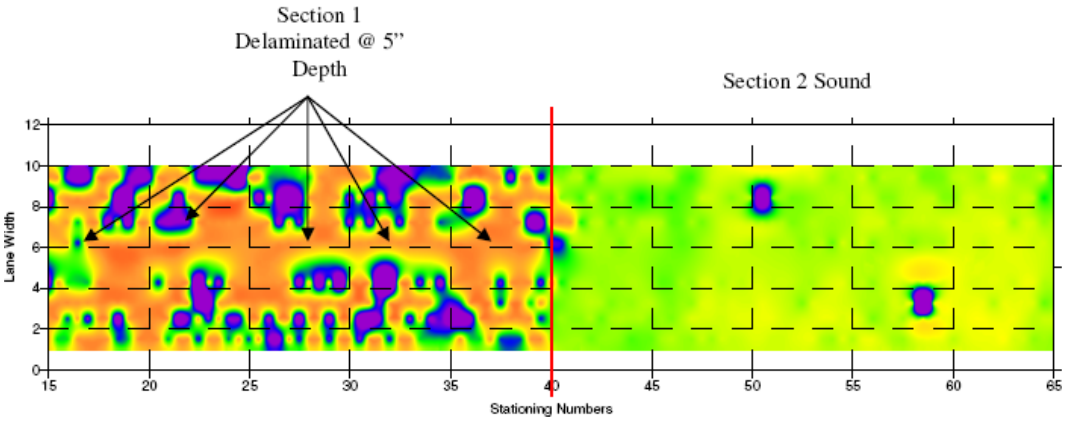

Figure 4.8. Scanning IE thickness plots for Sections 1 and 2.

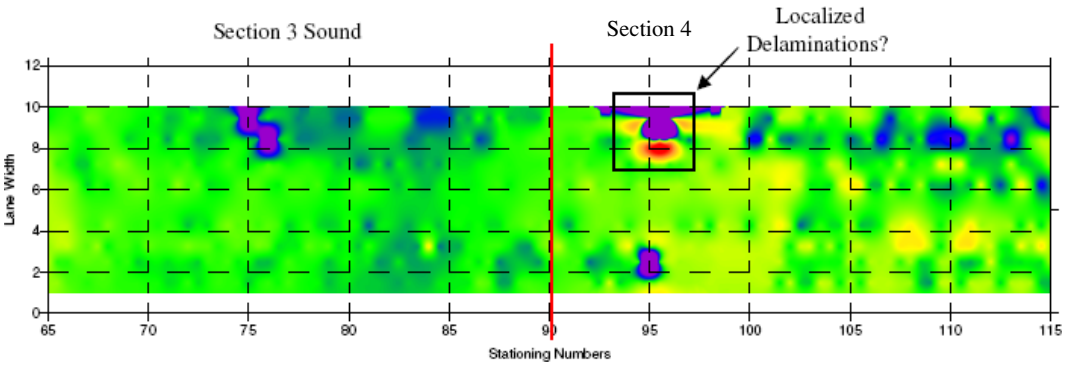

Figure 4.9. Scanning IE thickness plots for Sections 3 and 4.

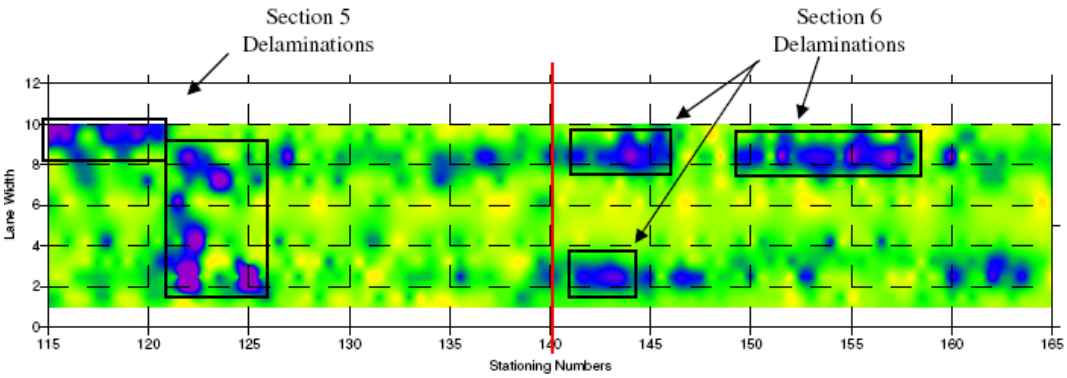

Figure 4.10. Scanning IE thickness plots for Sections 5 and 6.

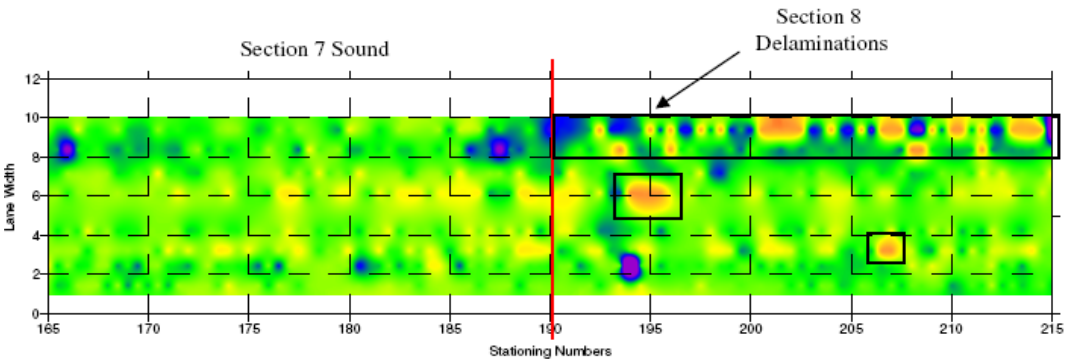

Figure 4.11. Scanning IE thickness plots for Sections 7 and 8.

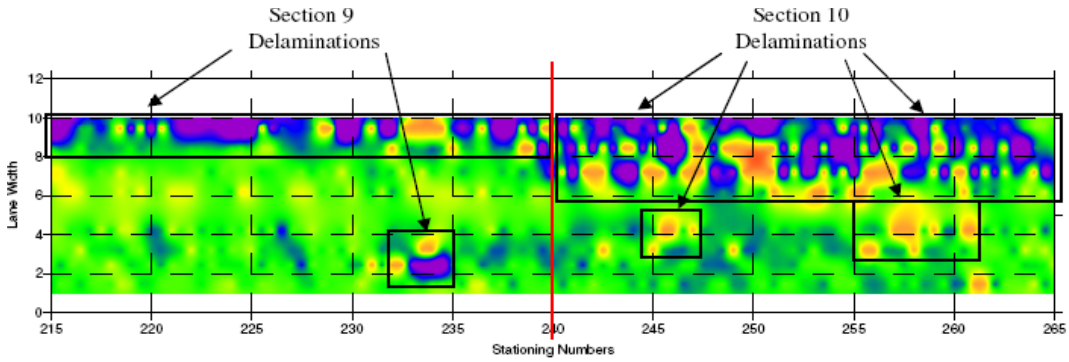

Figure 4.12. Scanning IE thickness plots for Sections 9 and 10.

frequency resonances, which indicate thin layers or thicker, deeper delaminations. Again, the conditions of Sections 1, 2, 3, 5, and 8 were known to the vendor. The results show that the scanning IE identified the bonded areas well and did a fair job of identifying the delaminations simulated with paper at a depth of 5 in. and the stripping simulated with RAP at a depth of 2 in. Overall, the scanning IE did a poor job of identifying the delaminations simulated with the baghouse dust at depths of 2 and 5 in.

It was important to try to quantify the results of the scanning IE to compare with the PSPA results. The same analysis procedure used for the PSPA was used with the scanning IE shown in Figures 4.8 through 4.12. However, only the results from the March testing were quantified for the scanning IE. Table 4.6 presents the results of the quantitative analysis. On the basis of the results, it appears that the IE method did a fair job of identifying the areas of delamination. Of course, the conditions of Sections 1, 2, 3, 5, and 8 were known before the data were analyzed. It was important to provide some data to the vendors so they could calibrate their equipment on the basis of known conditions. Most emphasis for delamination identification was placed on the predictions for Sections 4, 6, 7, 9, and 10, the sections unknown to the vendor. For those sections, the prediction was correct approximately 66% of the time.

The amount of testing with the MISW was minimized because of the test time required with this equipment. The MISW was performed at 12 locations on the test track. The results of the 12 tests along with the actual conditions are presented in Table 4.7. The MISW accurately identified

Table 4.6. Quantitative Results of Scanning IE for Identifying Delamination

Section	IE March 2010	Total Evaluated	Percentage Correct
1	10	10	100
2	20	20	100
3	20	20	100
4	5	12	42
5	5	20	25
6	5	12	42
7	20	20	100
8	12	12	100
9	6	10	60
10	13	20	65
Total	116	156	74
Known Sections	67	82	82
Unknown Sections	49	74	66

Table 4.7. Round 2 MISW Results on Test Track

Test	Station (ft)	V_s (ft/s)	Delaminated Depth (in.)	Predicted		In Situ	
				Condition	Analysis Note	Condition	Note
1	27.5	6,234	5.5	Delaminated	Low frequency peak	Delaminated	Section 1 = Delamination with baghouse dust at 5 in.
2	27.5	5,906	6	Delaminated	Low frequency peak	Delaminated	Section 1 = Delamination with paper at 5 in.
3	52.5	6,660	na	Bonded	Stiff supporting layer; surface wave velocity pulls up at lower frequency	Bonded HMA over PCC	Section 2
4	52.5	6,398	na	Bonded	Stiff supporting layer; surface wave velocity pulls up at lower frequency	Bonded HMA over PCC	Section 2
5	102.5	6,070	na	Bonded Layer	Low velocity layer near 5.5-in. depth	Bonded	Section 4
6	102.5	6,693	1.5	Delaminated	Some low frequency energy	Bonded	Section 4 = Bonded but near delaminated area
7	152.5	6,726	6.5	Bonded Layer		Bonded	Section 6
8	152.5	6,070	na	Bonded	No data beyond 10,000 Hz	Bonded	Section 6 = Bonded but near partial stripping area
9	202.5	6,726	6	Bonded Layer		Bonded	Section 8 = Bonded but near partial stripping area
10	202.5	6,857	10	Bonded		Bonded	Section 8
11	252.5	6,759	10	Bonded		Delaminated	Section 10 = Delamination with paper at 5 in.
12	252.5	6,693	10.5	Delaminated	Low frequency peak	Delaminated	Section 10 = Delamination with baghouse dust at 5 in.

Note: na = not applicable.

the bonded or delaminated areas of 10 of the 12 tests performed. However, of the 12 tests conducted, half of the conditions were known to the vendor. Also, no tests were conducted on the areas that had 2-in.-deep delaminations. Therefore, it was difficult to accurately judge the test method's potential for identifying HMA delamination.

Summary

After Round 1 testing, the vendor elected to remove the SIR and GPR from the program, since they did not provide a suitable answer and there were several other vendors using various forms of the GPR. The IE and MISW continued to be evaluated in Round 2. Both methods showed some promise for measuring delamination, but the MISW was time-consuming and not practical for rapid testing. The MISW limitations resulted in only a few data points taken. It was difficult to judge the potential for the MISW to identify HMA delamination accurately on the basis of the few data points collected. The scanning IE was quicker and easier to use, and it showed some potential for measuring delamination.

CHAPTER 5

Ultrasonic Tomography Testing at NCAT Pavement Test Track

This chapter was prepared by Kyle Hoegh, graduate research assistant, and Dr. Lev Khazanovich both at the University of Minnesota.

Introduction

This chapter summarizes the initial results of testing with an ultrasound tomography device (MIRA) at the NCAT Pavement Test Track (NPTT) in Opelika, Alabama. Testing was conducted on the morning of April 11, 2010, at 10 sections in the passing lane. Ultrasonic measurements were taken to locate the presence and extent of delamination, or the extent of delamination, at two-lift asphalt test sections. MIRA showed various consistent types of signals throughout the different sections. An initial diagnosis is presented in this chapter, including analysis of the intensity-based real-time Synthetic Aperture Focusing Technique SAFT signals as well as subsequent SAFT-Full Waveform (SAFT-FW) analysis. This analysis and the conclusions presented are preliminary, while disclosure of the constructed defect locations and forensic analysis can be used to verify or calibrate the actual diagnosis associated with the different types of signals.

The use of SAFT B-scans and D-scans, as well as SAFT-FW B-Scans, indicated the following bond conditions based on an initial analysis:

- Section 1 is a proper bond between the asphalt lifts.
- Section 2 is delamination between asphalt lifts.
- Section 4 is slight level of delamination.
- Section 5 is significant level of delamination.
- Section 6 is very slight delamination.
- Sections 3, 7, 8, 9, and 10 are inconclusive when using the current analysis method.
- Newly constructed asphalt debonded with asphalt base in the right wheelpaths (RWPs) and left wheelpaths (LWPs) of Sections 9 and 10 as well as in the beginning (190 ft to 200 ft) of the LWP in Section 8.

Testing

An ongoing SHRP 2 NCAT Pavement Delamination Project was initiated to investigate nondestructive methods of determining delamination between asphalt layers. The principal investigators of the project provided the testing layout where the ultrasonic tomography scans described below were carried out to determine the effectiveness of ultrasonic tomography in detection of delamination in asphalt. An ultrasonic tomography device, MIRA, was used to conduct a "blind test" of locations with various levels of fabricated distresses in the passing lane of the NPTT (see Figure 5.1).

Each approximately 1-s MIRA scan gives a 2-dimensional (2-D) depth cross section (SAFT B-scan) with the vertical axis indicating the depth of any reflection (caused by any change in acoustic impedance), and the horizontal axis indicating the location along the aperture of the device with 0 being the center of the scan location. Figure 5.2 shows the MIRA device in position to take a SAFT B-scan. The type of SAFT B-scan signal that should be expected from properly bonded two-lift asphalt on an aggregate base is shown in Figure 5.3. This example B-scan was taken in the Section 6 truck lane and indicates a reflection at the asphalt-aggregate base interface of approximately 150 mm in depth. It can be observed that even in this properly bonded case, there is low-intensity reflection at shallower depths most likely due to reflections from aggregates and air voids. It is important to note that this amount of shallower reflection should be expected as a baseline for properly bonded cases when considering the delamination analysis.

Auburn University personnel identified the general area where testing was needed to verify the capabilities of MIRA in delamination diagnostics (see Figure 5.4 for the approximate measurement zero point). The tested pavement was separated into ten 25-ft. sections for a total of 250 ft of scanning, with Section 1 starting at 15 ft in the longitudinal direction. MIRA scanning was conducted at various locations of the passing

Figure 5.1. NPTT blind test location.

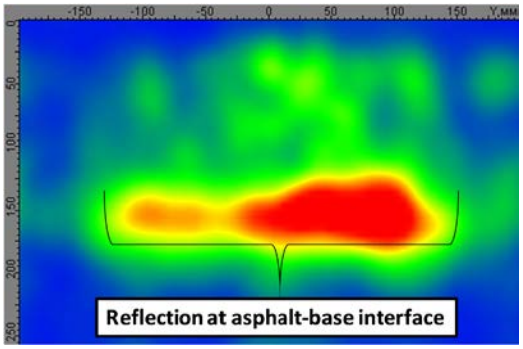

Figure 5.3. Example scan indicating properly bonded asphalt on grade.

lane. MIRA scans were taken with the long portion of the device aperture in transverse and longitudinal orientations at various positions within the 250-ft passing lane section, as described below:

- Longitudinal orientation (see Figure 5.2a): Scan is taken with the long portion of the MIRA device parallel with the direction of traffic. In this orientation, the horizontal axis indicates the longitudinal location, with 0 being at the center of the scan location.
- Transverse orientation (see Figure 5.2b): Scan is taken with the long portion of the MIRA device perpendicular to the direction of traffic. In this orientation, the horizontal axis indicates the transverse location, with 0 being at the center of the scan location.

Initial Analysis

Bands of measurements were taken in small step sizes (3 to 6 in.) in the transverse direction, with MIRA oriented longitudinally. By stitching these scans together, a profile below the surface in the transverse direction (TV) along the lane width (D-scan_TV) was realized. Similarly, bands of measurements taken in the transverse orientation with multiple small step sizes (~1 ft) in the longitudinal direction were stitched together to give a profile below the surface in both the right and left wheelpaths (D-scan_RWP and D-scan_LWP, respectively). These D-scans give an initial diagnosis of the amount of reflection occurring at different depths throughout the scanned section by averaging the intensity of reflection across the aperture of the device. The D-scans taken at each scanned location can be observed in Chapter 7.

As mentioned in the description of the B-scan in Figure 5.4, even in the case of properly bonded asphalt on grade, there are some lower intensity reflections at shallower depth due to aggregate and air voids. In addition, separating reflections from the transmitted shear wave from surface wave interference is less coherent near the surface (within 3 in. depth). Because the depth of the interface in question is near this shallower depth, analyzing the direct reflection from the asphalt lift interface is a challenging problem. Real-time analysis of intensity based SAFT B-scans or D-scans is highly dependent on the threshold and gain and insufficient for analysis of direct reflection at this depth without further signal processing. Therefore, use of backwall reflections (reflection at the depth of the newly constructed asphalt

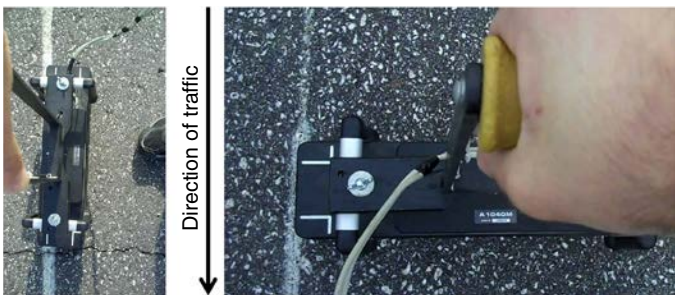

Figure 5.2. Ultrasonic tomography device (MIRA) in (a) longitudinal and (b) transverse orientations set for transverse and longitudinal step sizes, respectively.

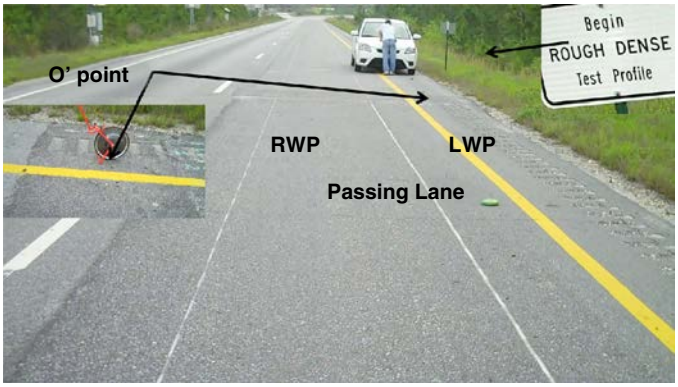

Figure 5.4. Approximate longitudinal zero point location for MIRA testing.

section) is valuable for diagnosis. In this case, the D-scan initial analysis of delamination can be based on the clarity of the backwall reflection. When this type of indirect analysis is used, a clear backwall reflection at the depth of the newly constructed asphalt would indicate properly bonded asphalt lifts. A less intense, less coherent backwall reflection, or the lack of a backwall reflection, would indicate locations where there is some sort of delamination or other flaw within the constructed asphalt layers that could be caused by debonding at the asphalt lift interface.

The type of analysis detailed above is effective for analysis where there is a consistent backwall reflection at the asphalt thickness depth. Therefore, cases where the asphalt is constructed over a concrete or aggregate base allow for the analysis method described in the previous paragraph because there is a large enough difference in acoustic impedance to cause a consistent backwall reflection as a reference. For the asphalt sections tested at the NPTT, this type of analysis was only effective for diagnosing delamination conditions in Sections 1 and 2 because those sections were located on top of concrete, while the remaining sections were constructed on top of existing asphalt. Figure 5.5 shows the left and right wheelpath D-scans for Section 1. It can be observed that similar types of signals were found in the left and right wheelpaths, indicating similar bond condition throughout the width of the lane. Section 1 scan locations showed a strong backwall reflection, indicating properly bonded asphalt layers. It can also be observed that the backwall reflection is less coherent with less intensity from approximately 40 to 50 ft where Section 2 starts (the full Section 2 D-scans can be observed in Chapter 7). This is most likely due to shadowing of the backwall from delamination or defects in the constructed asphalt.

While the analysis described above should be effective for getting an initial idea of the condition of the bond condition between lifts, the analysis is based only on reflection intensity. Additional information is available through analysis of the full waveform (including polarity of the reflected shear wave pulse). To use this additional information, a variation of the SAFT algorithm that uses the full waveform was applied. This was carried out with the SAFT-FW algorithm developed at the University of Minnesota, which accounts for the polarity of the reflected wave pulses. Figure 5.6 gives an example scan location from Section 1 (Figures 5.6A and 5.6B) taken approximately at stationing 00+19 ft and Section 2 (Figures 5.6C and 5.6D) taken at approximately 00+42 ft. Similar to the D-scan analysis, the SAFT B-scans shown on the left (Figures 5.6A and 5.6D) have a stronger, more coherent backwall reflection in Section 1 as compared to Section 2. Using SAFT-FW scans (Figures 5.6B and 5.6D) adds additional insight. It can be observed that the initial negative polarity (blue) arrival (indicative of a reflection from lower to higher impedance mediums) at the backwall reflection is nonexistent in the SAFT-FW scan of Section 2 (Figure 5.6D), while it is clear in the SAFT-FW scan of Section 1 (Figure 5.6B). Additional analysis of Figure 5.6D shows multiple reflections at smaller intervals than should be expected from a secondary backwall reflection, also indicating the presence of a shallower planar defect consistent with what should be expected from delamination at the asphalt lift. These types of comparisons were also observed in additional SAFT-FW B-scans as seen in Chapter 7.

As described above, analysis of asphalt over an asphalt base requires more detailed analysis that does not rely on

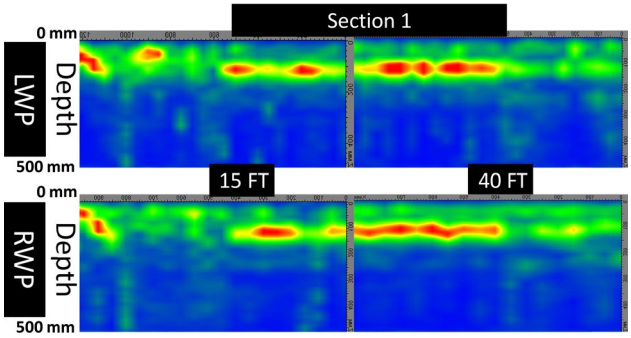

Figure 5.5. Analysis of MIRA D-scans in the left and right wheelpaths of Section 1 and in the start of Section 2 for asphalt over a concrete base.

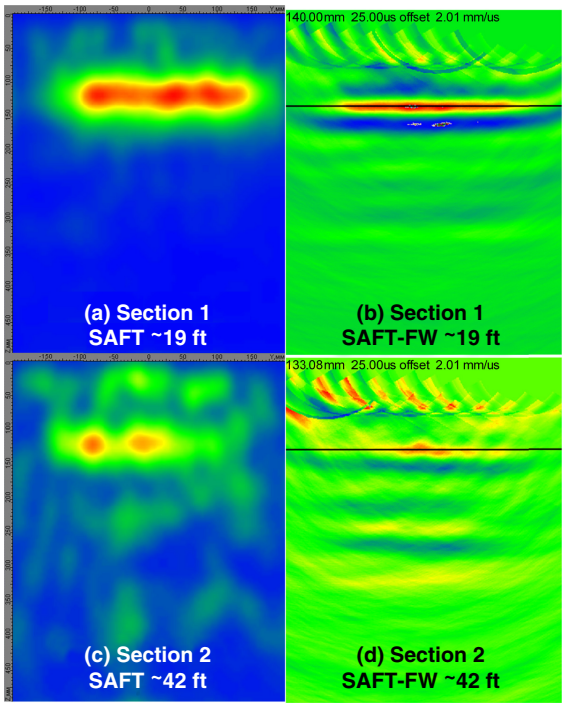

Figure 5.6. SAFT and SAFT-FW B-scans for representative locations of Section 1 (a and b, respectively) and Section 2 (c and d, respectively).

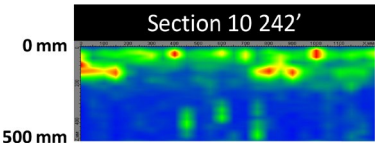

Figure 5.7. D-scan-TV taken along the transverse direction in the passing lane at about 242 ft in Section 10.

shadowing of the backwall reflection. In this case, if the constructed layer and asphalt base are properly constructed, the backwall reflection will be absent. If there is debonding of the constructed asphalt layer and asphalt base, the backwall reflection should be present. Both of these processes are independent of the asphalt lift bond condition, therefore making analysis of the backwall reflection inconclusive when simple reflection intensity analysis is used. Figure 5.7 shows a D-scan taken along the transverse direction in the passing lane at about 242 ft in Section 10. It can be observed that there is a coherent backwall reflection at the start of the D-scan (in the LWP), then again at approximately two-thirds of the transverse D-scan. It is likely that this type of observation was caused by a poor bond between the constructed asphalt and asphalt base at locations where there is a backwall reflection. While this type of analysis is of little help in examining the asphalt lift bond condition, it did indicate that an improper bond at the asphalt thickness was likely in the LWP and RWP of Sections 9 and 10, as well as in the LWP at the start of Section 8. See Chapter 7 for more indications of debonding between the newly constructed asphalt and the asphalt base.

For the other cases where a backwall reflection is largely absent (scans taken in Sections 3 through 7 and most scans taken in Section 8), each B-scan would need to be normalized so that reflections from any possible planar defect could be resolved from the structural noise and surface reflections. Through SAFT-FW normalization and analysis, characteristics of a shallow planar flaw were observed in certain locations. Figure 5.8 shows an SAFT B-scan (Figure 5.8A) and an SAFT-FW B-scan (Figure 5.8B) taken in Section 5, as well as the same scans shown in Figure 5.6 (Figures 5.8C and 5.8D) from Section 2. Although analysis of the SAFT B-scans does not show any similarity between Section 5 and Section 2, a similar trend was observed in the SAFT-FW B-scans (Figures 5.8B and 5.8D, respectively). While reflections at greater depths could not be resolved in Figure 5.8A, SAFT-FW analysis indicated multiple reflections at smaller intervals similar to those observed in Section 2 (Figure 5.8D), suggesting the presence of a shallower planar defect. This type of signal was consistently observed in Section 5, indicating the presence of delamination (see Chapter 7). Although less coherent and less frequent, signals that were similar were observed in Section 4,

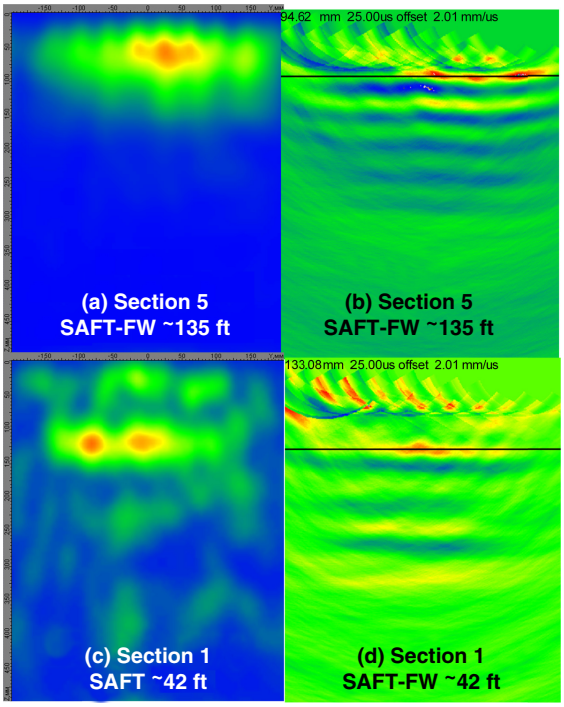

Figure 5.8. Sections 5 (top) and 2 (bottom) SAFT B-scans (left) and SAFT-FW B-scans (right).

also indicating the presence of slight delamination at the lift (see Chapter 7). Some even less significant and less frequent similar type of signals were observed in Section 6, indicating very slight delamination at the lift. Further investigation of scans at Sections 3, 7, and 8 would be required to determine the presence or extent of delamination, because the methods presented in this chapter did not show a strong or consistent indication of delamination.

Conclusions

Testing with an ultrasound tomography device (MIRA) at the NPTT in Opelika, Alabama, based on intensity of reflection B-scan and D-scan results showed different types of signals. The similarities between the left and right wheelpaths and coherent changes in their D-scans indicated multiple consistent trends in the asphalt conditions within most sections. The SAFT-FW algorithm was also used to give additional information about the asphalt condition in which real-time SAFT analysis needed further investigation. The results that follow are preliminary and are given on the basis of the current MIRA analysis.

Analysis of bond condition of asphalt lifts at 3 in. or less for asphalt constructed on a concrete or aggregate base is more straightforward than analysis for an asphalt base. However, initial analysis of asphalt constructed on asphalt base shows that delamination at greater depths can be observed by analyzing the direct reflection from MIRA SAFT B-scans.

Analysis using SAFT-FW allows for a more comprehensive analysis of bond condition of asphalt over a concrete base and also seems to give an indication of severe lift debonding, even for cases where the newly constructed asphalt is fully bonded to the asphalt base.

The use of SAFT B-scans and D-scans, as well as SAFT-FW B-scans, indicated the following bond conditions:

- Concrete base (Sections 1 and 2):
  - Section 1: Strong backwall reflection, indicating a proper bond between the asphalt lifts.
  - Section 2: Shadowing of backwall reflection in SAFT B-scans and D-scans, as well as multiple reflections at small depth intervals, indicating a significant level of delamination between asphalt lifts in Section 2.
- Asphalt base (Sections 3 through 10):
  - Bond between newly constructed asphalt and asphalt base.
  - Sections 3, 4, 5, 6, and 7: Absence of significant backwall reflection in D-scans and B-scans, indicating good bond between the newly constructed asphalt and the old asphalt.
  - Section 8: Backwall reflection in the LWP from 190 ft to 200 ft indicating debonding in LWP at the beginning of the section. Absence of significant backwall reflection in RWP and transverse direction at 192 ft, indicating good bond between the newly constructed asphalt and the old asphalt in those locations.
  - Sections 9 and 10: Backwall reflection from 225 ft to 250 ft in the RWP and LWP in the longitudinal D-scans as well as at the beginning and at the two-thirds mark of the Section 10 transverse D-scans, indicating debonding in both wheelpaths. No backwall reflection in the majority of the transverse direction D-scans, indicating proper bond in locations not located near the wheel paths. Bond between asphalt lifts in the newly constructed asphalt.
  - Section 4: SAFT-FW analysis shows a less coherent and less consistent amount of multiple reflections at small depth intervals, indicating a small level of delamination.
  - Section 5: SAFT-FW analysis shows multiple reflections at small depth intervals, indicating a significant level of delamination.
  - Section 6: Although less coherent than in Section 4, an SAFT-FW analysis shows slight multiple reflections at some locations, indicating very slight delamination.
  - Sections 3, 7, 8, 9, and 10: Little to no indication of multiple reflections in SAFT-FW analysis, indicating either no presence of delamination, or a need for a detailed analysis method for shallow-lift delamination detection of asphalt constructed on an asphalt base.

Section 1

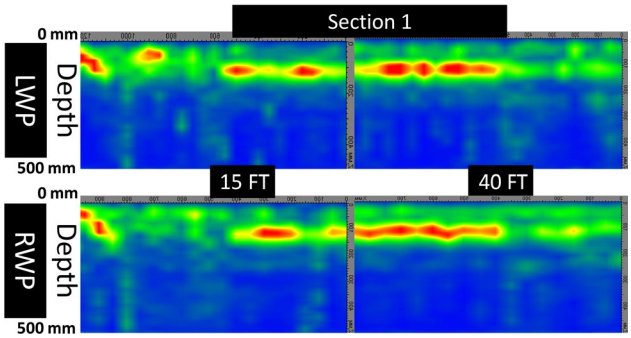

Figure 5.9. Left (top) and right (bottom) wheelpath D-scans with horizontal axis indicating longitudinal stationing and vertical axis indicating depth below the measurement.

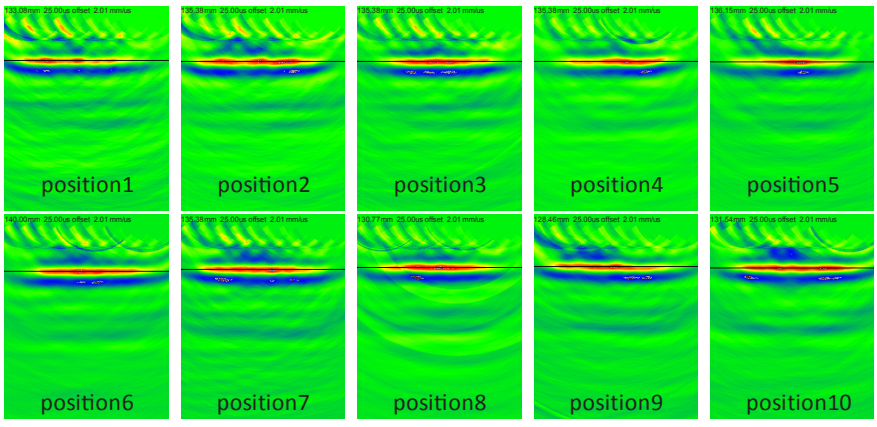

Section 1 into 0 Left Wheel Path

Figure 5.10. SAFT-FW B-scans taken from Position 1 (~25 ft) to Position 10 (~15 ft) in the LWP.

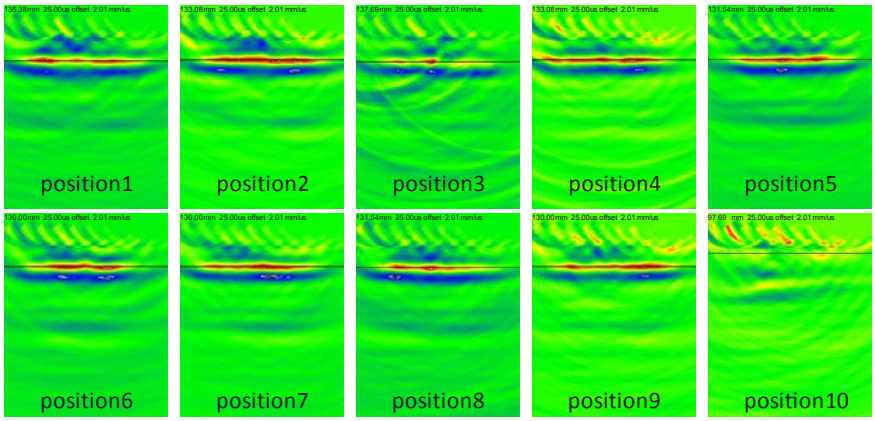

Section 1 into 0 Right Wheel Path

Figure 5.11. SAFT-FW B-scans taken from Position 1 (~25 ft) to Position 10 (~13 ft) in the RWP.

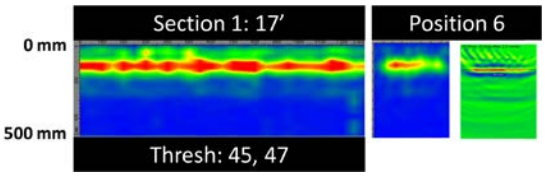

Note: Thresh. = threshold.

Figure 5.12. SAFT D-scan (left) taken at the beginning of Section 1 along the transverse direction along with an example SAFT and SAFT-FW B-scan at Position 6 (right).

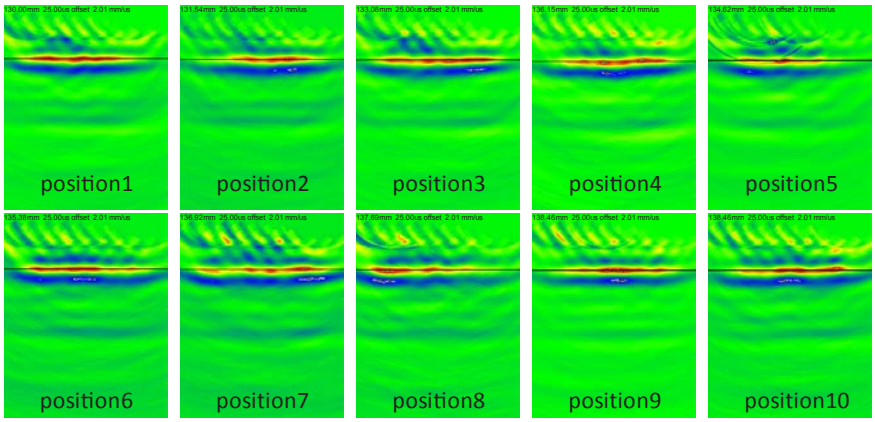

Section 1 Transverse Measurement (17' - 30 khz)

Figure 5.13. SAFT-FW B-scans at a center frequency of 30 kHz taken from a location at 17 ft along the transverse direction starting at the LWP through a location just before the center of the passing lane.

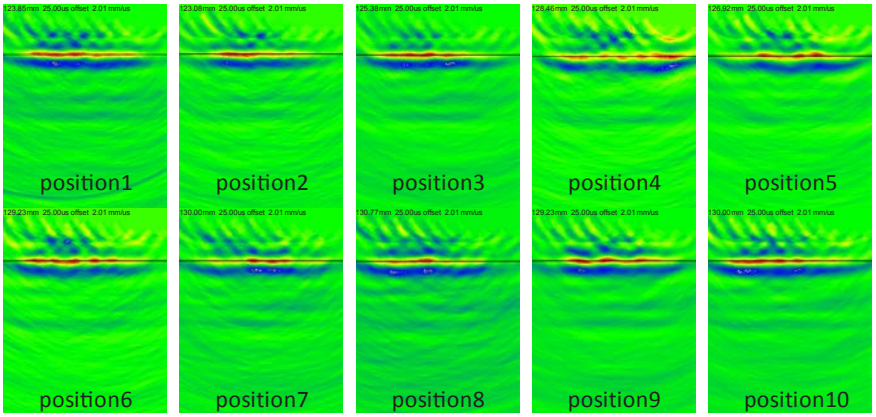

Section 1 Transverse Measurement (17' - 50 khz)

Figure 5.14. SAFT-FW B-scans at a center frequency of 50 kHz taken from at 17 ft along the transverse direction starting at the LWP through a location just before the center of the passing lane.

Section 2

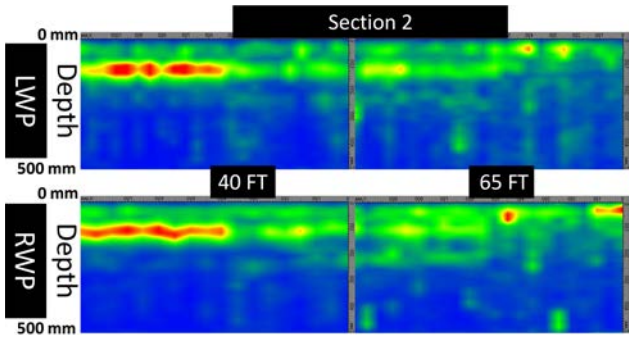

Figure 5.15. Left (top) and right (bottom) wheelpath D-scans with horizontal axis indicating longitudinal stationing and vertical axis indicating depth below the measurement.

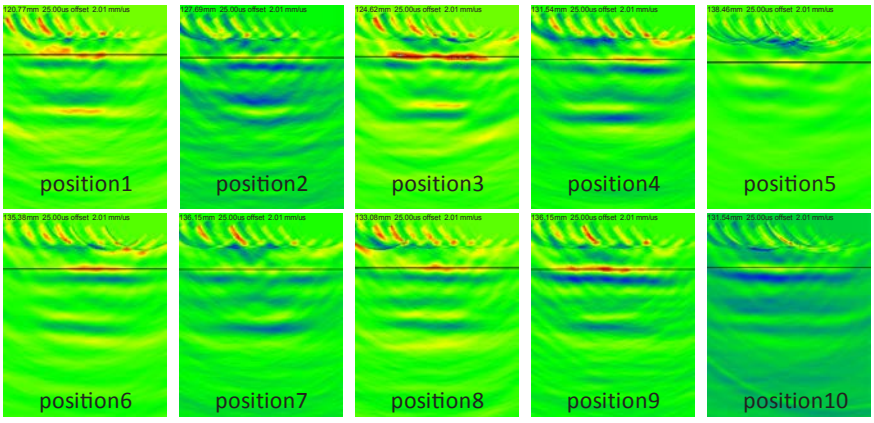

Section 2 into 1 Left Wheel Path

Figure 5.16. SAFT-FW B-scans taken from Position 1 (~50 ft) to Position 10 (~40 ft) in the LWP.

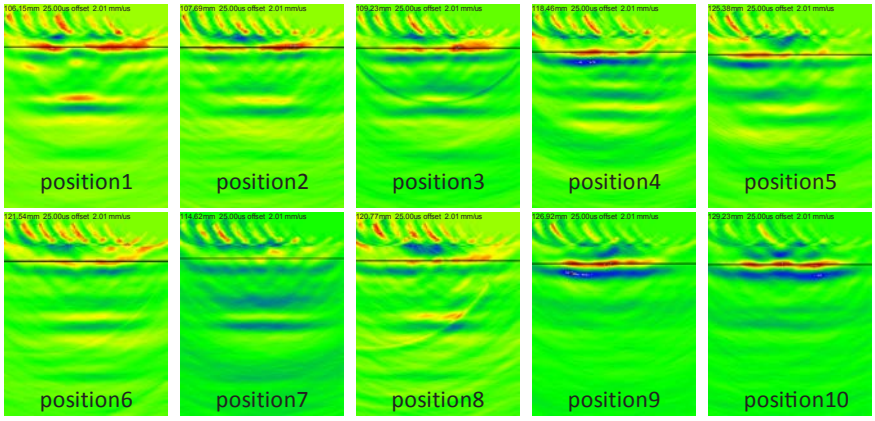

Section 2 into 1 Right Wheel Path

Figure 5.17. SAFT-FW B-scans taken from Position 1 (~50 ft) to Position 10 (~38 ft) in the RWP.

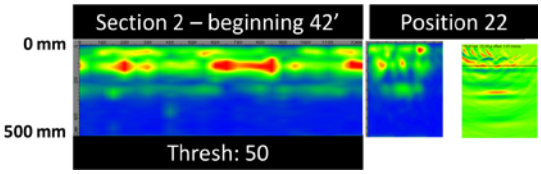

Note: Thresh. = threshold.

Figure 5.18. SAFT D-scan (left) taken at the beginning of Section 2 along the transverse direction along with an example SAFT and SAFT-FW B-scan at Position 22 (right).

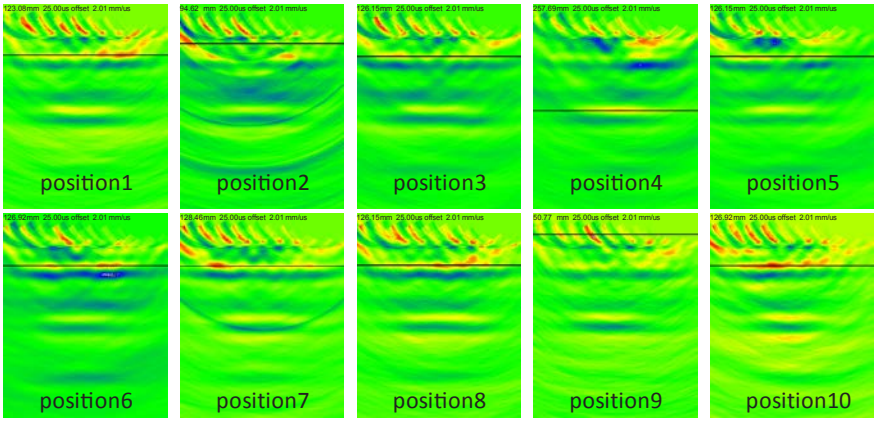

Section 2 Transverse Measurement (42' - 30 khz)

Figure 5.19. SAFT-FW B-scans at a center frequency of 30 kHz taken from a location at 42 ft along the transverse direction starting at the LWP through a location just before the center of the passing lane.

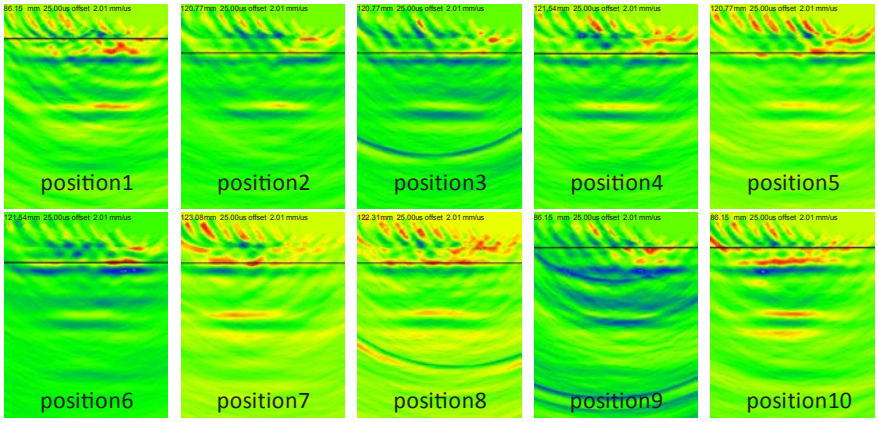

Section 2 Transverse Measurement (42' - 50 khz)

Figure 5.20. SAFT-FW B-scans at a center frequency of 50 kHz taken from a location at 42 ft along the transverse direction starting at the LWP through a location just before the center of the passing lane.

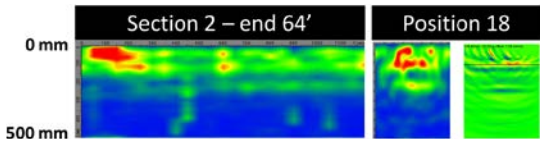

Figure 5.21. SAFT D-scan (left) taken at the end of Section 2 along the transverse direction along with an example SAFT and SAFT-FW B-scan at Position 18 (right).

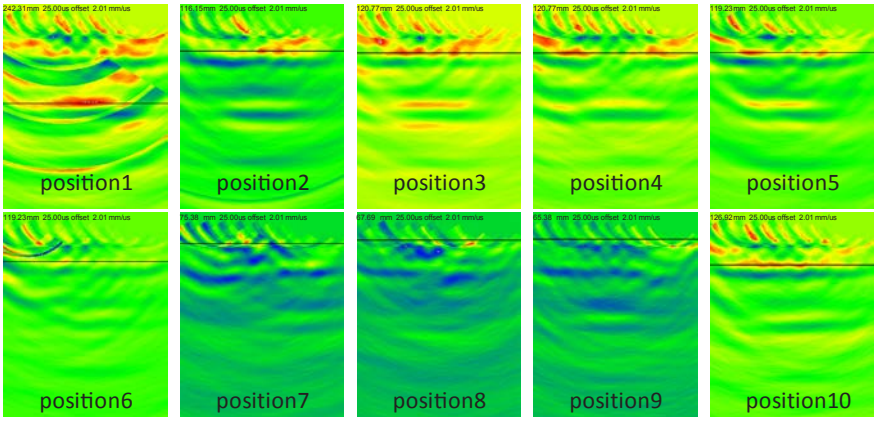

Section 2 Transverse Measurement (64' - 30 khz)

Figure 5.22. SAFT-FW B-scans at a center frequency of 30 kHz taken from a location at 64 ft along the transverse direction starting at the LWP through a location just before the center of the passing lane.

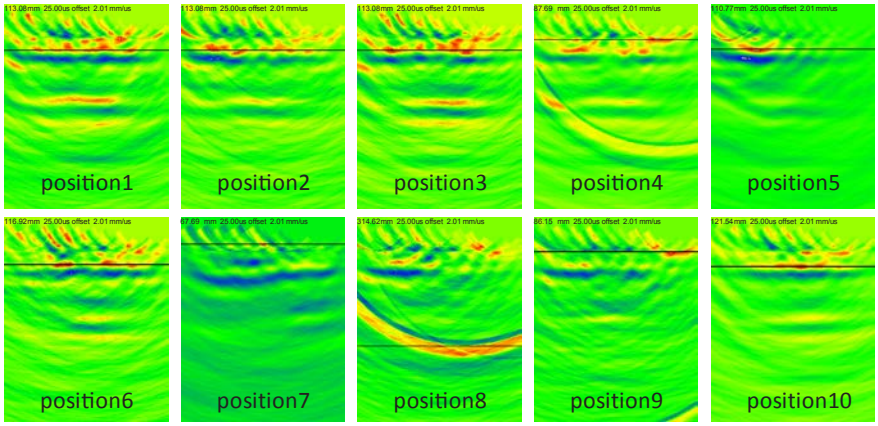

Section 2 Transverse Measurement (64' - 50 khz)

Figure 5.23. SAFT-FW B-scans at a center frequency of 50 kHz taken from a location at 64 ft along the transverse direction starting at the LWP through a location just before the center of the passing lane.

Section 3

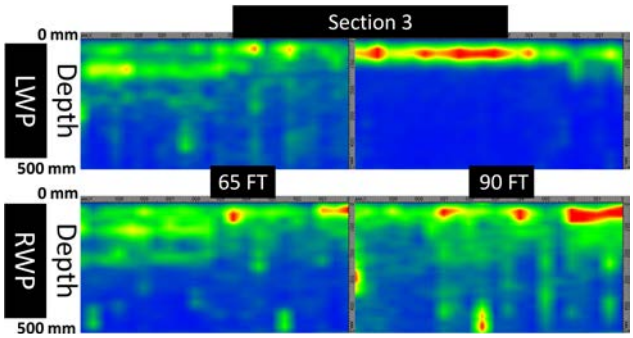

Figure 5.24. Left (top) and right (bottom) wheelpath D-scans with horizontal axis indicating longitudinal stationing and vertical axis indicating depth below the measurement.

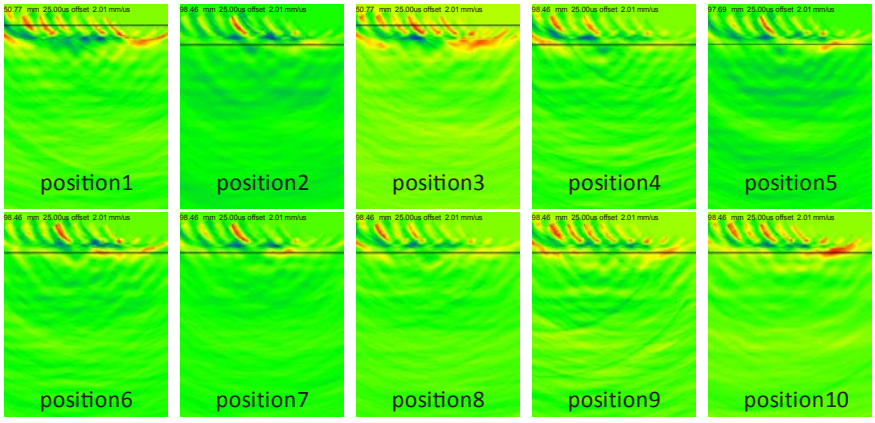

Section 3 into 2 Left Wheel Path

Figure 5.25. SAFT-FW B-scans taken from Position 1 (~75 ft) to Position 10 (~60 ft) in the LWP.

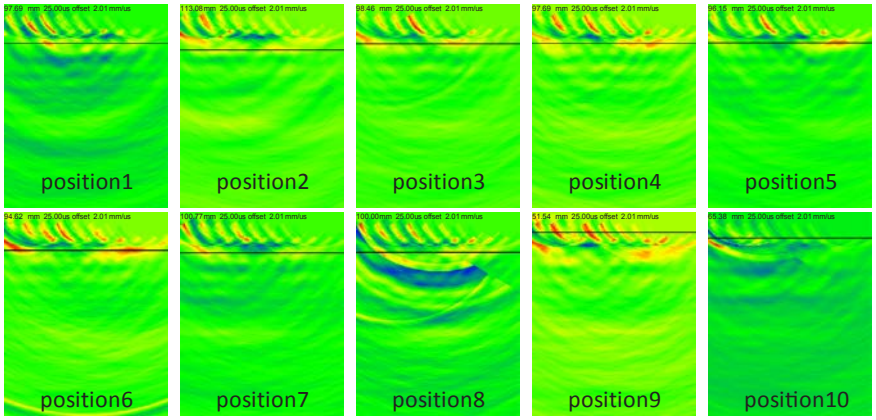

Section 3 into 2 Right Wheel Path

Figure 5.26. SAFT-FW B-scans taken from Position 1 (~75 ft) to Position 10 (~58 ft) in the RWP.

Section 4

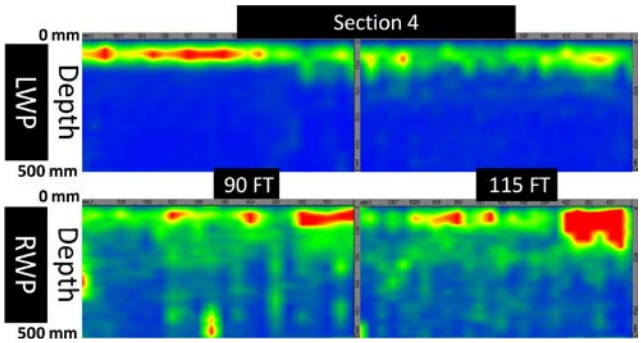

Figure 5.27. Left (top) and right (bottom) wheelpath D-scans with horizontal axis indicating longitudinal stationing and vertical axis indicating depth below the measurement.

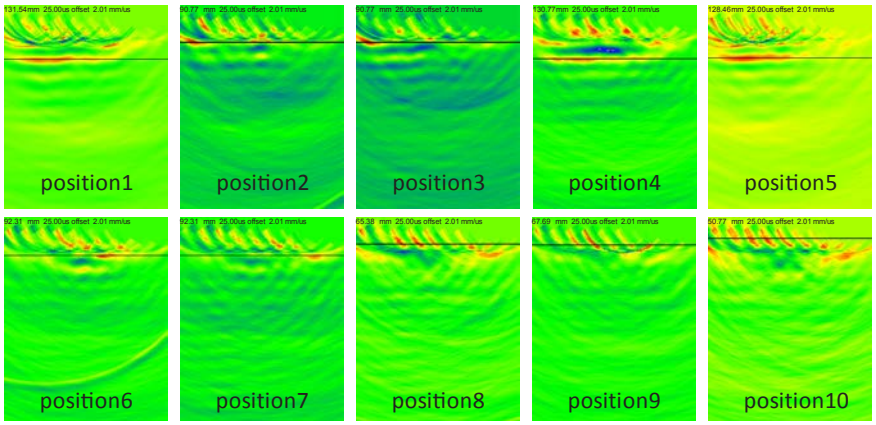

Section 4 into 3 Left Wheel Path

Figure 5.28. SAFT-FW B-scans taken from Position 1 (~100 ft) to Position 10 (~90 ft) in the LWP.

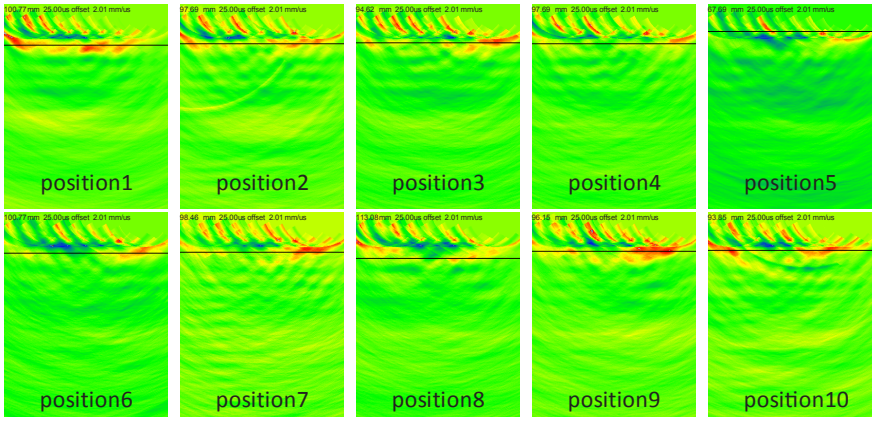

Section 4 into 3 Right Wheel Path

Figure 5.29. SAFT-FW B-scans taken from Position 1 (~100 ft) to Position 10 (~88 ft) in the RWP.

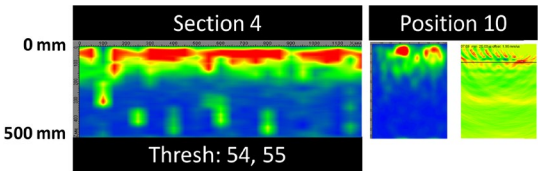

Note: Thresh. = threshold.

Figure 5.30. SAFT D-scan (left) taken at the beginning of Section 4 along the transverse direction along with an example SAFT and SAFT-FW B-scan at Position 10 (right).

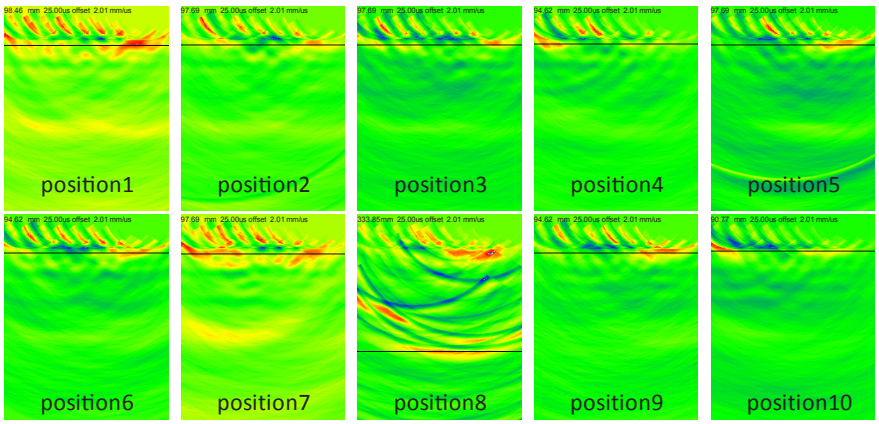

Section 4 Transverse Measurement (92' - 30 khz)

Figure 5.31. SAFT-FW B-scans at a center frequency of 30 kHz taken from a location at 92 ft along the transverse direction starting at the LWP through a location just before the center of the passing lane.

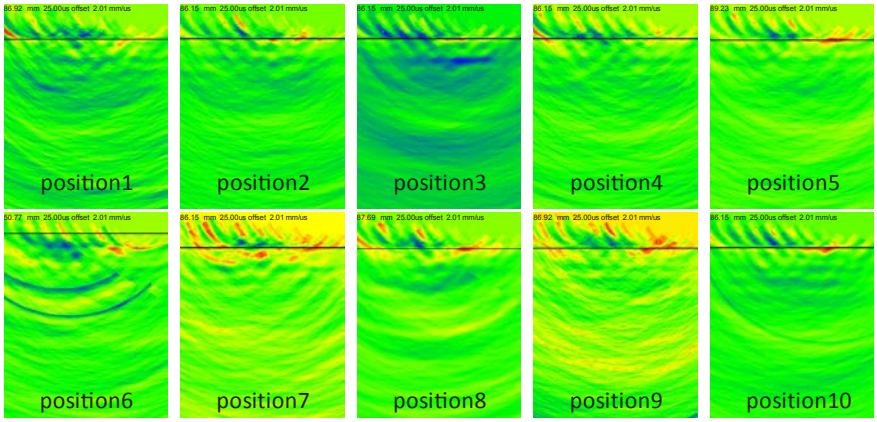

Section 4 Transverse Measurement (92' - 50 khz)

Figure 5.32. SAFT-FW B-scans at a center frequency of 50 kHz taken from a location at 92 ft along the transverse direction starting at the LWP through a location just before the center of the passing lane.

Section 5

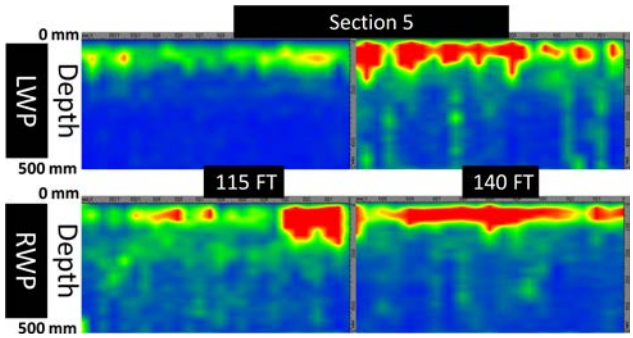

Figure 5.33. Left (top) and right (bottom) wheelpath D-scans with horizontal axis indicating longitudinal stationing and vertical axis indicating depth below the measurement.

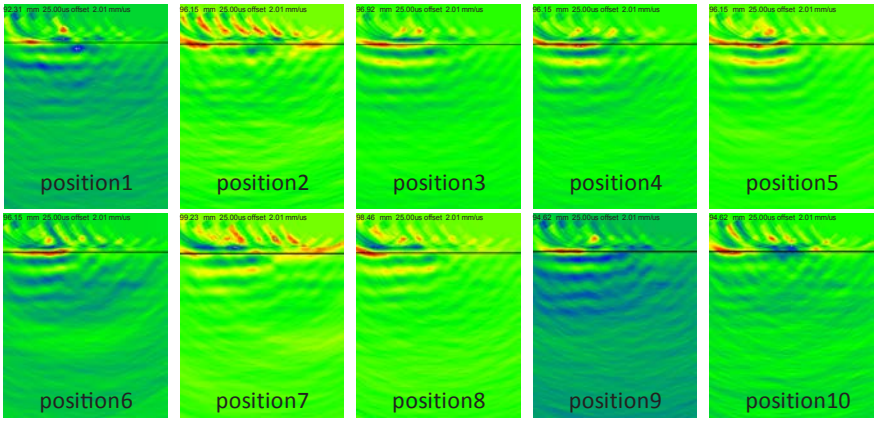

Section 5 into 4 Left Wheel Path

Figure 5.34. SAFT-FW B-scans taken from Position 1 (~125 ft) to Position 10 (~115 ft) in the LWP.

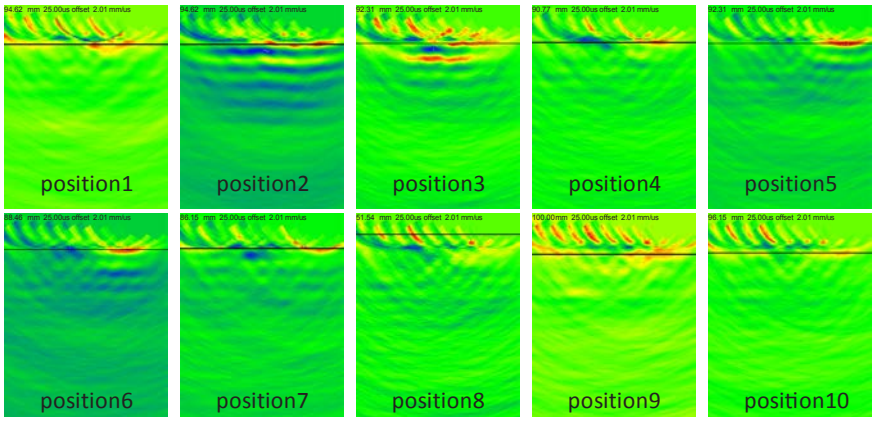

Section 5 into 4 Right Wheel Path

Figure 5.35. SAFT-FW B-scans taken from Position 1 (~125 ft) to Position 10 (~113 ft) in the RWP.

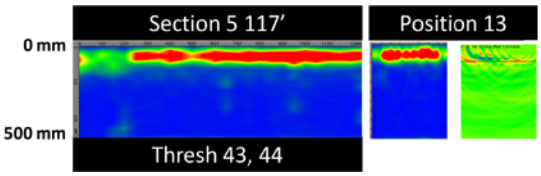

Note: Thresh. = threshold.

Figure 5.36. SAFT D-scan (left) taken at the beginning of Section 5 along the transverse direction along with an example SAFT and SAFT-FW B-scan at Position 13 (right).

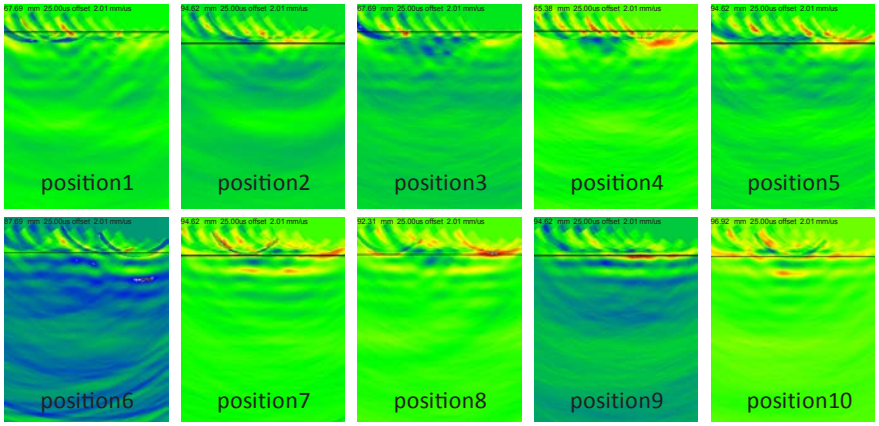

Section 5 Transverse Measurement (117' - 30 khz)

Figure 5.37. SAFT-FW B-scans at a center frequency of 30 kHz taken from a location at 17 ft along the transverse direction starting at the LWP through a location just before the center of the passing lane.

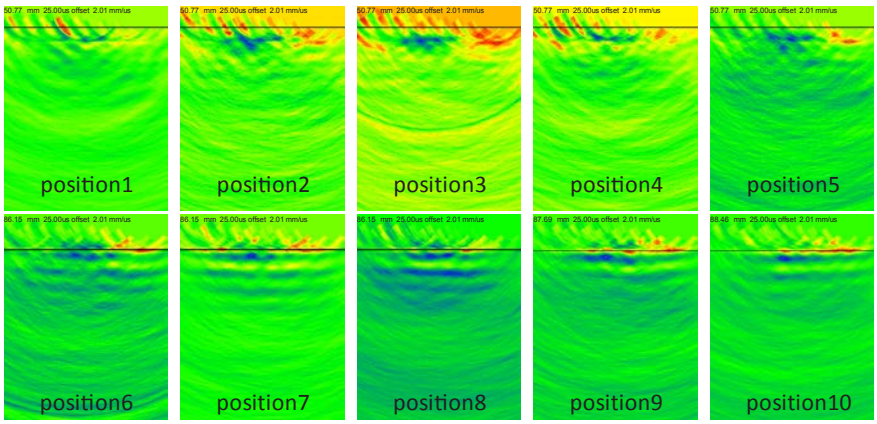

Section 5 Transverse Measurement (117' - 50 khz)

Figure 5.38. SAFT-FW B-scans at a center frequency of 50 kHz taken from a location at 17 ft along the transverse direction starting at the LWP through a location just before the center of the passing lane.

Section 6

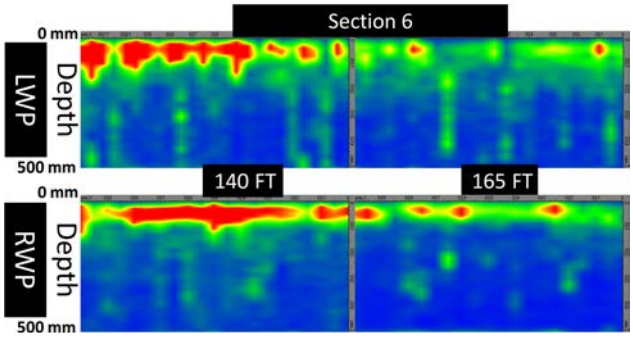

Figure 5.39. Left (top) and right (bottom) wheelpath D-scans with horizontal axis indicating longitudinal stationing and vertical axis indicating depth below the measurement.

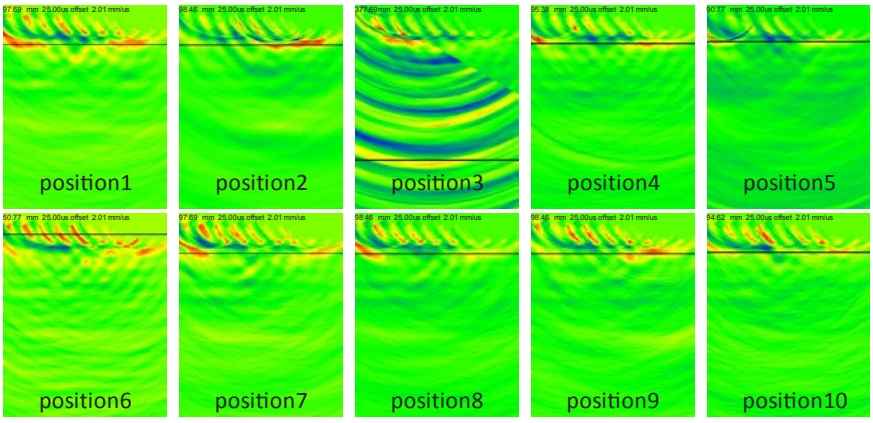

Section 6 into 5 Left Wheel Path

Figure 5.40. SAFT-FW B-scans taken from Position 1 (~150 ft) to Position 10 (~140 ft) in the LWP.

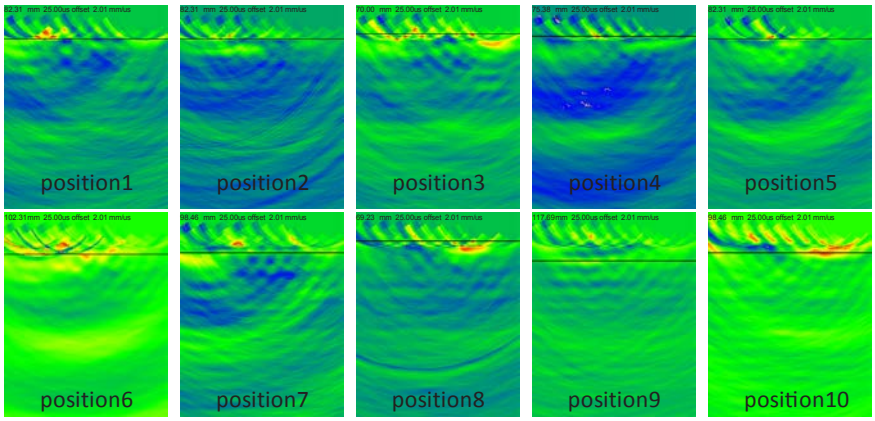

Section 6 into 5 Right Wheel Path

Figure 5.41. SAFT-FW B-scans taken from Position 1 (~150 ft) to Position 10 (~138 ft) in the RWP.

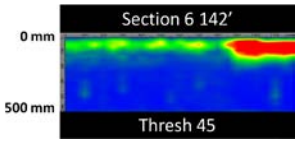

Note: Thresh. = threshold.

Figure 5.42. SAFT D-scan taken at the beginning of Section 6.

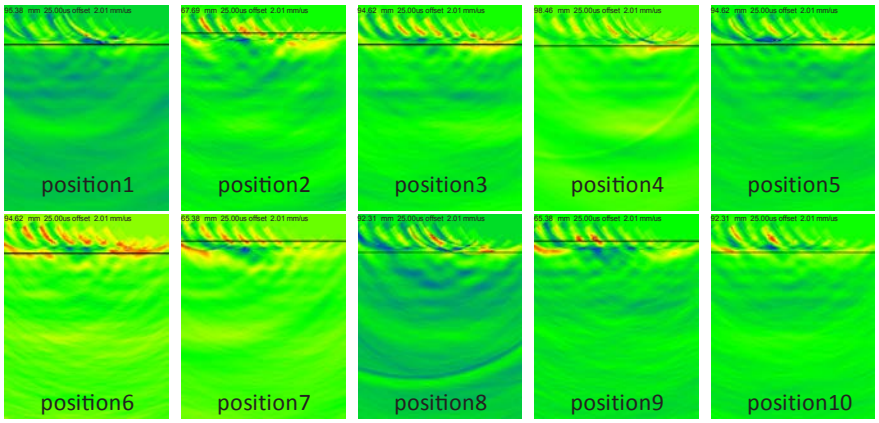

Section 6 Transverse Measurement (142' - 30 khz)

Figure 5.43. SAFT-FW B-scans at a center frequency of 30 kHz taken from a location at 142 ft along the transverse direction starting at the LWP through a location just before the center of the passing lane.

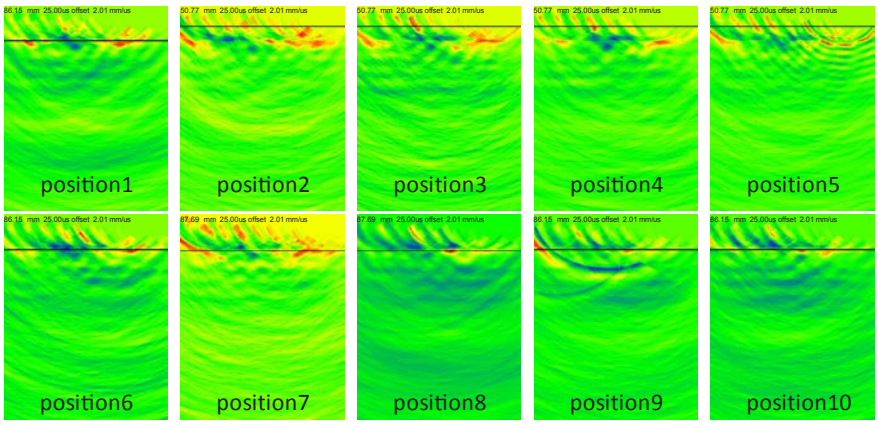

Section 6 Transverse Measurement (142' - 50 khz)

Figure 5.44. SAFT-FW B-scans at a center frequency of 50 kHz taken from a location at 142 ft along the transverse direction starting at the LWP through a location just before the center of the passing lane.

Section 7

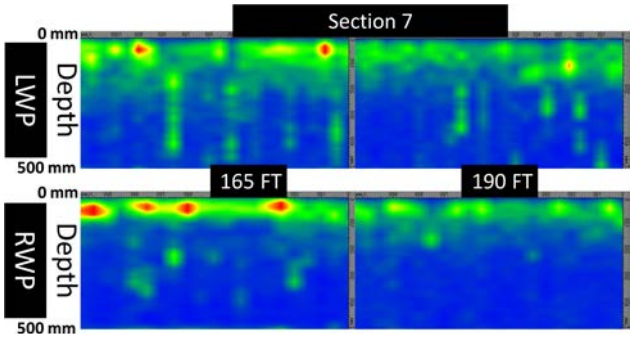

Figure 5.45. Left (top) and right (bottom) wheelpath D-scans with horizontal axis indicating longitudinal stationing and vertical axis indicating depth below the measurement.

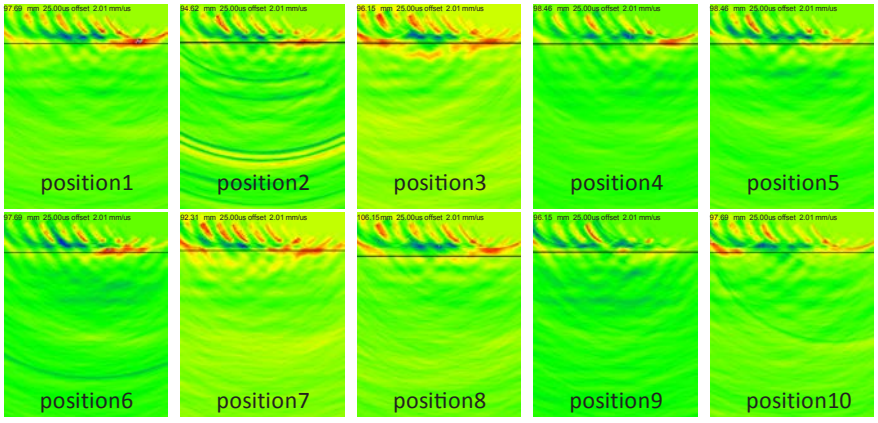

Section 7 into 6 Left Wheel Path

Figure 5.46. SAFT-FW B-scans taken from Position 1 (~175 ft) to Position 10 (~165 ft) in the LWP.

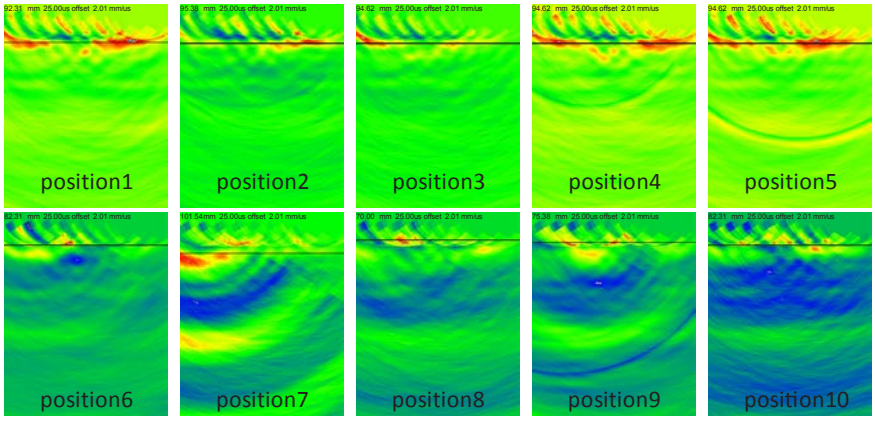

Section 7 into 6 Right Wheel Path

Figure 5.47. SAFT-FW B-scans taken from Position 1 (~175 ft) to Position 10 (~163 ft) in the RWP.

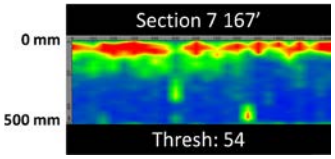

Note: Thresh. = threshold.

Figure 5.48. SAFT D-scan taken at the beginning of Section 7 along the transverse direction.

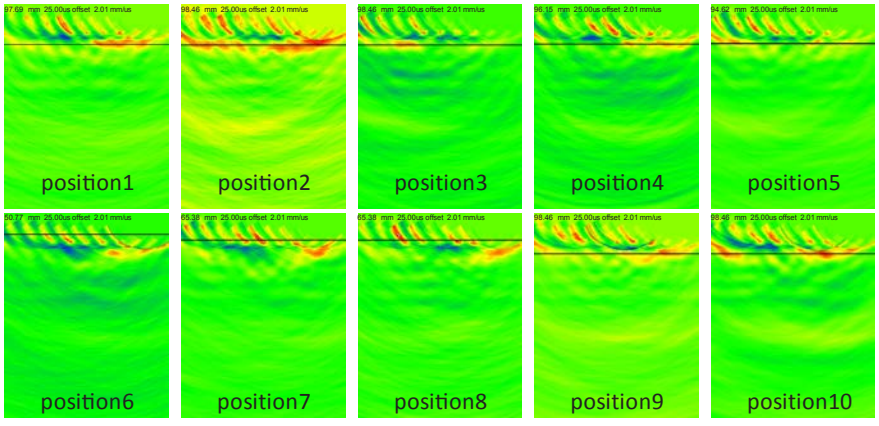

Section 7 Transverse Measurement (167' - 30 khz)

Figure 5.49. SAFT-FW B-scans at a center frequency of 30 kHz taken from a location at 17 ft along the transverse direction starting at the LWP through a location just before the center of the passing lane.

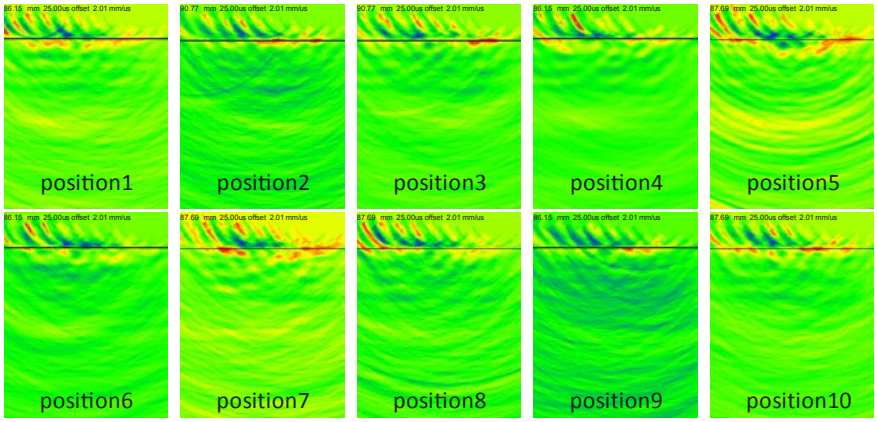

Section 7 Transverse Measurement (167' - 50 khz)

Figure 5.50. SAFT-FW B-scans at a center frequency of 50 kHz taken from a location at 17 ft along the transverse direction starting at the LWP through a location just before the center of the passing lane.

Section 8

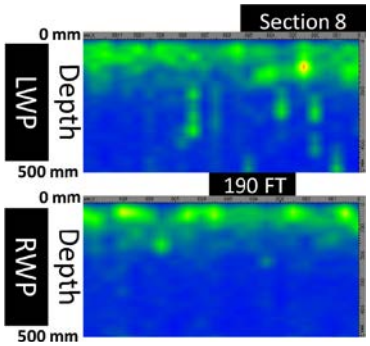

Figure 5.51. Left (top) and right (bottom) wheelpath D-scans with horizontal axis indicating longitudinal stationing and vertical axis indicating depth below the measurement.

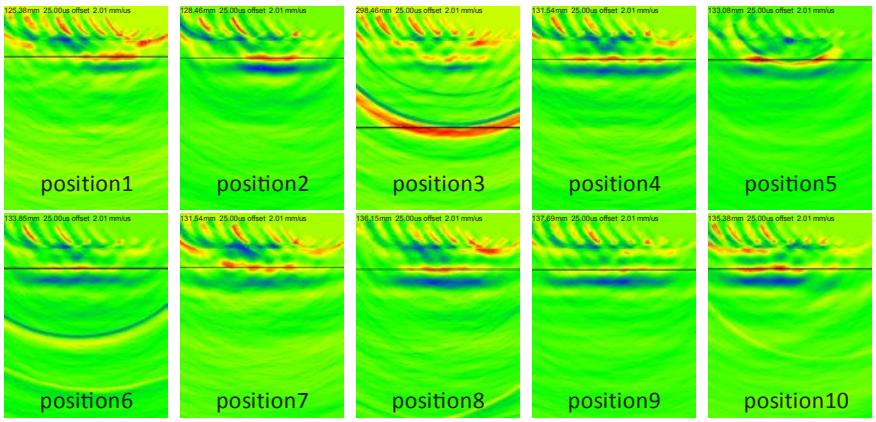

Section 8 into 7 Left Wheel Path

Figure 5.52. SAFT-FW B-scans taken from Position 1 (~200 ft) to Position 10 (~190 ft) in the LWP.

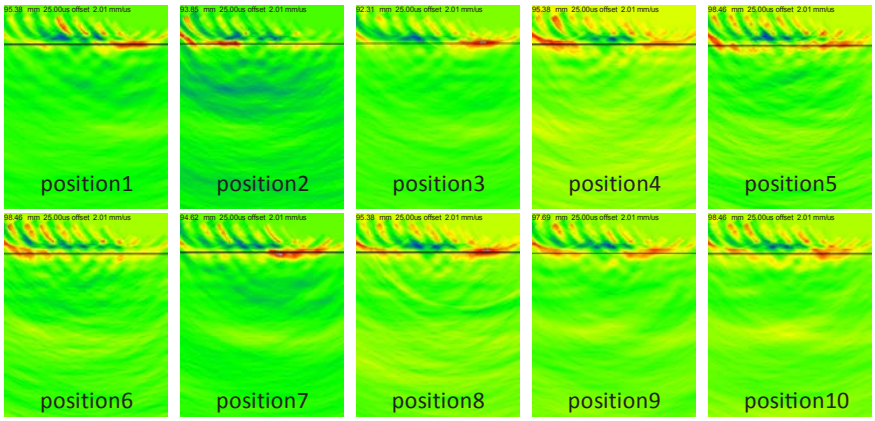

Section 8 into 7 Right Wheel Path

Figure 5.53. SAFT-FW B-scans taken from Position 1 (~200 ft) to Position 10 (~188 ft) in the RWP.

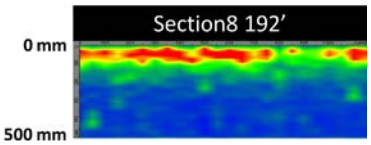

Figure 5.54. SAFT D-scan taken at the beginning of Section 8 along the transverse direction.

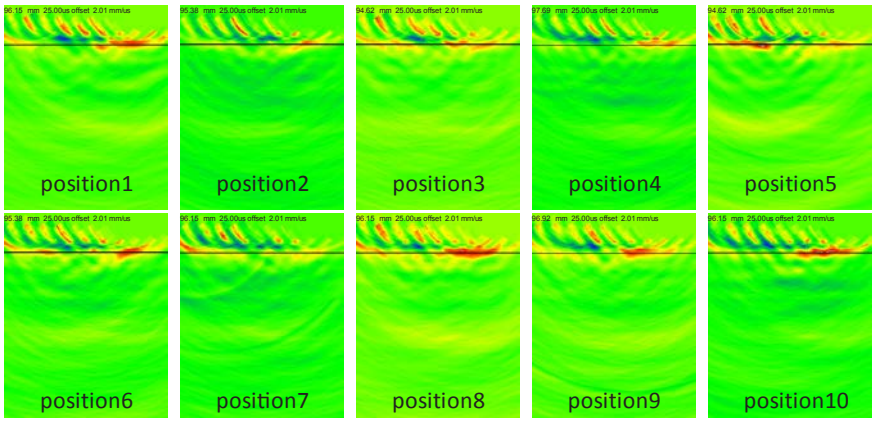

Section 8 Transverse Measurement (192' - 30 khz)

Figure 5.55. SAFT-FW B-scans at a center frequency of 30 kHz taken at a location 192 ft along the transverse direction starting at the LWP through a location just before the center of the passing lane.

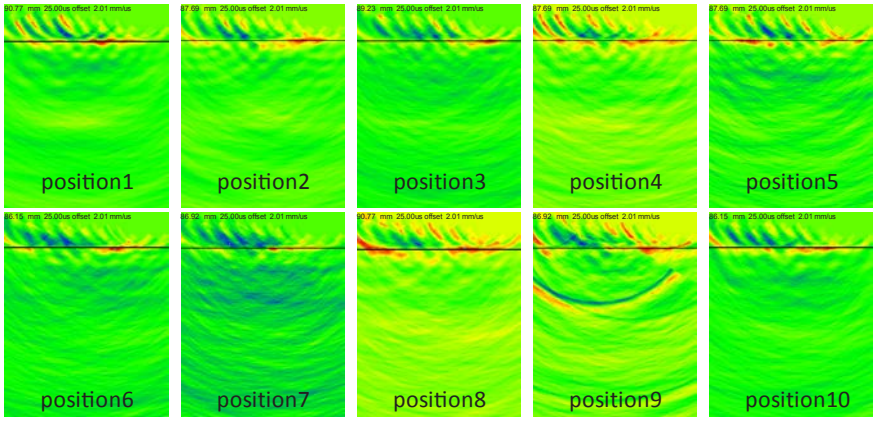

Section 8 Transverse Measurement (192' - 50 khz)

Figure 5.56. SAFT-FW B-scans at a center frequency of 50 kHz taken at a location 192 ft along the transverse direction starting at the LWP through a location just before the center of the passing lane.

Section 9

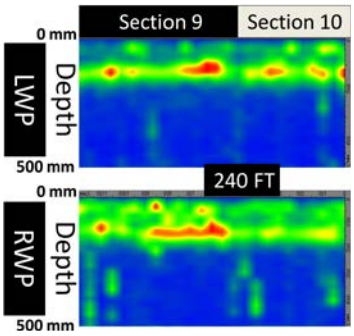

Figure 5.57. Left (top) and right (bottom) wheelpath D-scans with horizontal axis indicating longitudinal stationing and vertical axis indicating depth below the measurement.

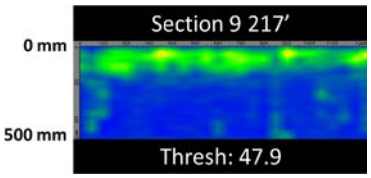

Note: Thresh. = threshold.

Figure 5.58. SAFT D-scan taken at the beginning of Section 9 along the transverse direction.

Section 10

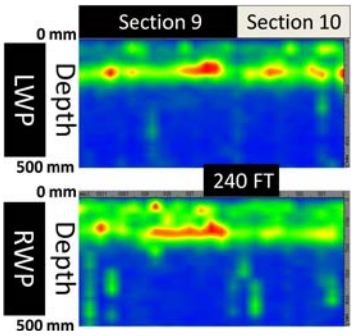

Figure 5.59. Left (top) and right (bottom) wheelpath D-scans with horizontal axis indicating longitudinal stationing and vertical axis indicating depth below the measurement.

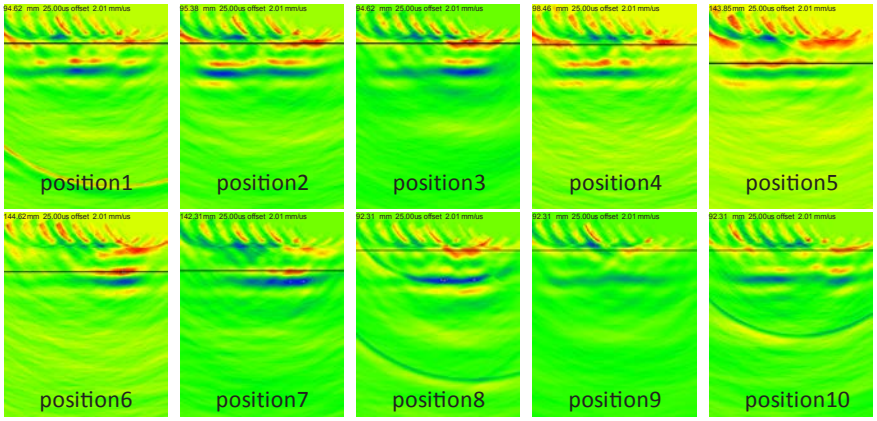

Section 10 into 9 Right Wheel Path

Figure 5.60. SAFT-FW B-scans taken from Position 1 (~250 ft) to Position 10 (~240 ft) in the RWP.

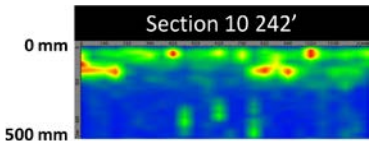

Figure 5.61. SAFT D-scan taken at the beginning of Section 10 along the transverse direction.

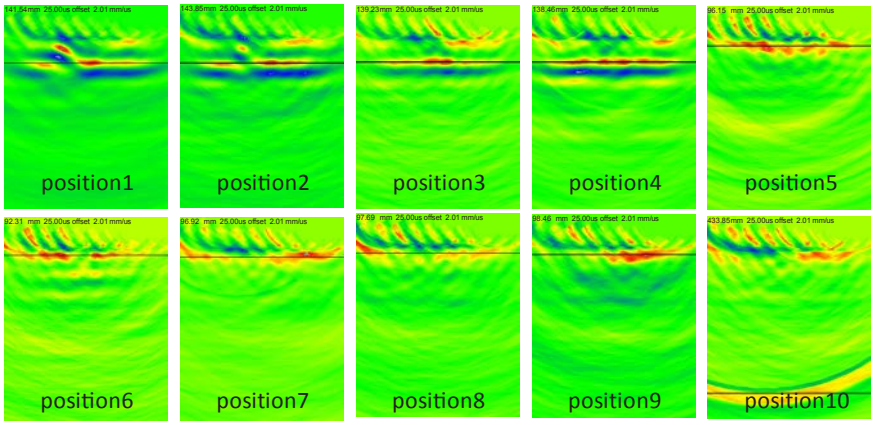

Section 10 Transverse Measurement (242' 30 khz)

Figure 5.62. SAFT-FW B-scans at a center frequency of 30 kHz taken from a location at 17 ft along the transverse direction starting at the LWP through a location just before the center of the passing lane.

CHAPTER 6

Controlled Evaluation of Lightweight Deflectometer

This chapter was prepared by Ray Brown and Haley Bell of the U.S. Army Corps of Engineers Engineering Research and Development Center (ERDC).

Introduction

The lightweight deflectometer (LWD) is a nondestructive testing (NDT) device that provides a structural evaluation of pavement by using a drop weight and one to three sensors (Figure 6.1). The drop weights for the LWD are selected from 22, 33, or 44 lb, and the loading plate diameter can be adjusted to 3.8, 7.8, or 11.8 in. The weight is dropped from an adjustable height onto a rubber buffer located on top of a load cell. The results are presented as a plot of the time history of the load cell and the geophones. Peak deflection (recorded in mm) and surface modulus measurements of each sensor are recorded. Peak deflection is recorded in mils, and a mil is one thousandth of an inch.

Round 1 testing took place in October 2009. The LWD was used to test hot-mix asphalt (HMA) samples in the National Center for Asphalt Technology (NCAT) laboratory and in field test sections on the NCAT Pavement Test Track. The purpose of this round of testing was to determine whether the LWD could identify sections with delamination at warmer temperatures. For the Round 2 testing conducted in February 2010, the LWD was tested only on test sections constructed on the NCAT test track. The purpose of the Round 2 testing was to evaluate the potential for using the LWD to identify delamination at cooler temperatures. The drop weight used for all LWD testing was 22 lb, and the spacing of the three geophones was approximately 6 in. The 7.8-in.-diameter load plate was also used.

During Round 1, at least three tests were conducted at each test point on the laboratory slabs and on the test track. During Round 2, LWD testing was conducted at every other test point on the test track, resulting in approximately half the number of data points collected from the Round 1 testing.

The LWD data were collected, inspected, and input into Excel spreadsheets. The waveforms from the raw data were evaluated for their shape and smoothness. If the waveform was not satisfactory, then the data were not included in the analysis. Measured deflection was the only data used for analysis, specifically Accelerometers D1 and D2, which were the two accelerometers closest to the weight. During both rounds of testing, Accelerometer D3 did not appear to provide much information; the measured deflections for D3 were close to zero in the field and in the laboratory. A closer inspection of D3, after the Round 2 evaluation was completed, proved that the accelerometer was not working properly during Round 1 and Round 2 testing.

Laboratory Testing

During the Round 1 laboratory testing with the LWD, the condition of the pavements was unknown. The measured deflections for the two slabs are shown in Tables 6.1 and 6.2. The laboratory results indicated that there were edge effects around the perimeters of each slab. This was indicated by a general increase in deflection of 20% to 100% around the edges. Because of the edge effects and the transition between two different sections in each slab, only four measured points for the two slabs were considered worthy for analysis. For Slab 1, the test locations used were Points 2-2 and 6-2 (highlighted in yellow in Table 6.1). For Slab 2, the test locations used were Points 9-2 and 13-2 (highlighted in yellow in Table 6.2).

On the basis of information provided in Tables 6.1 and 6.2, it appeared that the section of Slab 1 represented by Point 2-2 was fully bonded because it had less measured deflection than the other three test areas did. Points 6-2 and 9-2 had the most measured deflection and are therefore likely to be the ones that had delamination. Point 13-2 appeared to be in the middle of the measurements, so it is likely that this area had simulated stripping.

Figure 6.1. LWD testing on HMA pavement.

The assumptions were confirmed after analysis with a layout of the pavement structures and their deficiencies provided by the NCAT personnel. Point 2-2 was assumed to be fully bonded, and the layout showed that the condition of this area of Slab 1 was not delaminated. Points 6-2 and 9-2 were assumed to be debonded on the basis of measured deflections.

Table 6.1. Slab 1 LWD Laboratory Test Deflection Measurements (mil)

Slab 1	D1			D2		
Location	1	2	3	1	2	3
1	7.97	5.37	4.90	6.97	4.54	4.25
2	6.09	4.20	4.47	5.68	3.54	3.89
3	5.98	3.57	4.63	3.42	4.42	5.85
4	5.98	4.19	5.20	5.85	3.98	5.32
5	7.01	5.23	5.97	6.36	4.59	5.29
6	7.97	6.70	6.42	6.93	5.75	5.65
7	11.23	9.28	7.90	9.49	7.87	6.80

Table 6.2. LWD Laboratory Test Deflection Measurements for Slab 2 (mil)

Slab 2	D1			D2		
Location	1	2	3	1	2	3
8	7.43	6.67	12.77	6.37	6.00	11.72
9	6.22	6.18	11.18	5.35	5.75	10.65
10	6.02	5.90	10.50	5.68	5.41	9.32
11	6.69	5.69	8.35	6.71	5.39	7.02
12	7.50	5.36	6.25	7.01	5.25	6.39
13	7.97	5.39	5.46	8.12	5.25	5.19
14	8.96	5.77	5.24	8.69	5.47	4.93

The layout of the deficiencies of Slabs 1 and 2 showed that there was debonding at depths of 2 and 4 in., respectively. Point 13-2 was assumed to have stripping, which was also confirmed after analysis.

Field Testing

The pavement temperature at the beginning of the Round 1 tests was approximately 52°F, and the temperature at the end of the tests was approximately 70°F. For Round 2 testing, the pavement temperature ranged from 47°F to 56°F. Figure 6.2 shows the LWD testing on the test track. Significant differences were evident between the magnitude of the data collected on the test track and the data collected in the laboratory. The data collected at the track showed the deflections to be almost always less than 1 mil, whereas the laboratory measured deflections were generally above 4 to 5 mils. This

Figure 6.2. LWD testing on NCAT test track.

result is not too surprising, because it is not possible to construct the small sections to be as stiff as can be done at the track.

There were significant differences within the LWD data collected along the test section on the test track. Similar trends were seen with the Round 1 testing in October and the Round 2 testing in February. However, the average measured deflections from Round 2 testing were slightly lower, as shown in Figure 6.3. The measured deflections from Round 1 were approximately 80% higher than the measured deflections from Round 2, particularly in Sections 5 through 10. This result was expected because of the lower pavement temperatures. The pavement from Stations 0 to approximately 1+00 was backfilled with reclaimed asphalt pavement (RAP), which explains the higher measured deflections of Sections 1 through 4 compared to Sections 5 through 10.

Figures 6.4 through 6.7 present the results of Tests 1 through 4 at each station for Rounds 1 and 2 testing. Figures 6.4 and 6.5 are the results of D1 and D2, respectively, for Round 1 testing, while Figures 6.6 and 6.7 are the results of D1 and D2, respectively, for Round 2 testing. The amount of testing was reduced by approximately 50% during Round 2 to eliminate unneeded data points. Test 1 is the outside of the lane near the pavement shoulder, and Test 4 is the inside of the lane near the centerline. There is significant scatter among the lanes with the D1 measurements for both rounds of testing; however, there is little scatter among the four lines of data with the D2 measurements.

The 10 sections were also analyzed separately by using the information provided in the test track layout. The data points were analyzed to determine the differences in measured deflection between each of the sections by using the various methods to simulate delamination and to compare the measured deflections of a fully bonded area to a debonded area. The measured deflections for each type of simulated delamination and bonded area were compared to each other for Sections 7 through 10. Sections 1 through 6 were left out of the comparison because there was concern about the effect of the backfilled RAP material on deflections in these sections. Figures 6.8 and 6.9 show the results of the comparisons for Round 1 and Round 2, respectively.

As stated earlier, the analyses revealed the same conclusions for both rounds of testing. As shown in Figures 6.8 and 6.9, the fully bonded areas provided similar deflection measurements to those from areas with RAP and baghouse dust. Also, simulated debonding using paper had much higher deflections compared to the baghouse dust, RAP, and fully bonded areas. It seems as though using the paper created loss in bond and possibly some loss in friction between the two layers, while the baghouse dust may have resulted in a higher bond than when the paper was used. The higher measured deflections with paper may be an indication of little friction between the layers under loading, resulting in more relative movement at the interface between the two layers. As the load from the LWD is applied, the HMA layers are able to slide along the paper, resulting in increased movement and deflection. Some friction most likely exists within the delaminated areas simulated with baghouse dust because of the texture provided by the baghouse dust.

Summary

On the basis of laboratory and field testing results, the LWD appears to be able to show differences in deflection between the various sections. It is difficult to identify for sure what causes this change in deflection, but certainly a section that is delaminated should have more deflection than a section that is not delaminated. Although the LWD can detect changes in the pavement structure, it is doubtful that it can be used to identify what causes the change in deflection and the depths at which the delaminations occur.

The research team used an LWD on the test sections containing good bond and delamination. Since the LWD equipment can be included at no additional cost to the project, it is expected that the LWD equipment will continue to be used to identify delamination. Additional analysis approaches will be evaluated for the LWD to improve its ability to identify delamination.

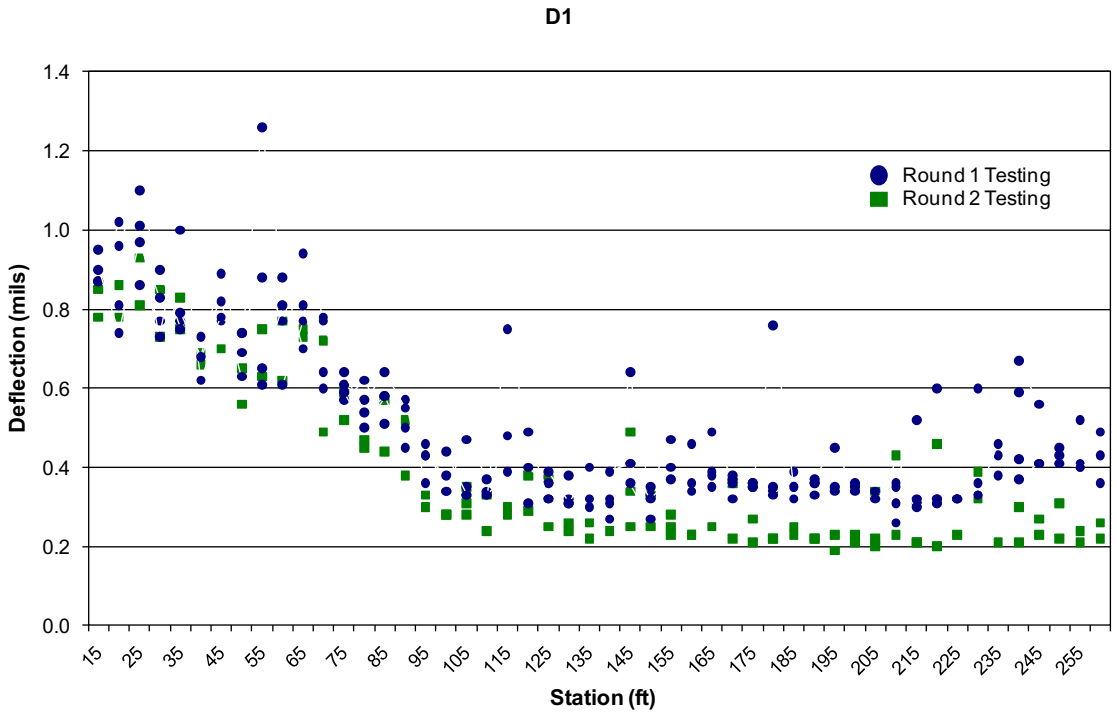

Figure 6.3. D1 average deflection measurements from Rounds 1 and 2 testing on test track.

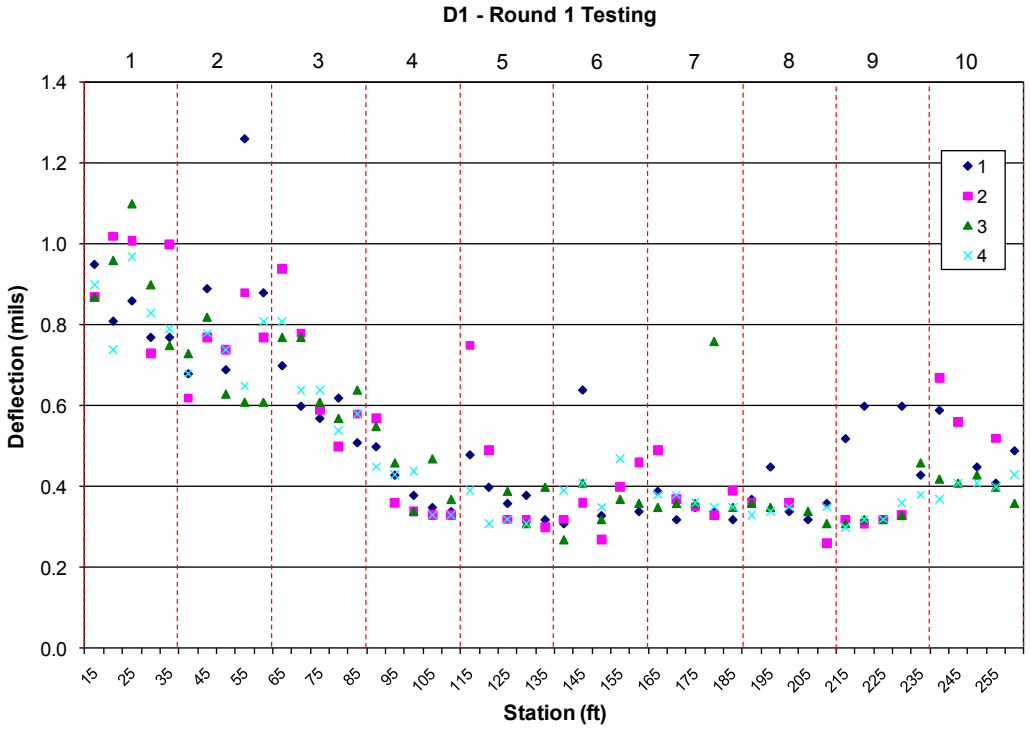

Figure 6.4. D1 measurements for Round 1 on each test location on test track.

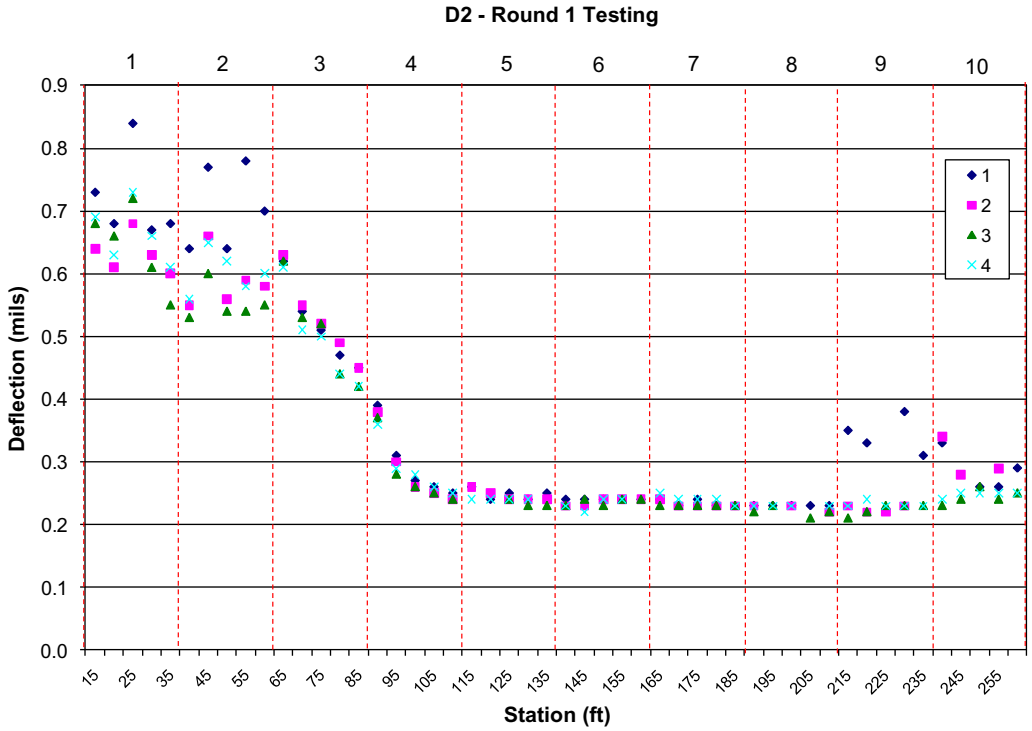

Figure 6.5. D2 measurements for Round 1 on each test location on test track.

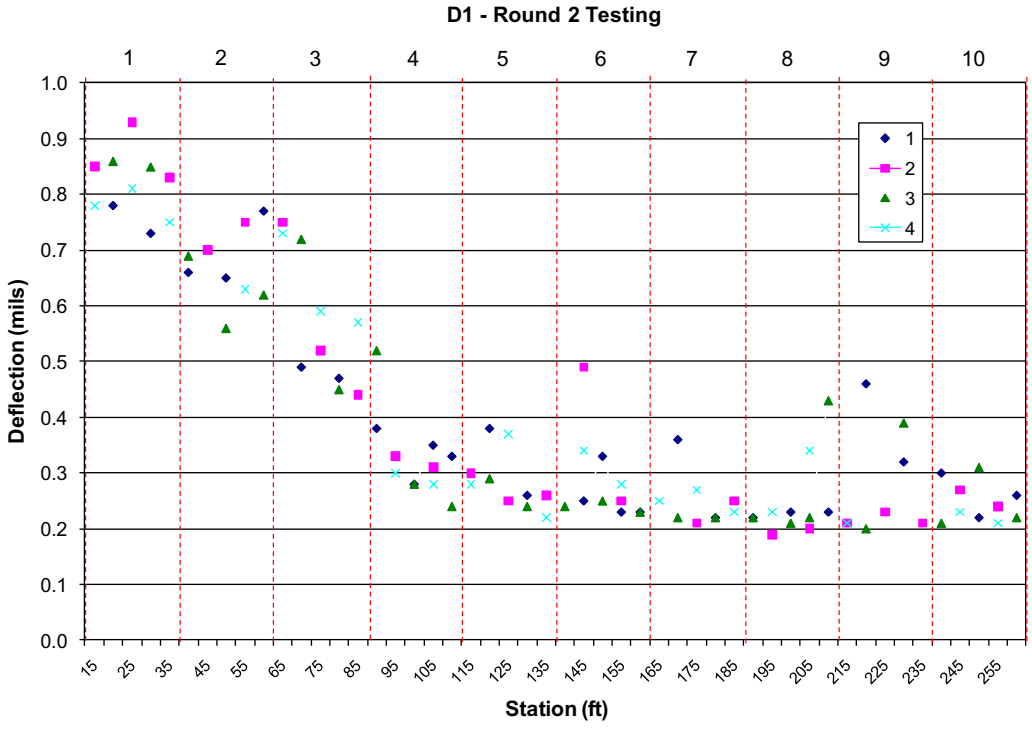

Figure 6.6. D1 measurements for Round 2 on each test location on test track.

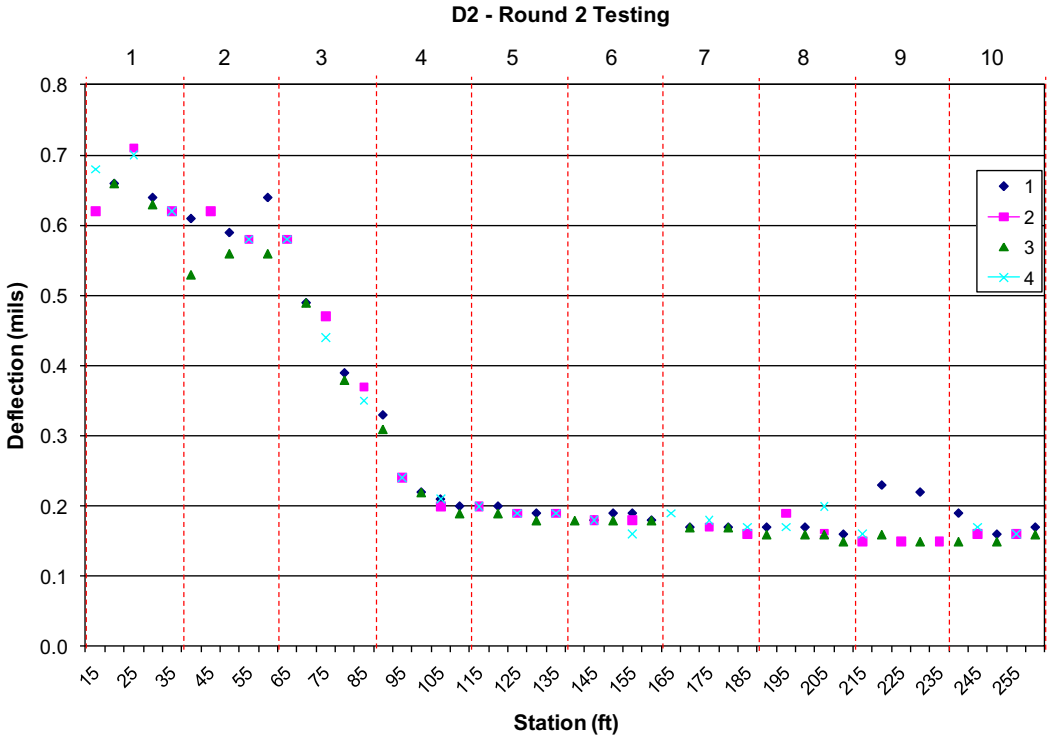

Figure 6.7. D2 measurements for Round 2 on each test location on test track.

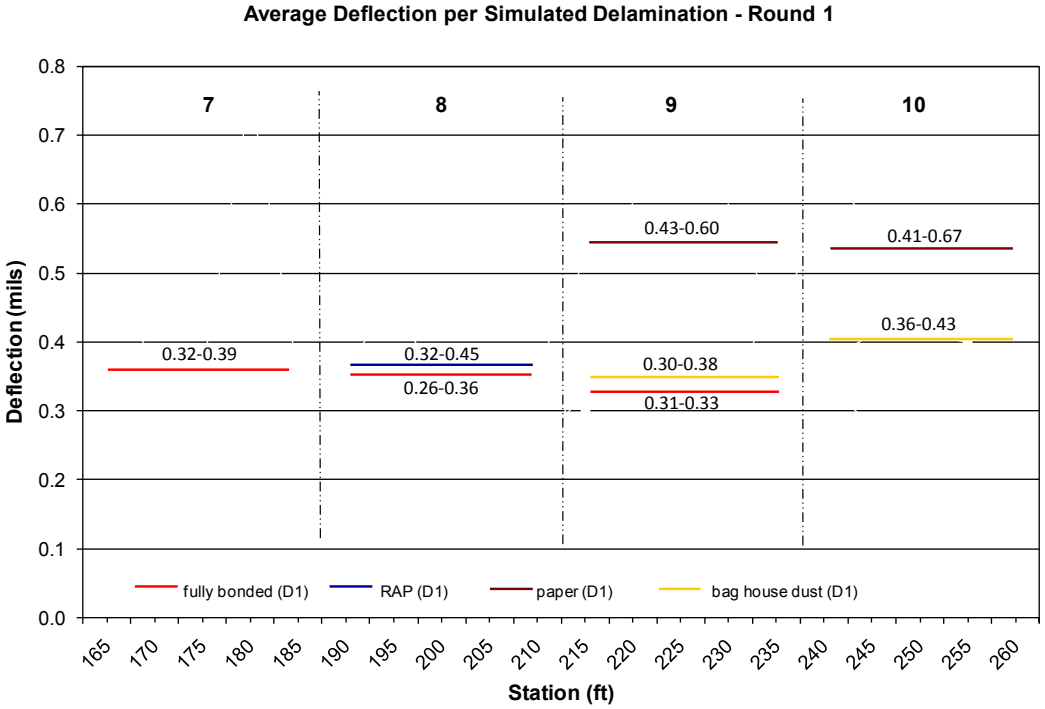

Figure 6.8. Average deflections of each delamination type in Round 1 from Sections 7 through 10.

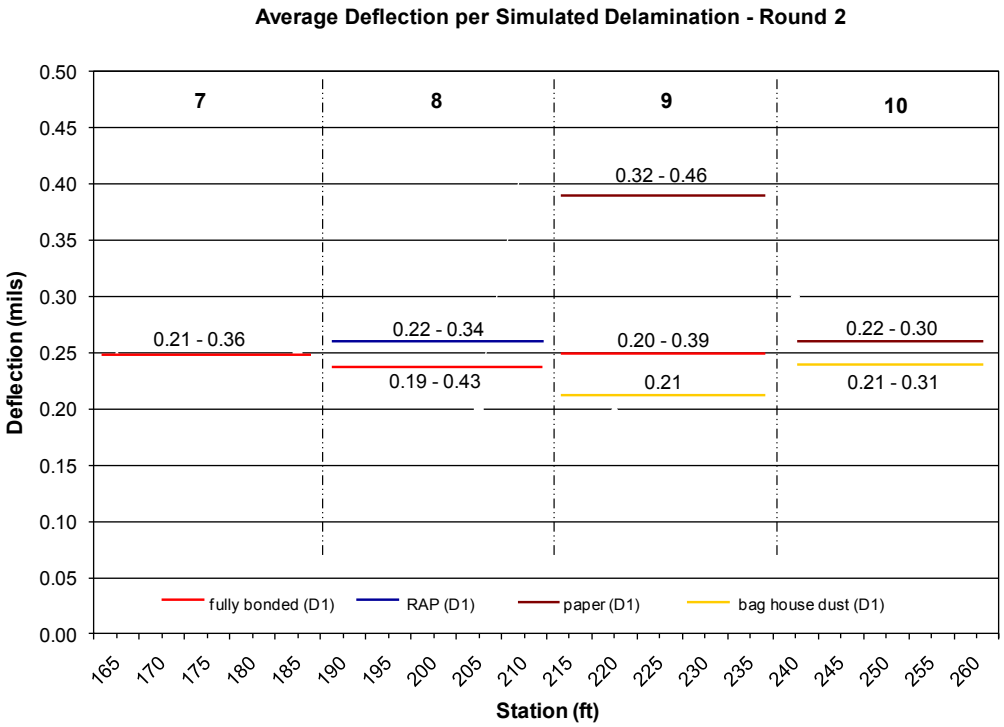

Figure 6.9. Average deflections of each delamination type in Round 2 from Sections 7 through 10.

CHAPTER 7

Controlled Evaluation of Falling Weight Deflectometer

This chapter was prepared by Halil Ceylan and Sunghwan Kim of Iowa State University.

Background and Introduction

The falling weight deflectometer (FWD) is a widely used test device for nondestructive evaluation of pavement systems. Numerous studies have tried to assess the suitability of the FWD for assessing delamination in hot-mix asphalt (HMA) layers. The higher FWD deflections are expected if poor bond exists between asphalt layers (Nazarian et al. 2010).

Lepert et al. (1992) summarized some of the earlier studies that concluded that deflection measurement devices such as deflect graph and FWD were not promising for assessing pavement layer interface debonding condition. However, recent research studies show some promising results for detecting the delamination of HMA layers by using the FWD (Al Hakim et al. 1997, 1998, 2000; Gomba 2004; Hammons et al. 2005). These studies include development of new backcalculation algorithms to calculate a new variable (interface stiffness) reflecting the layer bond condition (Al Hakim et al. 1997, 1998, 2000), comparing the slippage susceptibility at asphalt interfaces with FWD measurements (Gomba 2004), and calculating the bond stiffness from FWD deflection basin by using closed-form solutions (Hammons et al. 2005). However, those approaches have problems, including (1) the difficulty and uncertainty for assessment of bond condition between thin layers of asphalt (Al Hakim et al. 1997; Kruntcheva et al. 2000), (2) the uncertainty in backcalculating the moduli of thin HMA layers (Nazarian et al. 2010), (3) the empirical nature with noncalibration of FWD measurements (Nazarian et al. 2010), and (4) the uncertainty for HMA overlays on existing PCC or a strong sublayer.

As part of the Airport Asphalt Pavement Technology Program (AAPTP) Project 06-04, Nazarian et al. (2010) evaluated the FWD on a controlled pavement section to assess presence and extent of delamination of HMA airfield pavements. A controlled pavement section was constructed with about 8 in. of HMA placed in three lifts on a prepared sandy-silt subgrade. A controlled pavement section was also specifically constructed with various levels and depths of debonding. The FWD used in this study had a 12-in. diameter load plate and seven geophones at 1-ft intervals. An equivalent load of about 6,000 lb was applied on the asphalt section at selected locations. On the basis of results of this study, Nazarian et al. (2010) made the following conclusions:

- The FWD may be used for detecting the shallow fully debonded area, and with less certainty, the partially debonded area.
- The FWD is more effective in the cool-weather testing than in hot-weather testing, owing to the temperature susceptibility of HMA.
- A concern with the FWD is the number of false positive readings (estimating low modulus for intact point), especially during hot-temperature testing.

Since the constructed test section investigated in the study by Nazarian et al. (2010) was conventional HMA pavement with simple layer structure, it is still uncertain whether the FWD can detect delamination behavior in HMA overlaid pavement with strong sublayer structures as investigated in this research.

Research Approach Summary

The research approach adopted in this study consists of two parts: (1) to model both delaminated and control HMA sections by using the conventional Elastic Layer Program (ELP) and (2) to investigate FWD deflection results for control and delaminated pavement sections at the National Center for Asphalt Technology (NCAT) Pavement Test Track test sections. The investigation included the analysis of FWD deflection basin measurements, the comparisons of

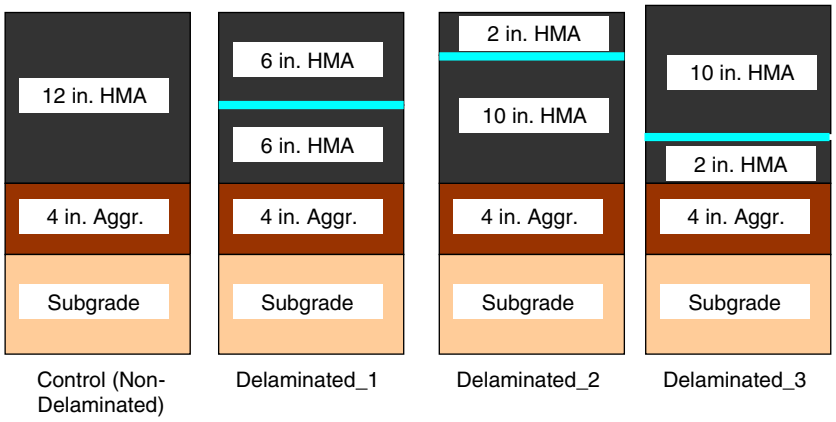

Note: Aggr. = aggregate.

Figure 7.1. Description of HMA pavements for Case 1, 12 in., scenario.

field-measured FWD deflections with ELP analysis results, and the investigation of FWD deflection time history.

Research Approach 1: BISAR—Analysis and Results

To investigate the effect of the delamination condition on HMA pavement response, the BItumen STructures Analysis in ROads (BISAR) was used as the mechanistic-based HMA pavement analysis program. The BISAR developed by Shell Global Solutions is a computer software program for computing stresses, strains, and displacements at any position in the elastic layered system under surface loading (DeJong 1973). All interfaces between layers have an interface friction factor that can vary from zero (fully unbounded) to 1,000 (unbounded) between layers. The BISAR is the extended version of BISTRO (BItumen STructures in ROads) (Peutz et al. 1968) developed earlier. The comparisons of BISAR predictions and actual measurements obtained from indoor and outdoor tests demonstrated that the BISAR can provide a fairly good approximation for pavement behavior (Claessen et al. 1977).

Two case scenarios of HMA pavement structure under 9-kips FWD loading were modeled. As shown in Figure 7.1, Case 1, representing thicker HMA pavement structures, has a 12-in. HMA pavement structure without delamination and with delamination at different depths (2 in., 6 in., and 10 in. below the top HMA surface). Figure 7.2 illustrates Case 2, representing thinner HMA pavement structures. Case 2 has 6-in. HMA pavement structure without delamination and with delamination at different depths (2 in., 3 in., and 4 in. below the top HMA surface). The predicted vertical deflection results from BISAR for Cases 1 and 2 are presented in Figures 7.3 and 7.4. A difference in vertical deflection predictions between control (nondelamination) and delamination sections was observed in both cases. The greater deflections in both cases were observed in the HMA pavement structure with delamination at the middle of the HMA layer, denoted as "Delamination_1" in Figures 7.3 and 7.4. These results indicate that BISAR can

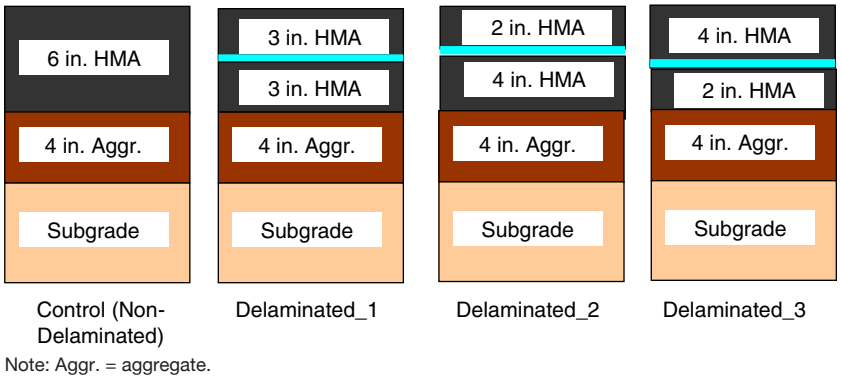

Note: Aggr. = aggregate.

Figure 7.2. Description of HMA pavements for Case 2, 6 in., scenario.

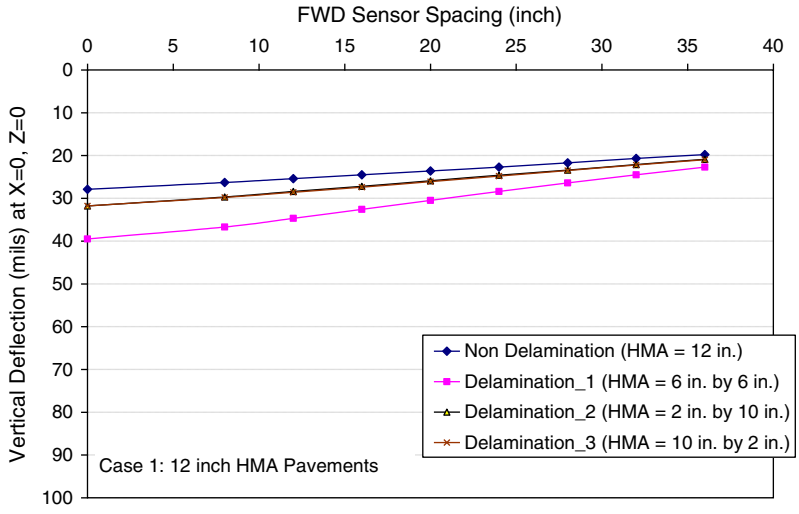

(a)

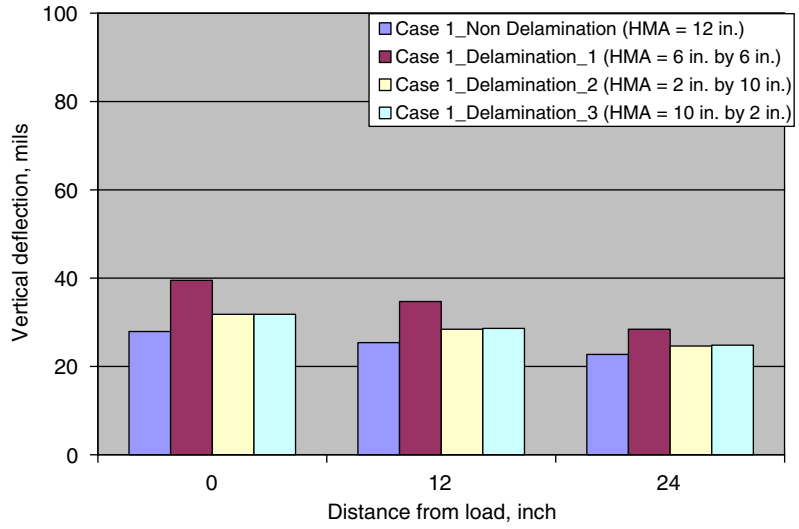

(b)

Figure 7.3. 9-kips loaded FWD deflections from BISAR for Case 1: (a) deflection bowls and (b) deflection measurements at distances of 0, 12, and 24 in. from FWD load plate.

characterize delamination in conventional HMA pavements in terms of vertical deflections.

Research Approach 2: NCAT FWD Data Analysis and Results

Description of FWD Testing in NCAT Sections

The description of the NCAT section obtained during Phase 2 of R06D is reproduced below.

Controlled field evaluations were conducted on 10 asphalt pavement sections built in the inside lane of the NCAT Pavement Test Track. All three bonding conditions were induced at the interfaces between the dense-graded asphalt layers: no-bond, partial-bond and good-bond. The bad-bond condition was enforced by the NCAT research team using bond breakers, including baghouse fines and two layers of brown paper, and good-bond condition was enforced by using a tack coat. The stripping condition was simulated with a separate 1-in.-thick, uncompacted coarse-fractionated reclaimed asphalt pavement (RAP) material.

The design for the controlled field test sections is illustrated in Figure 7.5. The test sections were designed to simulate 10 different bonded and debonded conditions that represent a majority of situations encountered in the top 5 in. of HMA pavements. Both full lane and partial lane debonding conditions were constructed for evaluating NDT methods. The

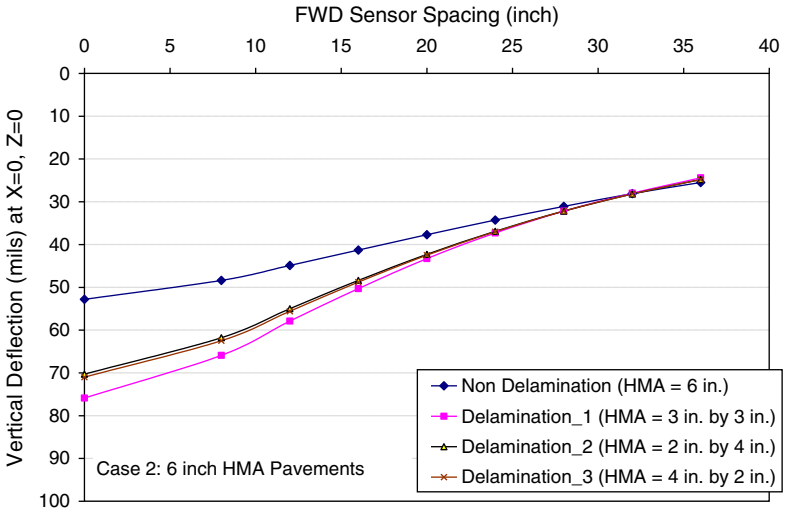

(a)

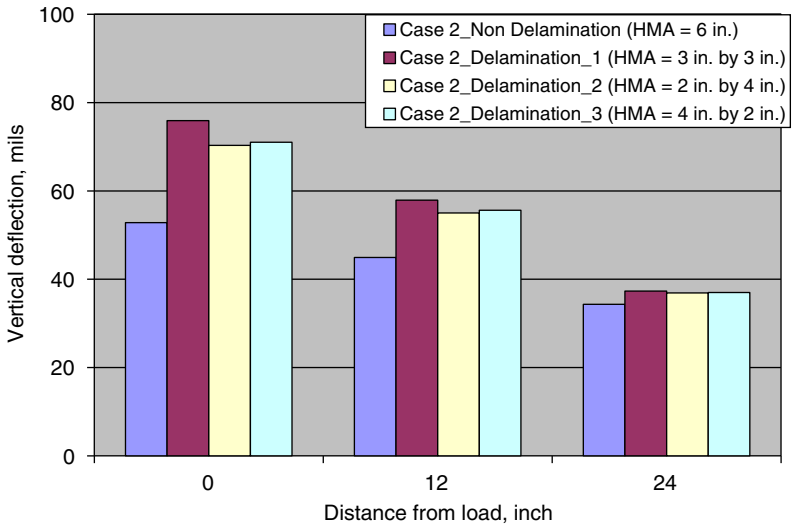

(b)

Figure 7.4. Vertical 9-kips loading FWD deflections from BISAR for Case 2: (a) deflection bowls and (b) deflection measurements at distances of 0, 12, and 24 in. from FWD load plate.

partial lane debonding condition included wheelpath and two 3-ft by 3-ft squared areas. Each test section is 12 ft wide (full paving width) and 25 ft long.

The FWD device used in this study consisted of an impact-loading mechanism and a set of nine geophones to measure vertical surface displacements. Four of the FWD load levels applied were about 6, 9, 13, and 18 kips. The locations of nine geophones of the FWD equipment used were at 0 ($D_{0\text{-in.}}$), 8 ($D_{8\text{-in.}}$), 12 ($D_{12\text{-in.}}$), 16 ($D_{16\text{-in.}}$), 20 ($D_{20\text{-in.}}$), 24 ($D_{24\text{-in.}}$), 28 ($D_{28\text{-in.}}$), 32 ($D_{32\text{-in.}}$) and 36 in. ($D_{36\text{-in.}}$) from the center of the FWD plate load. Two FWD tests were conducted on a single location and at each load level. The 17 series of FWD tests were conducted on 10 controlled asphalt pavement test sections. The descriptions of the 17 series of FWD tests on the NCAT test sections are summarized in Table 7.1 and Figure 7.6.

FWD Deflection Basin Measurements

The FWD Deflection Plots at NCAT Section in this chapter provides FWD surface deflections for all FWD tests conducted at NCAT test sections. The following figures present the pavement structure layout of some of the NCAT test sections and the FWD measurements of some of the FWD tests for discussion. Two-frequency FWD tests were conducted on a single location to identify the FWD sensor measurement errors. As seen in these figures, no significant differences were

	Section 1	Section 2	Section 3	Section 4	Section 5	Section 6	Section 7	Section 8	Section 9	Section 10
Top 2-inch lift	Full bond	Full bond	Full bond	Partial No bond	No bond	Partial stripping	Full bond	Full bond	Full bond	Full bond
Bottom 3-inch lift	No bond	Full bond	Full bond	Full bond	Full bond	Full bond	Full bond	Partial Stripping	Partial No bond	No bond
Existing surface	PCC	PCC	HMA	HMA	HMA	HMA	HMA	HMA	HMA	HMA

Section 1 – no bond between 5-inch HMA overlay and PCC pavement

Section 2 – full bond between 5-inch HMA overlay and PCC pavement (control section)

Section 3 – full bond between 5-inch HMA overlay and HMA pavement (control section 1 of 2)

Section 4 – partial bond between 2-inch HMA overlay surface lift and 3-inch HMA overlay leveling lift

Section 5 – no bond between 2-inch HMA overlay surface lift and 3-inch HMA overlay leveling lift

Section 6 – simulated stripping in the wheel path between 2-inch HMA surface lift and 3-inch HMA leveling lift

Section 7 – full bond between 5-inch HMA overlay and HMA pavement (control section 2 of 2)

Section 8 – simulated stripping in the wheel path between 3-inch HMA overlay leveling lift and HMA pavement

Section 9 – partial bond between 3-inch HMA overlay leveling lift and HMA pavement

Section 10 – no bond between 3-inch HMA overlay leveling lift and HMA pavement

Figure 7.5. Layout of controlled field test sections at NCAT test track.

Table 7.1. List of 17 Series of FWD Tests on NCAT Test Sections

Test ID	SHRP 2 Test Section	FWD Test ID	Station: IWP	Station: OWP	Condition
1	1	1	23	23	Delaminated (5 in. below)
2	1	2	33	33	Delaminated (5 in. below)
3	2	3	48	58	Control
4	3	4 IWP	73	na	Control
5	3	4 OWP	na	83	Control
6	4	5	98	98	Delaminated OWP (2 in. below)
7	4	6	108	108	Delaminated IWP (2 in. below)
8	5	7	123	123	Delaminated (2 in. below)
9	5	8	133	133	Delaminated (2 in. below)
10	6	9 and 10 OWP	148	148	Strip OWP (2 in. below)
			158	158	
11	7	9 IWP and 11 OWP	173	183	Control
12	8	10 IWP	198	198	Strip IWP (5 in. below)
13	8	11 IWP	208	208	Strip IWP (5 in. below)
14	9	12	223	223	Delaminated (5 in. below)
15	9	13	233	233	Delaminated (5 in. below)
16	10	14	248	248	Delaminated (5 in. below)
17	10	15	258	258	Delaminated (5 in. below)

Note: IWP = inside wheelpath; OWP = outside wheelpath; and na = not applicable.

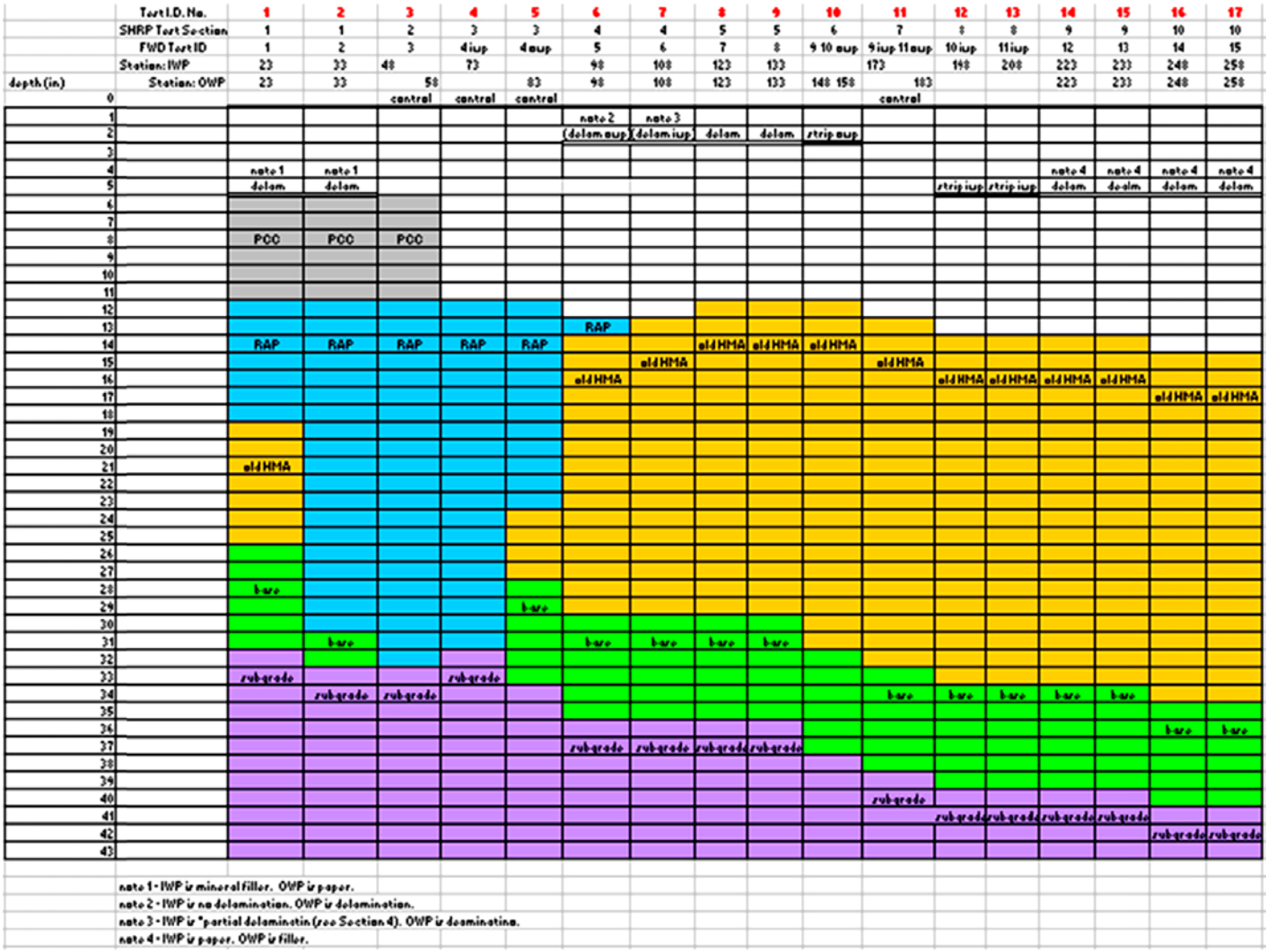

Figure 7.6. Summary of 17 Series of FWD tests on NCAT test sections.

observed, which indicated that the FWD can produce consistent results for the same test materials.

Figure 7.7 illustrates the pavement structure layout of NCAT Section 1, and Figure 7.8 presents FWD measurements of FWD Test 1 in NCAT Section 1. NCAT Section 1 was delaminated at 5 in. below the HMA surface by mineral filler in the inside wheelpath (IWP) and by paper in the outside wheelpath (OWP). No significantly different FWD measurements were observed between the IWP and the OWP. This result indicates that both materials (paper and mineral filler) could produce similar effects on pavement response.

Figure 7.9 illustrates the pavement structure layout of NCAT Section 2, and Figure 7.10 presents FWD measurements of FWD Test 3 on NCAT Section 2. NCAT Section 2 is a control section without delamination. FWD testing was conducted on the IWP of Station 48 and the OWP of Station 58. Because the pavement structure at both locations was the same,

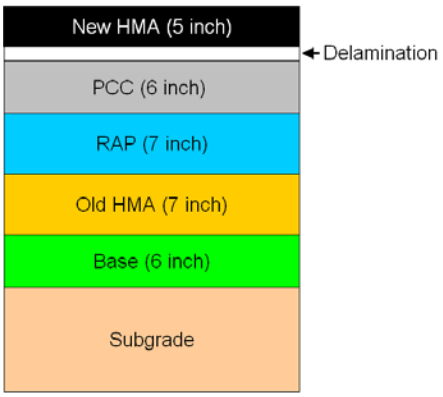

Note: PCC = portland cement concrete.

Figure 7.7. Pavement structure layout of NCAT Section 1 (not to scale).

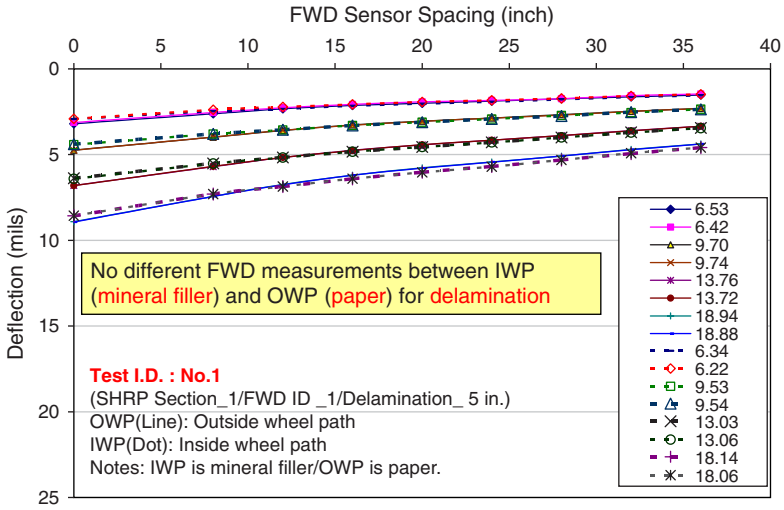

Figure 7.8. FWD deflections for Test 1 on NCAT Section 1.

similar deflection measurements were expected. However, the higher deflection measurements were obtained in the OWP of Station 58.

Figure 7.11 illustrates the pavement structure layout of NCAT Section 4. Figures 7.12 and 7.13 present FWD measurements of FWD Tests 6 and 7 conducted on NCAT Section 4, respectively. NCAT Section 4 consisted of two parts: one part had no delamination in the IWP and delamination in the OWP for FWD Test 6. The other part had partial delamination in the IWP and delamination in the OWP for FWD Test 7. Similar FWD measurements were observed at delaminated and non-delaminated FWD testing locations.

Deflection basin parameters (DBPs) from FWD deflection basin data were computed to see whether the FWD deflection basin could capture the effect of delamination on NCAT test sections.

The most widely used and effective DBPs were computed. These parameters were the AREA shape parameter, Area Under Pavement Profile (AUPP), Impact Stiffness Modulus (ISM), Surface Curvature Index (SCI), Base Curvature Index (BCI), and Base Damage Index (BDI). Overall, pavement structural strength condition can be related to the AREA shape parameter, AUPP, and ISM. The SCI can provide information on changes in relative strength of the near-surface layers. The BCI is a subgrade condition indicator, especially in aggregate base pavements, and is strongly related to the subgrade modulus. The BDI is related to base layer modulus. On the one hand, higher values of the AREA and ISM parameters mean higher pavement stiffnesses. On the other hand, lower values of the AUPP, SCI, BCI, and BDI parameters mean higher pavement stiffnesses. Detailed definitions of these DBPs and their significance are reported by Gopalakrishnan (2004) and are also included in the section later in this chapter on Deflection Basin Parameters of FWD Measurements at NCAT Test Sections.

The FWD measurements obtained at different load levels for each test were normalized to 9 kips to remove the effect of loading amplitude on pavement deflections. The 9-kips load normalized FWD measurements were used for the computation of DBPs. The DBP of FWD Measurements section also presents the computed DBPs from FWD measurements for all of the test sections. For illustration, Figure 7.14 illustrates the computed AREA values for each FWD test. As shown in this figure, it is difficult to see the effect of delamination on the basis of DBPs.

These findings indicate that the behavior of delamination in the investigated test sections is difficult to characterize in terms of FWD deflection basin measurements. Because

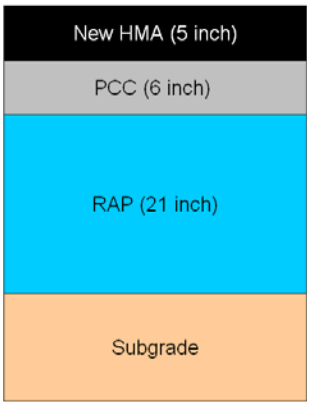

Figure 7.9. Pavement structure layout of NCAT Section 2 (not to scale).

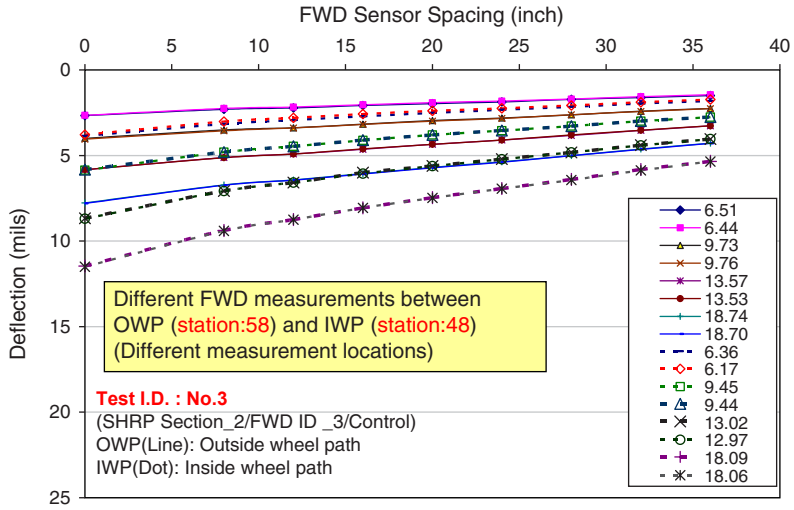

Figure 7.10. FWD deflections of Test 3 on NCAT Section 2.

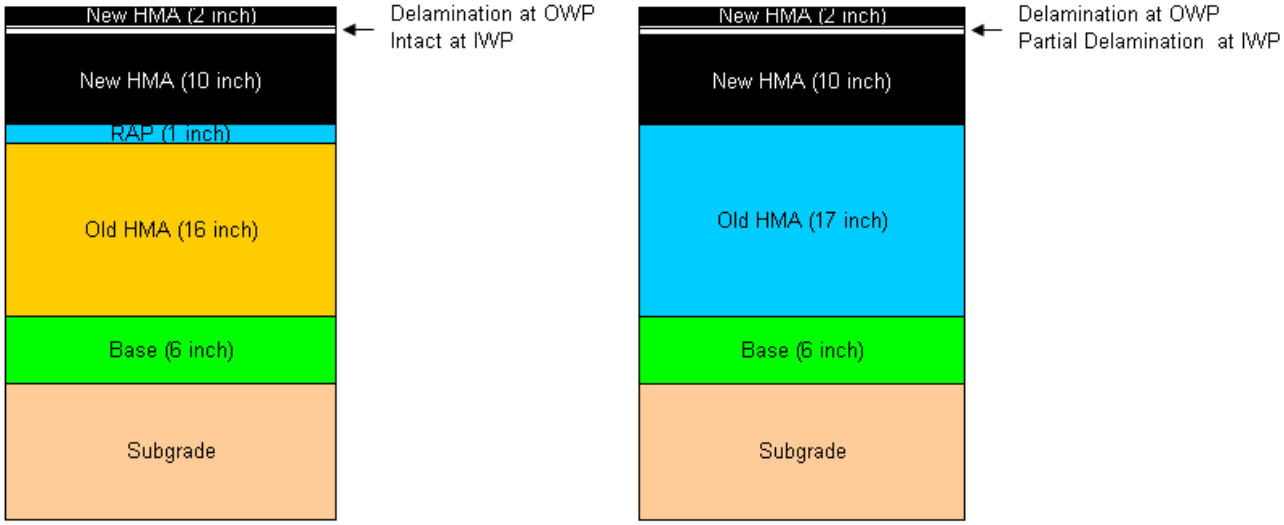

Figure 7.11. Pavement structure layout of NCAT Section 4 (not to scale) for (a) Test 6 and (b) Test 7.

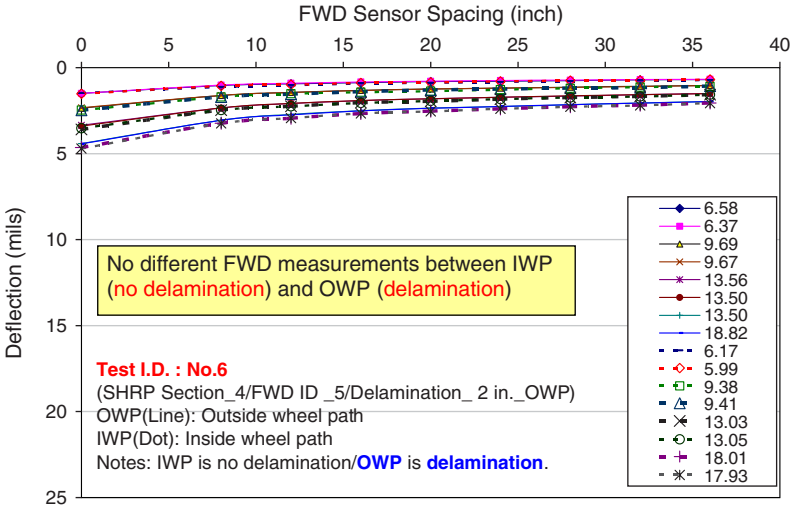

Figure 7.12. FWD deflections of Test 6 on NCAT Section 4.

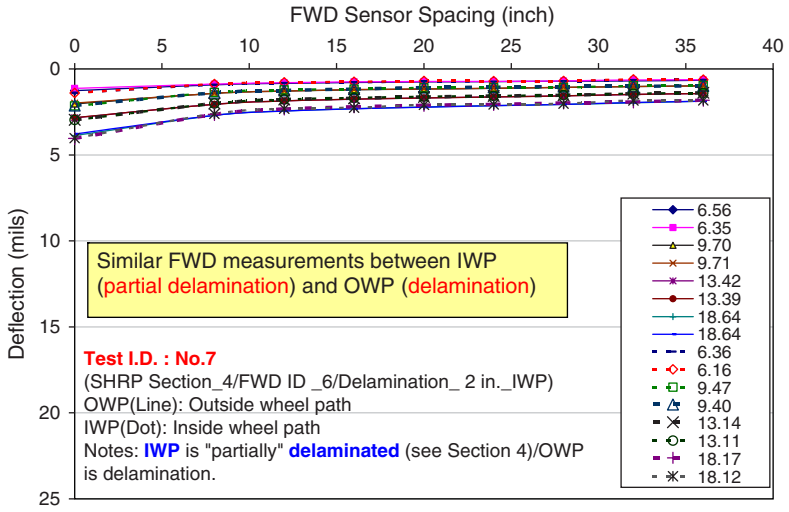

Figure 7.13. FWD deflections of Test 7 on NCAT Section 4.

NCAT test sections investigated were HMA-overlaid pavement sections with high thicknesses and strong sublayers, variability in thickness and modulus of sublayers can mask the detection of delamination for these pavement systems (Nazarian et al. 2008). The other feasible reason is relatively long FWD impulse duration, which results in difficulty in focusing on the top of thin HMA layers (Nazarian et al. 2008).

BISAR Analyses of FWD Testing on NCAT Sections

Research Approach 1 in this study demonstrated that BISAR Model was capable of successfully characterizing the presence of delaminations in terms of vertical deflections in conventional HMA pavement systems. The 17 series of FWD tests associated with NCAT test sections were simulated by using BISAR to examine whether BISAR could also characterize delamination in HMA-overlaid pavements. The assumed materials properties listed below were entered into BISAR:

- New HMA (top 5 in.) = 750 ksi;
- HMA leveling course (6 to 12 in. in Sections 3 through 10) = 1,200 ksi;
- Old HMA (more than 12 in.) = 750 ksi;
- Old PCC = 4,500 ksi;
- RAP subbase = 10 ksi;
- Aggregate base = 12.5 ksi; and
- Subgrade = 28.8 ksi.

Comparisons of BISAR-computed deflections with FWD test results for the NCAT test sections are presented later in this chapter. For discussion, Figures 7.15 and 7.16 present

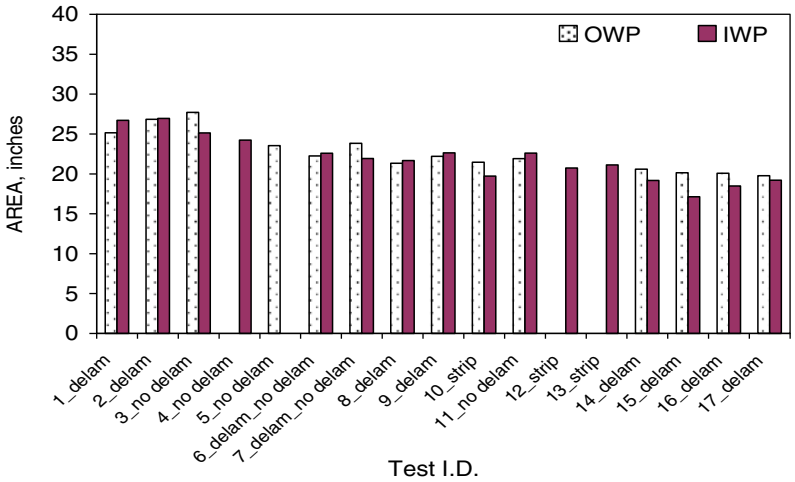

Figure 7.14. AREA of FWD measurements.

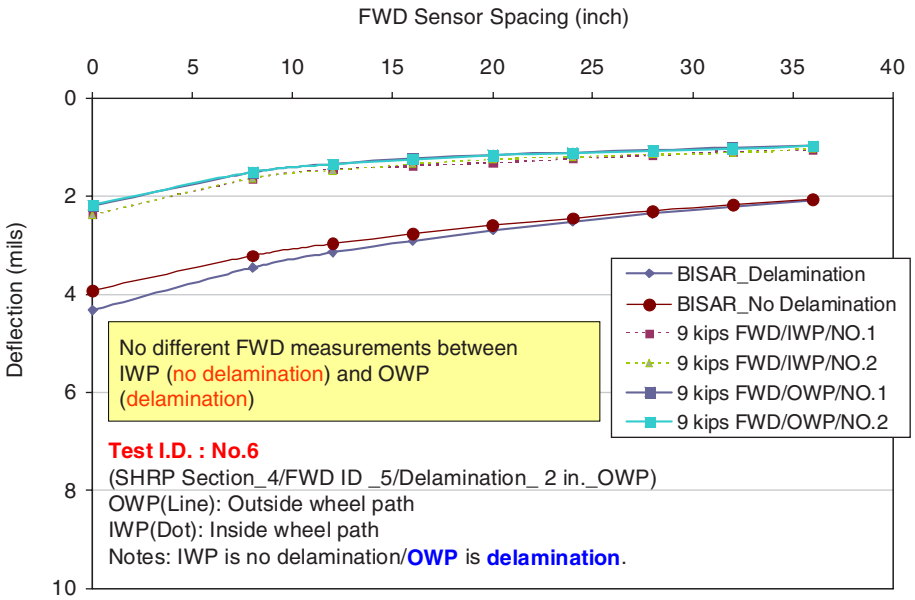

Figure 7.15. Comparisons of BISAR results with 9-kips loading normalized FWD measurements for FWD Test 6 at NCAT Section 4.

the comparisons for FWD Tests 6 and 7 in NCAT Section 4. As seen in these figures, small differences were observed in BISAR-predicted deflections between delamination and non-delamination cases.

FWD Deflection Time History

The feasibility of capturing delamination behavior from FWD deflection time history was investigated. For discussion, Figure 7.17 presents 18-kips load level of FWD Test 6 in NCAT Section 4. FWD Test 6 in NCAT Section 4 was conducted on the IWP without delamination and on the OWP with delamination. As seen in Figure 7.17, peak deflections of both locations under loading show no significant difference, but deflections of OWP (delamination) under unloading are quicker and higher recovered. This behavior was observed in some of the FWD test results in delaminated sections.

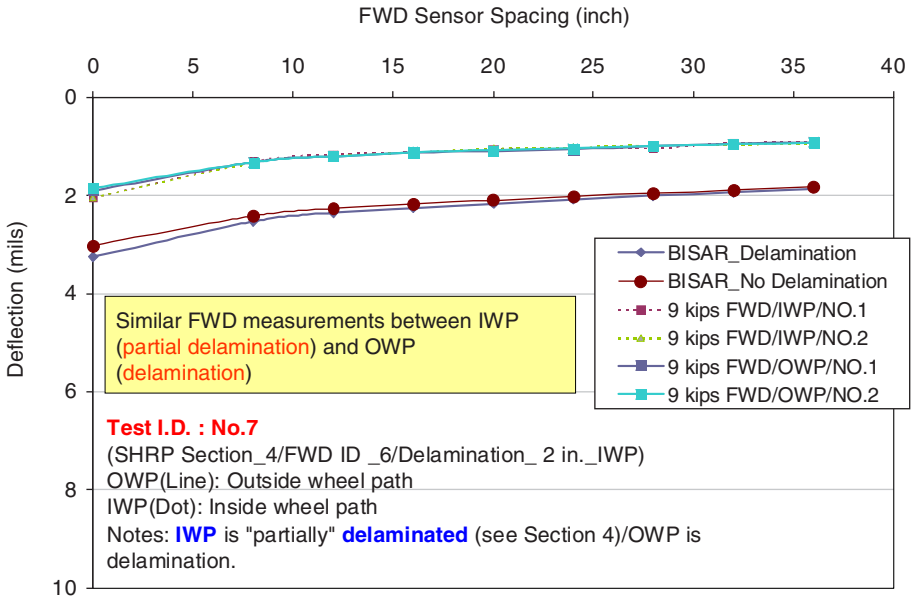

Figure 7.16. Comparisons of BISAR results with 9-kips loading normalized FWD measurements for FWD Test 7 at NCAT Section 4.

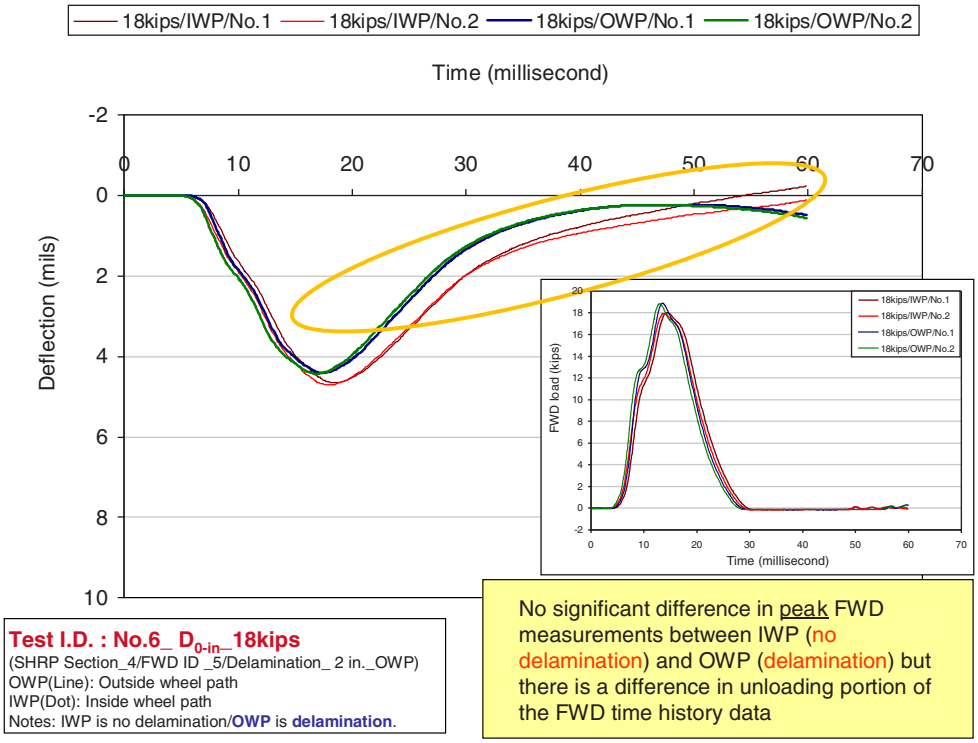

Figure 7.17. FWD deflection ($D_{0\text{-}in}$) time history under 18-kips loading for FWD Test 6 at NCAT Section 4.

FWD Deflection Plots at NCAT Section

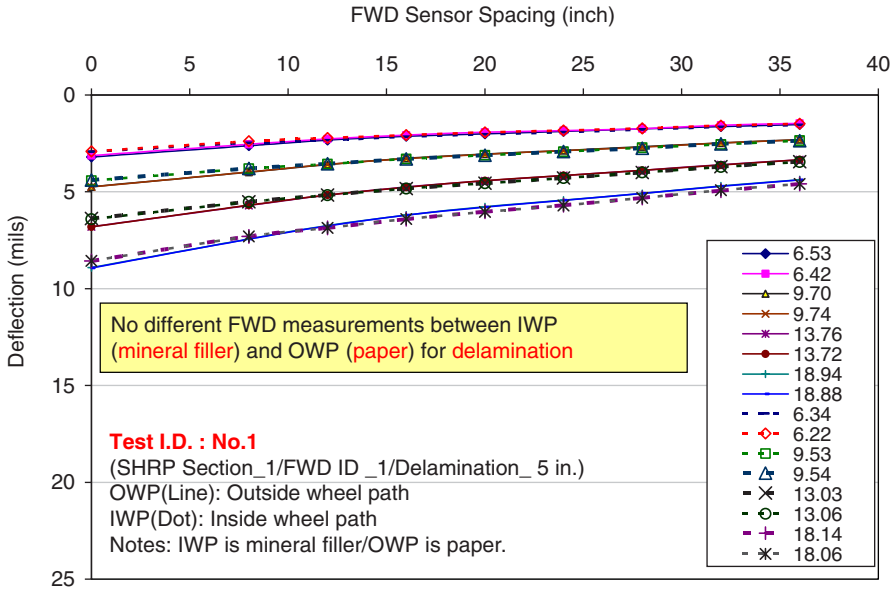

Figure 7.18. FWD deflections of Test 1 at NCAT Section 1.

(text continues on page 85)

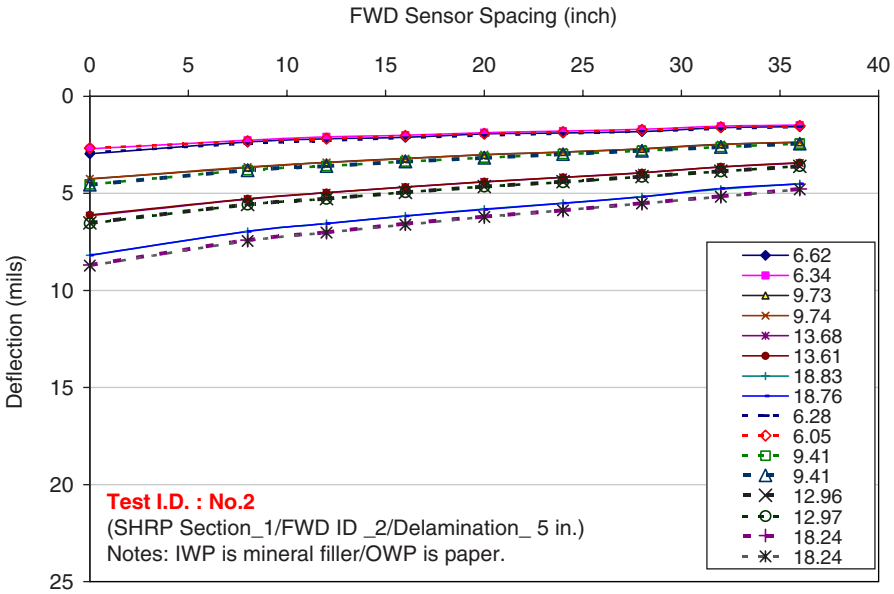

Figure 7.19. FWD deflections of Test 2 at NCAT Section 1.

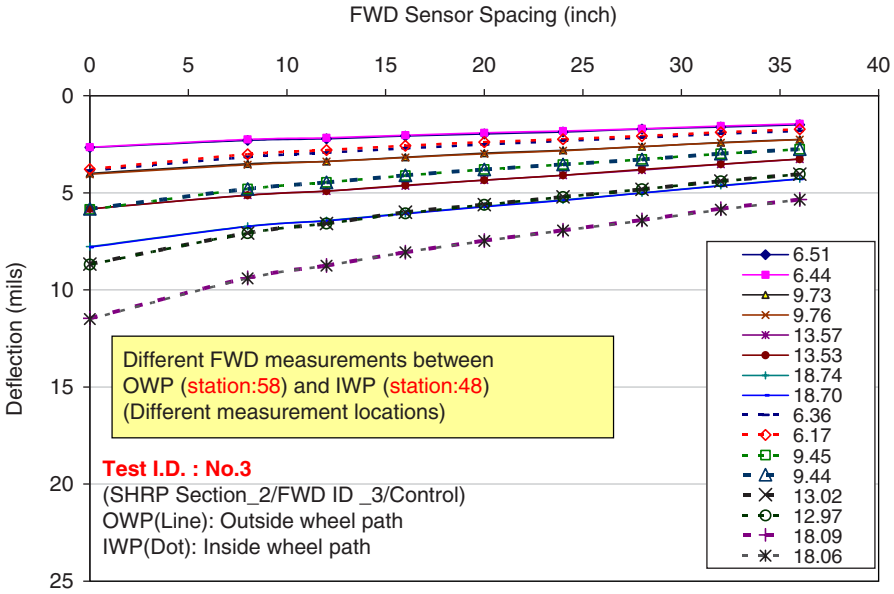

Figure 7.20. FWD deflections of Test 3 at NCAT Section 2.

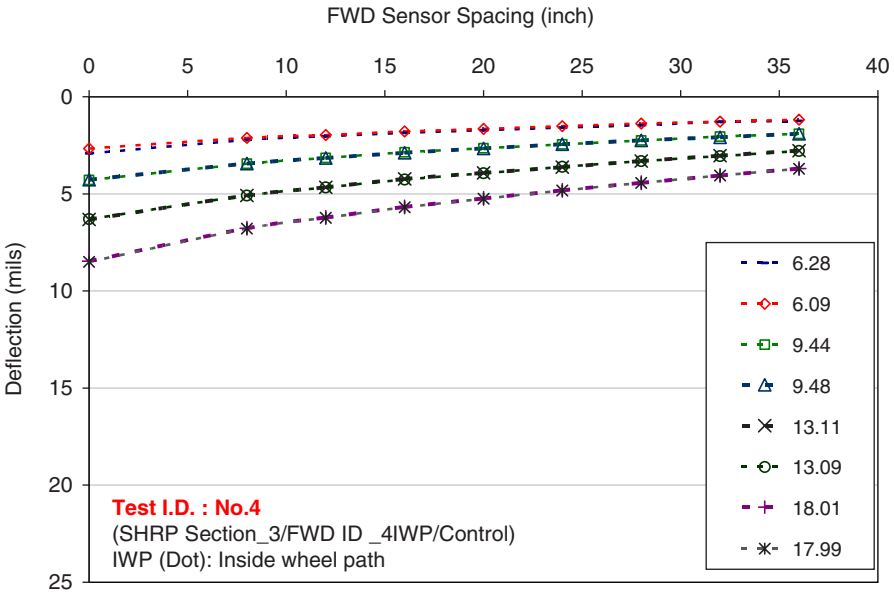

Figure 7.21. FWD deflections of Test 4 at NCAT Section 3.

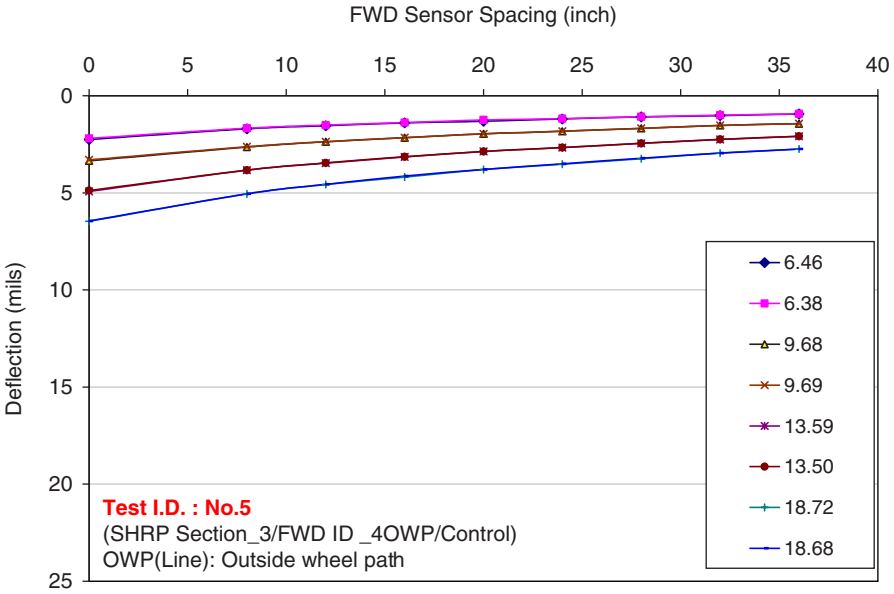

Figure 7.22. FWD deflections of Test 5 at NCAT Section 3.

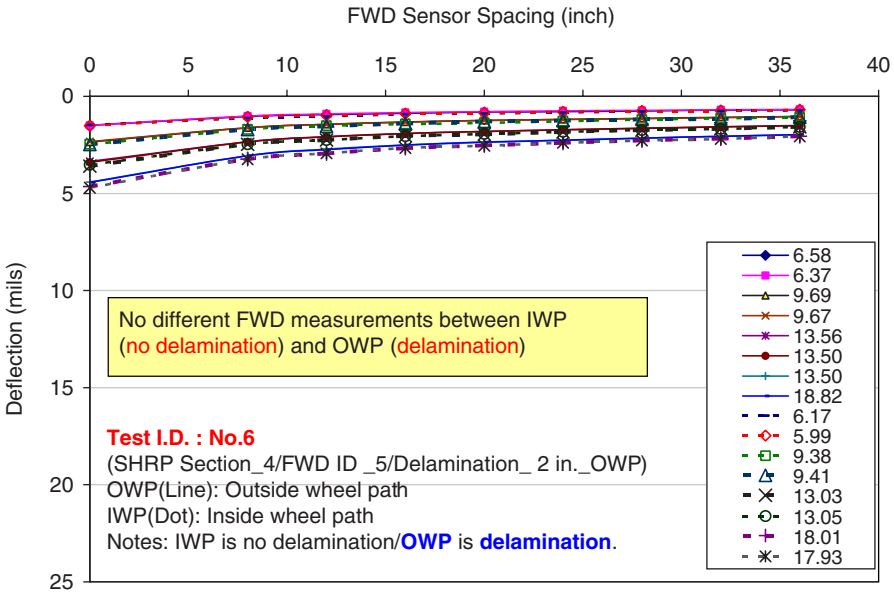

Figure 7.23. FWD deflections of Test 6 at NCAT Section 4.

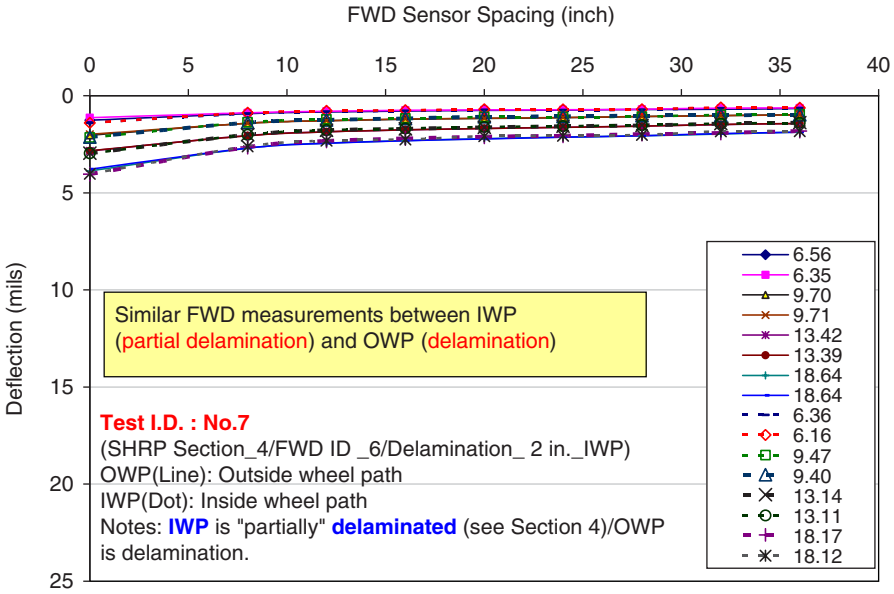

Figure 7.24. FWD deflections of Test 7 at NCAT Section 4.

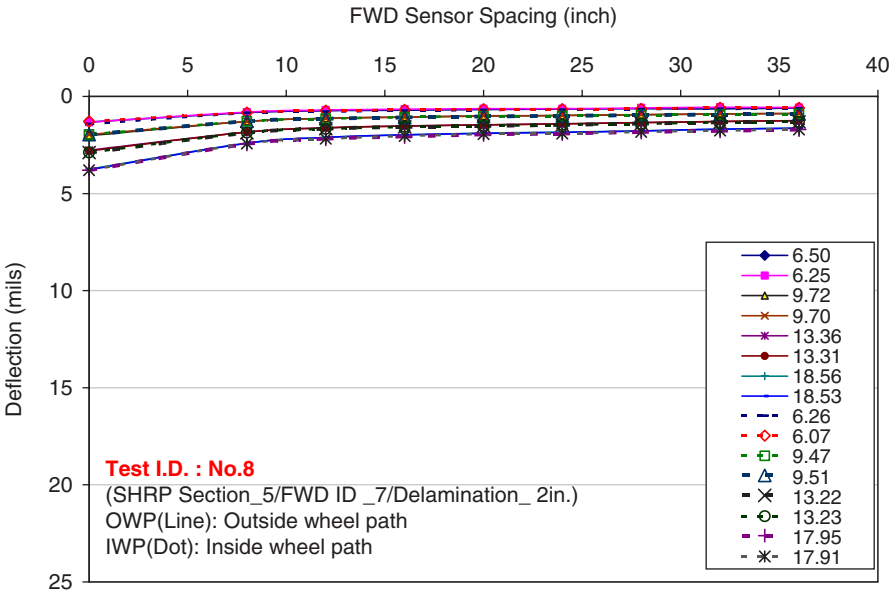

Figure 7.25. FWD deflections of Test 8 at NCAT Section 5.

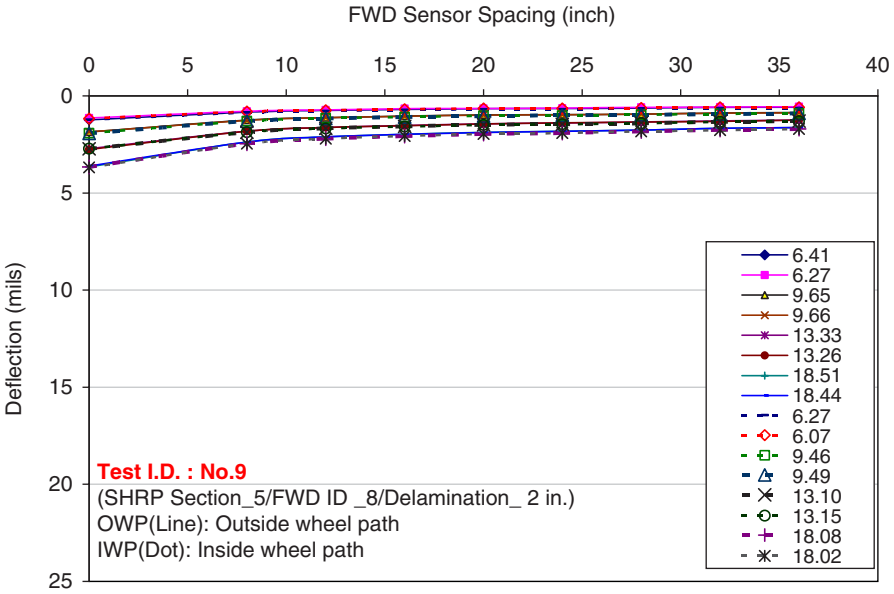

Figure 7.26. FWD deflections of Test 9 at NCAT Section 5.

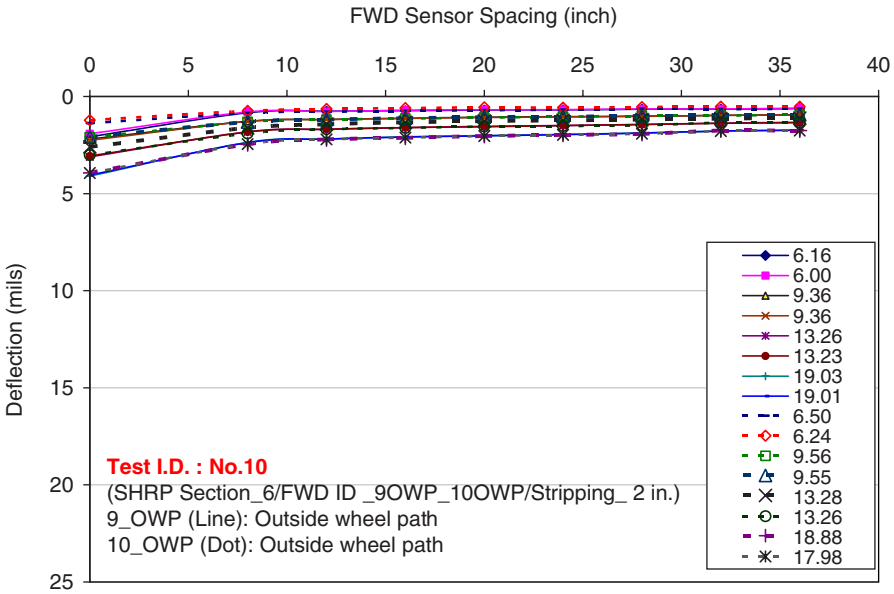

Figure 7.27. FWD deflections of Test 10 at NCAT Section 6.

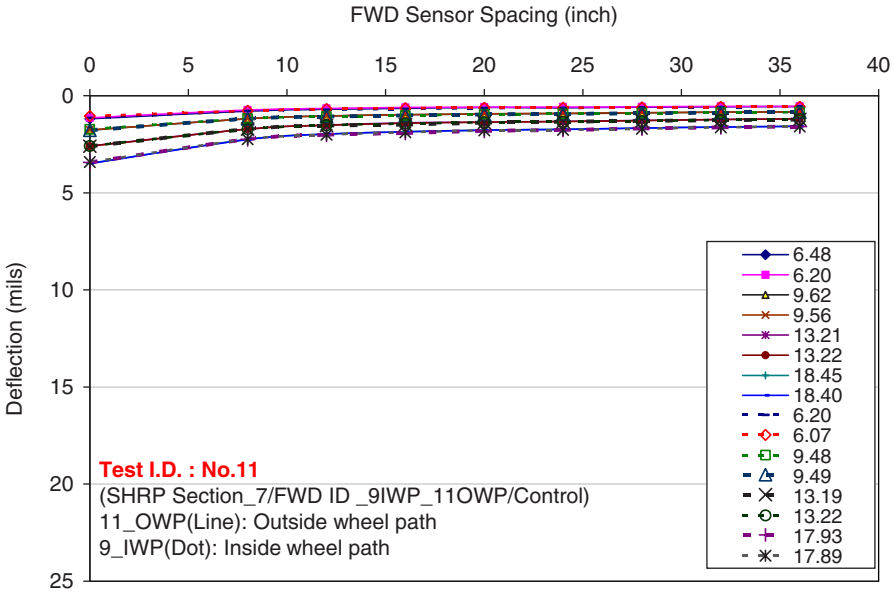

Figure 7.28. FWD deflections of Test 11 at NCAT Section 7.

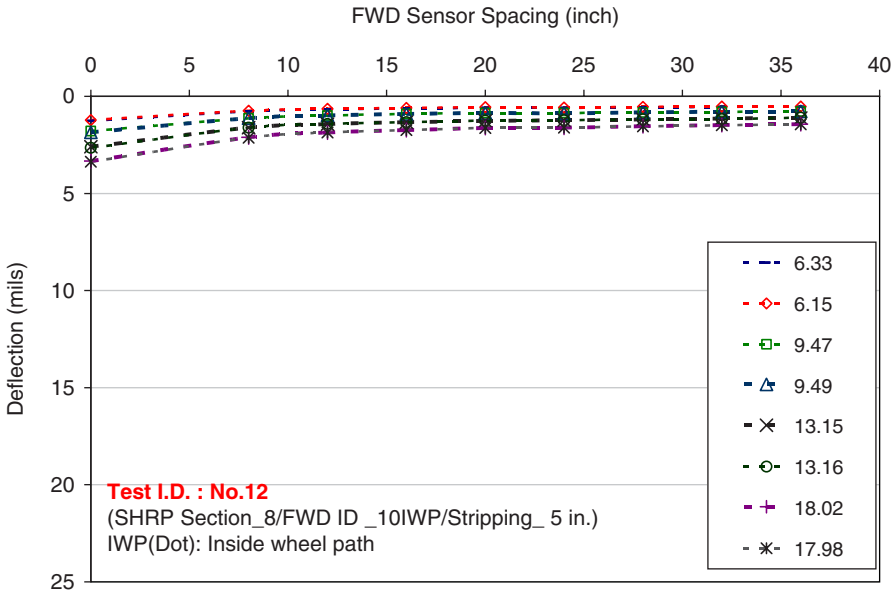

Figure 7.29. FWD deflections of Test 12 at NCAT Section 8.

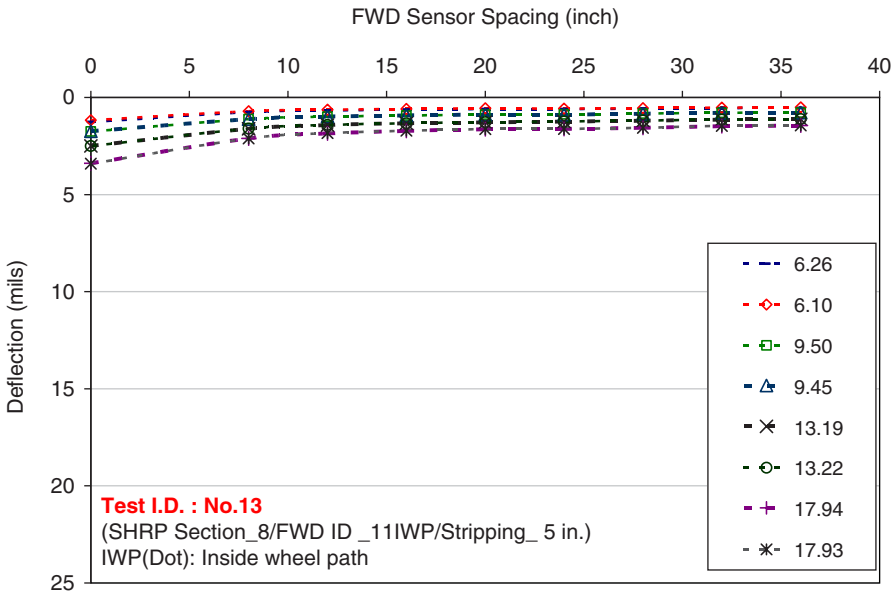

Figure 7.30. FWD deflections of Test 13 at NCAT Section 8.

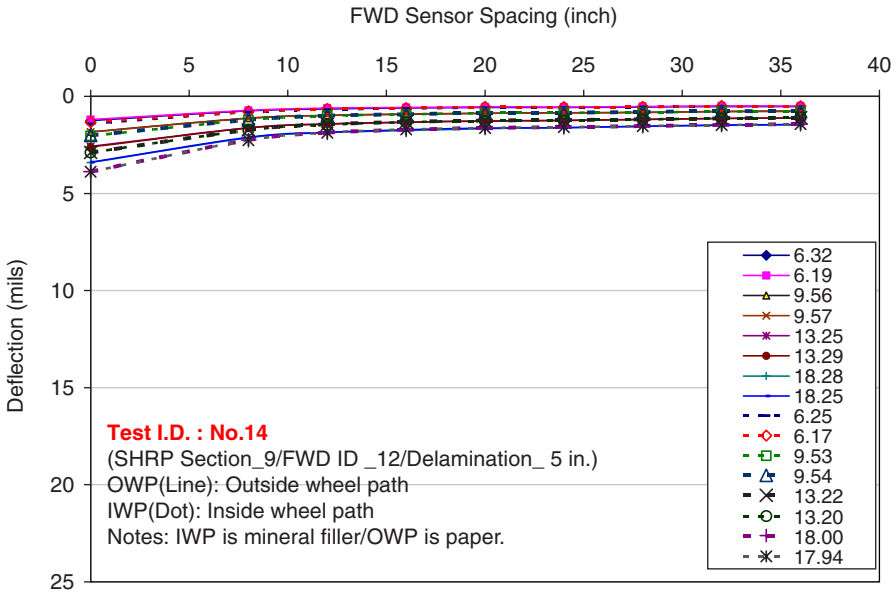

Figure 7.31. FWD deflections of Test 14 at NCAT Section 9.

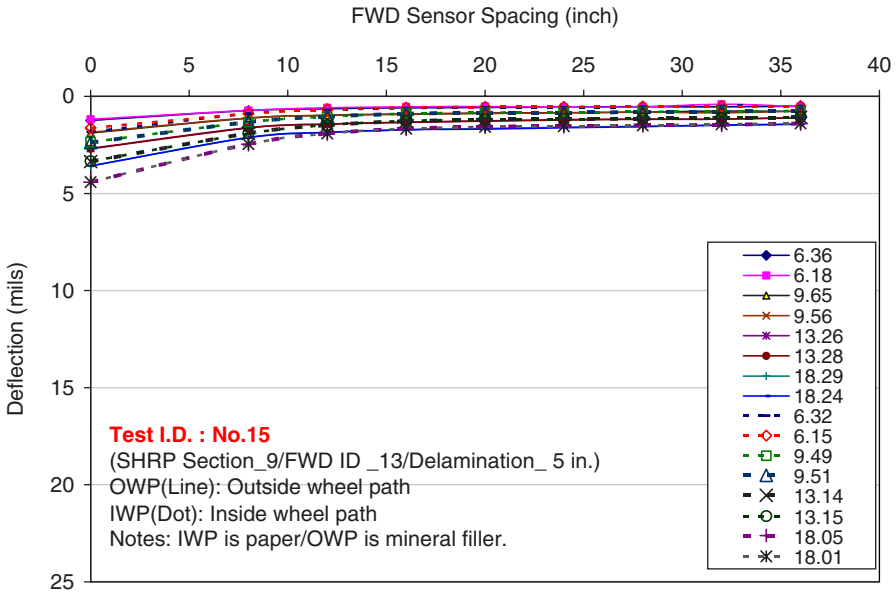

Figure 7.32. FWD deflections of Test 15 at NCAT Section 9.

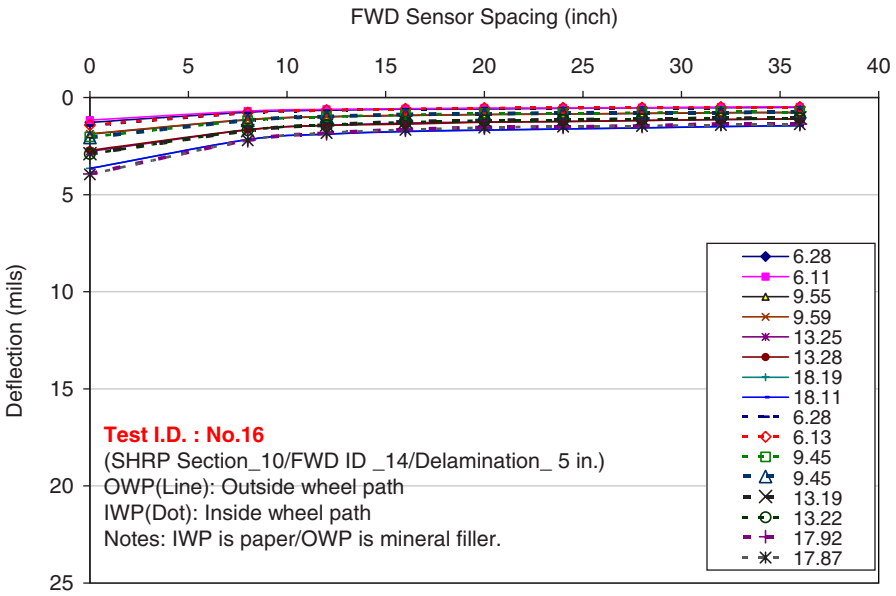

Figure 7.33. FWD deflections of Test 16 at NCAT Section 10.

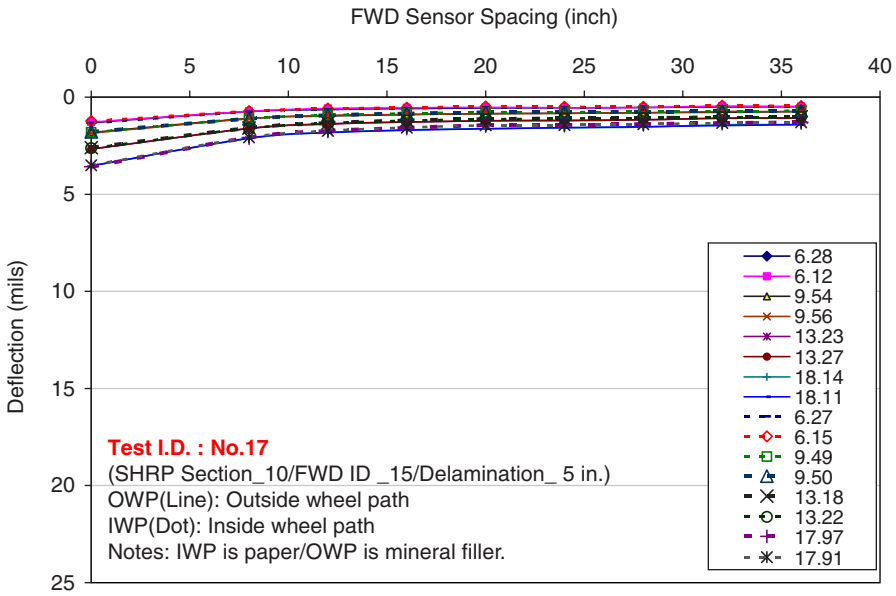

Figure 7.34. FWD deflections of Test 17 at NCAT Section 17.

(*continued from page 76*)

Deflection Basin Parameters of FWD Measurements at NCAT Test Sections

AREA: The AREA shape parameter defines the stiffness of the pavement structure as a shape factor. It is the area under the deflection basin curve (normalized with respect to D_0) using Simpson's rule. Thus, the AREA is a function of sensor location and has units of length (inches). The maximum value cannot be greater than 36 in., corresponding to the case when the four sensor measurements are equal. The minimum AREA can be assumed to be the value computed by using the elastic half-space model (Boussinesq model). For most pavements, the FWD AREA will range from 11.1 in. to 36 in. The AREA is defined as

$$AREA = \frac{6\left(D_0 + 2D_1 + 2D_2 + D_3\right)}{D_0}$$

AUPP: Area under pavement profile is also an FWD deflection basin shape parameter. Its definition is complementary to the AREA parameter, that is, a lower AUPP corresponds to higher pavement stiffness. On the basis of the extensive ILLI-PAVE database (Hill and Thompson 1988), the horizontal strain at the bottom of the asphalt concrete (AC) layer (ε_{AC}) has been correlated with the AUPP term for conventional and full-depth flexible pavements. Many research studies have validated the ε_{AC}–AUPP relations based on the analyses of MnROAD field data (FWD testing and AC strain gauge readings). They were found to be valid at various load levels. The AUPP is defined as

$$AUPP = \frac{5D_0 - 2D_1 - 2D_2 - D_3}{2}$$

ISM: Impact stiffness modulus is defined as the load required to produce unit deflection. It is computed as the ratio of FWD plate load (P) over maximum surface deflection (D_0) and is frequently used in airport pavement evaluation. The ISM is defined as

$$ISM = \frac{P}{D_0}$$

SCI: The D_0 deflection provides an indication of the overall pavement strength whereas the surface curvature index provides information on changes in relative strength of the near-surface layers, especially the AC layer. On the basis of their finite element (FE) analyses, Xu et al. (2001) found that for a certain thickness of the AC layer, the AC moduli and SCI values exhibit an approximately linear relationship in a log-log scale. The SCI has the same meaning as AUPP, that is, lower SCI values mean higher pavement stiffnesses. The SCI is defined as

$$SCI = D_0 - D_1$$

BCI: Base curvature index is a subgrade condition indicator, especially in aggregate base pavements, and is strongly related to the subgrade modulus. The BCI is defined as

$$BCI = D_2 - D_3$$

BDI: Base damage index is related to base layer modulus and is a critical DBP for subgrade condition evaluation in full-depth pavements. The BDI is defined as

$$BDI = D_1 - D_2$$

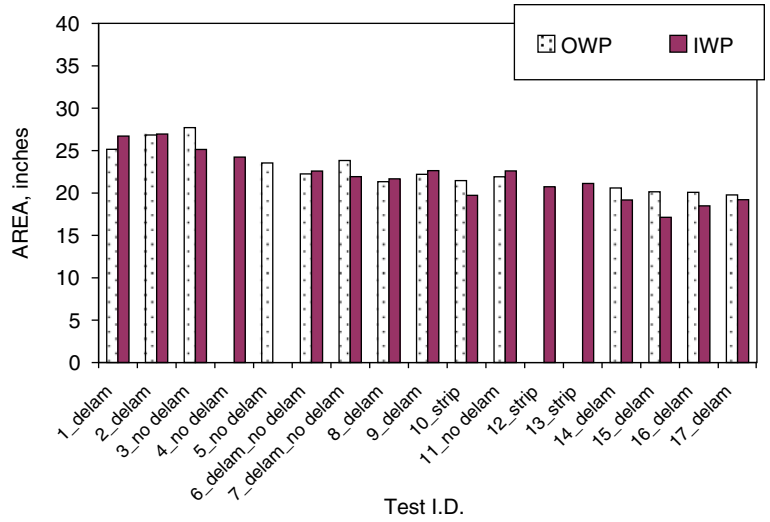

Figure 7.35. AREA of FWD measurements for FWD testing on NCAT test sections.

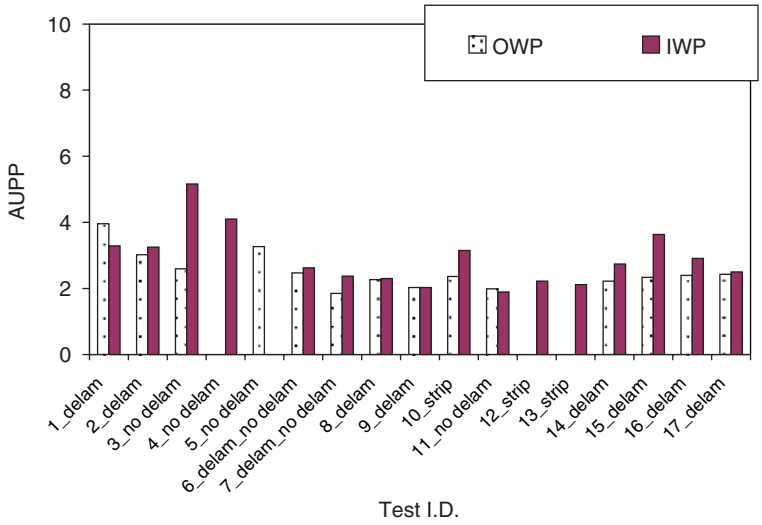

Figure 7.36. AUPP of FWD measurements for FWD testing on NCAT test sections.

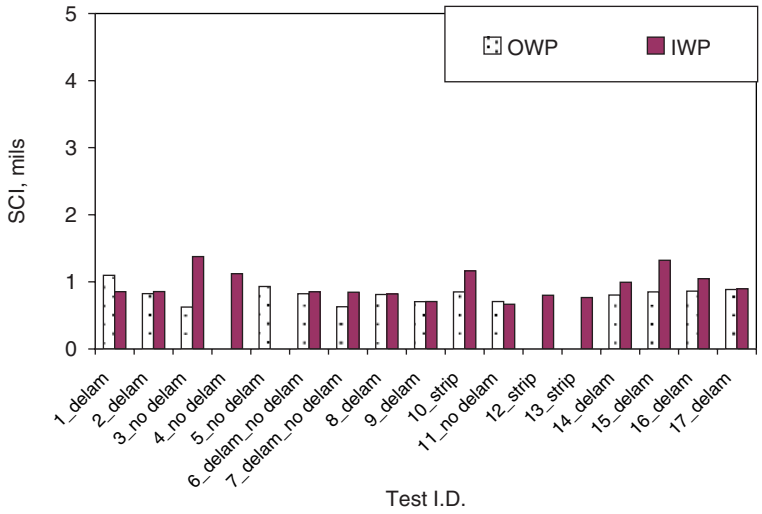

Figure 7.37. SCI of FWD measurements for FWD testing on NCAT test sections.

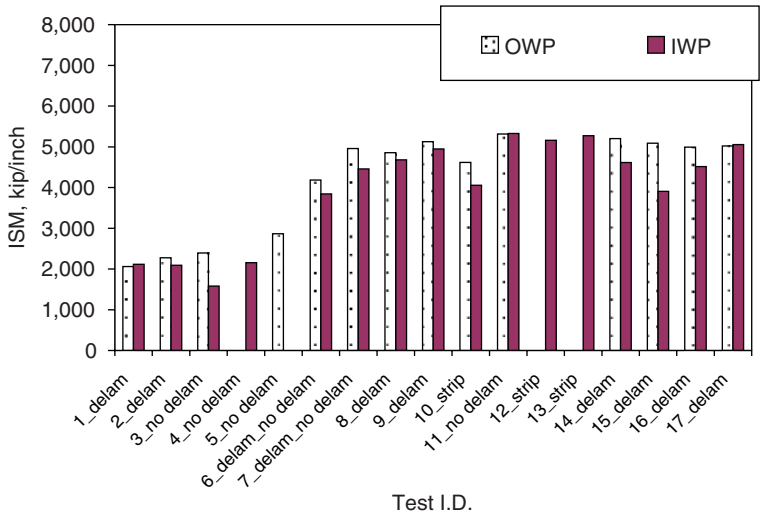

Figure 7.38. ISM of FWD measurements for FWD testing on NCAT test sections.

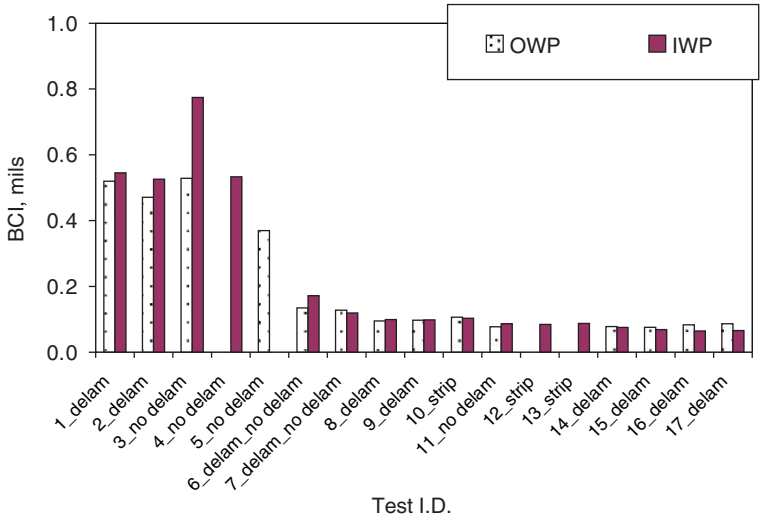

Figure 7.39. BCI of FWD measurements for FWD testing on NCAT test sections.

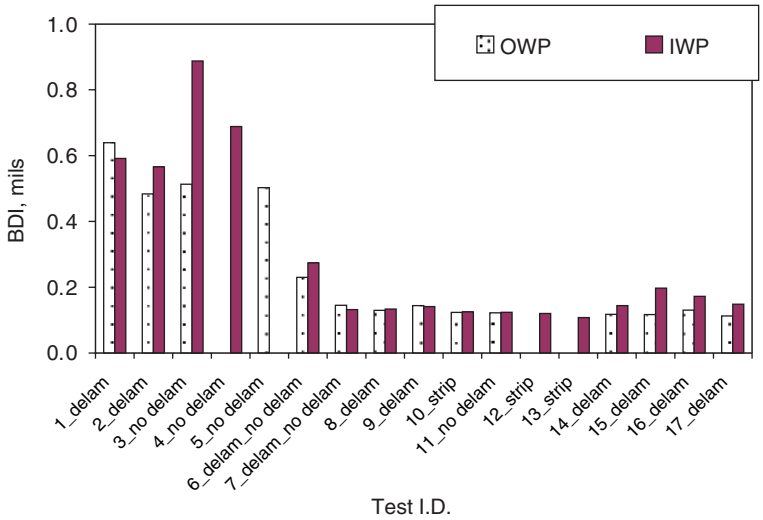

Figure 7.40. BDI of FWD measurements for FWD testing on NCAT test sections.

Comparisons of BISAR Results with 9-Kips Loading Normalized FWD Measurements for FWD Testing on NCAT Test Sections: Deflection Basins

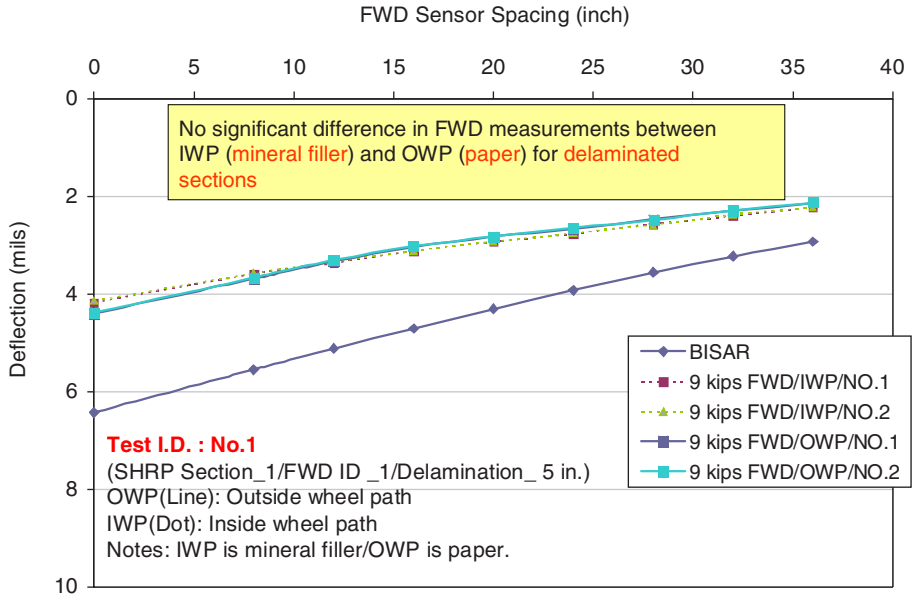

Figure 7.41. Comparisons of BISAR results with 9-kips loading normalized FWD measurements for FWD Test 1 at NCAT Section 1.

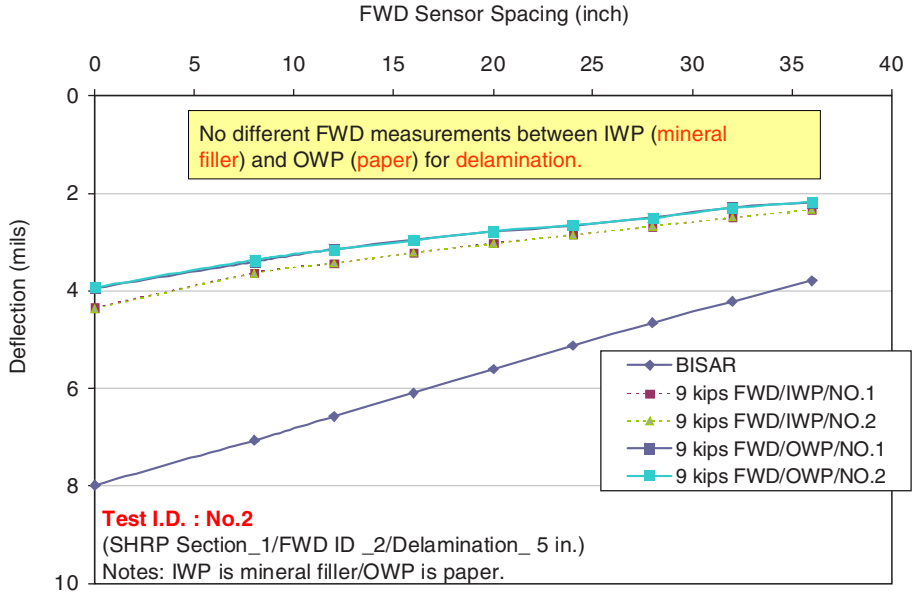

Figure 7.42. Comparisons of BISAR results with 9-kips loading normalized FWD measurements for FWD Test 2 at NCAT Section 1.

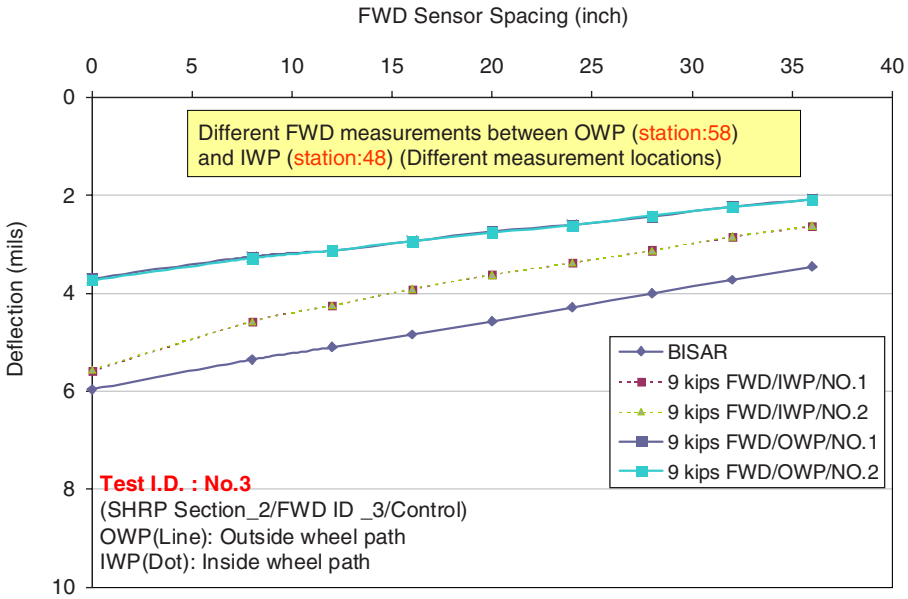

Figure 7.43. Comparisons of BISAR results with 9-kips loading normalized FWD measurements for FWD Test 3 at NCAT Section 2.

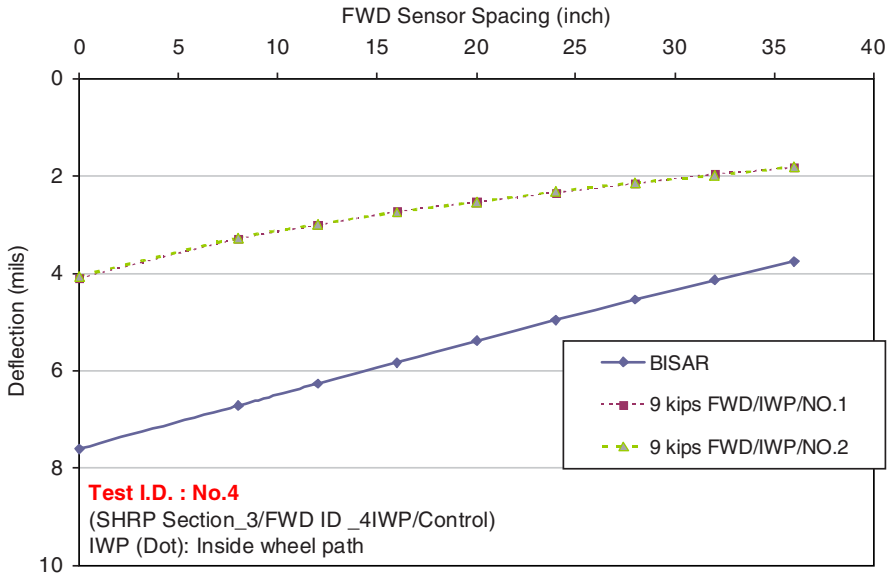

Figure 7.44. Comparisons of BISAR results with 9-kips loading normalized FWD measurements for FWD Test 4 at NCAT Section 3.

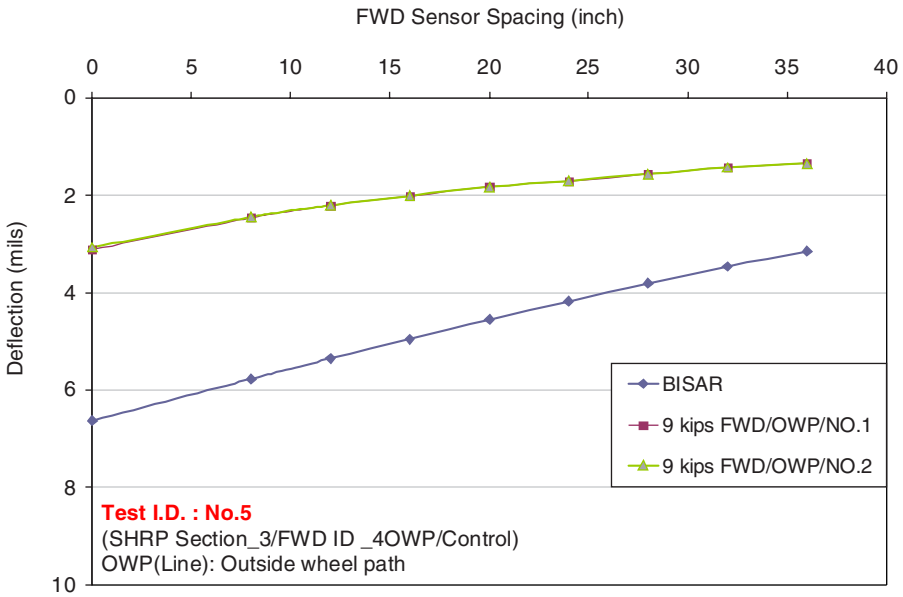

Figure 7.45. Comparisons of BISAR results with 9-kips loading normalized FWD measurements for FWD Test 5 at NCAT Section 3.

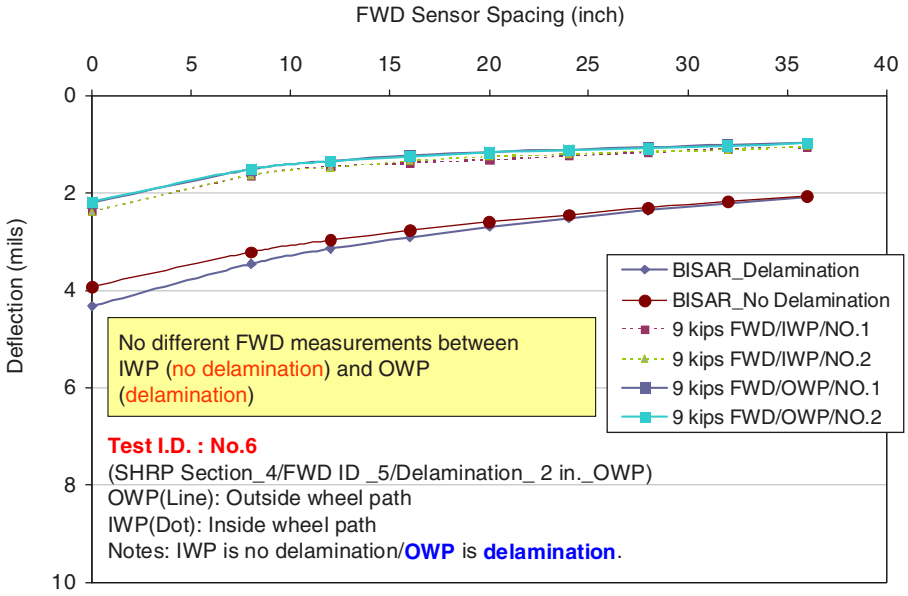

Figure 7.46. Comparisons of BISAR results with 9-kips loading normalized FWD measurements for FWD Test 6 at NCAT Section 4.

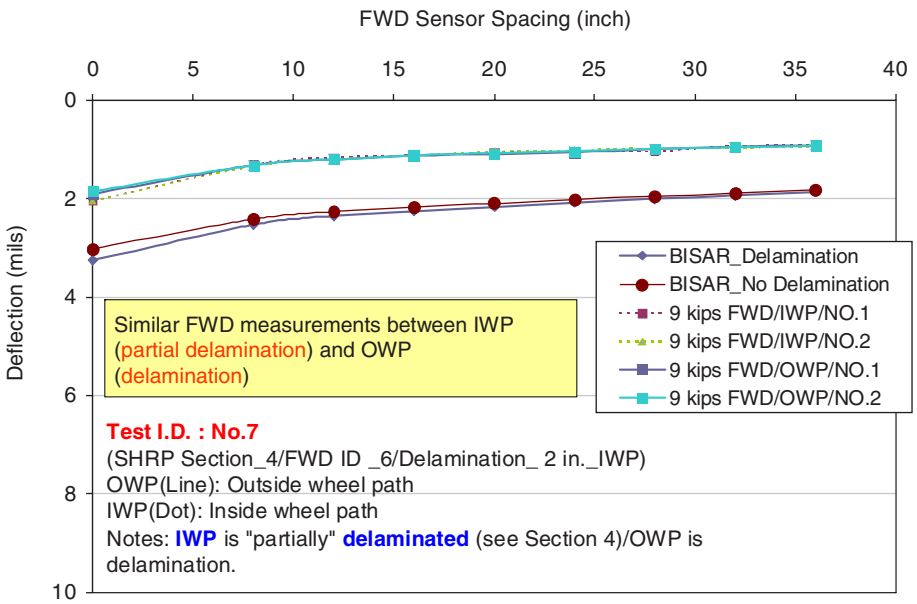

Figure 7.47. Comparisons of BISAR results with 9-kips loading normalized FWD measurements for FWD Test 7 at NCAT Section 4.

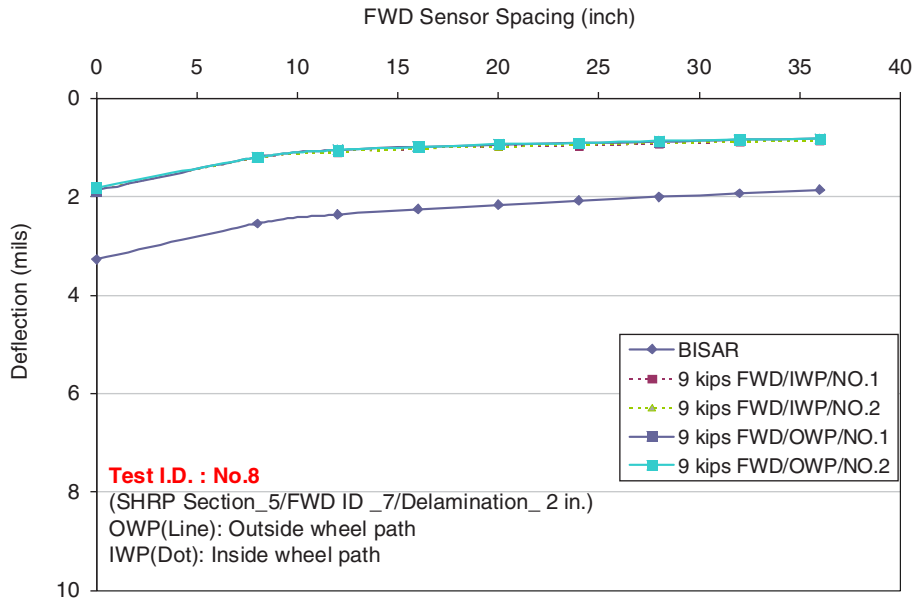

Figure 7.48. Comparisons of BISAR results with 9-kips loading normalized FWD measurements for FWD Test 8 at NCAT Section 5.

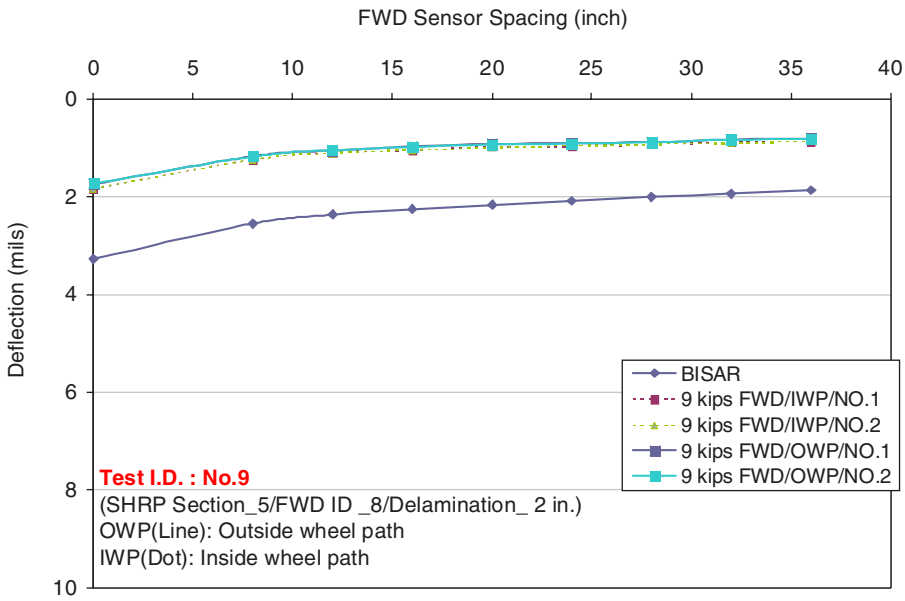

Figure 7.49. Comparisons of BISAR results with 9-kips loading normalized FWD measurements for FWD Test 9 at NCAT Section 5.

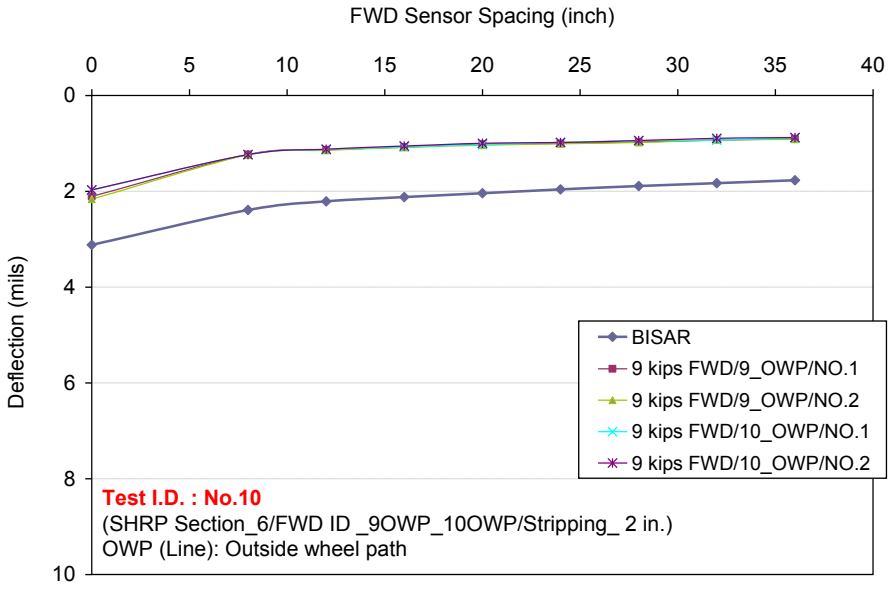

Figure 7.50. Comparisons of BISAR results with 9-kips loading normalized FWD measurements for FWD Test 10 at NCAT Section 6.

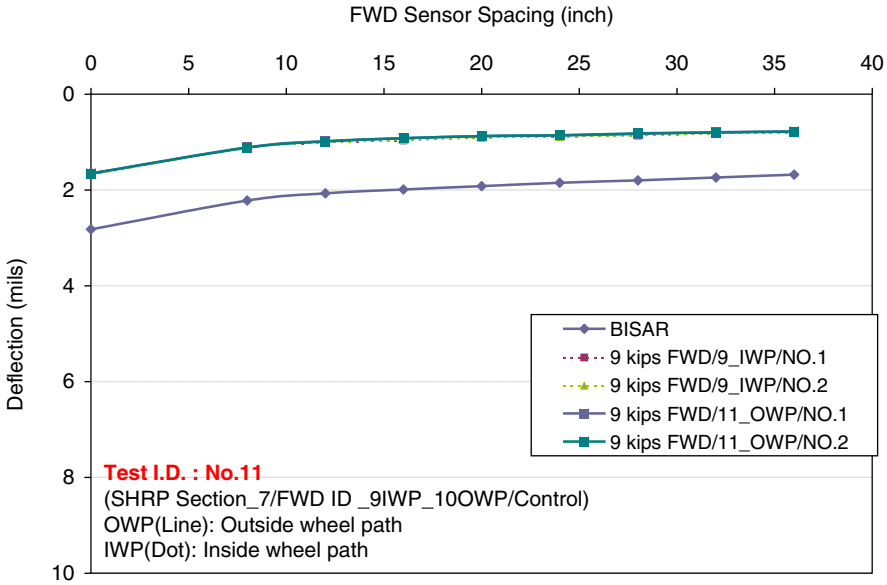

Figure 7.51. Comparisons of BISAR results with 9-kips loading normalized FWD measurements for FWD Test 11 at NCAT Section 7.

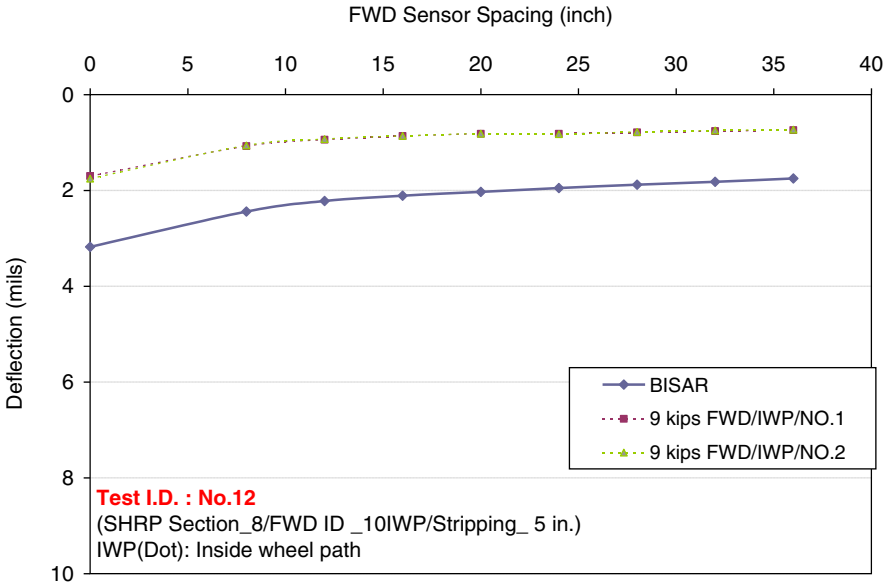

Figure 7.52. Comparisons of BISAR results with 9-kips loading normalized FWD measurements for FWD Test 12 at NCAT Section 8.

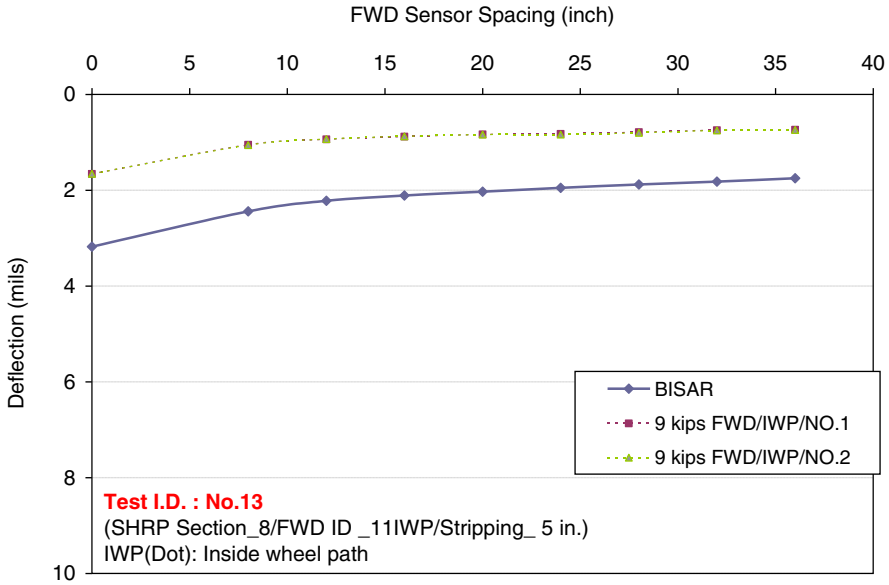

Figure 7.53. Comparisons of BISAR results with 9-kips loading normalized FWD measurements for FWD Test 13 at NCAT Section 8.

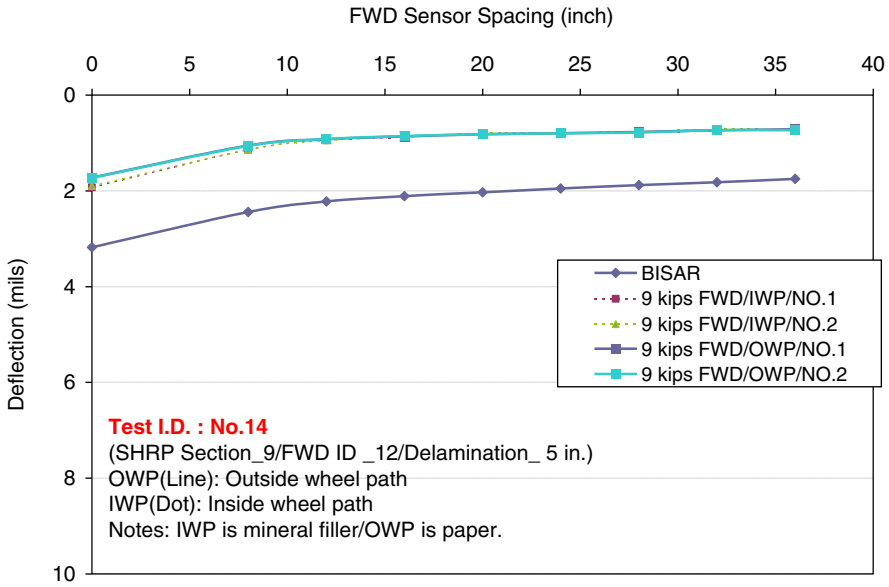

Figure 7.54. Comparisons of BISAR results with 9-kips loading normalized FWD measurements for FWD Test 14 at NCAT Section 9.

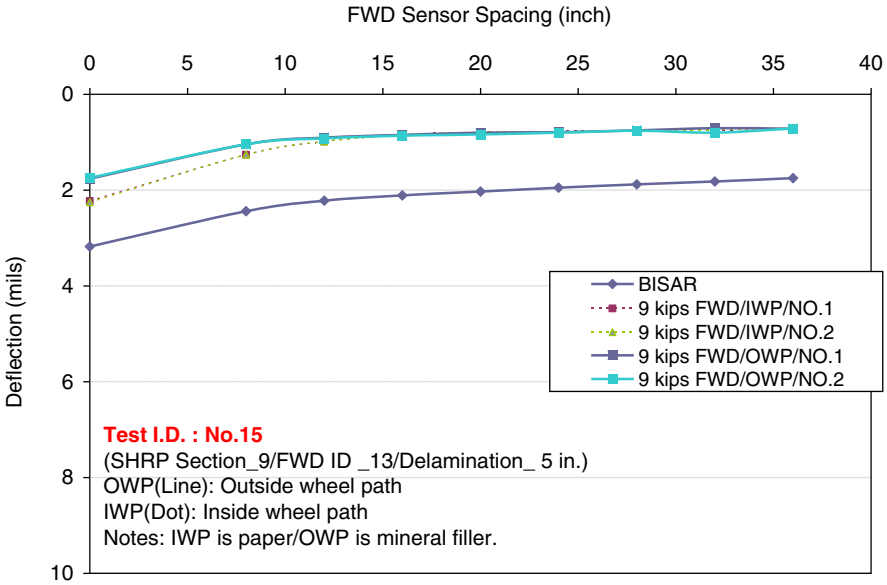

Figure 7.55. Comparisons of BISAR results with 9-kips loading normalized FWD measurements for FWD Test 15 at NCAT Section 9.

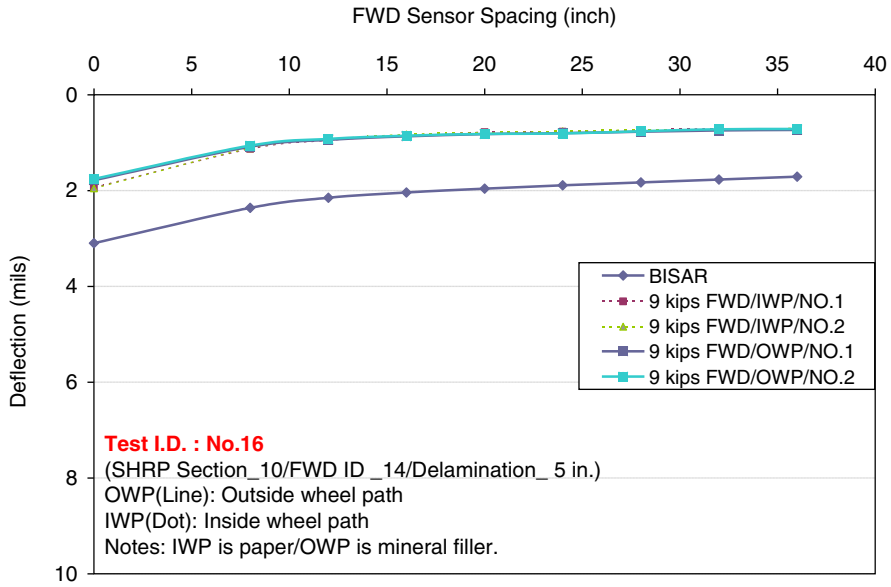

Figure 7.56. Comparisons of BISAR results with 9-kips loading normalized FWD measurements for FWD Test 16 at NCAT Section 10.

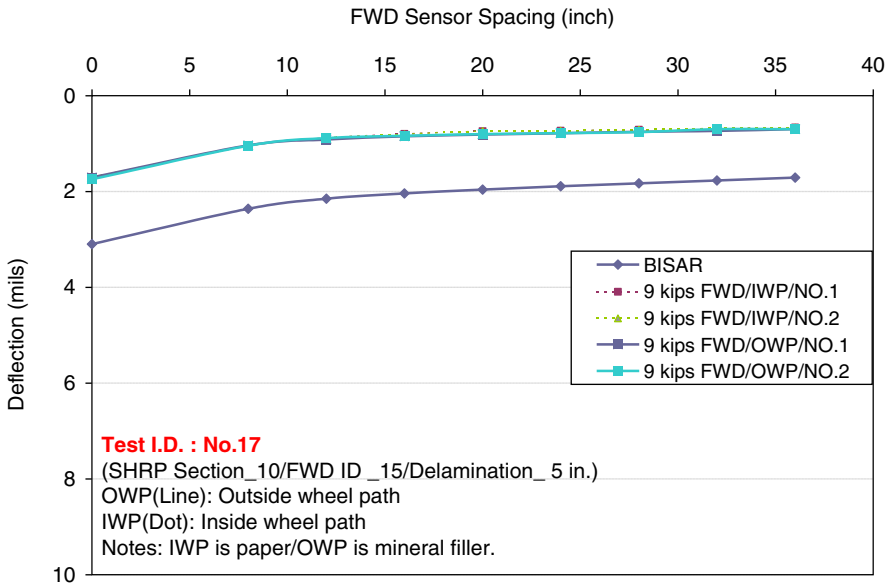

Figure 7.57. Comparisons of BISAR results with 9-kips loading normalized FWD measurements for FWD Test 17 at NCAT Section 10.

Comparisons of BISAR Results with Normalized 9-Kip Deflections for FWD Measurements for FWD Testing on NCAT Test Sections: Time History Curves

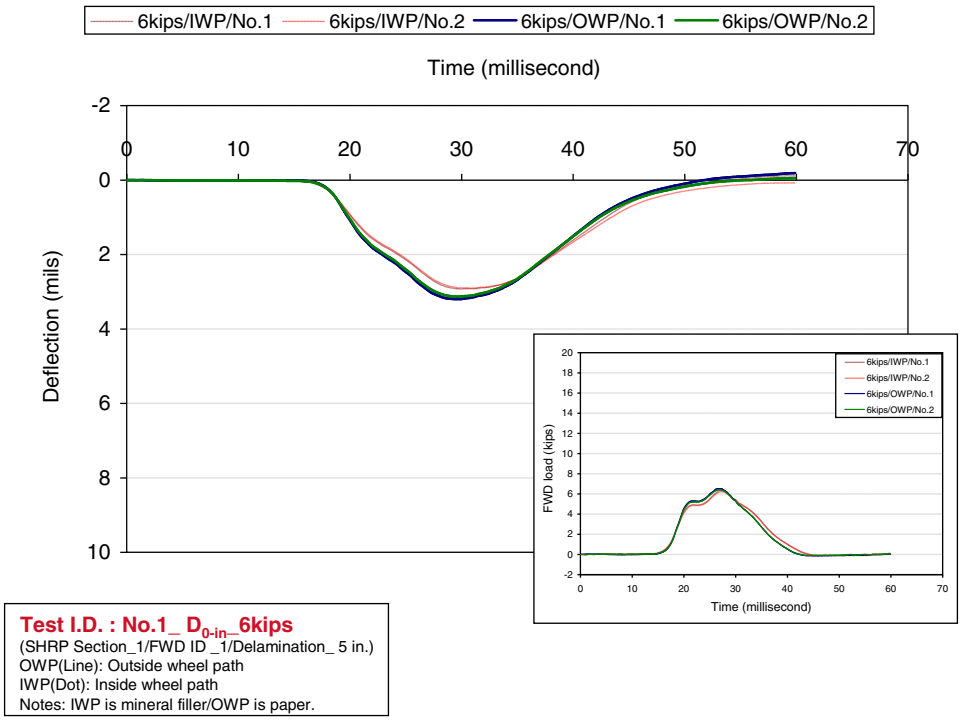

Figure 7.58. FWD deflection ($D_{0\text{-}in.}$) time history under 6-kips loading for FWD Test 1 at NCAT Section 1.

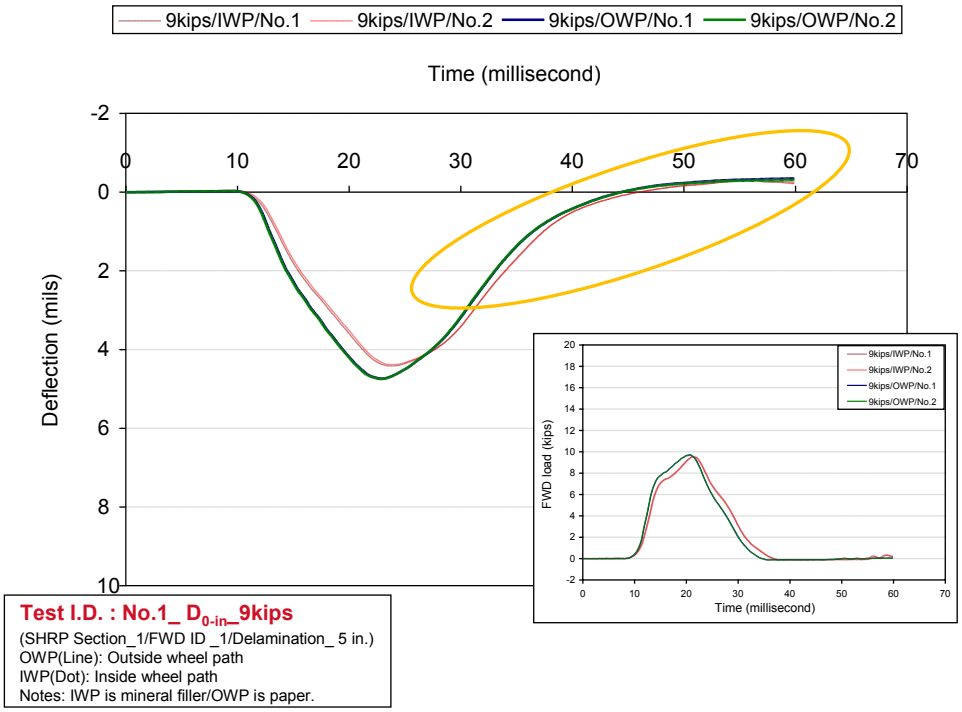

Figure 7.59. FWD deflection ($D_{0\text{-}in}$) time history under 9-kips loading for FWD Test 1 at NCAT Section 1.

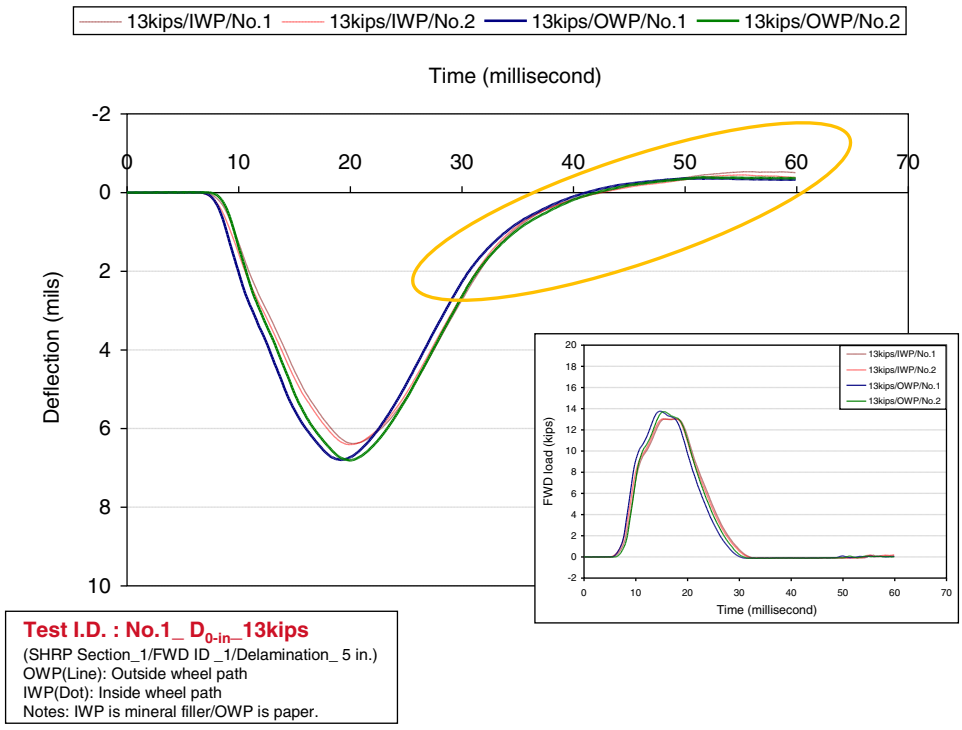

Figure 7.60. FWD deflection ($D_{0\text{-}in}$) time history under 13-kips loading for FWD Test 1 at NCAT Section 1.

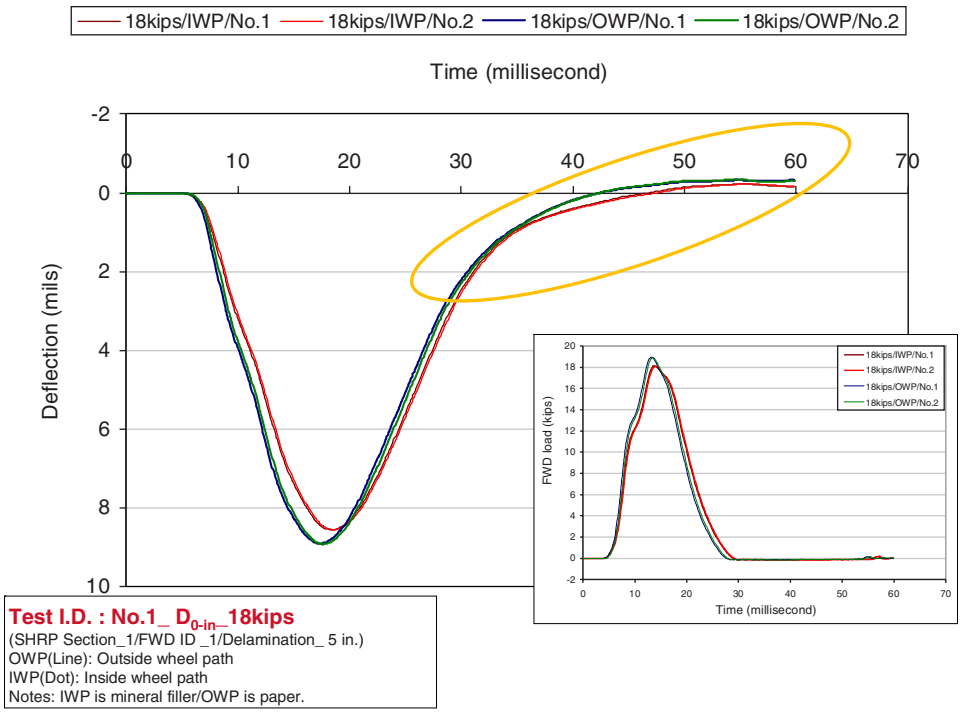

Figure 7.61. FWD deflection ($D_{0\text{-}in}$) time history under 18-kips loading for FWD Test 1 at NCAT Section 1.

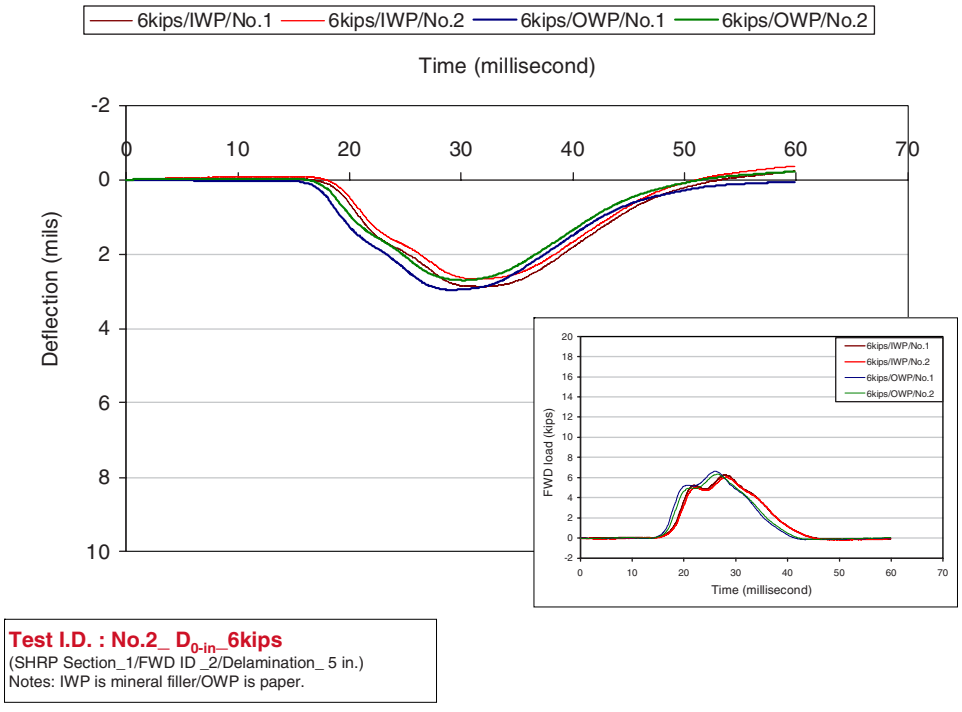

Figure 7.62. FWD deflection ($D_{0\text{-}in}$) time history under 6-kips loading for FWD Test 2 at NCAT Section 1.

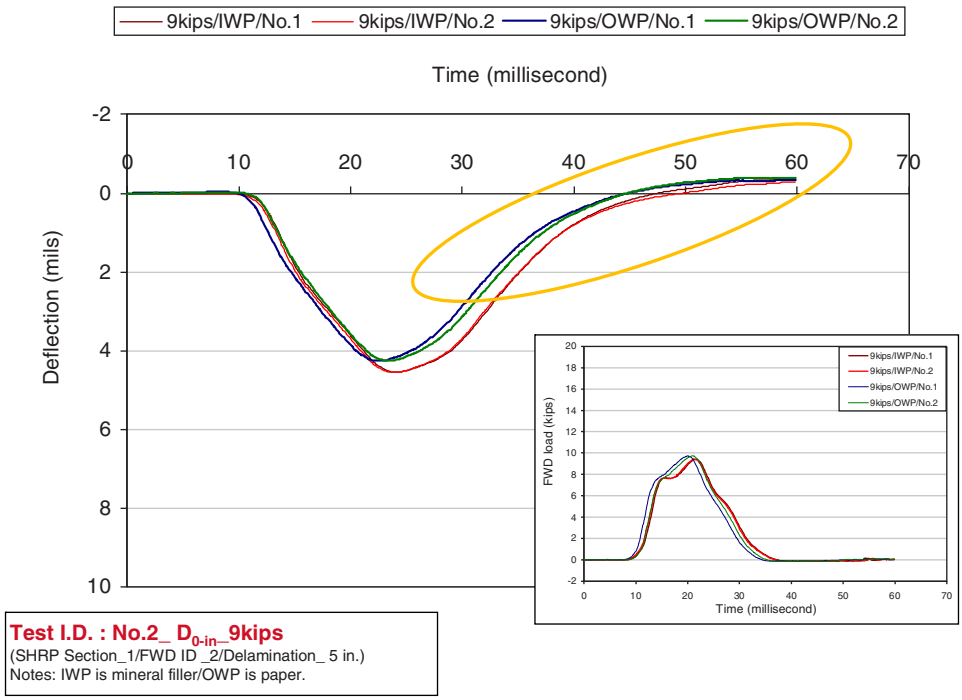

Figure 7.63. FWD deflection ($D_{0\text{-}in}$) time history under 9-kips loading for FWD Test 2 at NCAT Section 1.

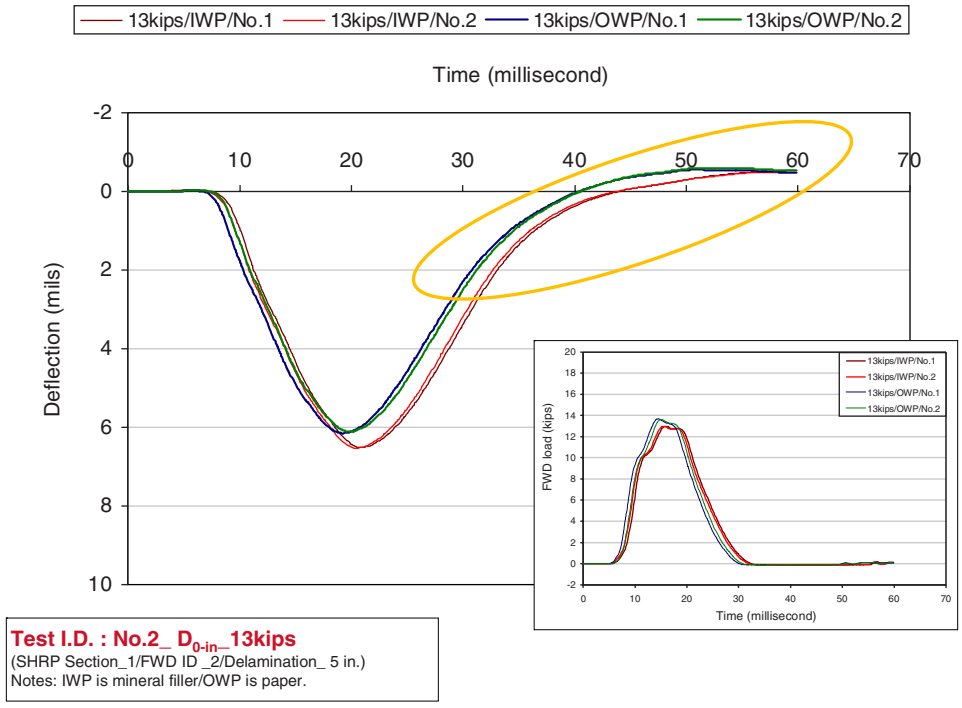

Figure 7.64. FWD deflection ($D_{0\text{-}in}$) time history under 13-kips loading for FWD Test 2 at NCAT Section 1.

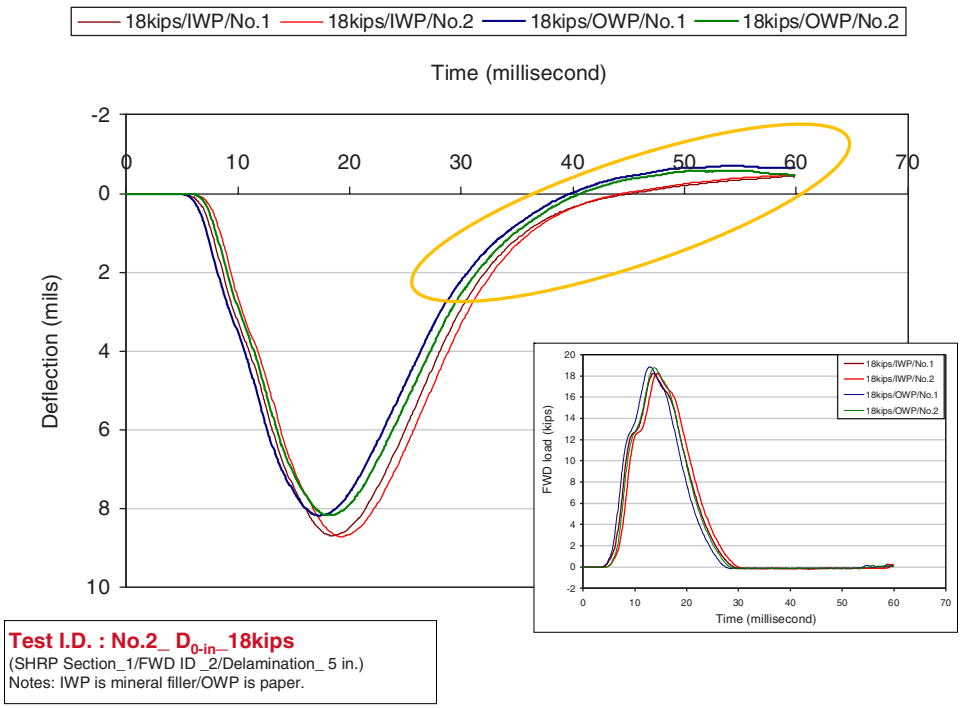

Test I.D. : No.2_ $D_{0\text{-}in}$_18kips
(SHRP Section_1/FWD ID _2/Delamination_ 5 in.)
Notes: IWP is mineral filler/OWP is paper.

Figure 7.65. FWD deflection ($D_{0\text{-}in}$) time history under 18-kips loading for FWD Test 2 at NCAT Section 1.

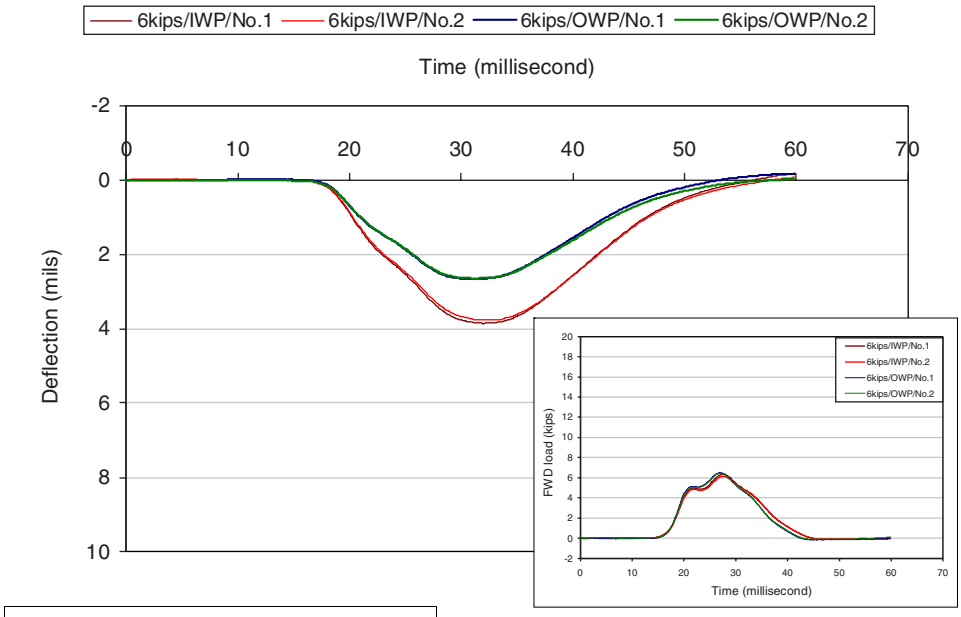

Test I.D. : No.3_ $D_{0\text{-}in}$_6kips
(SHRP Section_2/FWD ID _3/Control)
OWP(Line): Outside wheel path
IWP(Dot): Inside wheel path

Figure 7.66. FWD deflection ($D_{0\text{-}in}$) time history under 6-kips loading for FWD Test 3 at NCAT Section 2.

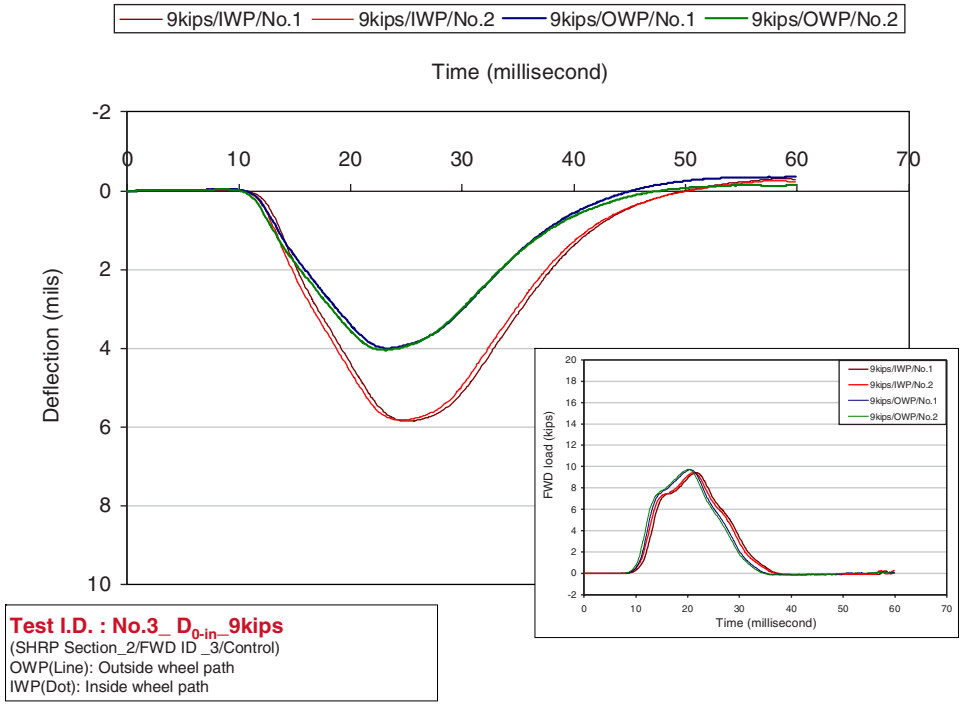

Figure 7.67. FWD deflection ($D_{0\text{-}in}$) time history under 9-kips loading for FWD Test 3 at NCAT Section 2.

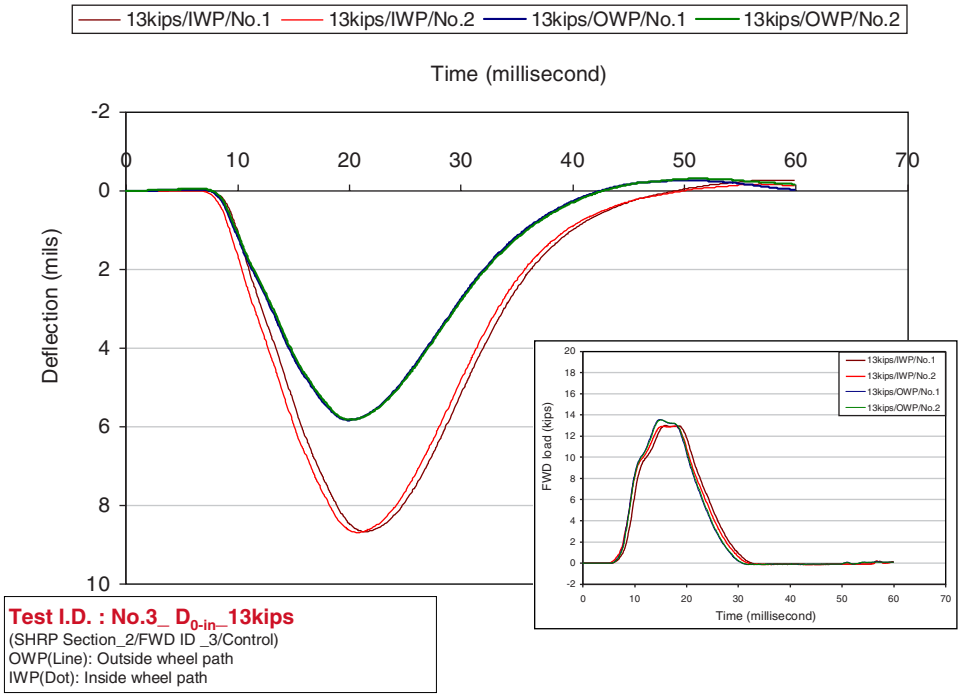

Figure 7.68. FWD deflection ($D_{0\text{-}in}$) time history under 13-kips loading for FWD Test 3 at NCAT Section 2.

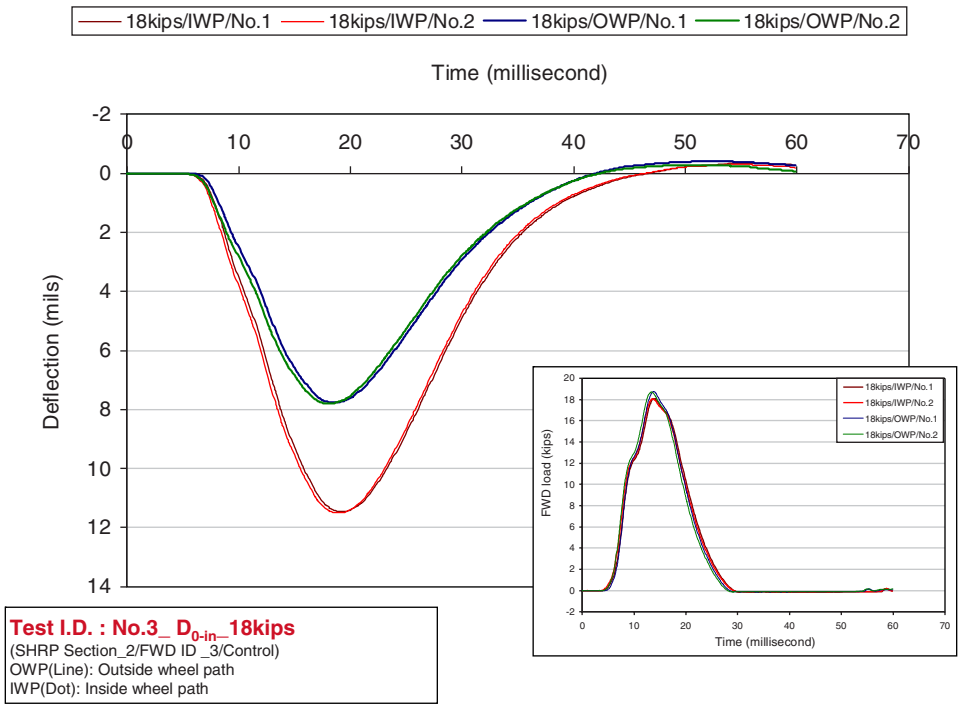

Figure 7.69. FWD deflection ($D_{0\text{-}in}$) time history under 18-kips loading for FWD Test 3 at NCAT Section 2.

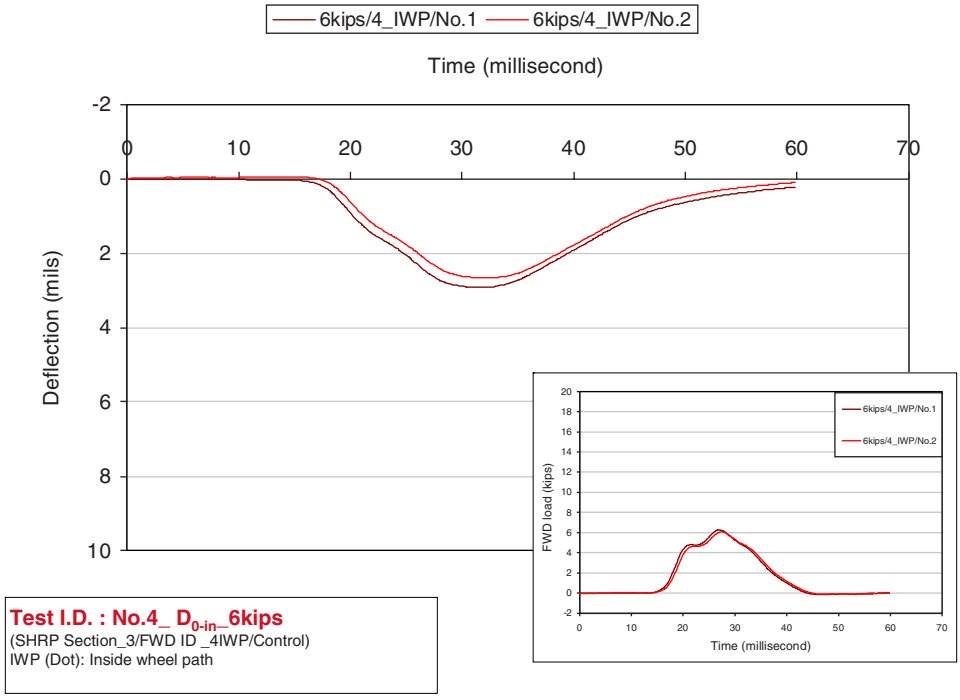

Figure 7.70. FWD deflection ($D_{0\text{-}in}$) time history under 6-kips loading for FWD Test 4 at NCAT Section 3.

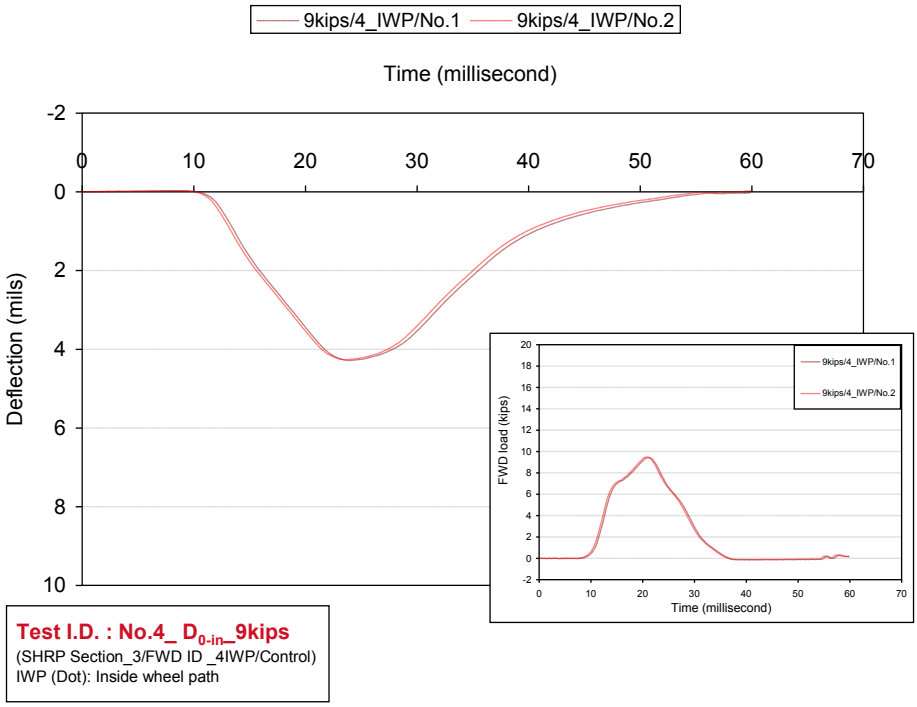

Figure 7.71. FWD deflection ($D_{0\text{-}in}$) time history under 9-kips loading for FWD Test 4 at NCAT Section 3.

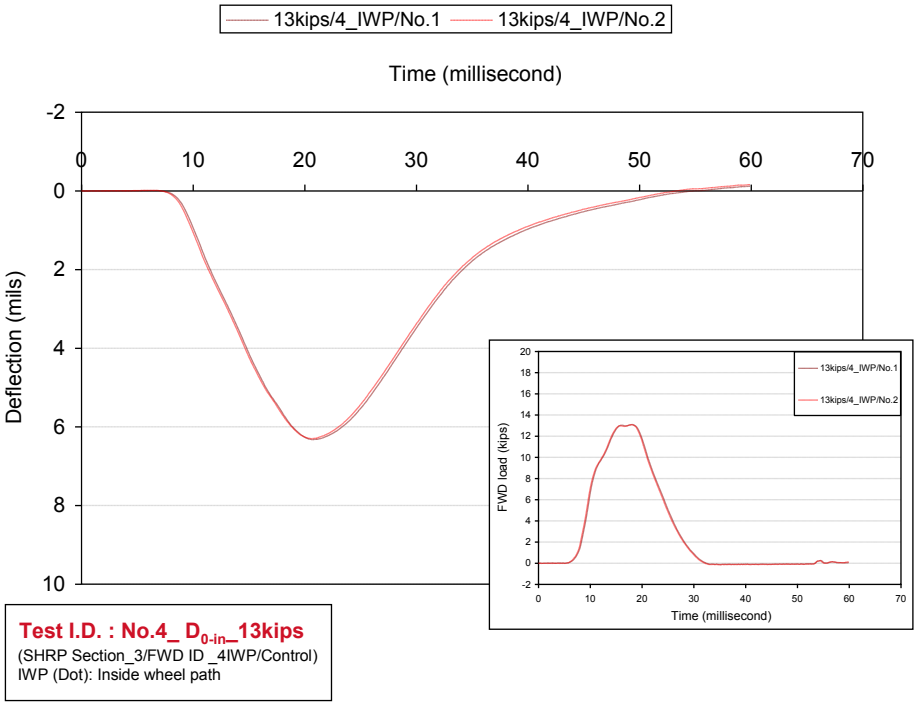

Figure 7.72. FWD deflection ($D_{0\text{-}in}$) time history under 13-kips loading for FWD Test 4 at NCAT Section 3.

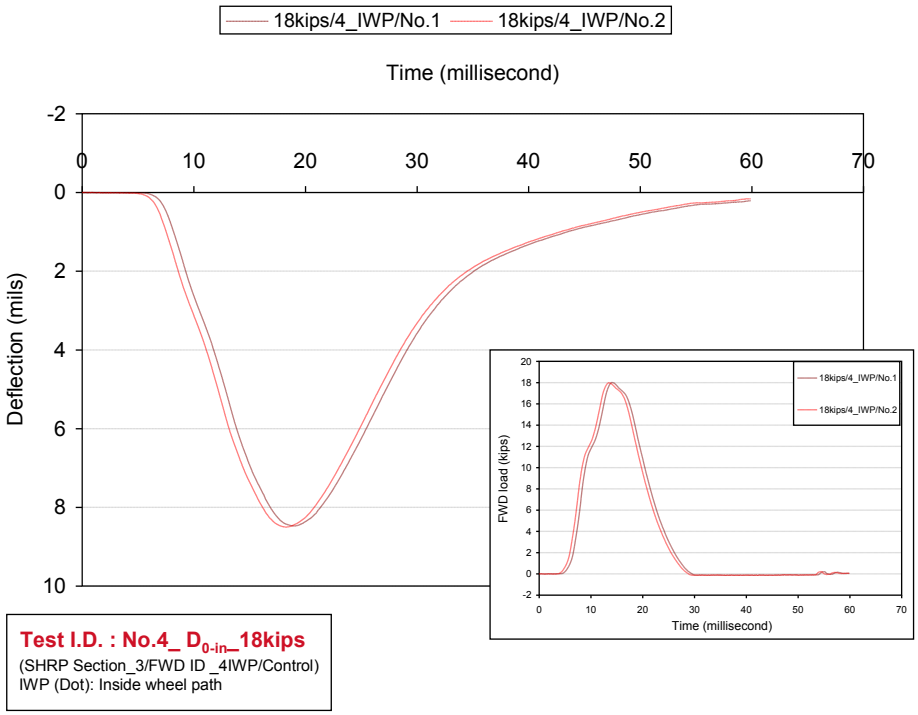

Figure 7.73. FWD deflection ($D_{0\text{-}in}$) time history under 18-kips loading for FWD Test 4 at NCAT Section 3.

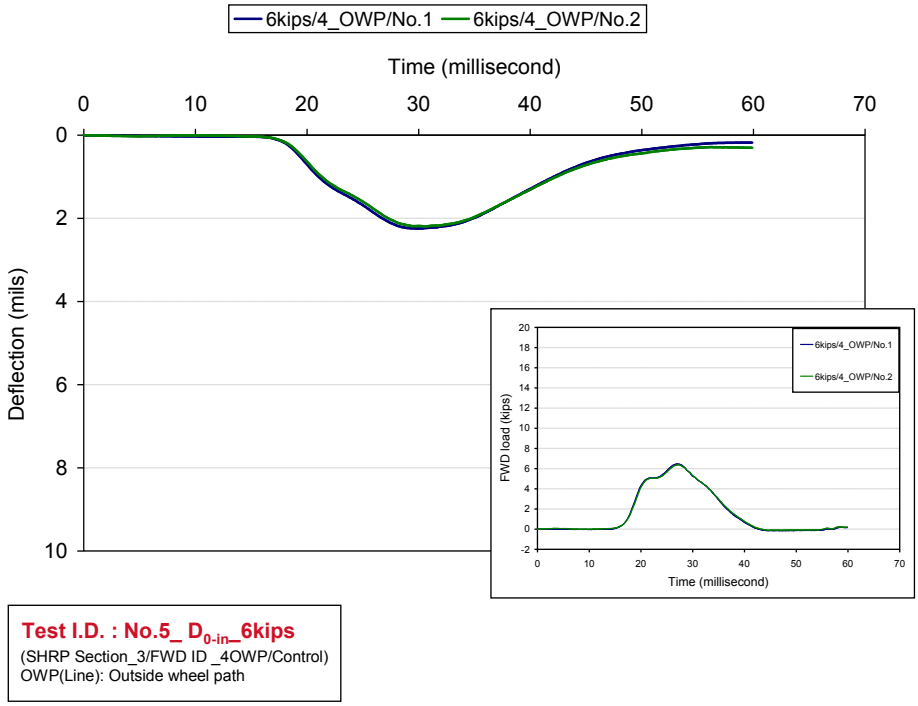

Figure 7.74. FWD deflection ($D_{0\text{-}in}$) time history under 6-kips loading for FWD Test 5 at NCAT Section 3.

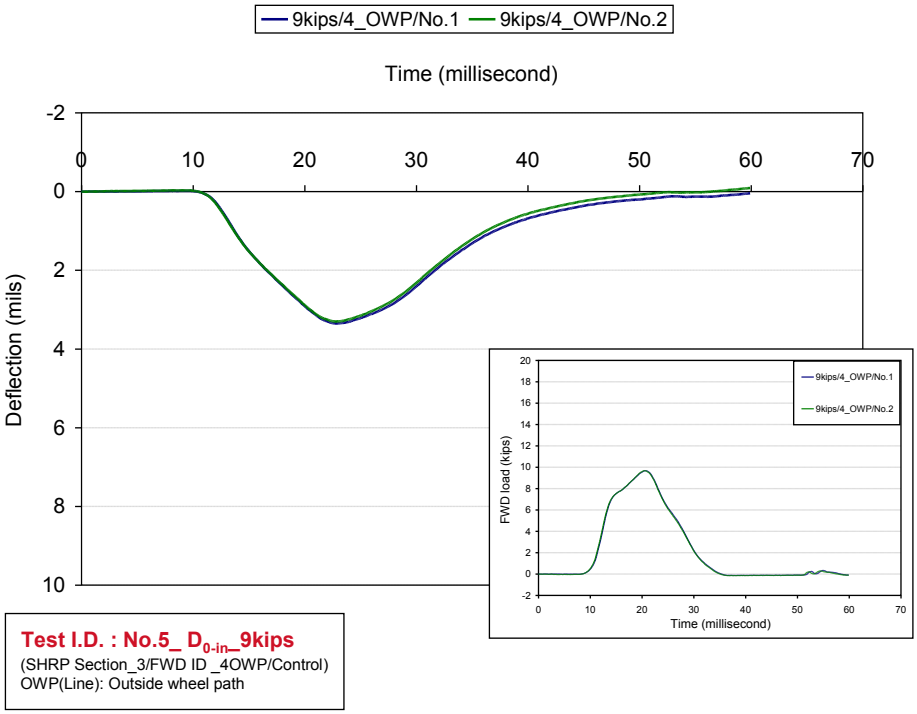

Figure 7.75. FWD deflection ($D_{0\text{-}in}$) time history under 9-kips loading for FWD Test 5 at NCAT Section 3.

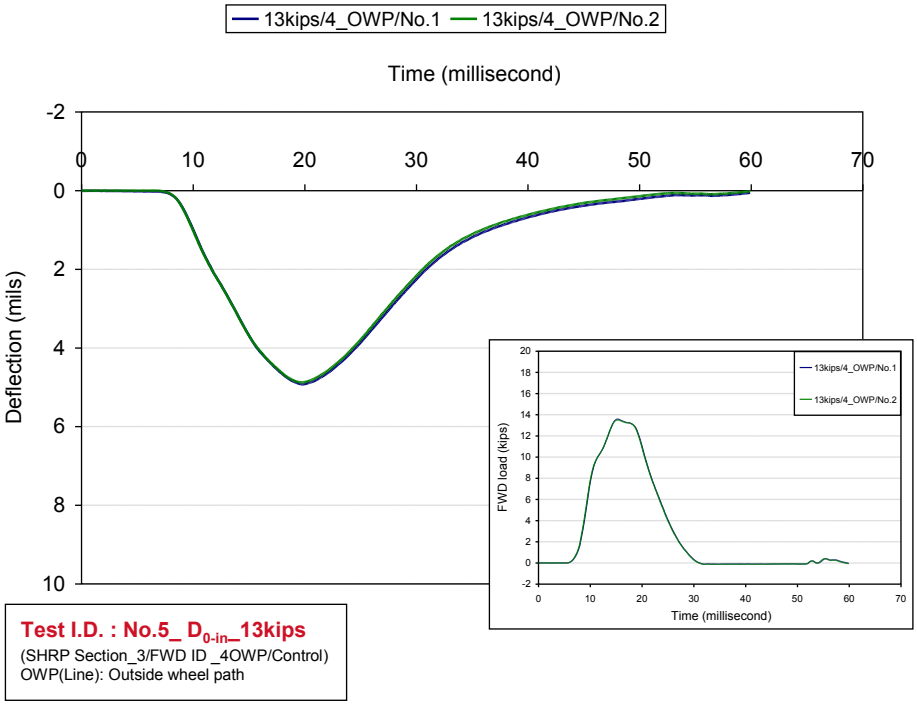

Figure 7.76. FWD deflection ($D_{0\text{-}in}$) time history under 13-kips loading for FWD Test 5 at NCAT Section 3.

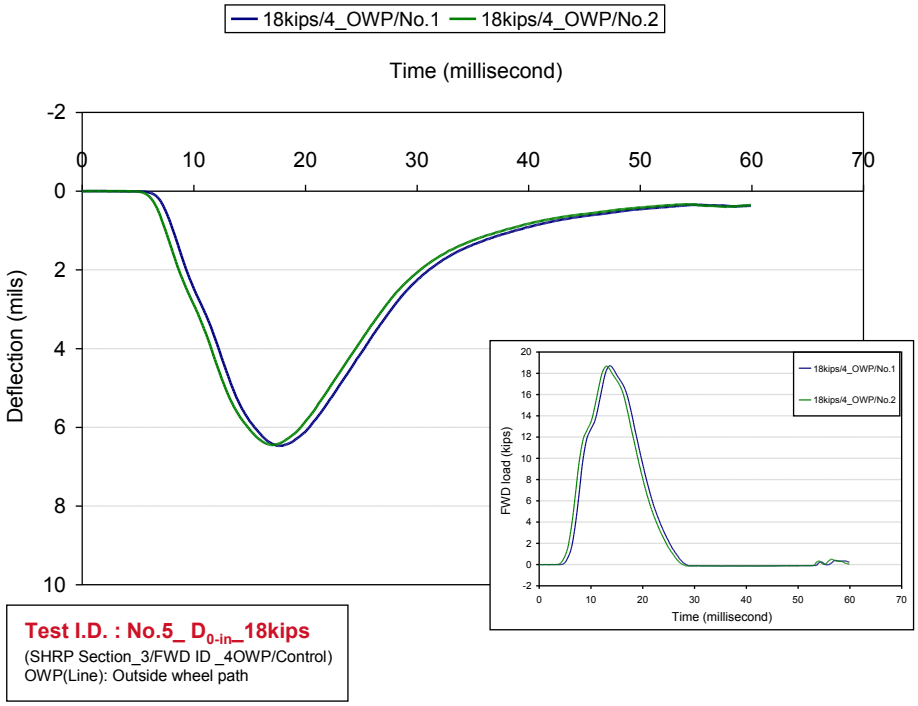

Figure 7.77. FWD deflection ($D_{0\text{-}in}$) time history under 18-kips loading for FWD Test 5 at NCAT Section 3.

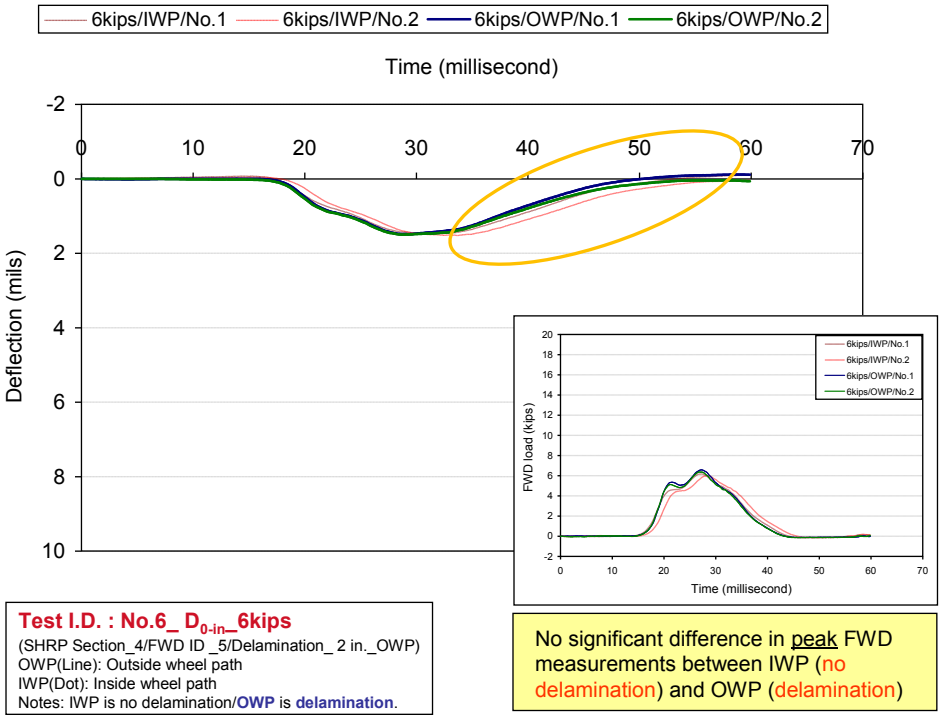

Figure 7.78. FWD deflection ($D_{0\text{-}in}$) time history under 6-kips loading for FWD Test 6 at NCAT Section 4.

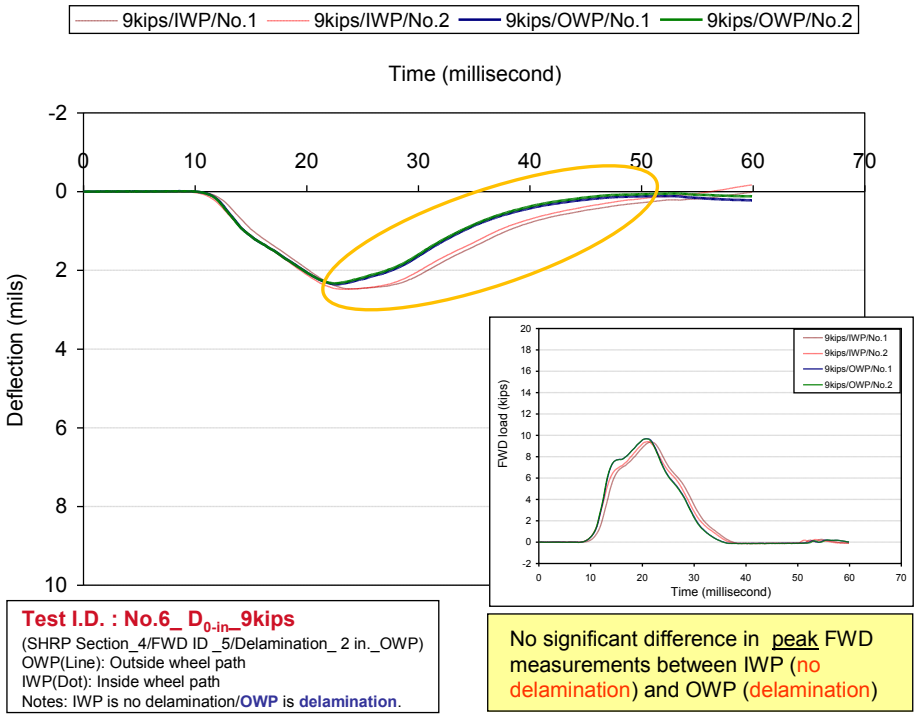

Figure 7.79. FWD deflection ($D_{0\text{-}in}$) time history under 9-kips loading for FWD Test 6 at NCAT Section 4.

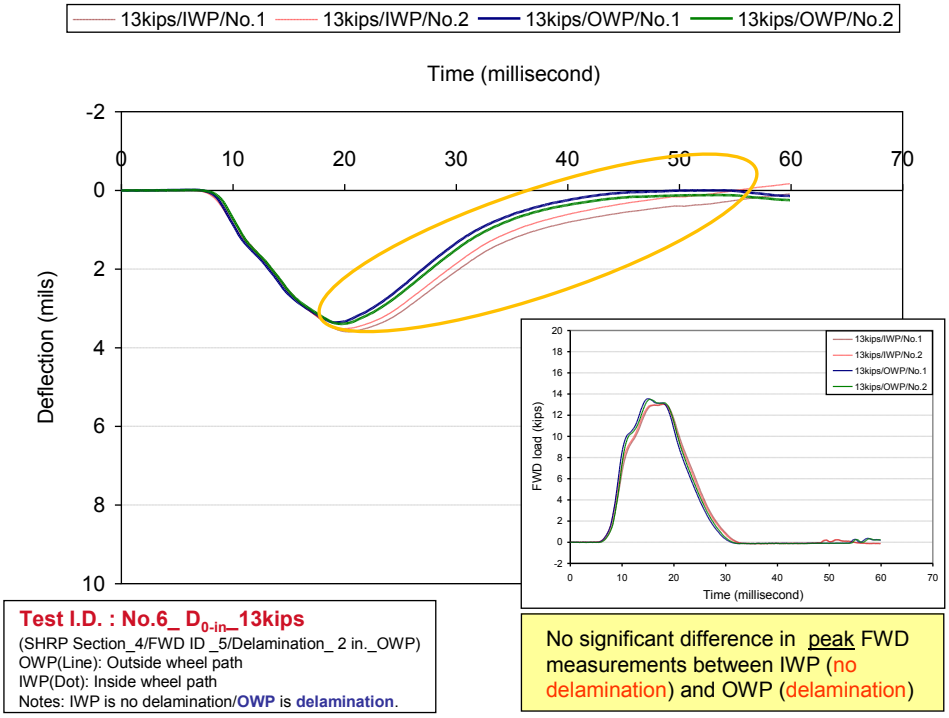

Figure 7.80. FWD deflection ($D_{0\text{-}in}$) time history under 13-kips loading for FWD Test 6 at NCAT Section 4.

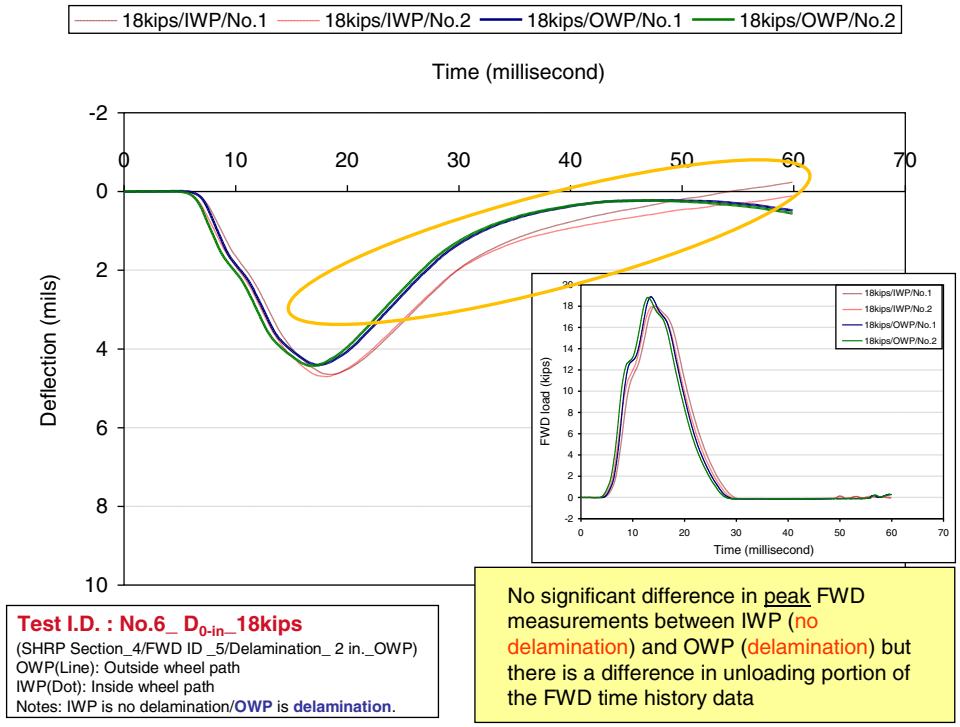

Figure 7.81. FWD deflection ($D_{0\text{-}in}$) time history under 18-kips loading for FWD Test 6 at NCAT Section 4.

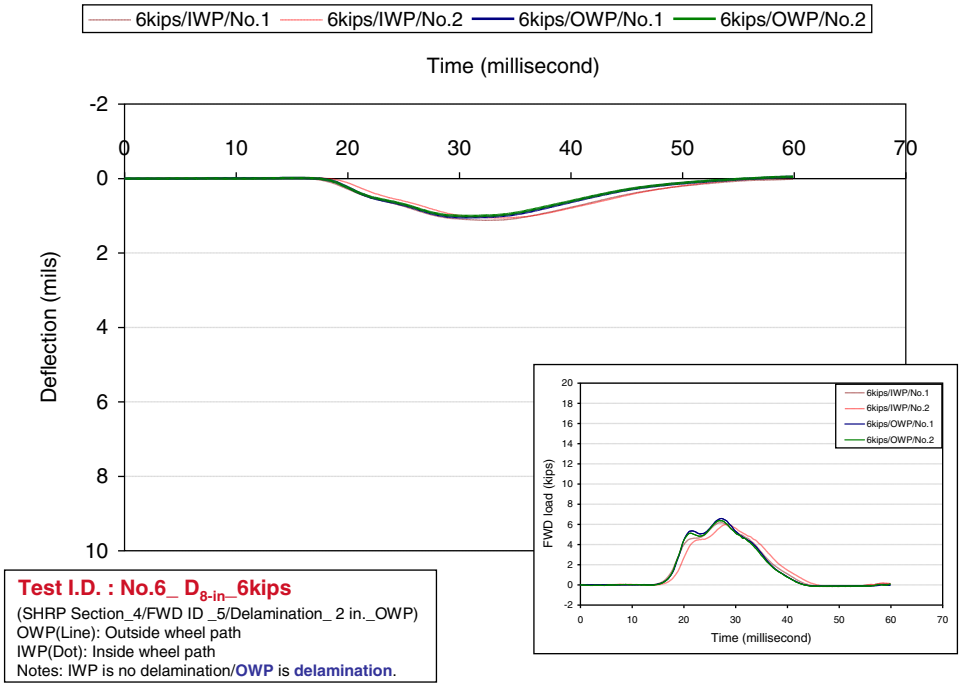

Figure 7.82. FWD deflection ($D_{8\text{-}in}$) time history under 6-kips loading for FWD Test 6 at NCAT Section 4.

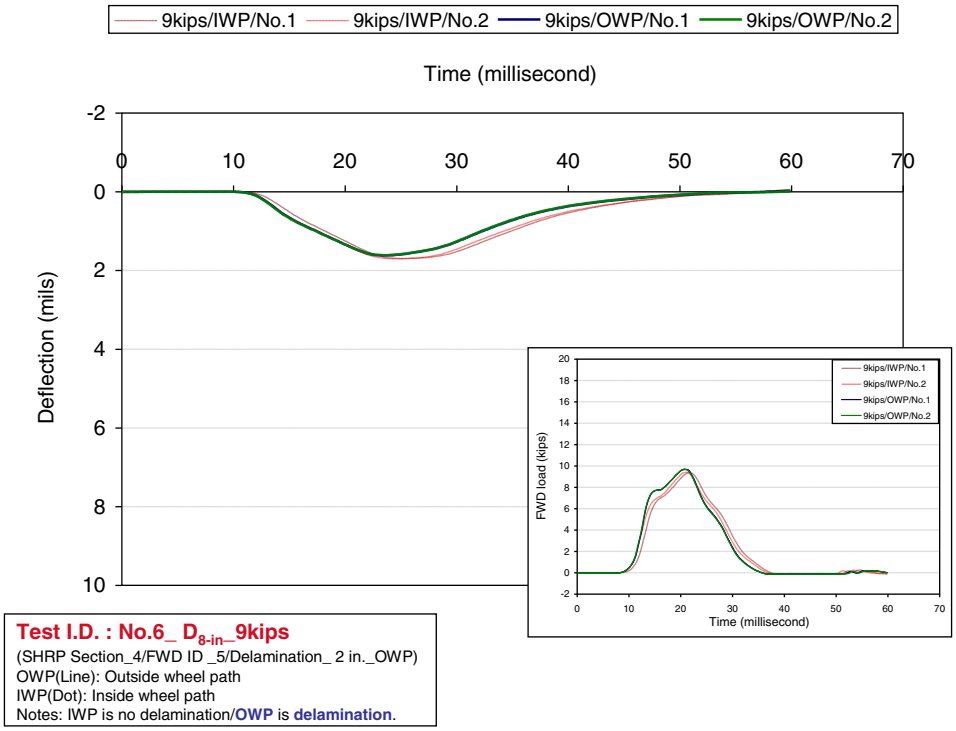

Figure 7.83. FWD deflection ($D_{8\text{-}in}$) time history under 9-kips loading for FWD Test 6 at NCAT Section 4.

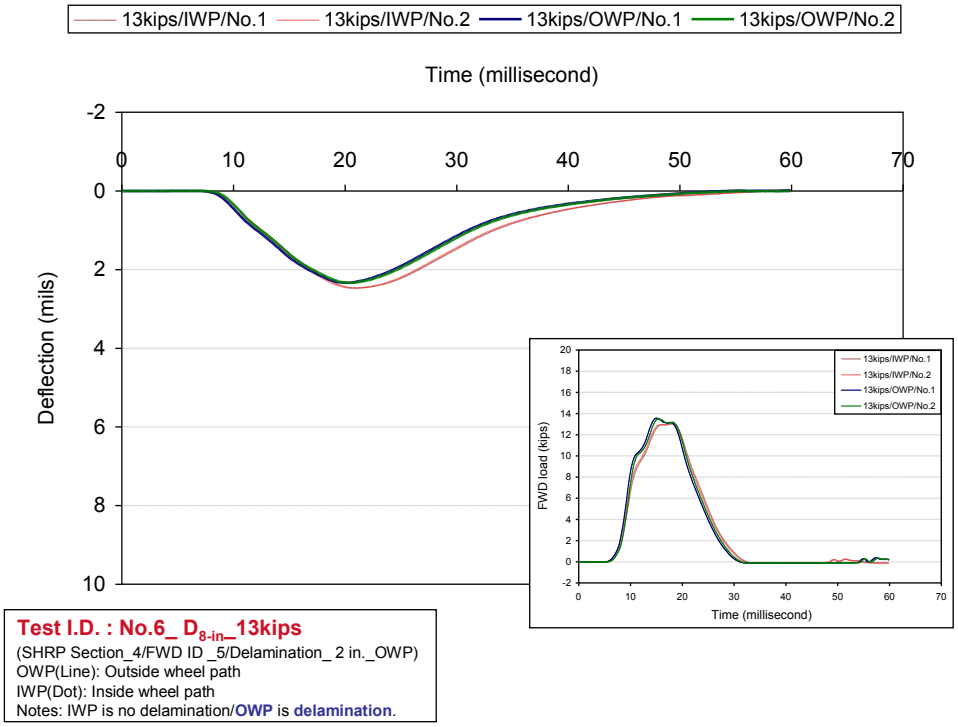

Figure 7.84. FWD deflection ($D_{8\text{-}in}$) time history under 13-kips loading for FWD Test 6 at NCAT Section 4.

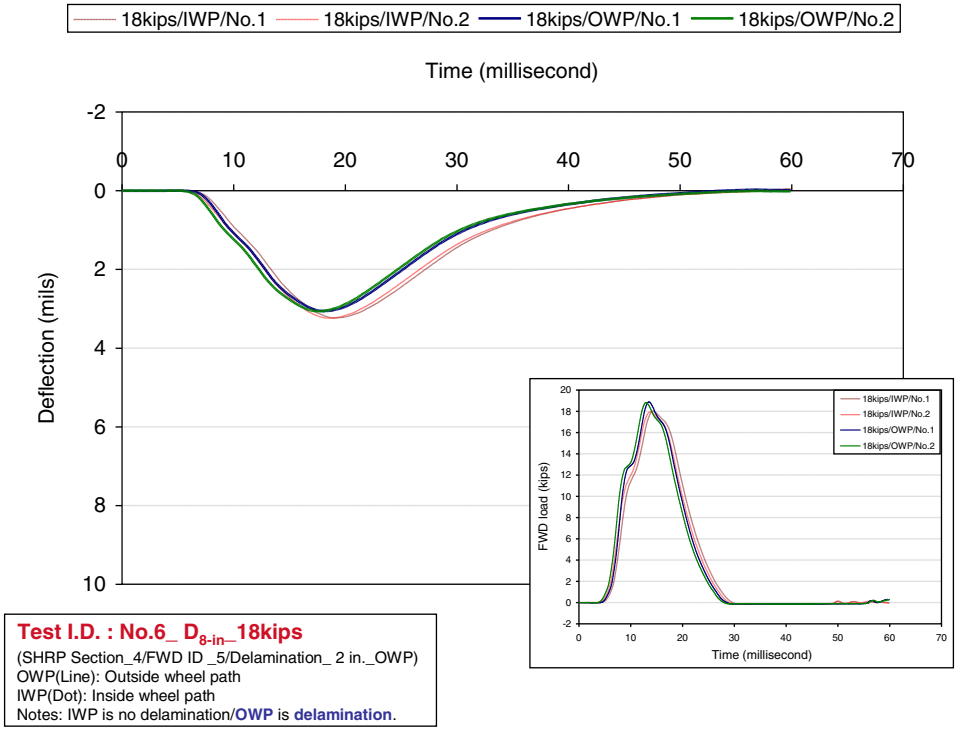

Figure 7.85. FWD deflection ($D_{8\text{-}in}$) time history under 18-kips loading for FWD Test 6 at NCAT Section 4.

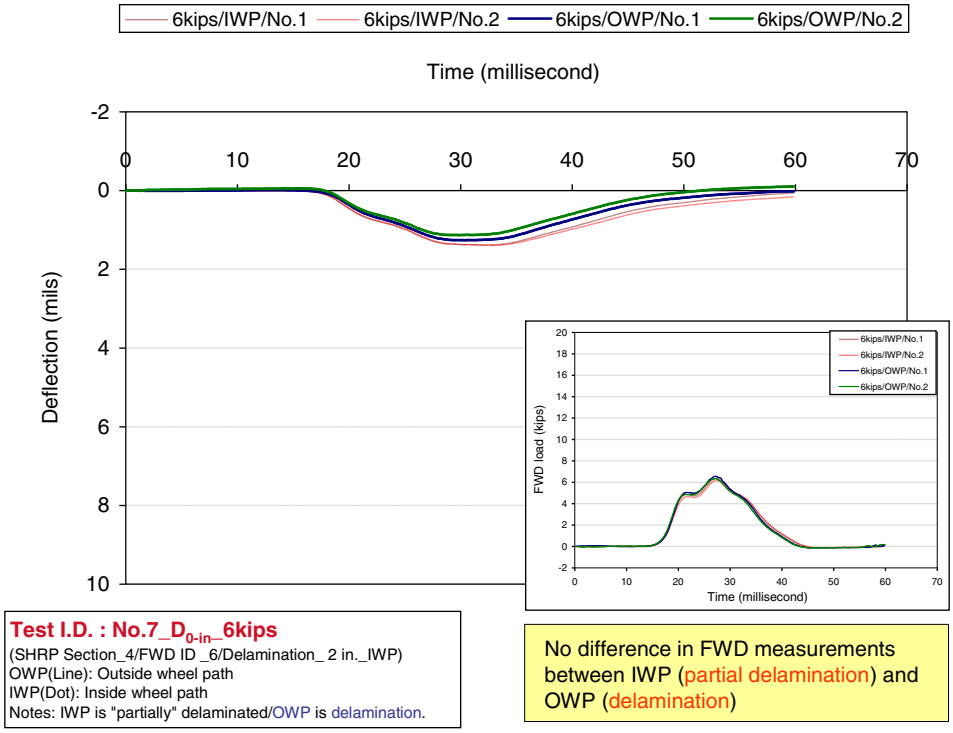

Figure 7.86. FWD deflection ($D_{0\text{-}in}$) time history under 6-kips loading for FWD Test 7 at NCAT Section 4.

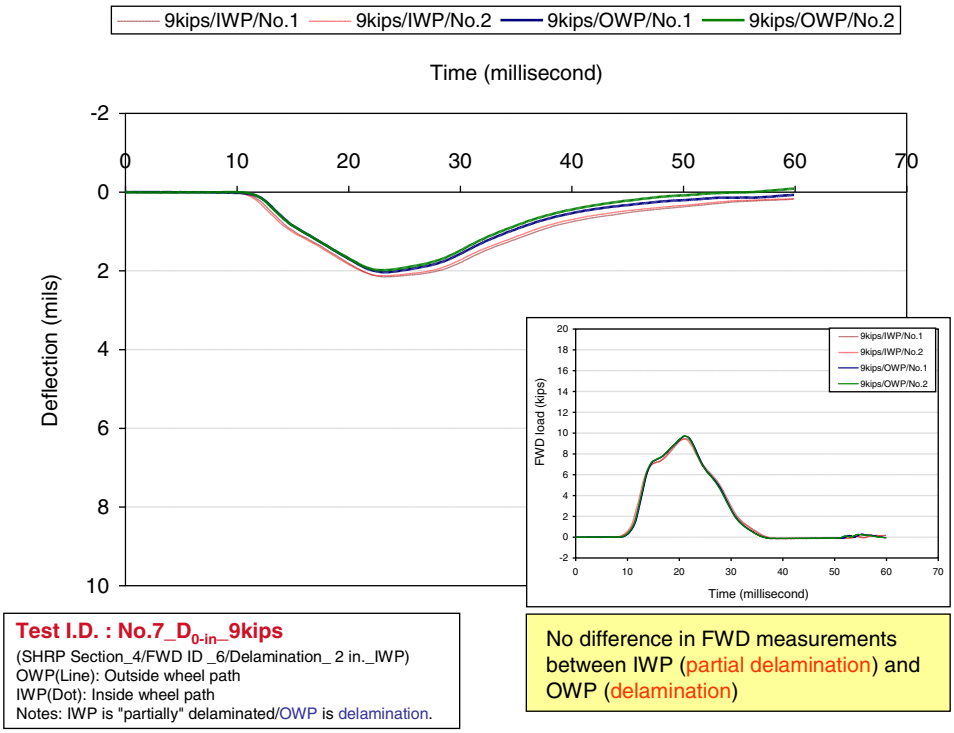

Figure 7.87. FWD deflection ($D_{0\text{-}in}$) time history under 9-kips loading for FWD Test 7 at NCAT Section 4.

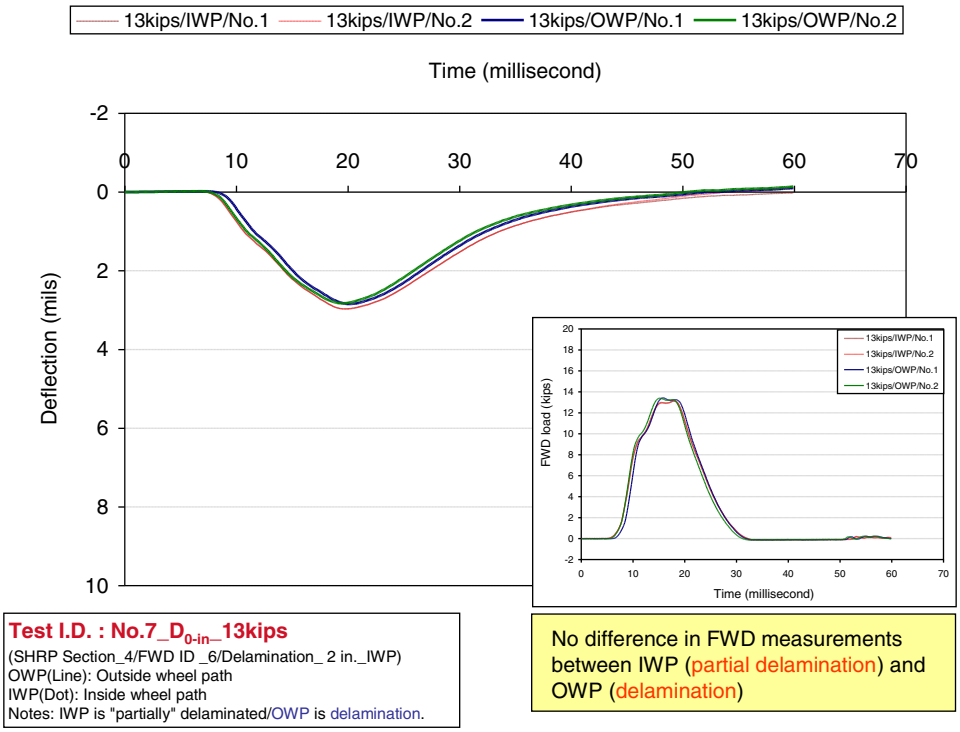

Figure 7.88. FWD deflection ($D_{0\text{-}in}$) time history under 13-kips loading for FWD Test 7 at NCAT Section 4.

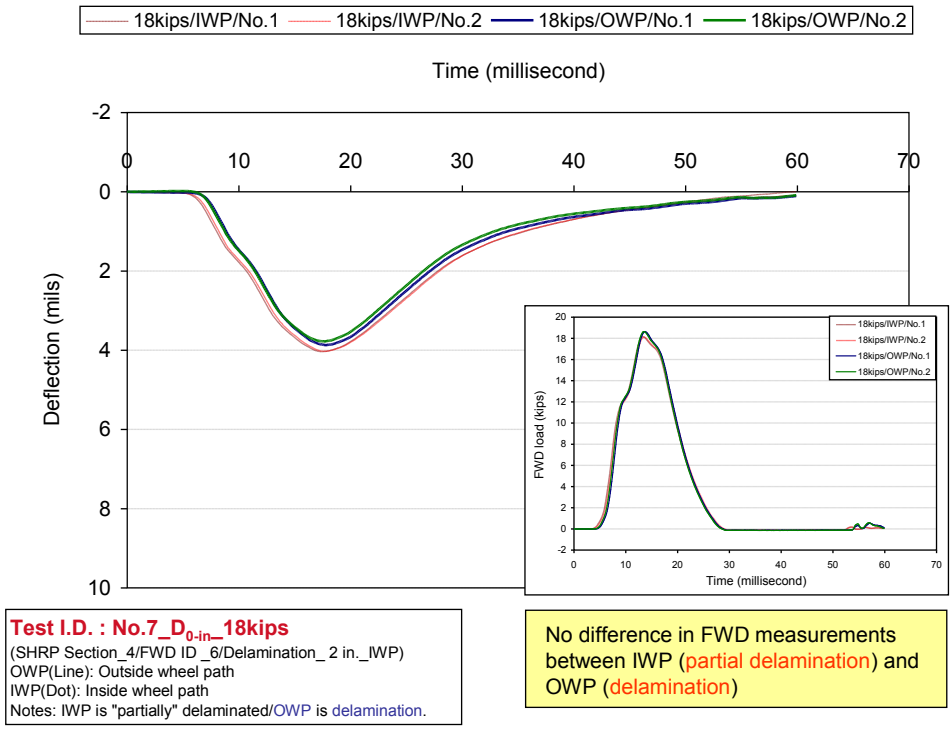

Figure 7.89. FWD deflection ($D_{0\text{-}in}$) time history under 18-kips loading for FWD Test 7 at NCAT Section 4.

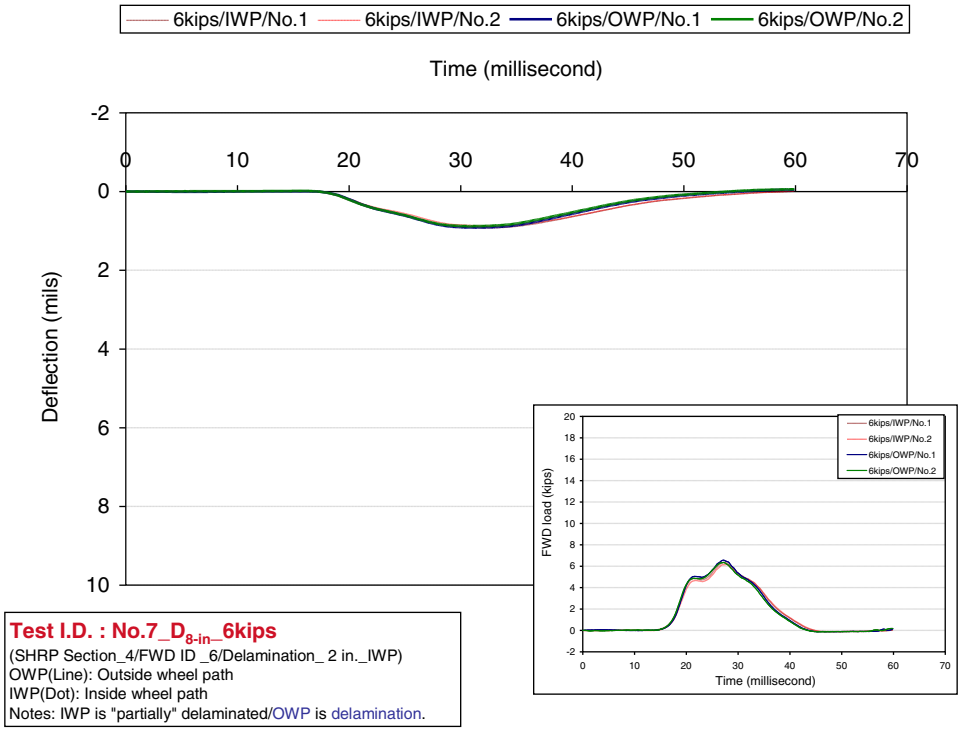

Figure 7.90. FWD deflection ($D_{8\text{-}in}$) time history under 6-kips loading for FWD Test 7 at NCAT Section 4.

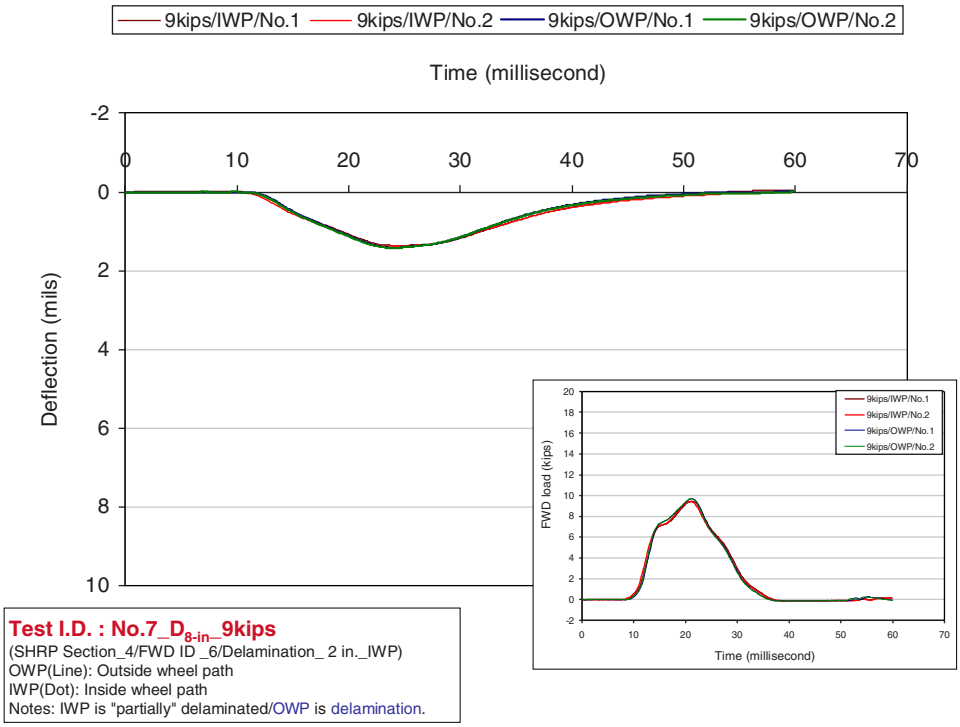

Figure 7.91. FWD deflection ($D_{8\text{-}in}$) time history under 9-kips loading for FWD Test 7 at NCAT Section 4.

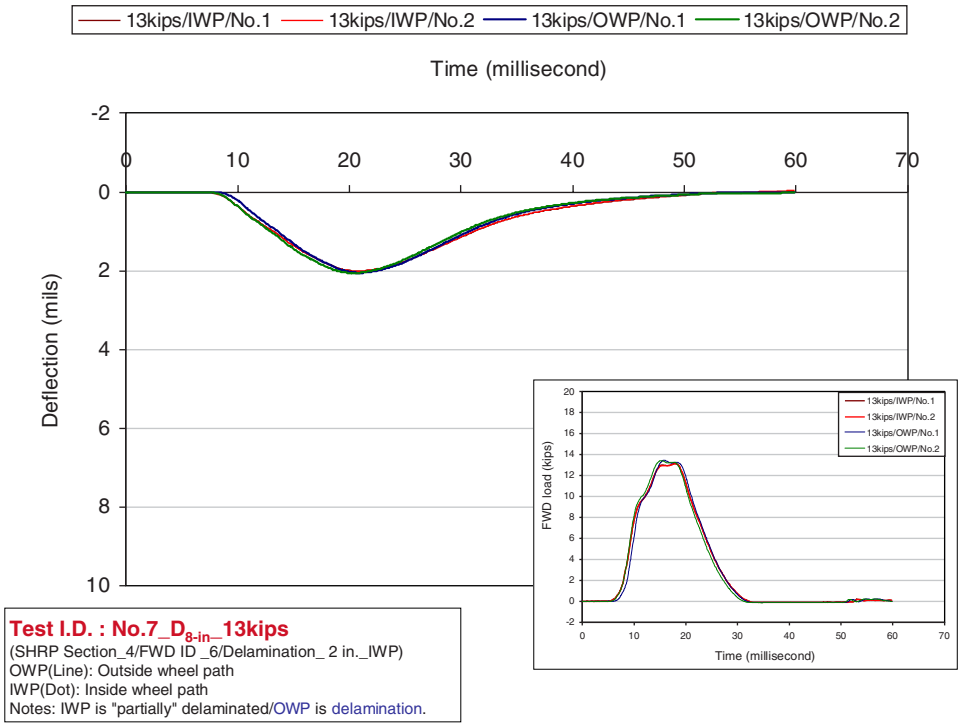

Figure 7.92. FWD deflection ($D_{8\text{-}in}$) time history under 13-kips loading for FWD Test 7 at NCAT Section 4.

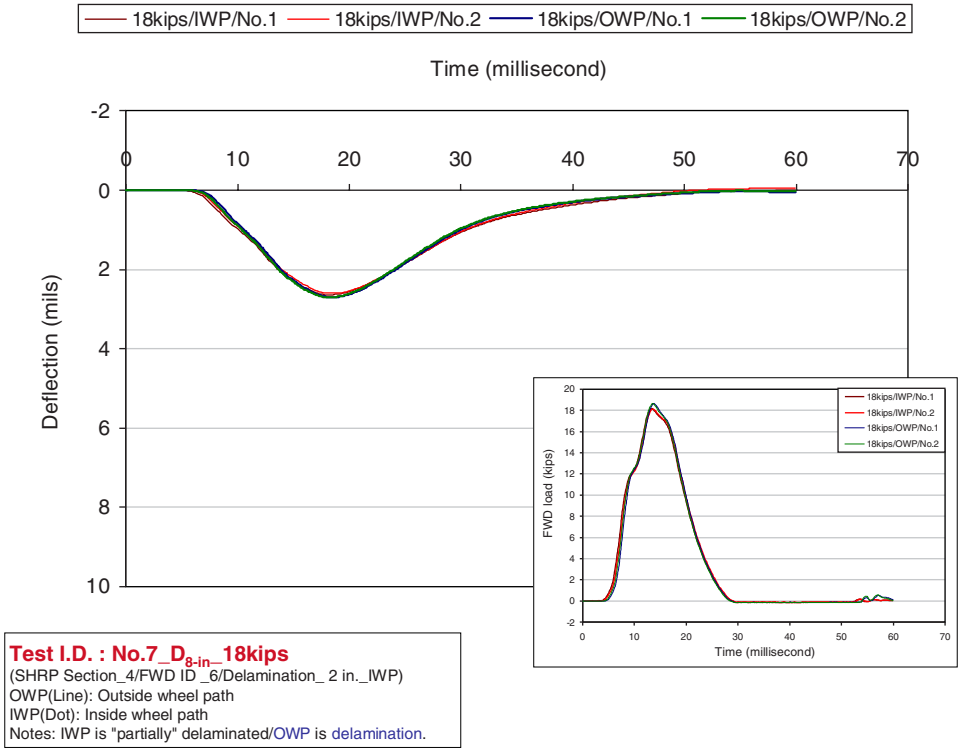

Figure 7.93. FWD deflection ($D_{8\text{-}in}$) time history under 18-kips loading for FWD Test 7 at NCAT Section 4.

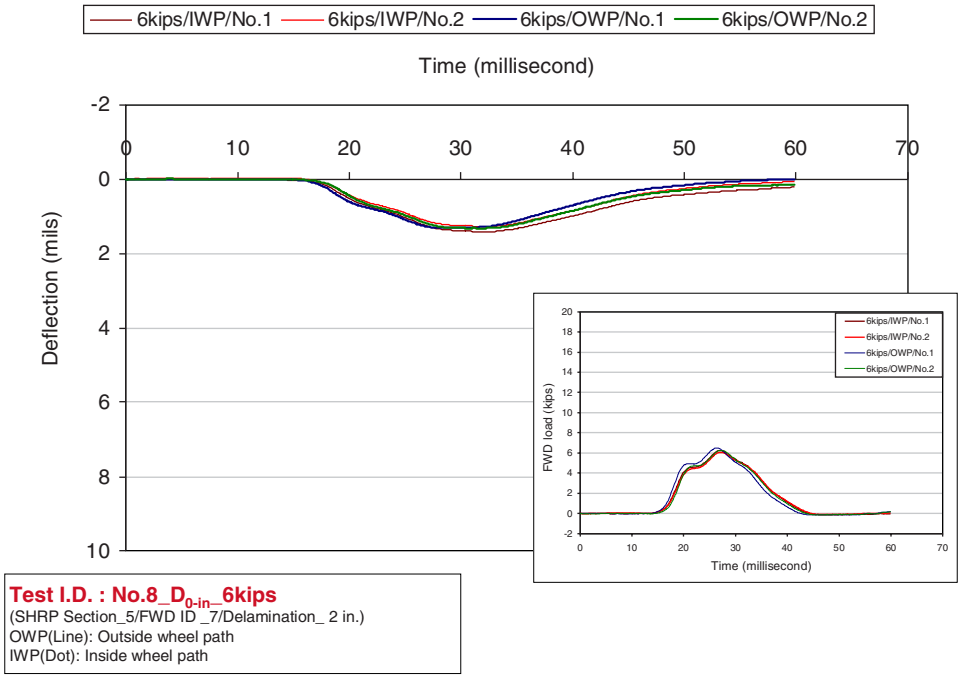

Figure 7.94. FWD deflection ($D_{0\text{-}in}$) time history under 6-kips loading for FWD Test 8 at NCAT Section 5.

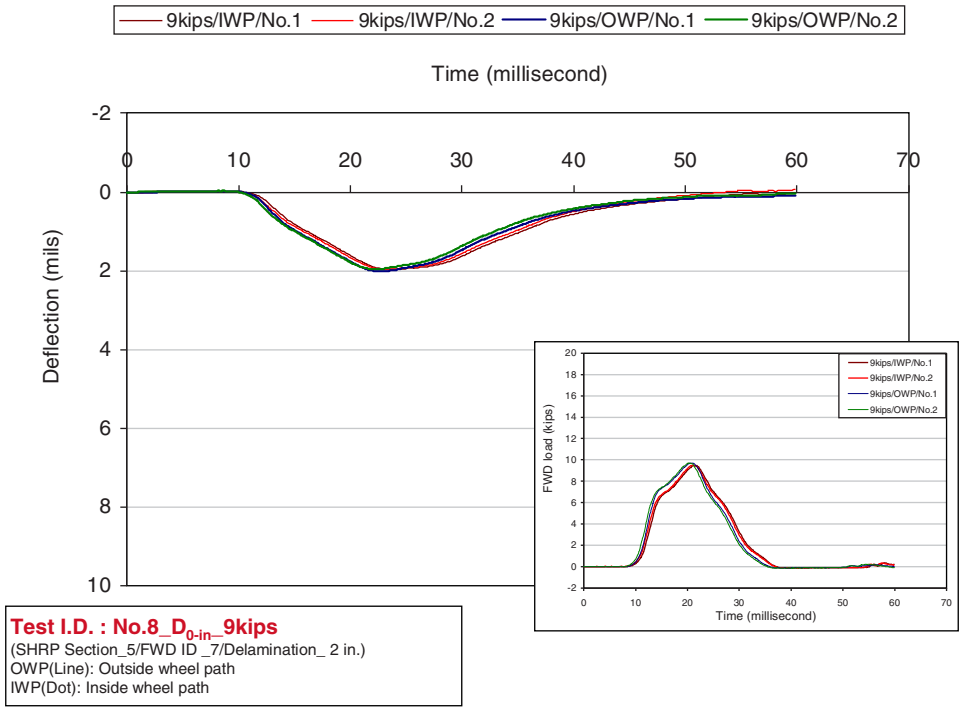

Figure 7.95. FWD deflection ($D_{0\text{-}in}$) time history under 9-kips loading for FWD Test 8 at NCAT Section 5.

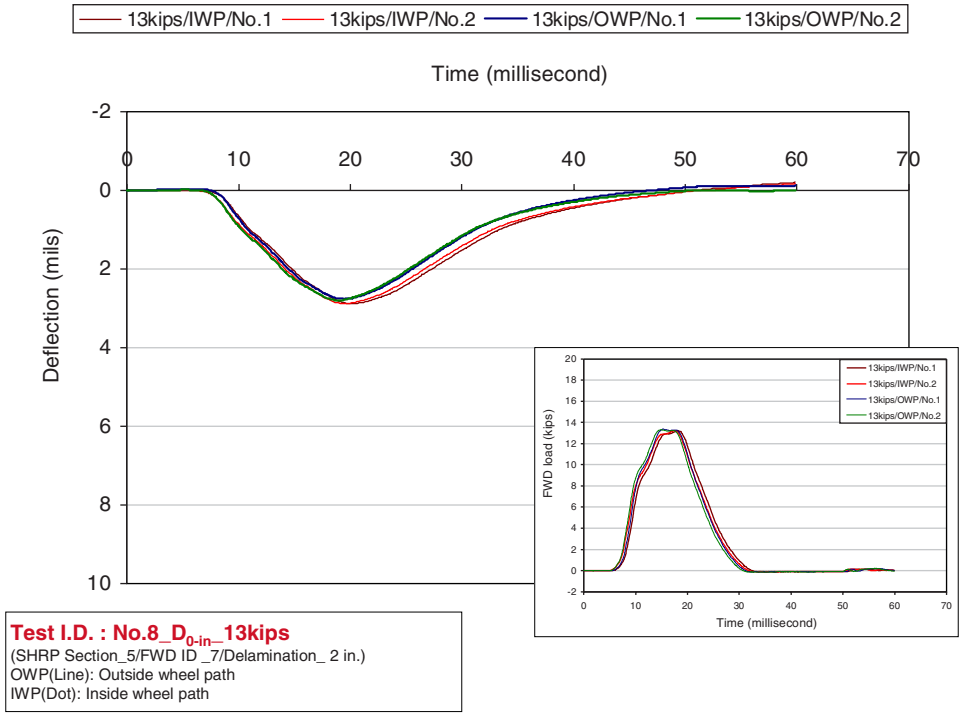

Figure 7.96. FWD deflection ($D_{0\text{-}in}$) time history under 13-kips loading for FWD Test 8 at NCAT Section 5.

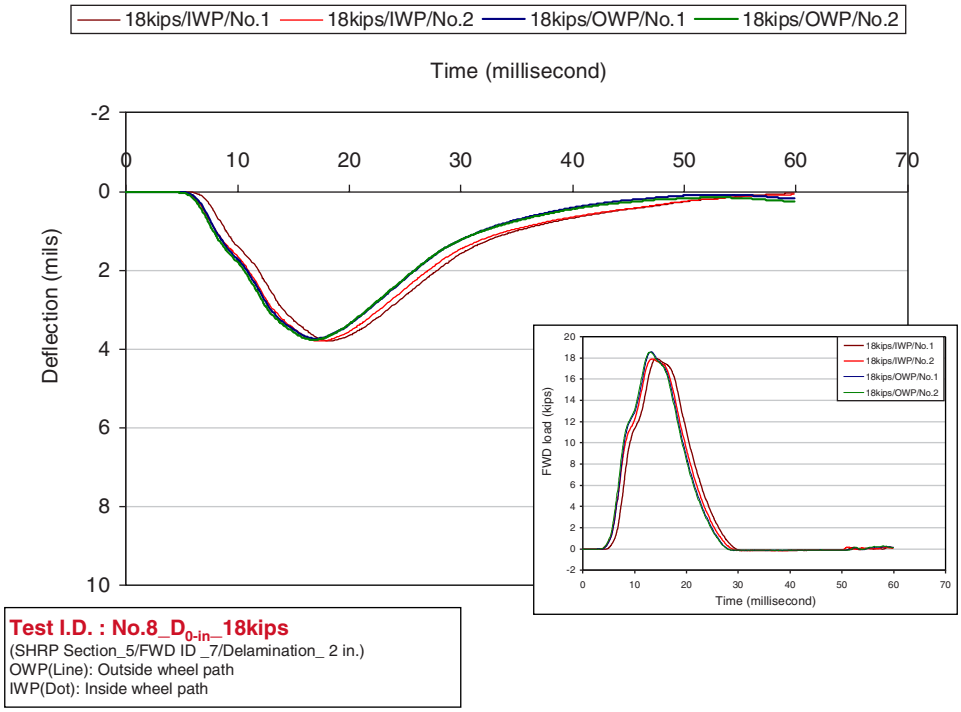

Figure 7.97. FWD deflection ($D_{0\text{-}in}$) time history under 18-kips loading for FWD Test 8 at NCAT Section 5.

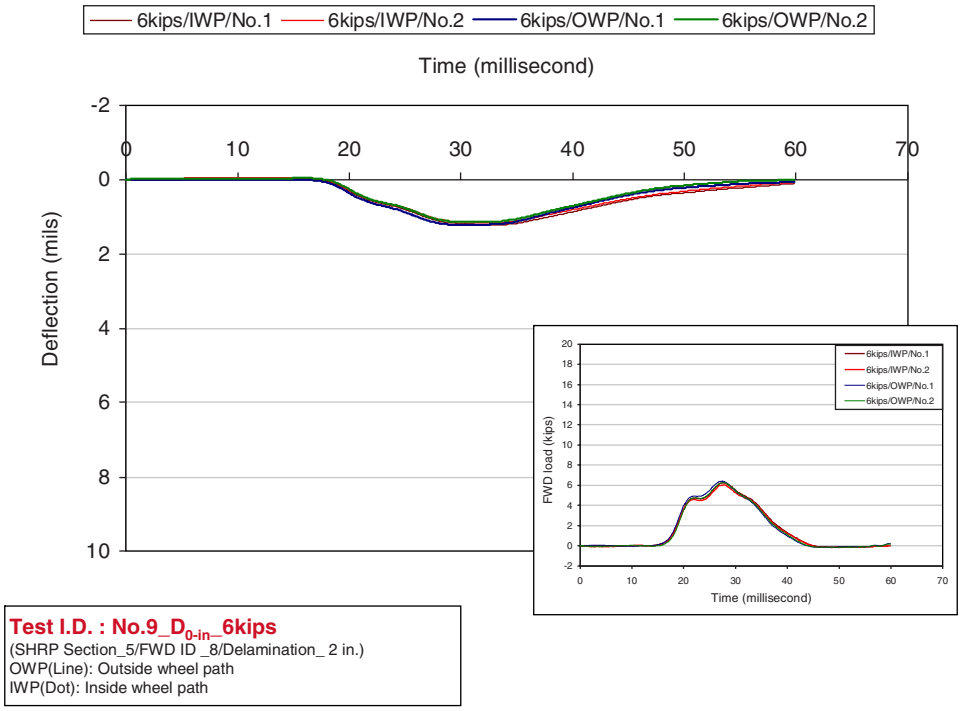

Figure 7.98. FWD deflection ($D_{0\text{-}in}$) time history under 6-kips loading for FWD Test 9 at NCAT Section 5.

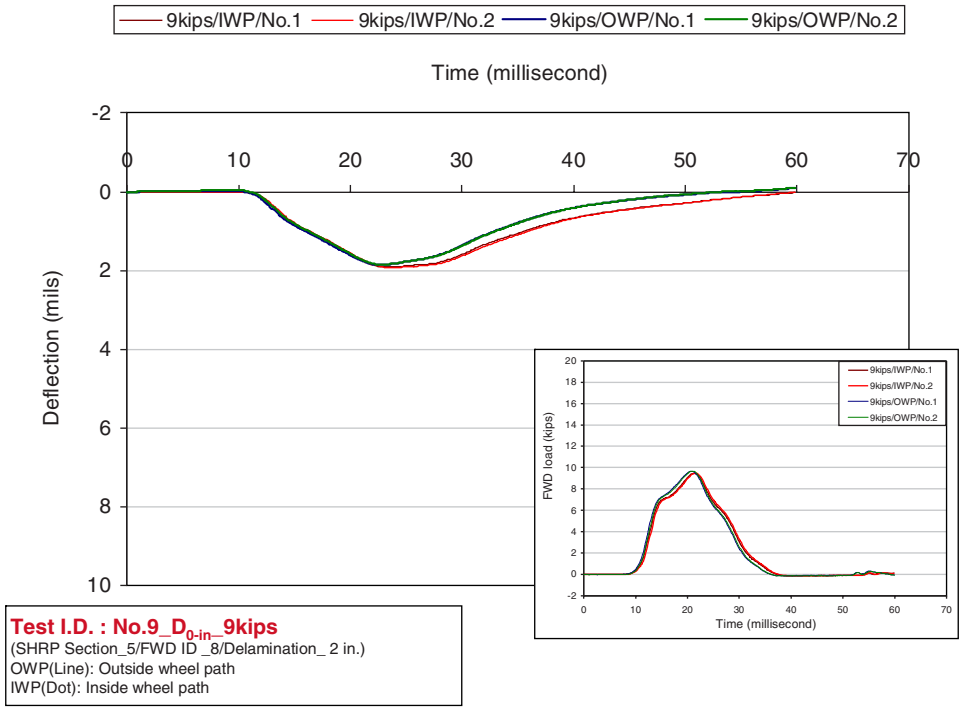

Figure 7.99. FWD deflection ($D_{0\text{-}in}$) time history under 9-kips loading for FWD Test 9 at NCAT Section 5.

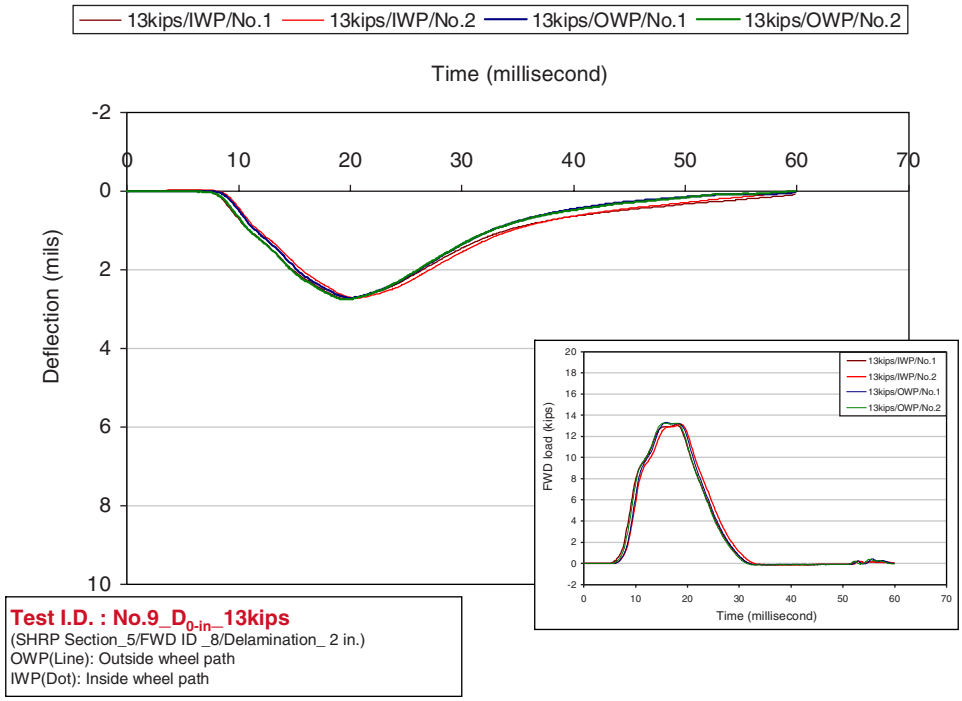

Figure 7.100. FWD deflection ($D_{0\text{-}in}$) time history under 13-kips loading for FWD Test 9 at NCAT Section 5.

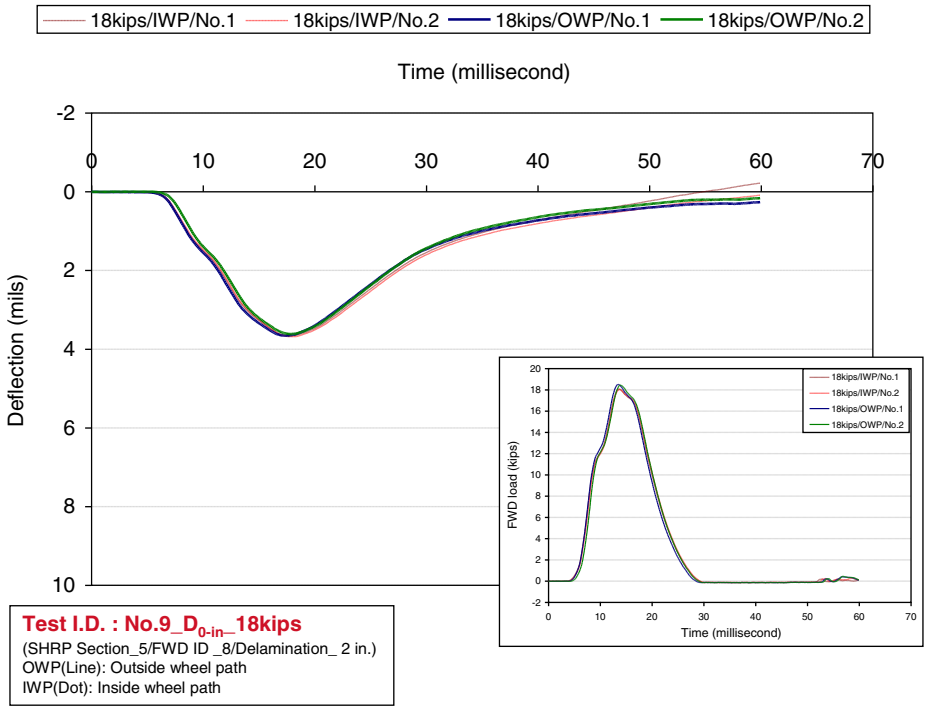

Figure 7.101. FWD deflection ($D_{0\text{-}in}$) time history under 18-kips loading for FWD Test 9 at NCAT Section 5.

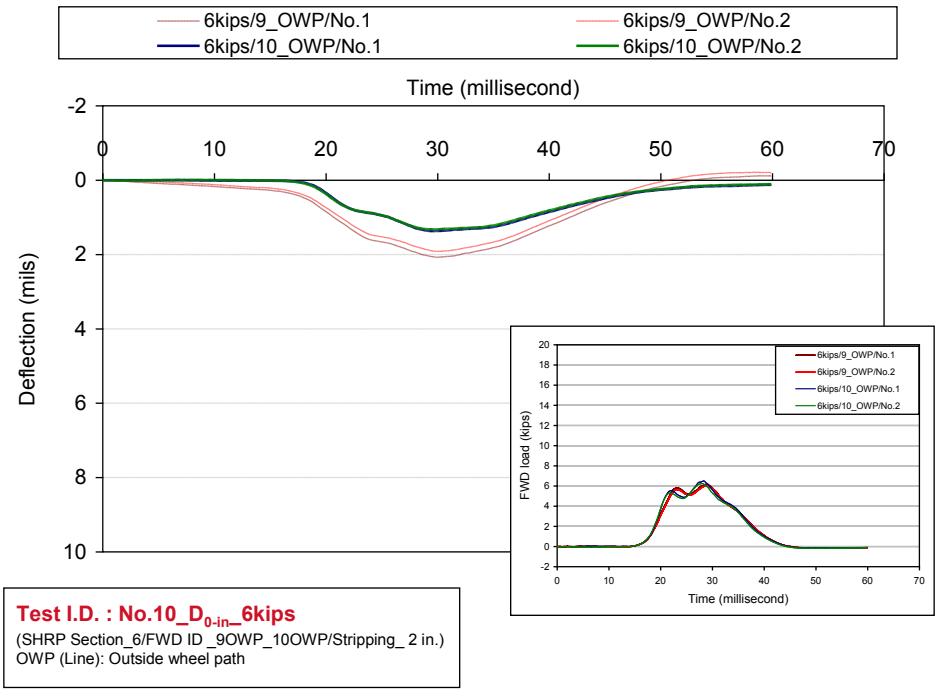

Figure 7.102. FWD deflection ($D_{0\text{-}in}$) time history under 6-kips loading for FWD Test 10 at NCAT Section 6.

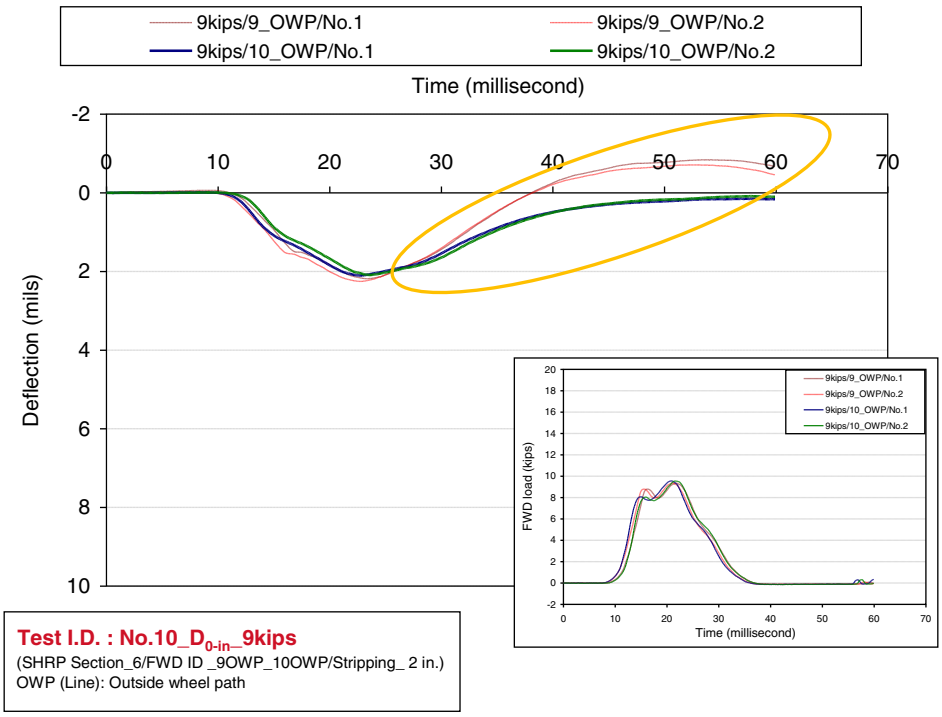

Figure 7.103. FWD deflection ($D_{0\text{-}in}$) time history under 9-kips loading for FWD Test 10 at NCAT Section 6.

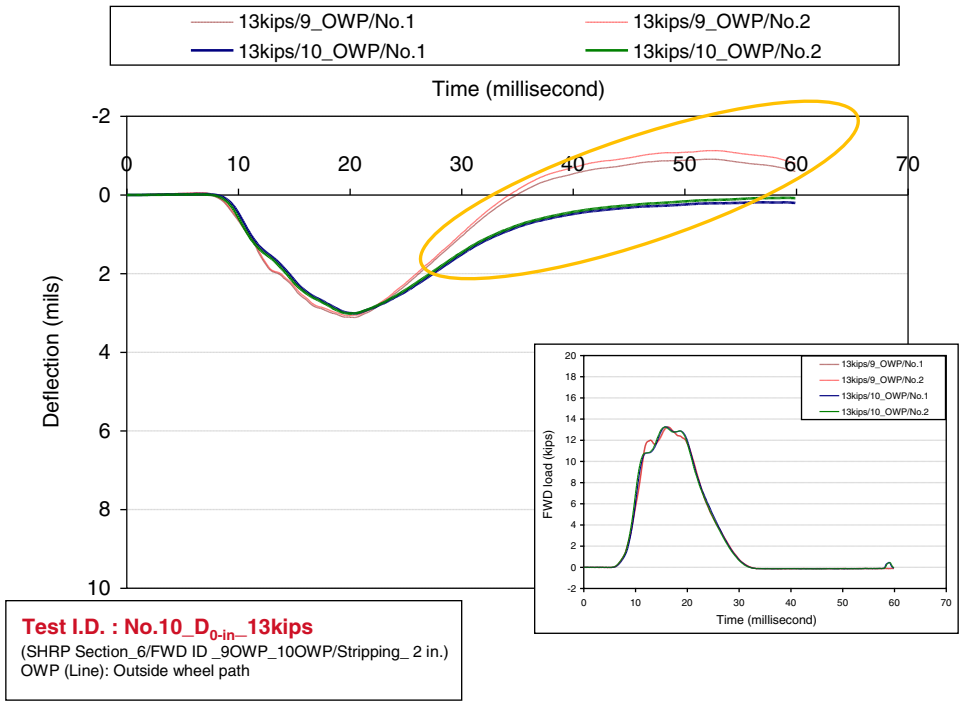

Figure 7.104. FWD deflection ($D_{0\text{-}in}$) time history under 13-kips loading for FWD Test 10 at NCAT Section 6.

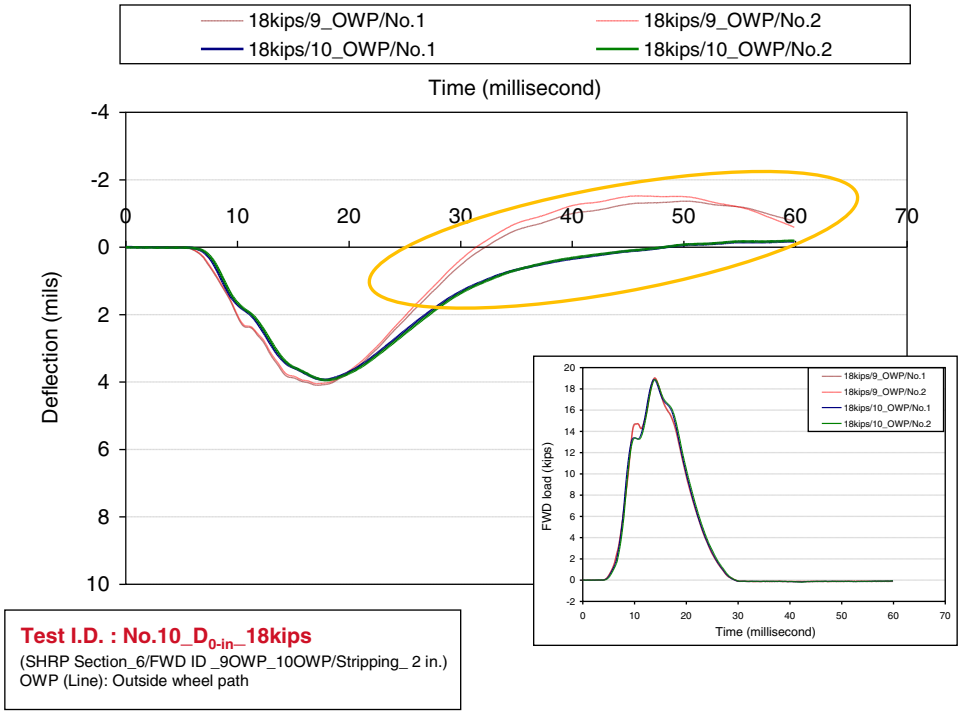

Figure 7.105. FWD deflection ($D_{0\text{-}in}$) time history under 18-kips loading for FWD Test 10 at NCAT Section 6.

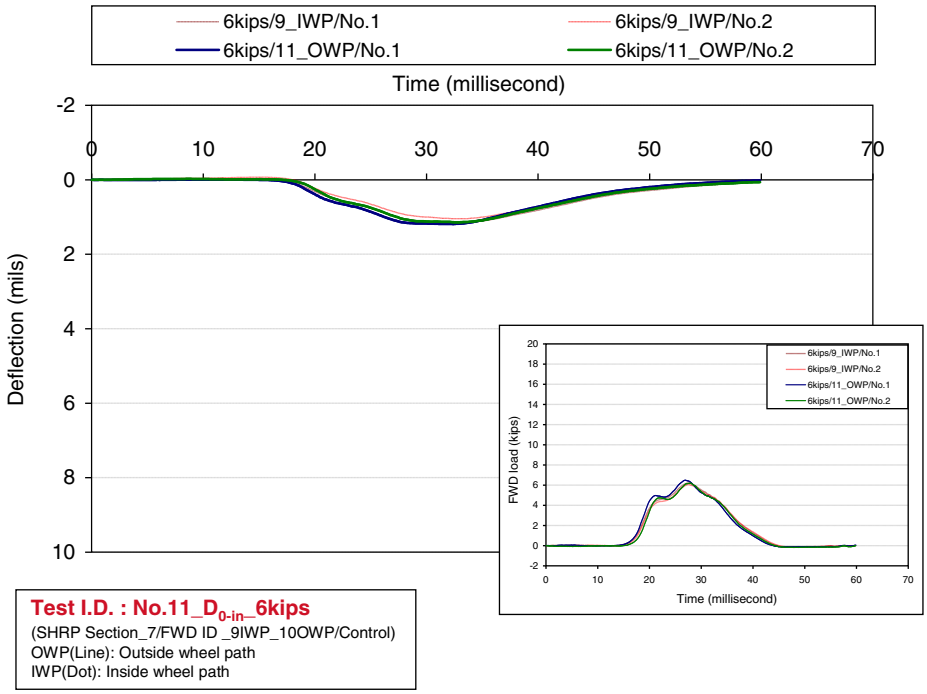

Figure 7.106. FWD deflection ($D_{0\text{-}in}$) time history under 6-kips loading for FWD Test 11 at NCAT Section 7.

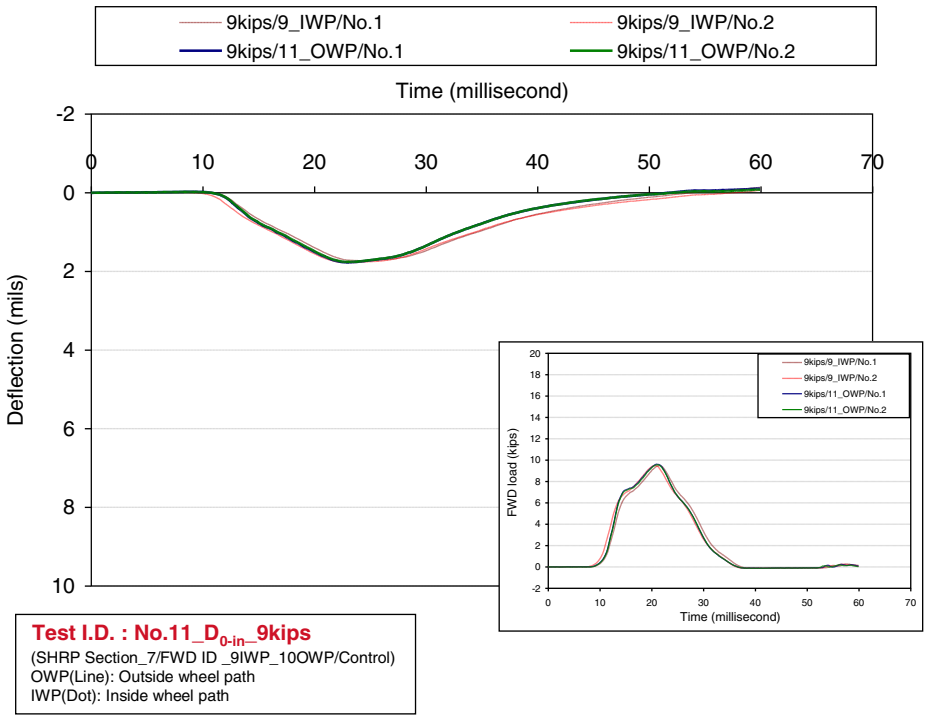

Figure 7.107. FWD deflection ($D_{0\text{-}in}$) time history under 9-kips loading for FWD Test 11 at NCAT Section 7.

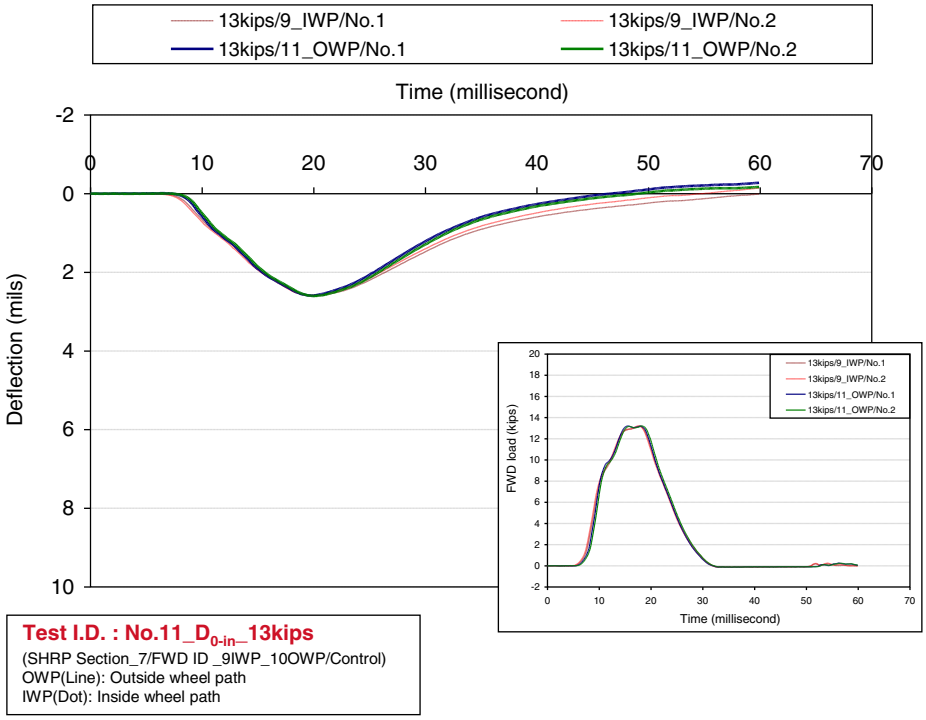

Figure 7.108. FWD deflection ($D_{0\text{-}in}$) time history under 13-kips loading for FWD Test 11 at NCAT Section 7.

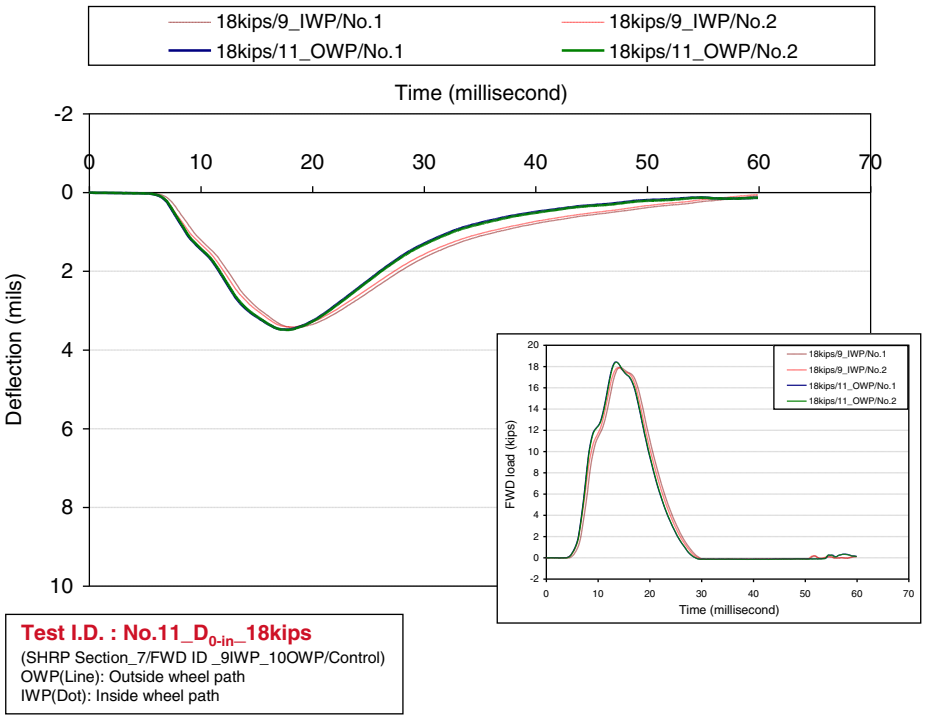

Figure 7.109. FWD deflection ($D_{0\text{-}in}$) time history under 18-kips loading for FWD Test 11 at NCAT Section 7.

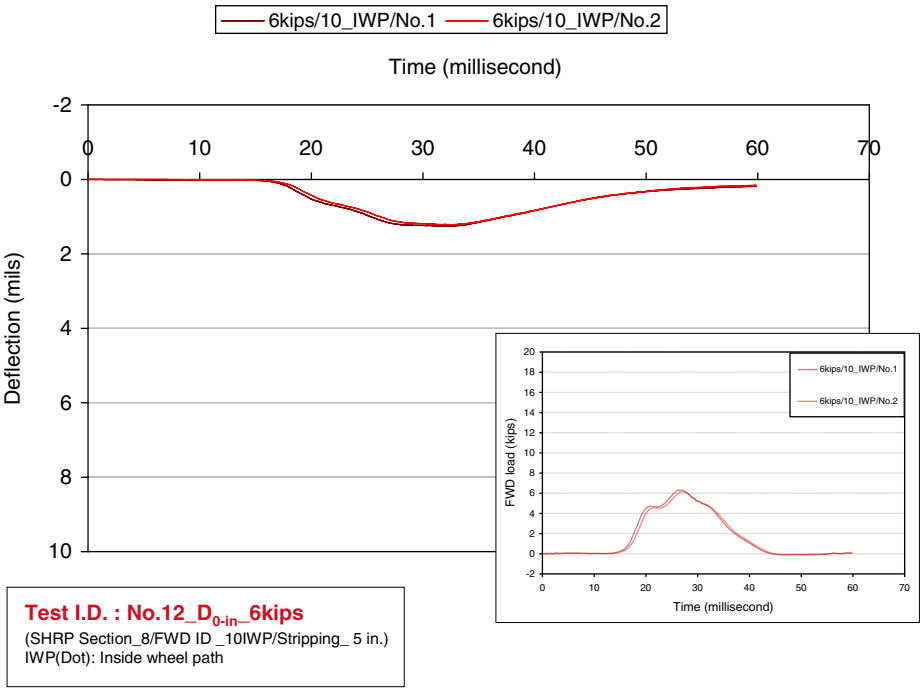

Figure 7.110. FWD deflection ($D_{0\text{-}in}$) time history under 6-kips loading for FWD Test 12 at NCAT Section 8.

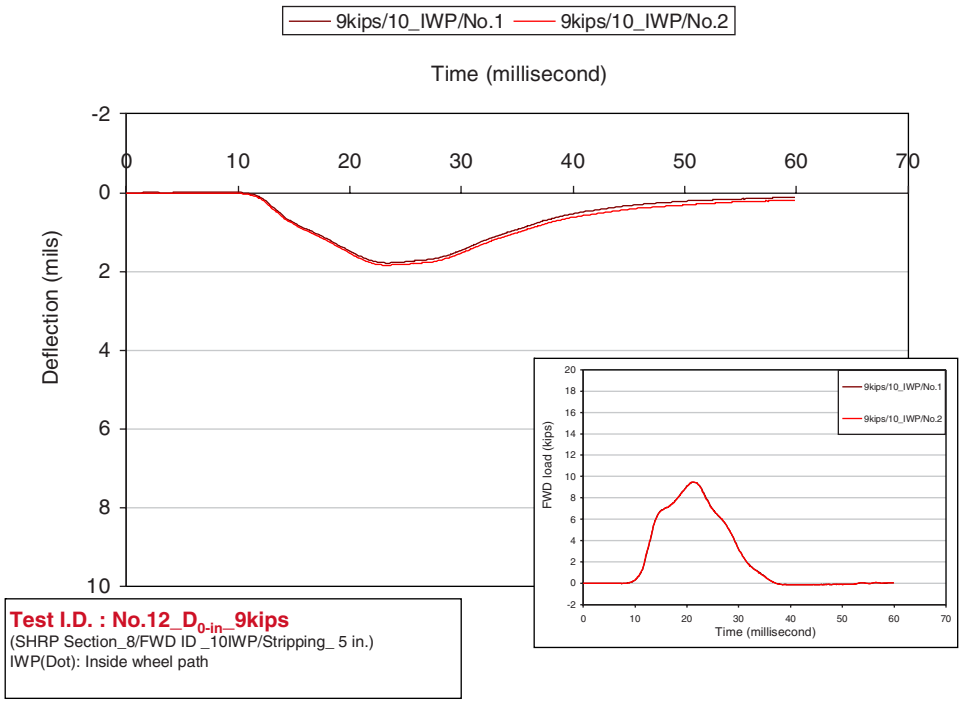

Figure 7.111. FWD deflection ($D_{0\text{-}in}$) time history under 9-kips loading for FWD Test 12 at NCAT Section 8.

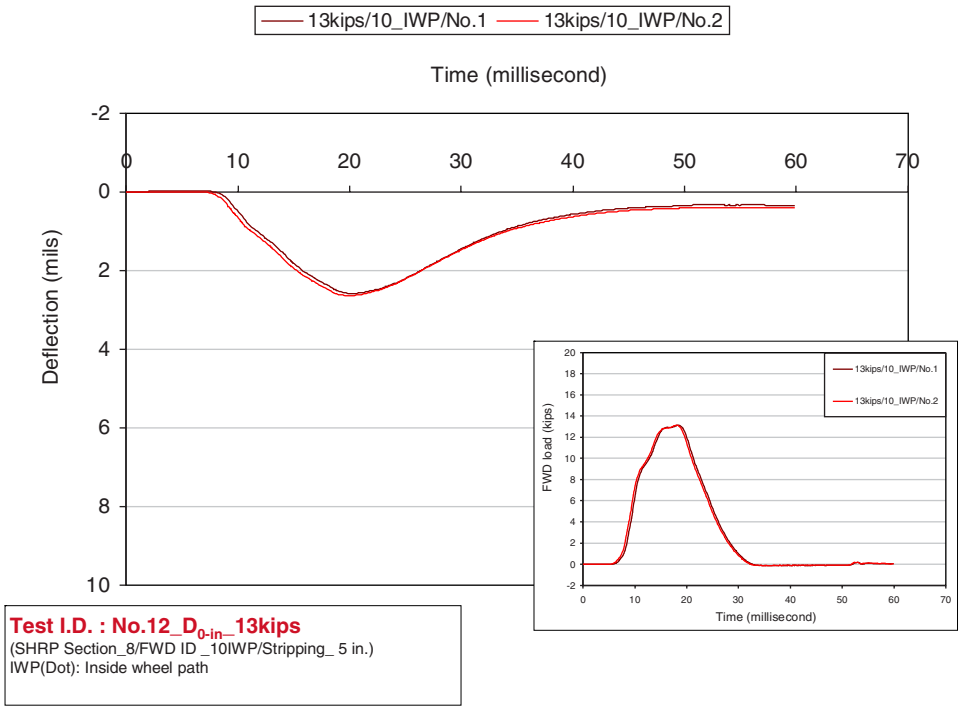

Figure 7.112. FWD deflection ($D_{0\text{-}in}$) time history under 13-kips loading for FWD Test 12 at NCAT Section 8.

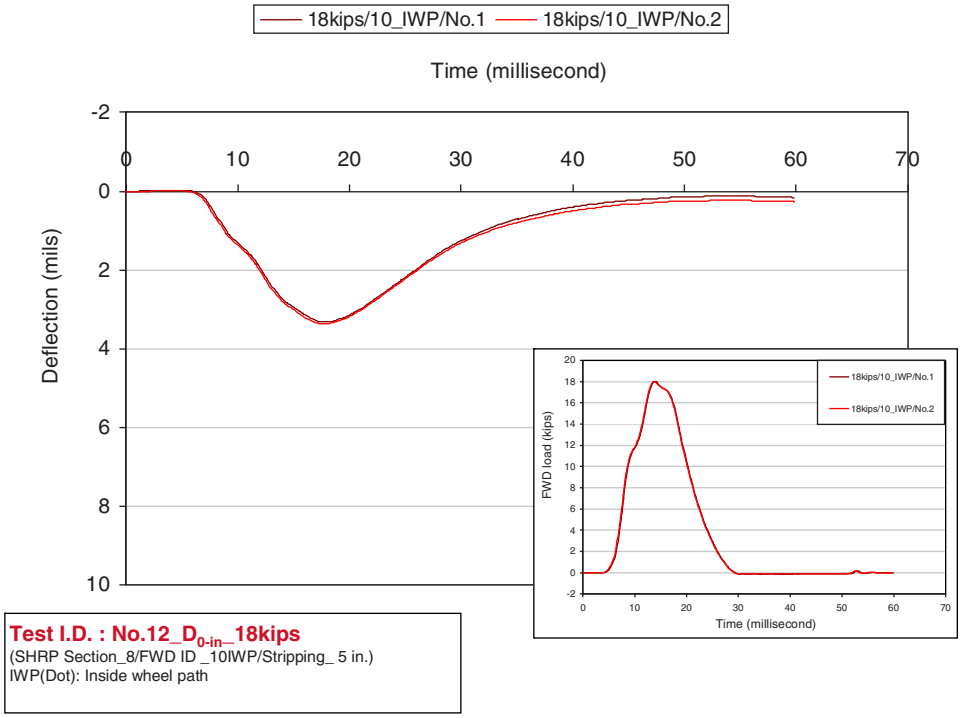

Figure 7.113. FWD deflection ($D_{0\text{-}in}$) time history under 18-kips loading for FWD Test 12 at NCAT Section 8.

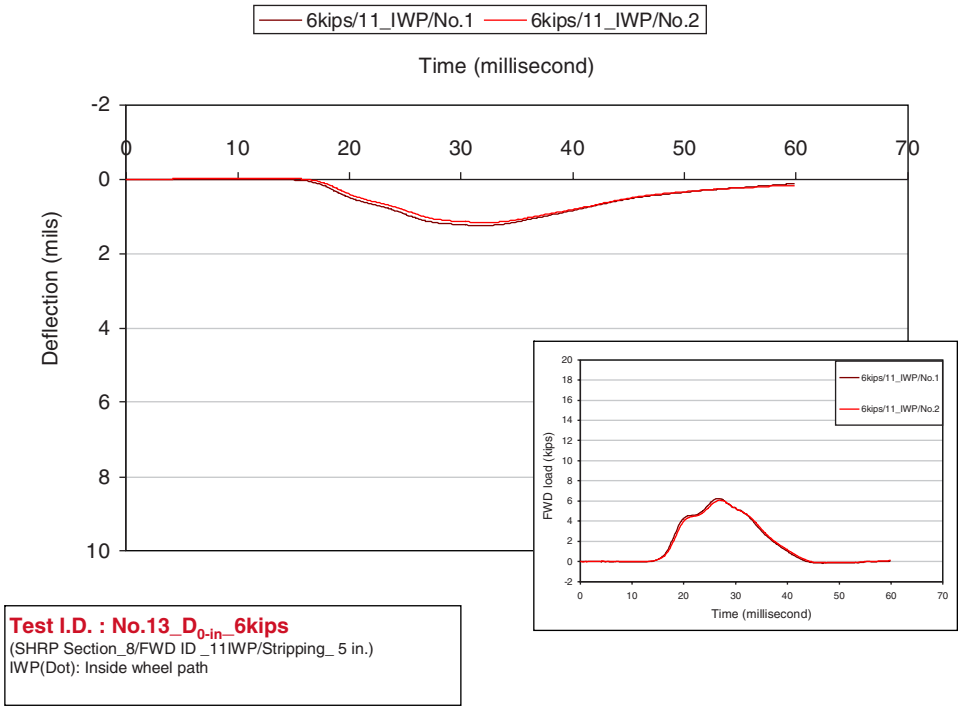

Figure 7.114. FWD deflection ($D_{0\text{-}in}$) time history under 6-kips loading for FWD Test 13 at NCAT Section 8.

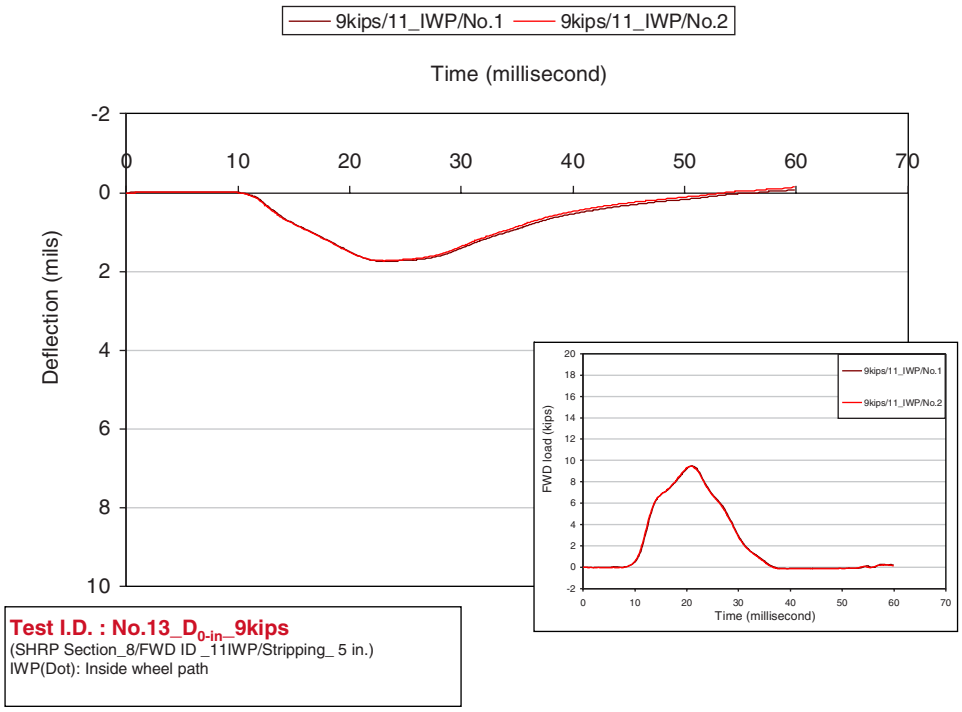

Figure 7.115. FWD deflection ($D_{0\text{-}in}$) time history under 9-kips loading for FWD Test 13 at NCAT Section 8.

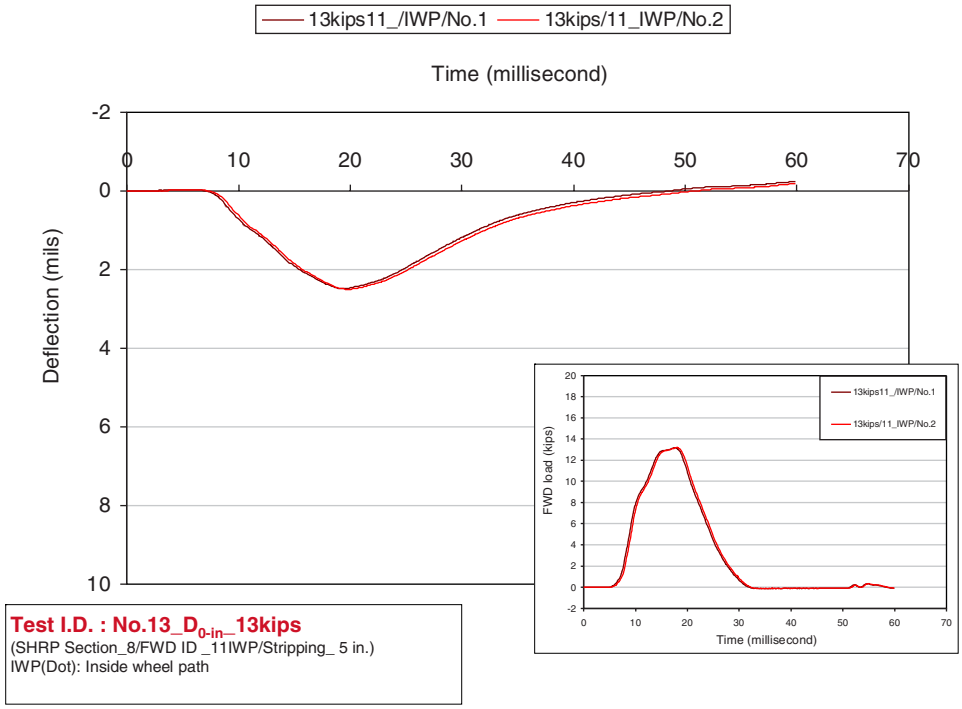

Figure 7.116. FWD deflection ($D_{0\text{-}in}$) time history under 13-kips loading for FWD Test 13 at NCAT Section 8.

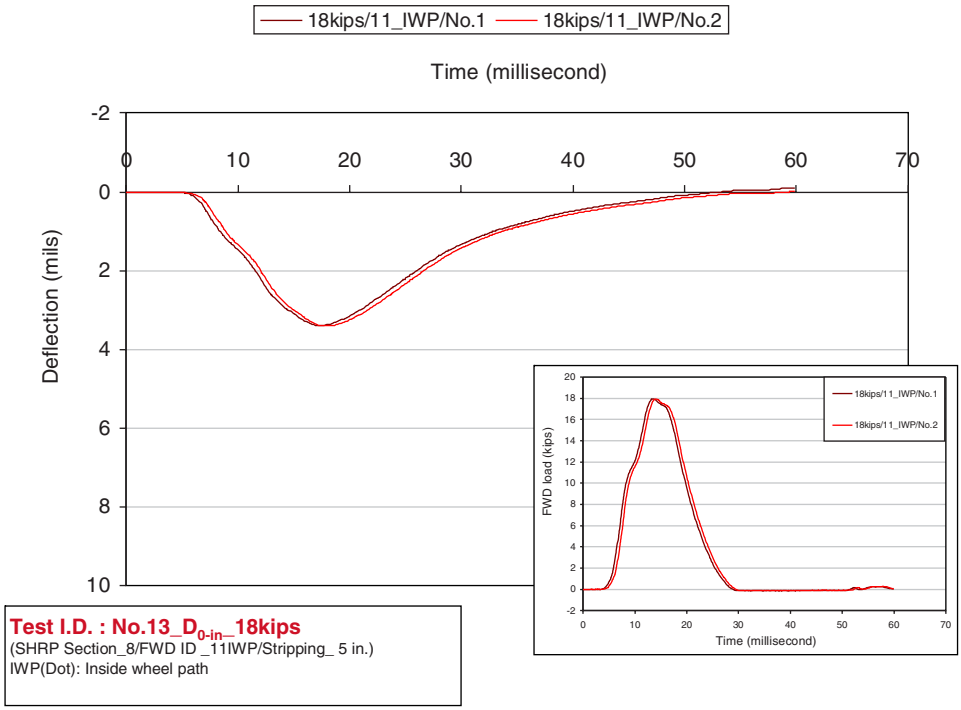

Figure 7.117. FWD deflection ($D_{0\text{-}in}$) time history under 18-kips loading for FWD Test 13 at NCAT Section 8.

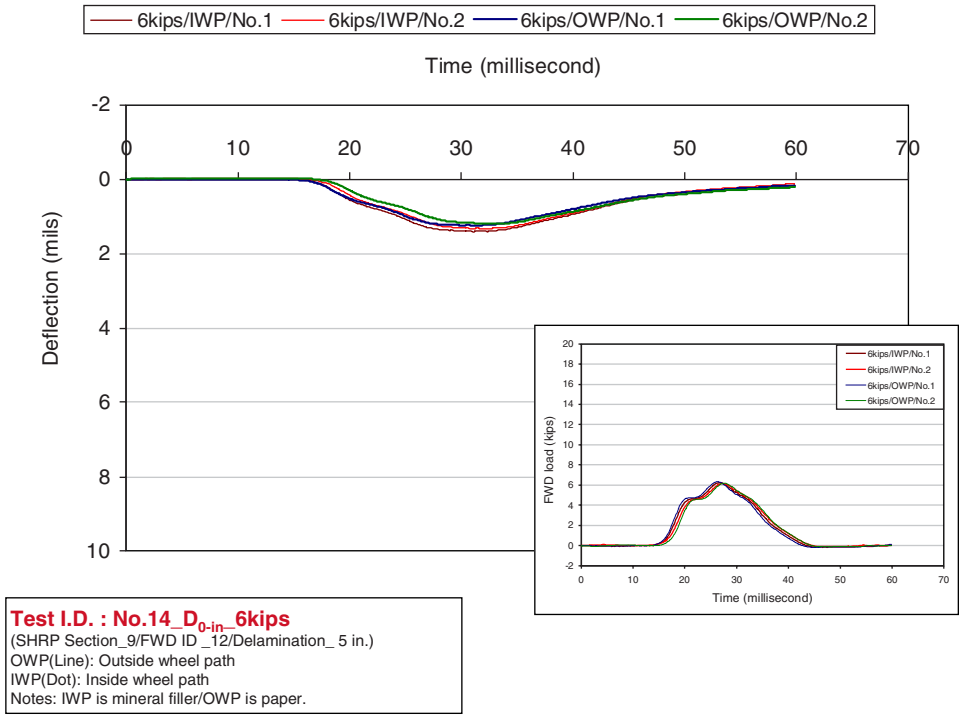

Figure 7.118. FWD deflection ($D_{0\text{-}in}$) time history under 6-kips loading for FWD Test 14 at NCAT Section 9.

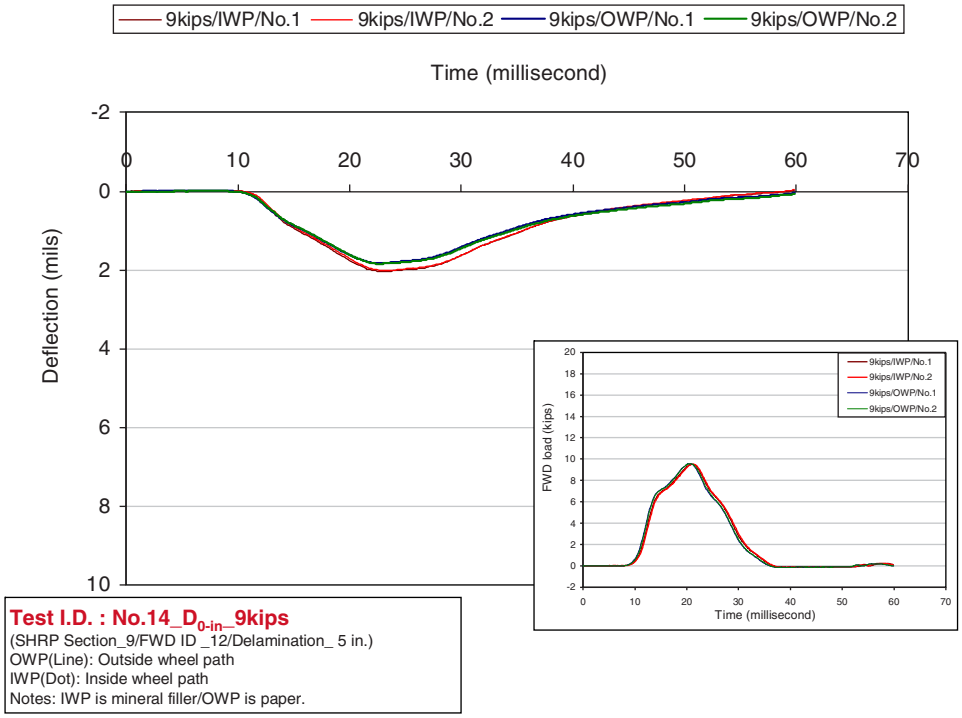

Figure 7.119. FWD deflection ($D_{0\text{-}in}$) time history under 9-kips loading for FWD Test 14 at NCAT Section 9.

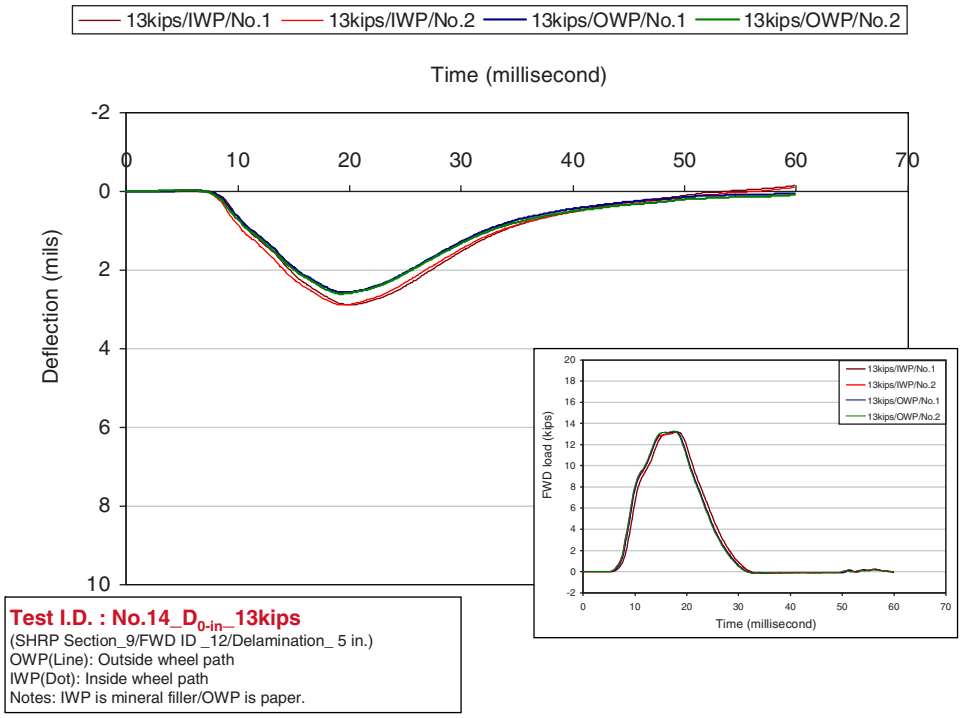

Figure 7.120. FWD deflection ($D_{0\text{-}in}$) time history under 13-kips loading for FWD Test 14 at NCAT Section 9.

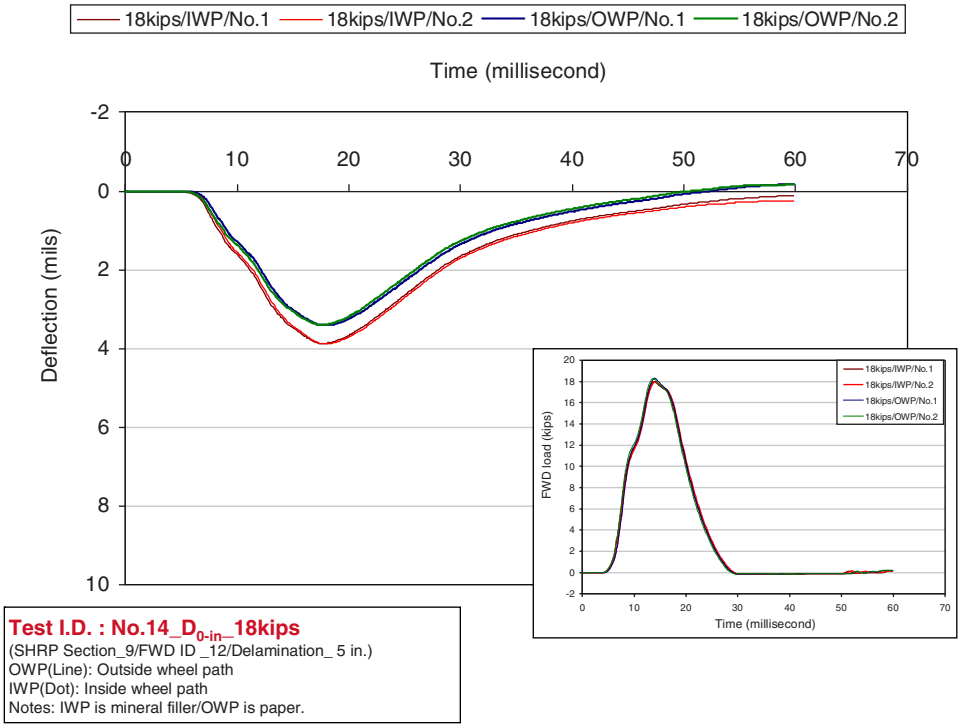

Figure 7.121. FWD deflection ($D_{0\text{-}in}$) time history under 18-kips loading for FWD Test 14 at NCAT Section 9.

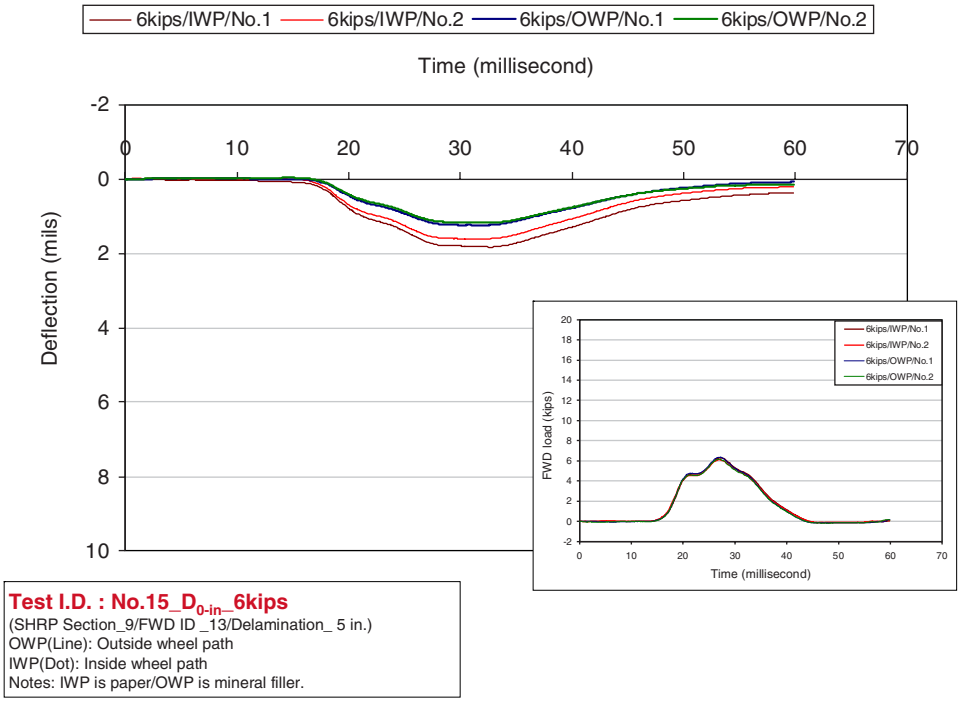

Figure 7.122. FWD deflection ($D_{0\text{-}in}$) time history under 6-kips loading for FWD Test 15 at NCAT Section 9.

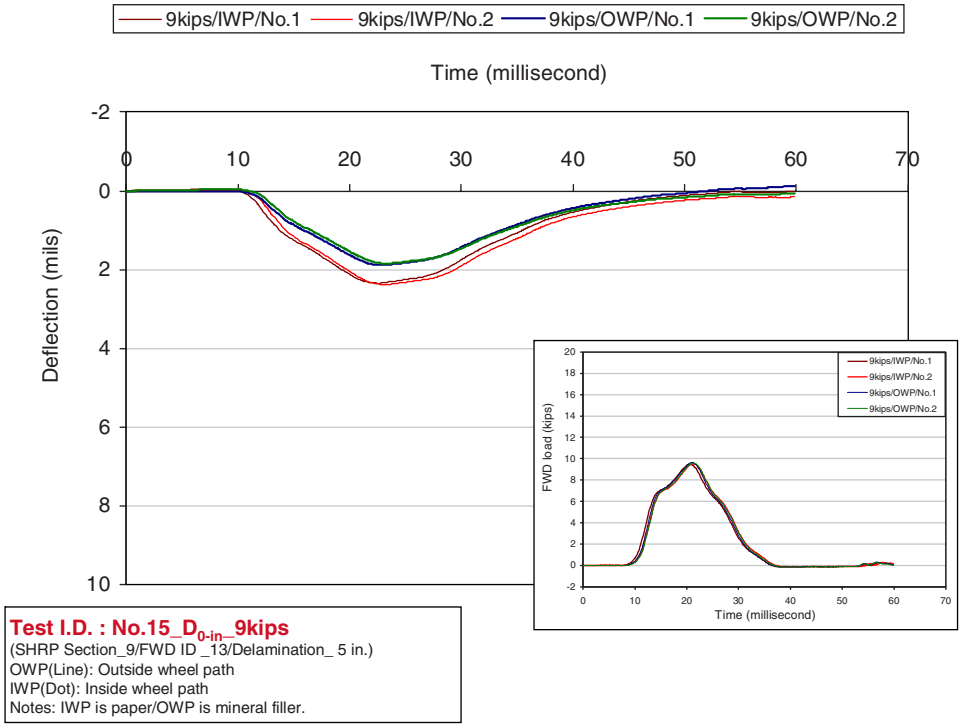

Figure 7.123. FWD deflection ($D_{0\text{-}in}$) time history under 9-kips loading for FWD Test 15 at NCAT Section 9.

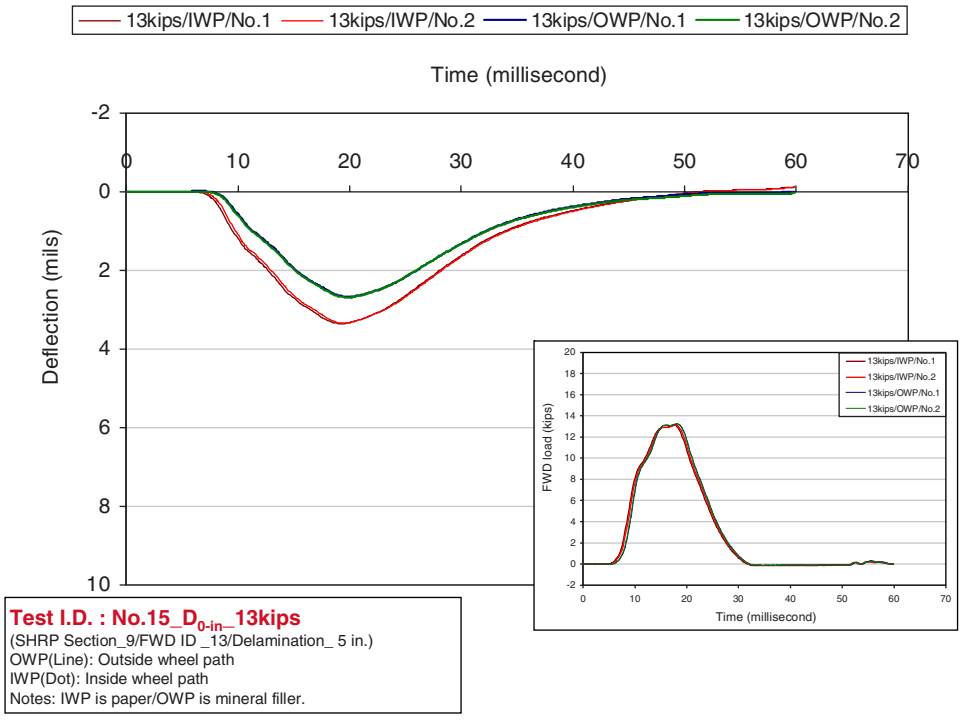

Figure 7.124. FWD deflection ($D_{0\text{-}in}$) time history under 13-kips loading for FWD Test 15 at NCAT Section 9.

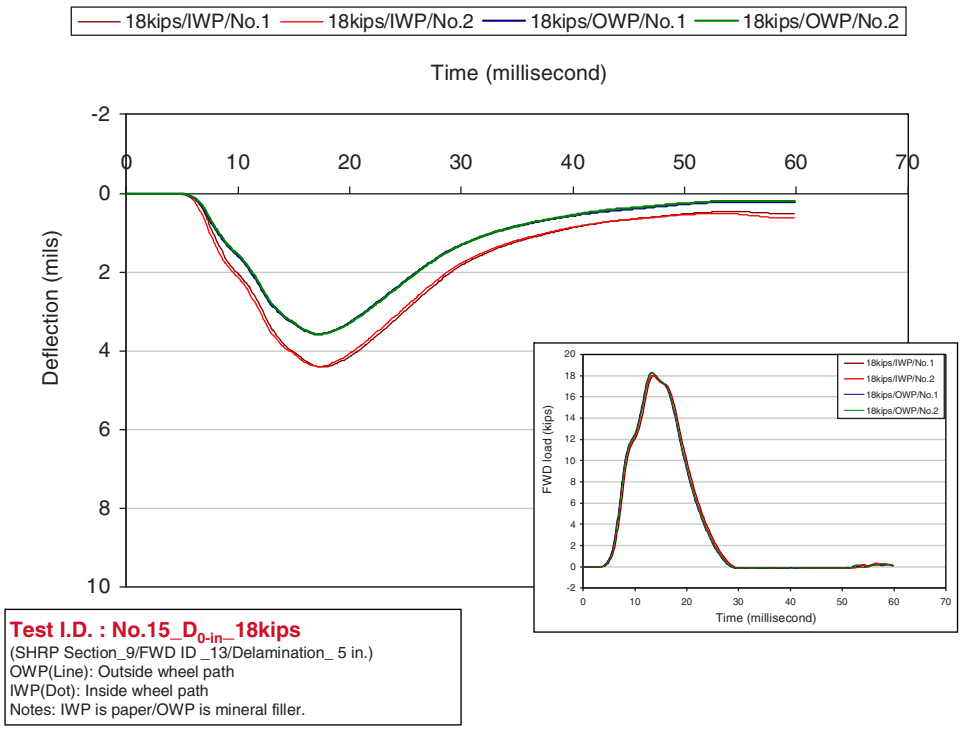

Figure 7.125. FWD deflection ($D_{0\text{-}in}$) time history under 18-kips loading for FWD Test 15 at NCAT Section 9.

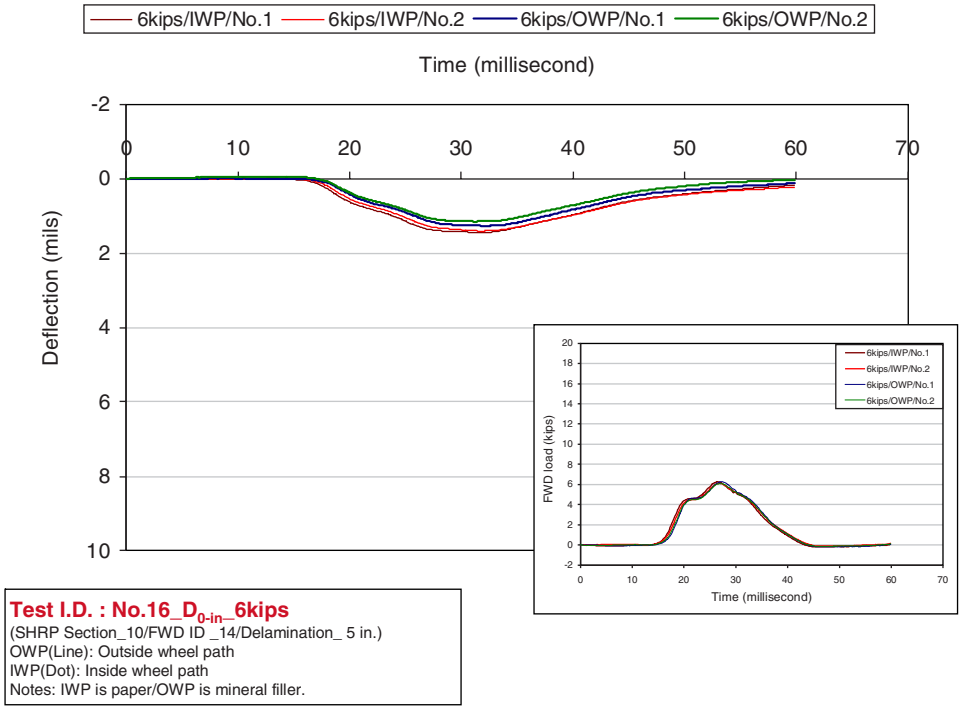

Figure 7.126. FWD deflection ($D_{0\text{-}in}$) time history under 6-kips loading for FWD Test 16 at NCAT Section 10.

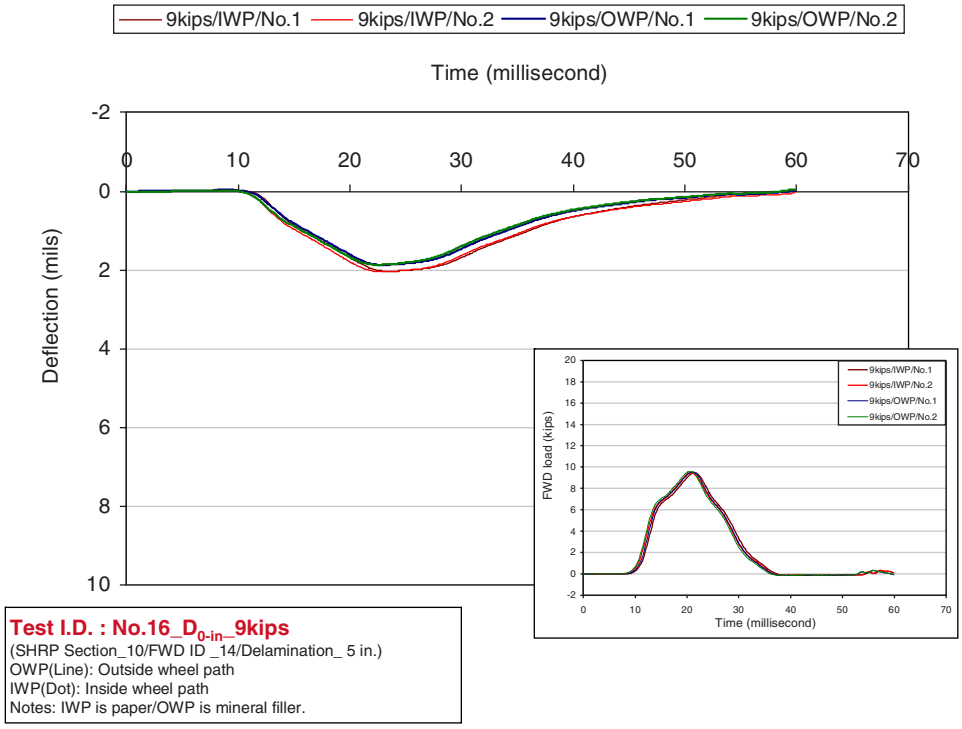

Figure 7.127. FWD deflection ($D_{0\text{-}in}$) time history under 9-kips loading for FWD Test 16 at NCAT Section 10.

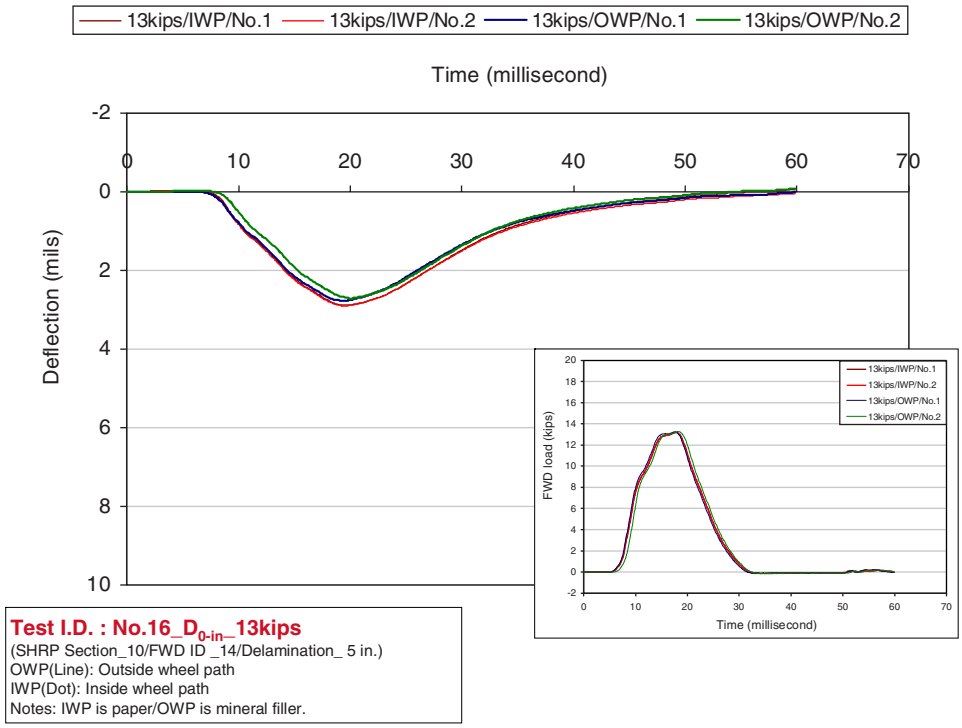

Figure 7.128. FWD deflection ($D_{0\text{-}in}$) time history under 13-kips loading for FWD Test 16 at NCAT Section 10.

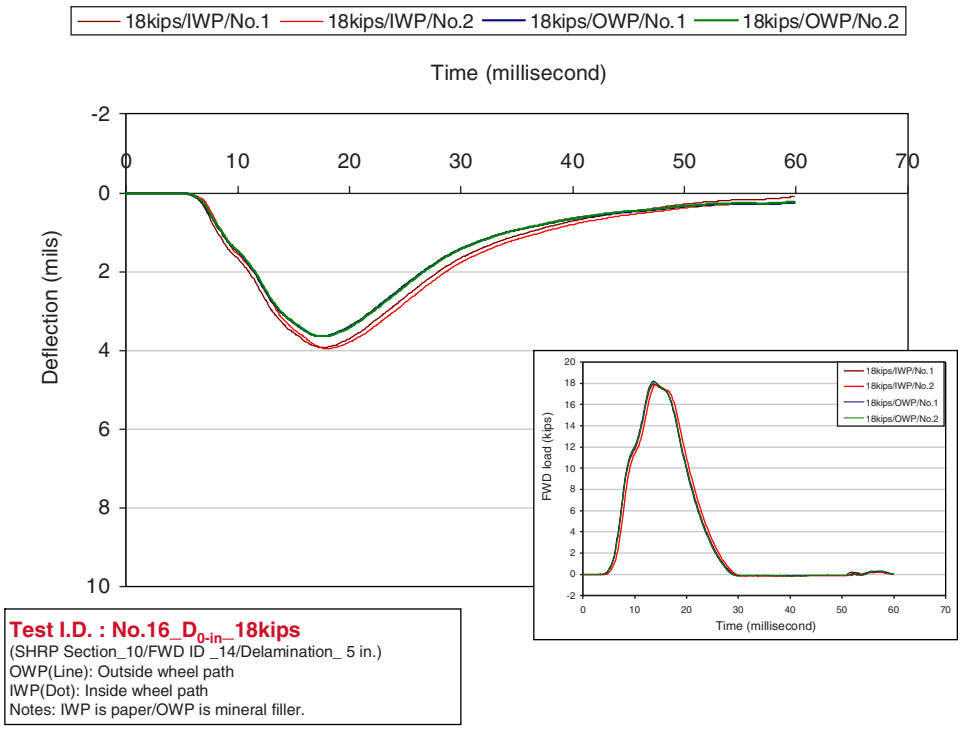

Figure 7.129. FWD deflection ($D_{0\text{-}in}$) time history under 18-kips loading for FWD Test 16 at NCAT Section 10.

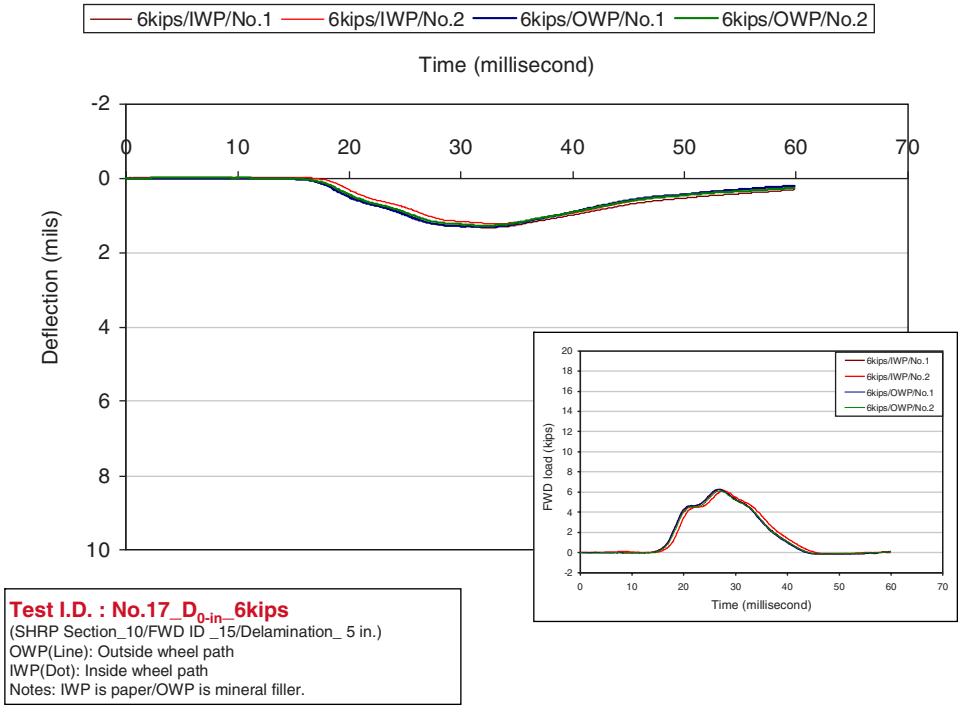

Figure 7.130. FWD deflection ($D_{0\text{-}in}$) time history under 6-kips loading for FWD Test 17 at NCAT Section 10.

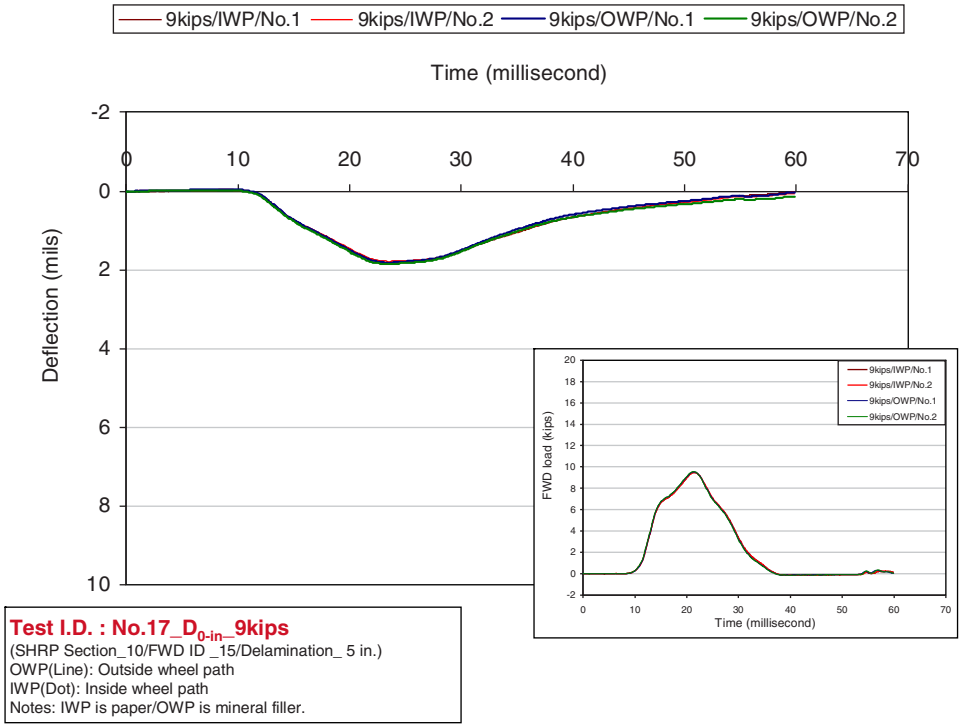

Figure 7.131. FWD deflection ($D_{0\text{-}in}$) time history under 9-kips loading for FWD Test 17 at NCAT Section 10.

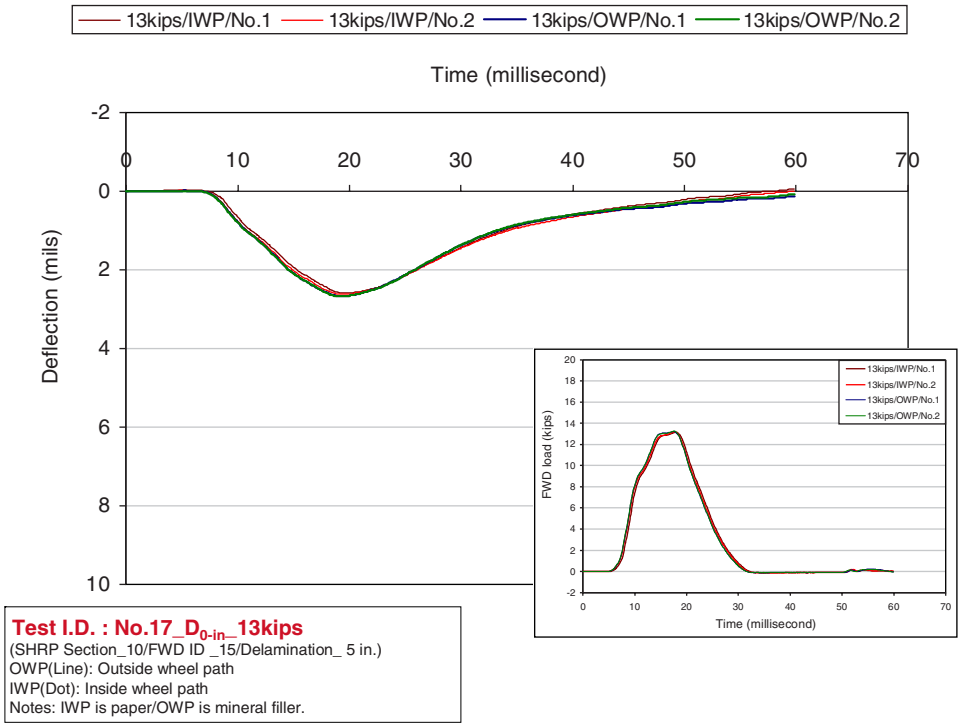

Figure 7.132. FWD deflection ($D_{0\text{-}in}$) time history under 13-kips loading for FWD Test 17 at NCAT Section 10.

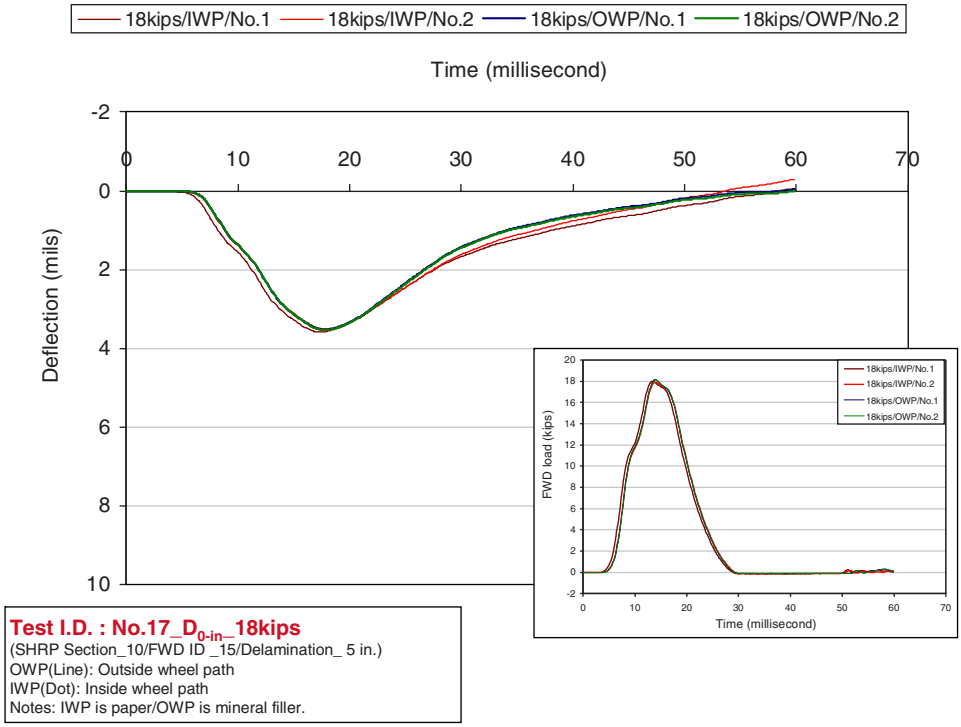

Figure 7.133. FWD deflection ($D_{0\text{-}in}$) time history under 18-kips loading for FWD Test 17 at NCAT Section 10.

Summary

On the basis of this study, the following findings and recommendations for future research were drawn.

Major Findings

- In terms of the maximum deflections for each sensor/geophone, there is no significant difference in FWD measurements in NCAT sections with and without delamination. This result is due to the high thickness and strong pavement sublayers of the NCAT test sections.
- By accounting for FWD time-history data, there is a higher possibility of detecting the presence of delamination in test sections, especially if there is an intact control section to do comparisons.
- Although there is no significant difference in peak FWD measurements between delaminated and intact pavement sections, there seems to be a difference especially in the unloading portion of the FWD time history data for these sections.
- The BISAR model can be used to characterize the effect of delamination in terms of vertical deflections for conventional HMA pavement systems.
- The BISAR model seems to overestimate the vertical deformations for the assumed pavement layer moduli values for the NCAT HMA pavement test sections. This overestimation can easily be fixed by changing the moduli values assigned for each pavement layer.
- Performing the backcalculation of pavement layer moduli is not easy because of the complex history of the NCAT test sections (e.g., variations in pavement thickness values, having thicker HMA and HMA base layers, the presence of an RAP layer, the compaction of the pavement foundation during past traffic loadings).

Recommendations for Future Research

- New flexible pavement sections are needed with relatively thin HMA layers for better study of the detection of delaminations with FWD testing. There will be a higher contrast in FWD readings between the delaminated and intact cases for such test sections. This outcome can be easily achieved during the identification of flexible pavement sections for future testing.
- The FWD is more effective during the cool-weather testing than during the hot-weather testing for delamination-detection purposes. One concern with the FWD testing is the number of false positive readings (estimating low modulus for intact point), especially during the high-temperature testing.
- For conventional HMA pavements, it is possible to use peak FWD measurements for delamination detection with temperature correction of FWD deflection readings.

- Temperature corrections need to be done for the FWD readings before performing the pavement layer backcalculation task.
- For HMA overlaid pavements having complex construction history (e.g., NCAT test sections), FWD time-history data for delamination detection is a more promising resource. This finding, however, requires more in-depth investigation. FWD data from future test sections can be used for such purposes.
- FWD tests should be conducted on the same location with the same pavement structure (having the same thickness and moduli values for each pavement layer) for control (intact) and delaminated test sections (such as Test 6 of NCAT FWD tests). With this approach, FWD readings and time histories can then easily be compared with each other for each pavement case.
- Higher FWD load levels should be considered to better study the impact of delaminations. A bigger FWD loading plate should be considered for thick HMA pavement sections, especially if the delaminated layers are located deep in the pavement system.

References

Al Hakim, B., H. Al Nageim, D. Pountney, and L. Lesley. 1997. The Development of an Improved Pavement Backcalculation. *Proc., 1st International Conference on Rehabilitation and Development of Civil Engineering Infrastructure Systems,* Lebanon.

Al Hakim, B., R. Armitage, and N. H. Thom. 1998. Pavement Assessment Including Bonding Condition: Case Studies. *Proc., 5th International Conference on Bearing Capacity of Roads and Airfields,* University of Trondheim, Norway, Vol. 1, pp. 439–448.

Al Hakim, B., L. W. Cheung, and R. Armitage. 2000. Use of FWD Data for Prediction of Bonding Between Pavement Layers. *International Journal of Pavement Engineering,* Vol. 1, No. 1, pp. 49–59.

Claessen, A. I. M., J. M. Edwards, P. Sommer, and P. Uge. 1977. Asphalt Pavement Design—The Shell Method. *Proc., 4th International Conference on Structural Design of Asphalt Pavements,* Vol. 1, pp. 39–74.

DeJong, D. L. 1973. *Computer Program: BISAR.* Royal/Shell Laboratory, External Report AMSR 0006.73, Amsterdam, Netherlands.

Gomba, S. M. 2004. *Evaluation of Interlayer Bonding in Hot Mix Asphalt Pavements.* MS thesis. Rowan University, Glassboro, N.J.

Gopalakrishnan, K. 2004. *Performance Analysis of Airport Flexible Pavement Subjected to New Generation Aircraft.* PhD dissertation, University of Illinois at Urbana–Champaign.

Hammons, M., H. Von Quintus, K. Maser, and S. Nazarian. 2005. *Detection of Stripping in Hot-Mix Asphalt.* Applied Research Associates Report 16355 for Georgia Department of Transportation.

Hill, H. J., and M. R. Thompson. 1988. Early Life Study of the FA409 Full-Depth Asphalt Concrete Pavement Sections. Unpublished University of Illinois research report, University of Illinois at Urbana–Champaign.

Kruntcheva, M. R., A. C. Collop, and N. H. Thom. 2000. *The Portable Seismic Pavement Analyzer: Laboratory Trials.* Project Report PGR 2000-02, University of Nottingham, United Kingdom.

Lepert, P., J. P. Poilane, and M. Villard-Bats. 1992. Evaluation of Various Field Measurement Techniques for the Assessment of Pavement Interface Condition. *Proc., 7th International Conference on Asphalt Pavements,* Vol. 3, pp. 224–237.

Nazarian, S., D. Mejía, C. Celaya, S. Iyer, C. Rao, and P. Shokouhi. 2008. *A Work Plan toward Evaluation of Technologies to Assess Presence and Extent of Delamination of HMA Airfield Pavements.* Interim Report for AAPTP Research Project 06-04, Center for Transportation Infrastructure Systems, The University of Texas at El Paso.

Nazarian, S., C. Celaya, D. Mejía, S. Ertem, C. Rao, F. Von Quintus, and P. Shokouhi. 2010. *Evaluation of NDT Technologies to Assess Presence and Extent of Delamination of HMA Airfield Pavements.* Final Report for AAPTP Research Project 06-04, Center for Transportation Infrastructure Systems, The University of Texas at El Paso.

Peutz, M. G. F., H. P. M. Van Kempen, and A. Jones. 1968. Layered Systems Under Normal Surface Loads. *Highway Research Record, No. 228,* HRB, National Research Council, Washington, D.C., pp. 34–45.

Xu, B., S. R. Ranjithan, and Y. R. Kim. 2001. Development of Relationships Between FWD Deflections and Asphalt Pavement Layer Condition Indicators. Presented at 81st Annual Meeting of the Transportation Research Board, Washington, D.C.

Related SHRP 2 Research

Nondestructive Testing to Identify Concrete Bridge Deck Deterioration (R06A)

Evaluating Applications of Field Spectroscopy Devices to Fingerprint Commonly Used Construction Materials (R06B)

Using Infrared and High-Speed Ground-Penetrating Radar for Uniformity Measurements on New HMA Layers (R06C)

Real-Time Smoothness Measurements on Portland Cement Concrete Pavements During Construction (R06E)

Assessment of Continuous Pavement Deflection Measuring Technologies (R06F)

Mapping Voids, Debonding, Delaminations, Moisture, and Other Defects Behind or Within Tunnel Linings (R06G)